Université Blaise Pascal – Clermont-Ferrand II
(U.F.R. de Recherche Scientifique et Technique)

ÉCOLE DOCTORALE DES SCIENCES FONDAMENTALES

THÈSE

Présentée pour obtenir le grade de

DOCTEUR D'UNIVERSITÉ

Spécialité : Volcanologie

par

Mathieu GOUHIER
Diplômé de Master Recherche

Application du radar Doppler (VOLDORAD) à l'étude de la dynamique des éruptions Stromboliennes de l'Etna

Soutenue publiquement le 28 Novembre 2008 devant la commission d'examen composée de :

Patrick ALLARD	Laboratoire Pierre Süe, CE – Saclay	Rapporteur
Mauro COLTELLI	INGV – Sezione di Catania (Italia)	Rapporteur
Sylvie VERGNIOLLE	Institut de Physique du Globe de Paris	Examinatrice
Jean-François LÉNAT	Université Blaise Pascal, Clermont-Ferrand II	Président
Franck DONNADIEU	Université Blaise Pascal, Clermont-Ferrand II	Directeur de thèse
Timothy DRUITT	Université Blaise Pascal, Clermont-Ferrand II	Directeur de thèse

Université Blaise Pascal – Clermont-Ferrand II
(U.F.R. de Recherche Scientifique et Technique)

ÉCOLE DOCTORALE DES SCIENCES FONDAMENTALES

THÈSE

Présentée pour obtenir le grade de

DOCTEUR D'UNIVERSITÉ

Spécialité : Volcanologie

par

Mathieu GOUHIER
Diplômé de Master Recherche

Application of Doppler radar (VOLDORAD) to the study of Strombolian eruptions dynamics at Etna

Soutenue publiquement le 28 Novembre 2008 devant la commission d'examen composée de :

Patrick ALLARD	Laboratoire Pierre Süe, CE – Saclay	Rapporteur
Mauro COLTELLI	INGV – Sezione di Catania (Italia)	Rapporteur
Sylvie VERGNIOLLE	Institut de Physique du Globe de Paris	Examinatrice
Jean-François LÉNAT	Université Blaise Pascal, Clermont-Ferrand II	Président
Franck DONNADIEU	Université Blaise Pascal, Clermont-Ferrand II	Directeur de thèse
Timothy DRUITT	Université Blaise Pascal, Clermont-Ferrand II	Directeur de thèse

F. Liszt (Mazeppa)

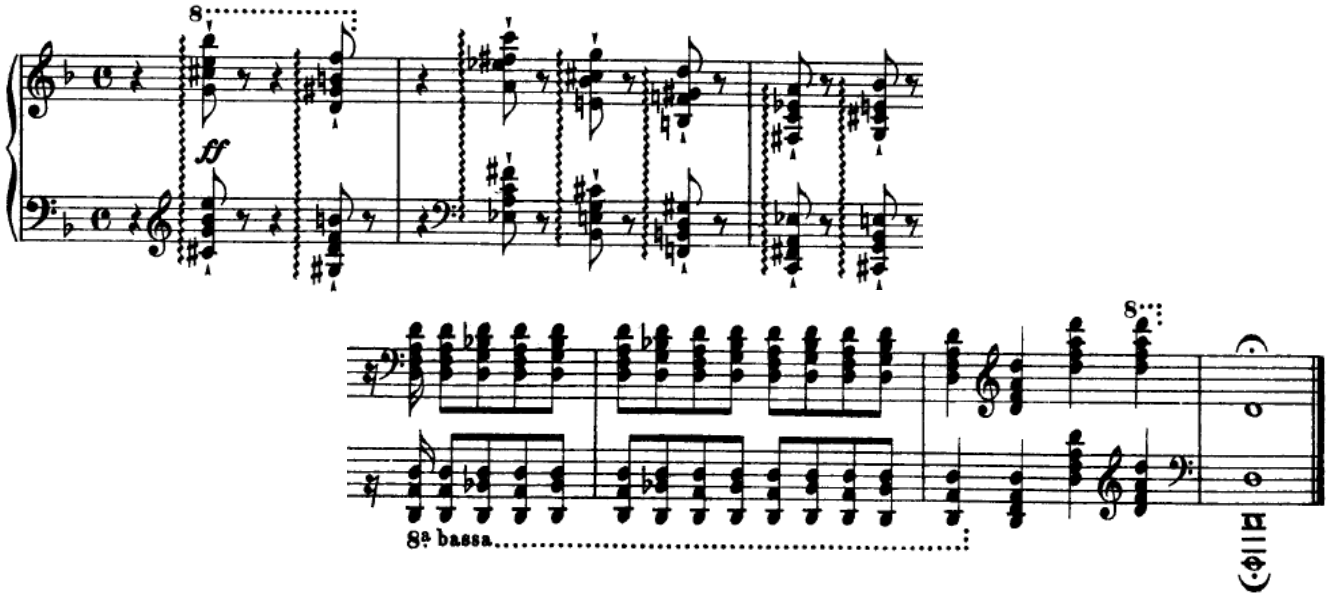

«Il tombe enfin!... et se relève Roi!»
(Victor Hugo.)

REMERCIEMENTS

Tout d'abord, je tiens à remercier aussi sincèrement que chaleureusement Franck Donnadieu pour son encadrement sur ce sujet technique et tout à fait nouveau. Merci de m'avoir fait confiance en me laissant notamment beaucoup d'autonomie et d'indépendance dans la réalisation de mon travail de thèse. Tu as été encadrant et collaborateur à mon sens, ce qui m'a permis, je crois, une vraie émancipation dans ma démarche de recherche, grâce notamment, aux nombreux conseils et discussions que nous avons pu avoir. J'ai beaucoup apprécié nos relations de travail, avec simplicité et bonne humeur, ce qui est à mon avis, indispensable au bon déroulement d'un travail en collaboration. Dès le DEA, où nous avons fait du terrain ensemble au Costa Rica, mais aussi par la suite, j'ai pu apprécier tes qualités humaines qui m'ont rendu ces quatre années fort agréables. J'espère ainsi que nous aurons à nouveau l'occasion de travailler ensemble.
Merci à mon deuxième directeur de thèse: Tim Druitt, notamment pour son aide quant à la rédaction des articles de ma thèse, mais aussi pour ses précieux conseils et son expérience.
Merci au Laboratoire Magmas et Volcans et les deux directeurs que j'ai connu pendant ces quatre années, Olivier Merle et Pierre Schiano, pour m'avoir permis la réalisation de ce travail de thèse.

Mes remerciement se tournent maintenant vers les personnes sans qui ce travail sur VOLDORAD n'aurait pas pu être réalisé, je veux parler de tous ceux qui ont contribué de près ou de loin à la réalisation de ce projet à Clermont-Ferrand, depuis sa germination jusqu'à la fabrication du radar et à l'acquisition des données à l'Etna, en particulier J. Kornprobst, G. Dubosclard, Roland Cordesses, Claude Hervier, Jacques Fournet-Fayard ainsi que l'ensemble des membres du Service de Développement Technique de l'OPGC. Les soutiens durables de Jean-François Lénat, Timothy Druitt, Claude Jaupart (contrat INSU-PNRN) et de Patrick Allard (contrat CEE MVRRS: Monitoring Volcanic Risks by Remote Sensing, ENV4-CT96-288, coordonné par Peter Francis) ont également été très précieux.

Un grand merci à Sylvie Vergniolle, tout d'abord pour avoir mis à disposition ses données acoustiques, mais surtout pour son aide indispensable sur ce travail de corrélation radar-acoustique. Merci a Patrick Allard qui a contribué aux mesures radar des 4, 7, 13 Juillet 2001, pour avoir effectué seul les mesures radar des 29 et 31 Juillet, et fourni ses enregistrements vidéo.

Je tiens aussi à remercier le jury d'avoir accepté de juger mon travail, et permis l'amélioration de mon manuscrit de thèse : les rapporteurs Patrick Allard et Mauro Coltelli, Sylvie Vergniolle en tant qu'examinatrice, et le président du jury Jean-François Lénat.

A présent mes remerciements se tournent vers mes collègues : des thésards avant tout ! Je vais être bref et non exhaustif sinon je crois que je devrais écrire une seconde thèse rien que de « private jokes » et autres spéciales dédicaces. Alors un grand merci à tous pour ces trois années passées entre les quatre murs du LMV où les cinq continents se côtoyèrent tous les jours pour mon plus grand plaisir. Je n'oublie pas non plus les extérieurs J/E/R qui se reconnaîtront…il est loin le temps du gormen's.

Je souhaite maintenant remercier ma famille qui fut toujours à mes coté pendant toutes ces années d'études…et même avant ! Enfin, mes plus grands mercis se tournent vers la personne la plus chère à mon cœur, ma mie : Armelle, qui a aussi passé pas mal de temps avec VOLDORAD ces trois dernières années. Elle m'a apporté tellement que ces quelques mots ne suffisent évidemment pas à retranscrire l'importance et la nécessité de sa présence à mes cotés.

Abstract

VOLDORAD, a low power UHF Doppler radar, is a portable ground-based system, developed by the Observatoire de Physique du Globe de Clermont-Ferrand (France), especially for the study of explosive volcanic activity. The capabilities of such remote sensing methods to probe safely hazardous eruption jets and plumes constitute a real step forward regarding the in-depth analysis of physical processes controlling the dynamics of volcanic eruptions. The main objective of this work is to bring more stringent constraints, particularly from the development of methodological procedures, on the interpretation of Doppler radar data, with the final aim of better understanding the explosive dynamics. This study has been achieved from Doppler radar measurements carried out at Etna Southeast crater during the eruption of July 4, 2001, and focused on the Strombolian activity. However, processing methods, theoretical forward models and inversion procedures developed here have been achieved with the scope of a more general application, i.e., for various types of eruptions. The thorough analysis of Strombolian explosions by ground-based Doppler radar has permitted to obtain a wide range of source parameters, mainly related to kinetic, loading and geometrical features. Accurate quantitative assessment of these parameters and their evolution with time is crucial for (1) monitoring and early warning of active volcanoes, and (2) to provide better constraints on assumptions included in models of eruptive dynamics, useful for the volcanological community, as well as for ash dispersal prediction models used for risk mitigation.

Résumé

VOLDORAD, un radar Doppler UHF moyenne puissance, est un système portable basé au sol, développé par l'Observatoire de Physique du Globe de Clermont-Ferrand (France), spécifiquement pour l'étude de l'activité volcanique explosive. La capacité de ces méthodes de télédétection à sonder l'intérieur des jets et des panaches volcaniques dangereux constitue un vrai pas en avant concernant l'analyse des paramètres physiques qui contrôlent la dynamique des éruptions volcaniques. L'objectif principal de cette thèse est d'apporter des contraintes plus précises, notamment à partir du développement de procédures méthodologiques, sur l'interprétation des données radar Doppler, dans le but final d'améliorer notre compréhension de la dynamique explosive. Ce travail a été réalisé à partir de mesures radar Doppler acquises pendant l'éruption du cratère Sud-est de l'Etna en Juillet 2001, et s'intéresse plus particulièrement à l'activité Strombolienne. Cependant, les méthodes de traitement, les modèles directs et les procédures d'inversion développés dans cette étude ont été réalisés dans une optique plus générale, et applicable sur différents types de dynamismes. L'étude détaillée de l'activité Strombolienne par la méthode radar Doppler a permis d'obtenir une large gamme de paramètres sources, notamment : les vitesses et masses de gaz et de particules, ainsi que les caractéristiques géométriques des jets. L'estimation quantitative précise de ces paramètres, et de leur évolution au cours du temps est cruciale pour (1) la surveillance et la détection précoce de l'activité volcanique, ainsi que (2) pour l'apport de contraintes sur les hypothèses formulées dans les modèles de dynamique éruptive et dans les modèles de prédiction de dispersion des cendres, indispensables à la minimisation des risques.

CONTENTS

INTRODUCTION

Volcanoes: a dynamic phenomenon actively displaying tremendous spectacles, remain the seat of too often unexpected killing disasters, reminding us the importance of better understanding eruptive mechanisms.

The study of eruptive dynamics is however very complex, particularly because of the spatial evolution of physicochemical processes integrated over the whole edifice scale. Indeed, the diversity of volcanic surface activities is the result of deeply rooted mechanisms emerging from the chamber (bubble nucleation and coalescence, foam collapsing, etc.) and evolving in the conduit (exsolution, coalescence, gas overpressurisation and fragmentation) up to the free surface of the magma column (bubble expansion and bursting, lava clots ejection). Moreover, the evolution of these processes on various time scales adds to the difficulties of understanding eruption dynamics. Besides, some technical difficulties of measurements related to huge and hazardous volcanic phenomena also make the study of volcanic activity not easy. Indeed, in some cases, *in situ* measurements are unfeasible, particularly for the explosive dynamics (Strombolian activity, ash plumes or pyroclastic flows), but also regarding deep mechanisms occurring from the magma chamber to the conduit surface. Therefore, remote sensing instruments turn out to be key tools for in-depth analysis of integrated eruptive processes. Many remote sensing techniques have been used for a few decades in order to better understand the dynamics of explosive eruptions. Satellite imagery and ground-based weather radars have been used rather to monitor the long-range evolution of ash dispersion than dynamics itself.

A major challenge is now to measure physical quantities closer to the vent in order to retrieve directly the true source parameters (1) that potentially provide more stringent constraints on the eruption dynamics, and (2) that permits close volcano monitoring for early warnings and risks mitigation: such is the purpose of this thesis.

In this work, we focus on the study of Strombolian dynamics at Mount Etna volcano by means of a pulsed ground-based Doppler radar (VOLDORAD = **Vol**cano **Do**ppler **Rad**ar) developed by the Observatoire de Physique du Globe de Clermont-Ferrand (France) specifically for the sounding of explosive volcanic activity. First studies, carried out at Etna during the eruption of October 1998 (Dubosclard et al., 1999, 2004) for the testing of VOLDORAD, had pointed out the great potential of Doppler radar techniques for volcanic applications. Further works realized at Etna (Italy) during the eruption of July-August 2001,

and at Arenal volcano (Costa Rica) in February 2004, have proved the powerful capabilities of VOLDORAD to retrieve quantitative estimates of source parameters on various types of volcanic activity (Donnadieu et al., 2003, 2005). A second step has been achieved in this thesis with the retrieval of loading parameters (Gouhier and Donnadieu, 2008). In addition, some efforts have been made in the understanding of Doppler radar signals for a better interpretation of kinetic and geometric parameters particularly.

The analysis of surface processes by ground-based Doppler radar potentially permits to obtain two sets of fundamental parameters: (1) velocimetric parameters (e.g., particle and gas velocities, gas fluxes, kinetic energy), and (2) loading parameters (e.g., ejected particle mass, ejecta concentration, volume, mean particle diameter, mass fluxes, thermal energy). Furthermore, information on geometrical features of lava jets and plumes can also be assessed.

This thesis work has particularly focused on the development of methodological procedures that aimed at improving our interpretation of the Doppler radar data, with the final goal of better understanding eruption processes and source parameters valuable to the volcanological community. This work has been achieved from Doppler radar measurements carried out at Etna southeast crater (SEC) during episodes of Strombolian activity in July 2001. Nevertheless, processing methods, theoretical forward models and inversion procedures developed in this study have been realized with the scope of a more general application, i.e., for various types of eruptive dynamisms, ranging from mild Strombolian activity to large ash plumes. Thus, we did not aim at investigating in depth physical mechanisms at work at Etna but rather to develop some general tools that could be further used routinely in volcano monitoring as well as for scientific investigations of a given eruptive behaviour. Mount Etna is rather used as first-rate example of explosive basaltic volcano to test and improve the interpretations of Doppler radar data.

Also, comparisons with other techniques (video, acoustic) probing the same object but with different angle shots has been carried out. Video methods portray the surface activity as well as VOLDORAD and hence permit close correlations valuable to validate interpretations of Doppler radar signals. Acoustic methods are particularly interesting to describe shallow processes at the interface between the surface and the chamber. Comparisons with Doppler radar signals must bring interesting constraints on the decoupling of physical processes from depth to the surface. Comparisons between Doppler radar and other techniques that represent

a smaller part of this thesis have to be regarded as preliminary works. However, they appear promising in the study of eruption dynamics to unravel the links between degassing processes at depth and the surface eruptive behaviour of a volcano.

The first chapter of this manuscript gives a brief overview of the volcanological context at Mt. Etna: the explosive basaltic dynamism and particularly the description of the eruption that took place in July, 2001. We then review remote sensing techniques applied to volcanic eruptions described in the literature.
The second chapter is devoted to the detailed presentation of VOLDORAD, whose data have been used extensively, and more generally to the Doppler radar technique.

In a first part, that comprises the chapters III, IV and V, we focus on the study of Doppler radar data, in particular for the analysis of kinetic, loading and geometrical features:

- The third chapter is devoted to the study of Doppler radar velocity measurements from a coupled approach with ballistic numerical modelling and video analysis. We particularly focus on gas/particle discrimination, and quantitative assessment of source parameters such as initial gas and particle velocities.
- In chapter four we present a method to estimate particle loading parameters (mass, volume, concentration, mean particle diameter particularly) of eruptive jets by inversion of echo-power data measured by VOLDORAD. The automatic inversion algorithm uses the complete Mie (1908) formulation of electromagnetic scattering waves. We also present an alternative approximation specifically devoted to the rapid assessment of loading parameters for real-time volcanic monitoring purposes.
- The fifth chapter presents a complete synthetic model of Doppler radar spectra devoted to the understanding of geometrical properties of Strombolian jets, based on both ballistic and electromagnetic scattering models mentioned previously.

The second part, which comprises the chapters VI and VII, is devoted to the correlations of acoustic-video and acoustic-radar methods:

- In chapter six we focus on acoustic and video measurements for the study of bubble oscillation and bursting mechanisms at the top of the magma column. In spite of some difficulties related to the visual observations, the thorough analysis of video snapshots permits to build video-derived acoustic waveforms subsequently compared with

recorded acoustic waveforms. In addition, by best fit matching of synthetic acoustic waveforms generated by a theoretical bubble vibration model with video-derived and recorded acoustic waveforms, we can estimate crucial physical parameters such as bubble overpressure and volume.

- In the last chapter, we have carried out preliminary correlations between acoustic and radar measurements. Processes recorded by these two methods are different but directly linked, as the overpressurized bubble bursting is at the origin of the fragmentation and ejection of lava clots subsequently recorded by VOLDORAD.

CHAPTER I

Basics of explosive dynamics at Mt. Etna and introduction to remote sensing methods in volcanology

I.1 Mt. Etna Volcano and its explosive dynamisms

We present here some general elements related to the geological framework of Mount Etna Volcano and some basics related to the explosive dynamism. However, bearing in mind the technical purposes of this thesis that shed light on methodological aspects rather than focusing on the volcanic dynamism itself, we just aim at giving a brief introduction necessary to the understanding of that work.

I.1.1. Volcanological context of Mt. Etna

I.1.1.1. Geodynamical setting

Mount Etna is the largest European active volcano covering an area of 1250 km² and reaching 3340 m elevation. It lies on the Sicilian continental crust (30 km thick), at the boundary with the African and European plates (Figure I.1), and the Ionian micro-plate constituted by a thinner (10-12 km) oceanic crust that undergoes subsidence and consumption below Calabria (Scandone et al., 1981).

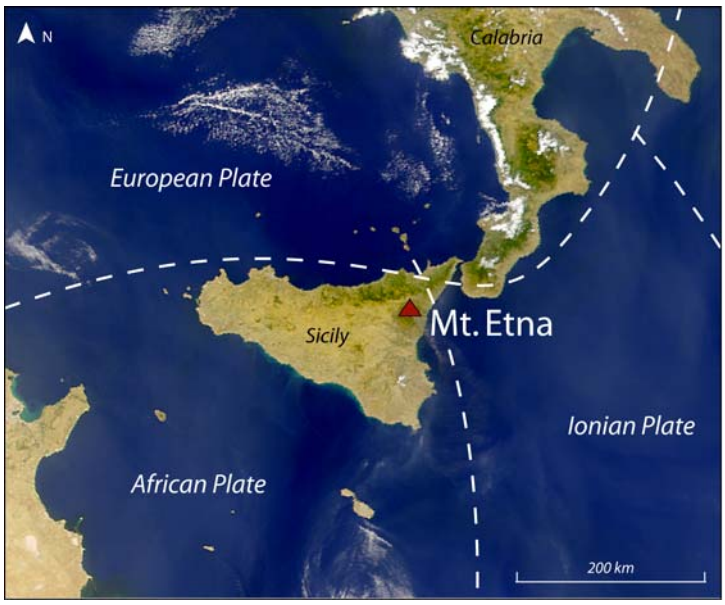

Figure I.1. Satellite-based view of Mt. Etna (Sicily) showing its focal position between African/European plates, and the Ionian micro-plate (courtesy of NASA).

The geodynamical context of Mt. Etna volcano is complex and the origin of the volcanism is still a matter of debate. Hotspot origin has long been suggested associated with upwelling of deep mantle material (e.g., Tanguy et al., 1997; Clocchatti et al., 1998), but more recent studies have also pointed out the possible contribution of subduction-related mechanisms (Schiano et al., 2001). Further shallow structural processes have been proposed to explain the edification of Mt. Etna. As many volcanoes, it was first assumed that Etna derives from an extensional strain field. On the contrary, taking into account the regional framework of eastern Sicily, Lentini (1982) concludes that Etna functions in a sector undergoing compression. More recent studies, owing to the distribution of the discontinuities have suggested that recent volcanic activity at Etna is controlled by deep-seated "rift zones" oriented mainly N-S, (e.g., Tanguy and Kieffer., 1993; Lanzafame et al., 1997b). Numerous geophysical studies (e.g., Chiarabba, 2000; Patanè et al., 2002) have provided some constraints on the structure of the crust that revealed two main units: the first one is constituted (0 – 3.5 km) of flysch nappes and the second one (3.5 – 10 km) of carbonated nappes. These sediments lie on 8 – 10 km of crystalline crust constituted of metamorphic rocks. This substratum is intersected by a wide plutonic body that represents the dykes' network of the feeding system.

I.1.1.2. Past activity and Etna edification

The earliest geological studies of Etna volcano were performed during the first half of the 19th century (e.g., Gemmellaro, 1858). They compiled the first geological map of Etna and performed the first stratigraphic studies that allowed them to recognize the polygenetic origin of the volcano. More recent stratigraphic and structural data (e.g., Rittman, 1973, Branca et al., 2004) have allowed subdividing the almost continuous evolution of Etnean volcanism into four main phases lying from about 600 Ka to present day.

(1) The first phase, called pre-etnean (600-250 ka) consists mainly of sub-alkaline tholeiitic basalts (Condomines et al., 1995). (2) The Timpe phase, (250-100 ka) is related to a volcanism that crop out in the lower and intermediate portion of tectonic escarpments locally known as Timpe (Corsaro et al., 2002). In the volcanic succession formed during that period, the transition from sub-alkaline to alkaline lavas is recorded. (3) During the Valle del Bove phase (80- 40 ka), the products emitted are essentially lava flows. These rocks mostly outcrop in the walls of the Valle del Bove, forming stratigraphic sections (Gillot et al., 1994). Lavas compositions vary from hawaiitic to benmoreitic. (4) The stratovolcano phase, (40 ka to

present day), is related to an eruptive activity that was essentially fed by two central volcanic edifices: Ellitico and Mongibello, which lavas composition range from alkali-basalts to trachytes. If current Etna's activity is at the present time considered to be the site of mild explosive eruptions, such as Strombolian activity, to effusive eruptions, note however that in the past 100 ka, several main periods of subplinian to plinian activity have been recorded (Coltelli et al., 2000, Del Carlo et al., 2004). After the end of Ellitico activity, Mongibello activity started filling the caldera with its products and built the volcano edifice from which the historical and present activity originates (Gillot et al., 1994; Condomines et al., 1995). Nowadays, the Mt. Etna activity is mainly located north-westward to the Valle del Bove, and centred on four summit craters: Northeast crater, Voragine, Bocca Nuova and Southeast Crater.

I.1.2. Eruptive dynamics at Etna

Mount Etna is among the few volcanoes on Earth that erupt nearly continuously, emitting large amount of gas even during quiescence periods (Allard et al., 1991). As a comparison, SO_2 emissions of Mt. Etna volcano represent about 10% of the total amount produced by volcanoes on earth. However, its activity undergoes significant fluctuations in time. The analysis of the eruptive dynamics at Etna (Allard et al., 2006) has revealed the existence of long-term eruptive cycles lasting several centuries, and assumed to reflect a general magma draining from the shallow plumbing system (FigureI.2). On the other hand, short-term eruptive cycles extending over several decades have been pointed out corresponding mostly to the refill of the plumbing system (Behncke and Neri, 2003a,b). Long-term cycles consist of three phases, beginning with low-level activity followed by nearly continuous summit activity and culminating with a series of flank eruptions, the last commonly being the most voluminous. In contrast, short-time eruptive cycles consist of three distinct phases, starting with a short period of quiescence following by increasing activity centred at the summit and ending with a series of flank eruptions (Behncke et al., 2004).

The feeding system at Mt. Etna is complex; nevertheless, many studies carried out in the last few decades, particularly from the tomography, geochemistry and gas analyses have permitted the understanding of the present plumbing system. It has become widely accepted that no major shallow magma reservoir currently exists beneath Etna, the magma thus rises rapidly from the mantle, about 18 – 20 km under the volcano, although shallow magma storage area are necessary to account for the magma differentiation (Corsaro and Pompilio, 2004a,b).

Indeed, geophysical studies (De Gori et al., 2005; Murru et al., 2005) suggest the presence of two main active magma ponding zones at depths of 10±2 km and 5±1 km below the sea level, included in a large plutonic complex 5 – 10 km wide emplaced in the sedimentary basement. Further results, based on the analysis of melt inclusions depth entrapment during flank eruptions of 2001 and 2002-2003, confirm the existence of such a shallow ponding area (Métrich et al., 2004; Spilliaert et al., 2006). Seismic and ground deformation data acquired since 1993, suggest that Etna's magmas ascend across the plutonic body, generating internal overpressures, the shallower ponding zone acting as a temporary storage system that regulates the eruptive activity (Patanè et al., 2003a). Additional studies based on volcanic gas fluxes show that between 1975 – 1995, about 4 times more magma had degassed than extruded, implying that magma degassing is predominantly intrusive in the long term (Allard, 1997).

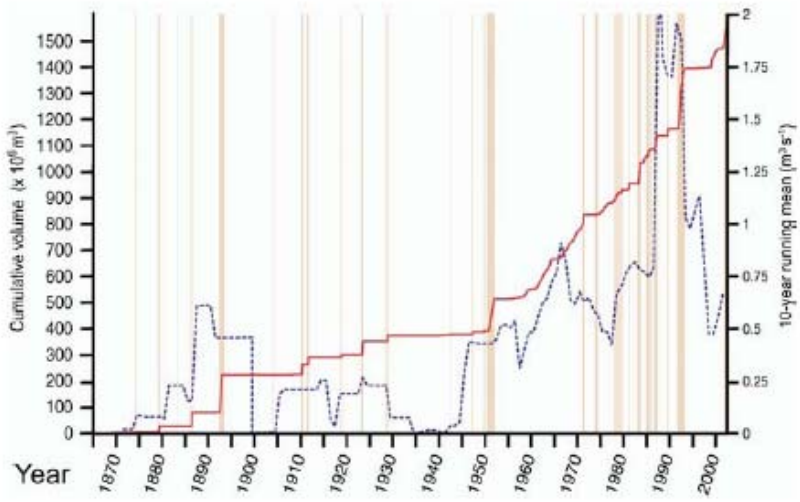

Figure I.2. Plot of cumulated erupted lava volume at Etna between 1865 and 2001 (plain line), and the variation of effusion rate averaged on 10 years (dotted line), from Behncke and Neri (2003a)

I.1.3. The July-August 2001 eruption

The July-August 2001 eruption takes part in a new short-term cycle, initiated in 1993, after a major flank eruption that drained all magma from the shallow plumbing system (Rymer et al., 1995). From April 1993 until July 1995 the activity is characterized by a profound quiescence and only non-eruptive degassing from the summit craters. From late July 1995, the eruptive activity increased progressively, but still confined at the summit craters until the flank eruption of July 17, 2001. Indeed, over 6 years the summit activity had increased progressively starting with lava fountains at Northeast Crater (NEC), followed by explosive paroxysms sometimes reaching Sub-Plinian intensity (Crater Voragine, 1998). Finally, series

of about 100 lava fountains of high intensity arose at Southeast Crater (SEC) in 09/1998 – 02/1999; 01/2000 – 07/2000; and 05/2001 – 07/2001. The progressive increase of the summit activity stresses the refilling of the shallow plumbing system pressurizing until the surfacing of the flank eruption in July 17, 2001 (Figure I.3). Note that flank eruptions are not related to simple magma drainage of the central conduits but rather to the intrusion of distinct dykes propagating from depth.

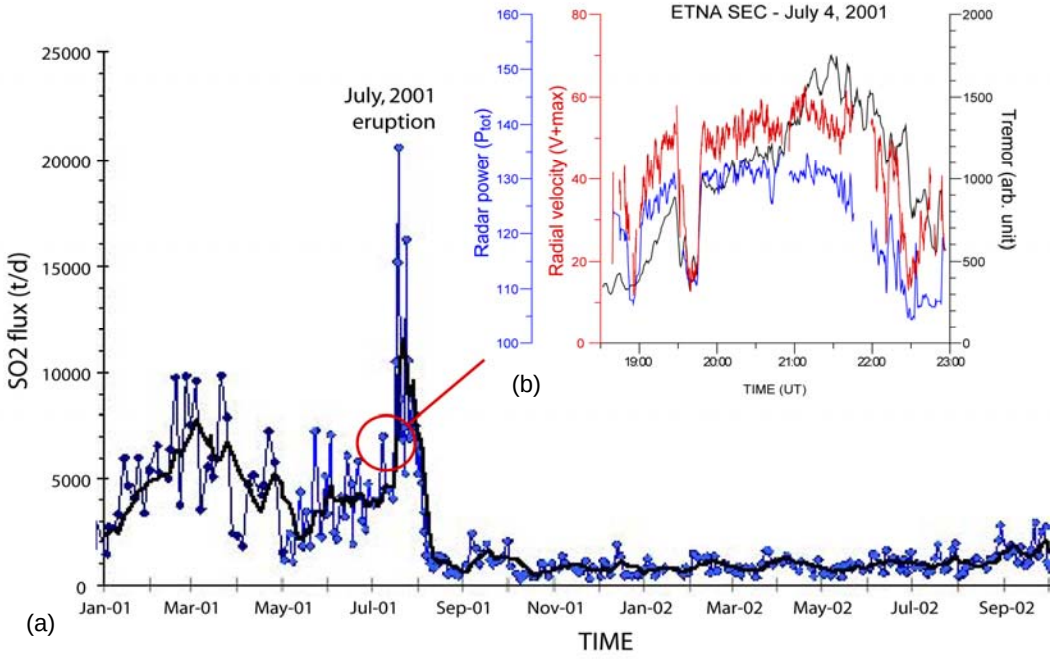

Figure I.3. (a) Plot of SO_2 flux at Mount Etna from January, 2001 to October, 2002 showing particularly a progressive augmentation from May to early July, 2001 followed by a sudden dramatic increase of the SO_2 flux during the flank eruption of July 17, 2001 (courtesy INGV). (b) Focus plot of the maximum radial velocity and radar power evolution during the eruption of July 4, 2001 showing successive periods of quiescence and intense activity with a paroxysm phase between 2100:00 UT and 2200:00 UT as shown simultaneously by the tremor signal (Donnadieu et al., in prep).

In this general context, and after more than 8 months of minor activity (slow lava flows, degassing, light ash emission, and low-level Strombolian activity), a new episode of vigorous activity began at the Southeast Crater on 9 May 2001. From then until July 17, 2001, eruptions occurred at Etna SEC every 3-5 days, each lasting on average a few hours and involving multiple Strombolian explosions and lava fountaining. Doppler radar measurements used for this thesis were carried out over about 5 hours during the eruption of July 4, 2001. The activity began at about 18:00 UT and at first involved small explosions repeated every ~10 s in average. The intensity then increased progressively, culminating in very powerful Strombolian explosions every 2-3 s, with the bursting of very large bubbles sometimes rising above the crater rims, between 21:00 UT and 22:00 UT but without real lava fountains. The

eruption intensity then decreased rapidly from 22:00 UT and ended at 23:00 UT after about five hours of mainly Strombolian activity. This eruption with especially high eruptive intensity showed a typical Strombolian activity, and constitutes an ideal framework for the study of explosive dynamics by mean of remote sensing techniques. Radar measurements carried out in July 7, 13 at Etna SEC, showed an increase in eruptive intensity until the flank eruption. Additional radar measurements were realized by P. Allard in July 29-31 on laghetto (~2700 m a.s.l) newly formed cone.

I.2. Dynamics of explosive basaltic eruptions

I.2.1. Strombolian vs. Hawaiian activity

Strombolian activity takes its name from the frequent, small-scale, transient explosions exhibited by Stromboli, a volcano which forms one of the Aeolian Islands north of Sicily. The term ‘‘Strombolian’’ is most commonly used to denote the relatively mild explosions that occur from the accumulation of gas beneath the cooled upper surface of a magma column (e.g., Blackburn et al., 1976; Wilson, 1980). But in a more general way, the Strombolian and Hawaiian activities are the end members’ expression of explosive basaltic eruptions.

Strombolian activity is associated with discrete explosions at the surface of the magma column owing to the bursting of a large overpressurized bubble (Figure I.4). The overlying magmatic film thus breaks into fragmented lava clots ejected violently in the surrounding air by the gas release. Note that in Strombolian explosion, the gas amount can exceed the solid fraction (e.g., Chouet et al., 1974; Allard et al., 1994a,b), showing a possible gas separation at depth. Nevertheless some difficulties remain on understanding of shallow two-phase flow mechanisms.

Figure I.4. Photograph of typical Strombolian explosion by B. Chouet in December 1969, showing a close view of Stromboli Volcano (Italy) erupting incandescent molten lava fragments.

Hawaiian activity, although less frequent at Etna, displays tremendous spectacle in form of fire fountains. They are almost continuous jets propelling fragmented magma rather vertically with a high gas fraction. (Figure I.5).

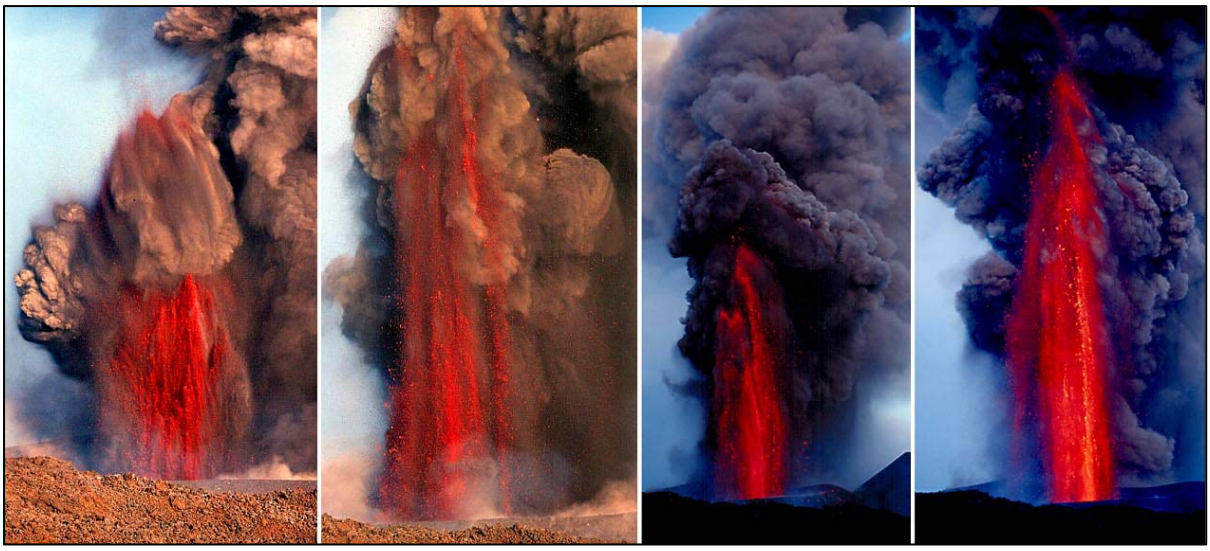

Figure I.5. Scene of a ~ 200-m-tall fountain of lava appeared at Etna (Sicily) on 24 July 2001. The fountain emerged from a 150-m-wide crater formed along a fissure at ~ 2,500 m. Copyrighted photo provided by courtesy of Tom Pfeiffer.

Although these eruptions are generally much less violent than their more silicic counterparts they are, nonetheless, explosive and need to be considered as part of a continuum of explosive activity that embraces not only the familiar explosive basaltic eruption styles (Hawaiian and Strombolian) but includes sub-Plinian, Plinian, and ultra-Plinian (Figure I.6). Walker (1973) proposed a classification of explosive eruption styles based on the magma fragmentation degree and the dispersal of pyroclasts. At Etna, excluding some exceptional sub-plinian (July 22, 1998) or plinian (122 BC) eruptive phase (Coltelli et al., 2005), the very large majority of explosive episodes present a Strombolian activity associated with discrete explosions, and less frequently Hawaiian activity related to lava fountains.

Our understanding of the mechanisms of explosive basaltic eruptions has advanced considerably during the past ~30 years due to the collection and analysis of new field data (e.g., McGetchin et al., 1974; Self, 1976; Parfitt, 1998), volcano monitoring (e.g., Chouet et al., 1974; Blackburn et al., 1976; Vergniolle and Brandeis, 1994, 1996; Ripepe, 1996; Hort and Seyfried, 1998; Dubosclard et al., 2004; Allard et al., 2005), laboratory studies (e.g.,

Jaupart and Vergniolle, 1988; Seyfried and Freundt, 2000) and through mathematical modelling (Sparks, 1978; Wilson, 1980; Vergniolle and Jaupart, 1986; Jaupart and Vergniolle, 1988; Woods, 1993; Parfitt and Wilson, 1995, 1999).

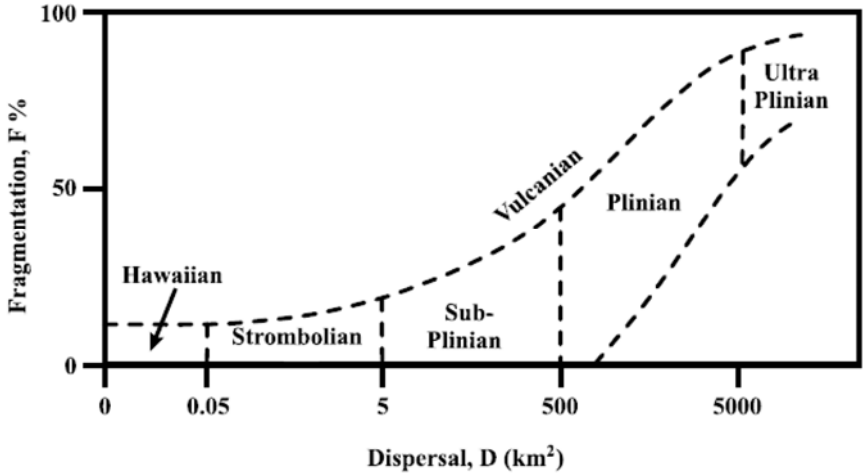

Figure I.6. Diagram showing Walker's (1973) classification scheme for explosive volcanic eruptions which is based on the degree of fragmentation (F) of the magma and the dispersal area (D) of the tephra.

I.2.2. Deep origin of explosive basaltic eruptions

It is now widely accepted that Strombolian eruptions result from the formation and bursting of a gas pocket (slug) close to the surface (e.g., Blackburn et al., 1976; Wilson, 1980; Vergniolle and Brandeis, 1994, 1996), although some details of the mechanism are still disputed. Indeed, two contrasting models of the dynamics of explosive basaltic eruptions are in current usage: the rise speed dependent (RSD) model (Wilson, 1980; Head and Wilson, 1987; Fagents and Wilson, 1993; Parfitt and Wilson, 1994, 1999; Parfitt 2004) and the collapsing foam (CF) model (Vergniolle and Jaupart, 1986, 1990; Jaupart and Vergniolle, 1988, 1989; Vergniolle, 1996). Both models do not differ very much in their view of Strombolian activity. They both treat this explosive activity as occurring from gas accumulation forming large bubbles that cause a raising and up-doming of the surface of the magma column. Actually, the main difference between the models concerns where and how does gas accumulation occur within the magmatic system. More recent studies (Burton et al., 2007) demonstrate that gas slugs may originate from as deep as the volcano-crust interface (~3 km at Stromboli volcano), where both structural discontinuities and differential bubble-rise speed can promote slug coalescence. The observed decoupling between deep slug genesis and shallow (~250-meter)

explosion quakes may be a common feature of strombolian activity, determined by the geometry of plumbing systems.

I.2.2.1. Collapsing foam (CF) model

In the CF model, magma is assumed to be stored within some sort of storage area (a shallow magma chamber or a dike system) at a depth at which gas can exsolve from the magma. The gas bubbles, once formed, rise and accumulate at the roof of the storage area and become close-packed into a foam layer. When the foam layer reaches a critical thickness, it becomes unstable and collapses, with bubbles coalescing to form a gas pocket. The slug then rises up an open vent system and is erupted. Strombolian eruptions, represent repeated partial foam collapse events, called "slug flow" (Figure I.7a) whereas fire fountains occur from complete and almost instantaneous foam collapse called "annular flow" (Figure I.7b). This model is based on separated two-phase flow regime, and implies a differential transfer of the gas phase.

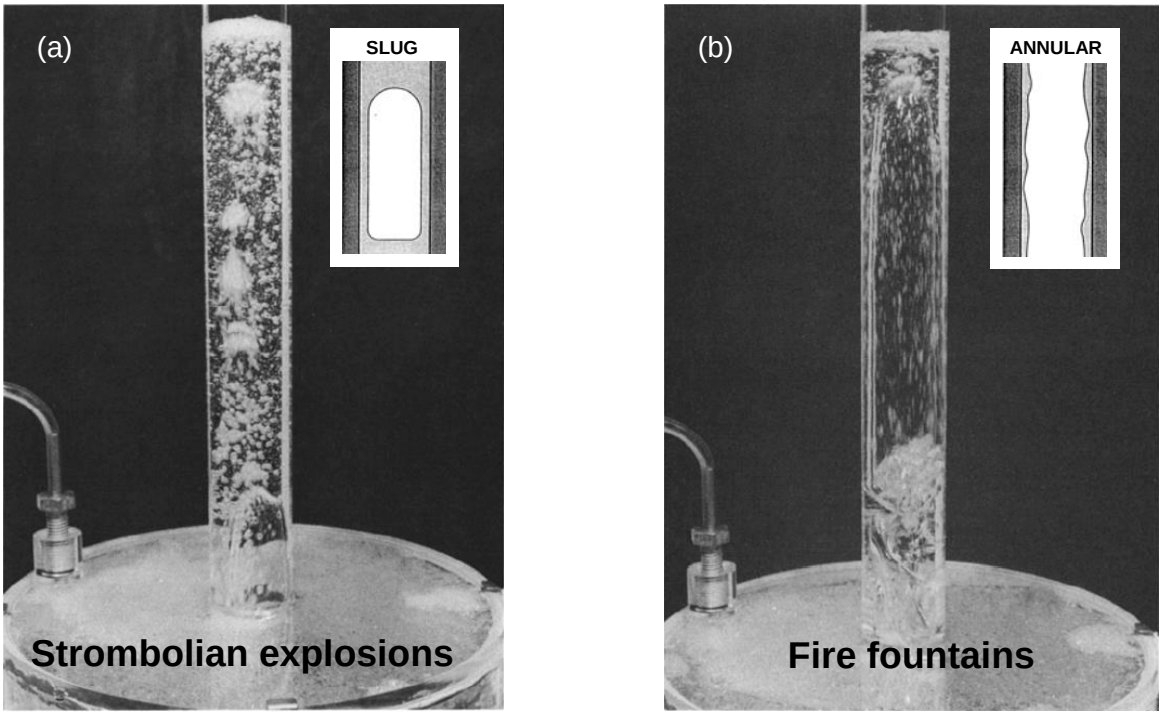

Figure I.7. Experiments of the alternating regimes of foam build up and collapse model (from Jaupart and Vergniolle, 1989). After bubble accumulation at the roof of the tank, the foam collapses at a critical thickness (a) either partially into successive pulsed single gas pockets (slug flow) which start erupting as Strombolian explosions, (b) or completely and continuously (annular flow) with a central gas jet erupting as fire fountains (experiments from Vergniolle and Jaupart, 1990).

I.2.2.2. Rise speed dependent (RSD) model

The RSD model is based on the observation that larger bubbles rise faster than smaller ones and therefore have the opportunity to overtake and coalesce with smaller bubbles. However, coalescence is possible if bubbles have the opportunity to move upwards relative to the magma, i.e., as long as the magma rise speed is low (Figure I.8a). For low magma rise speed, bubbles can coalesce easily, leading in extreme case to the formation of a single large slug producing a Strombolian explosion at the surface. In contrast, if the magma rise speed is high, there is no bubble coalescence leading to the formation of fire fountains. At a given gas content, the eruptive style is therefore directly dependent on the magma rise speed (Figure I.8b). This model is based on homogeneous two-phase flow regime, and implies mainly syn-eruptive gas segregation.

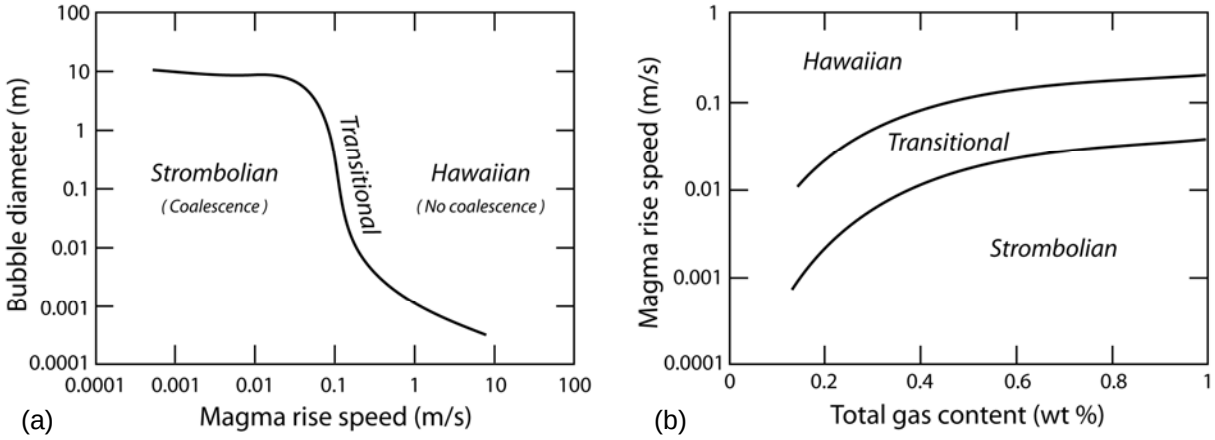

Figure I.8. (a) Plot showing the relationship between final bubble size and magma rise speed. (b) Plot showing the controls of magma rise speed and gas content on basaltic eruption style as predicted by the RSD model (Parfitt and Wilson, 1995).

Both models show the importance of the gas phase in the dynamics of explosive basaltic eruption. However, they significantly depart on the origin of the gas phase which should betray different chemical signature. In situ measurements of the gas composition inside lava fountains have been carried out at Etna from Open-Path Fourier Transform Infrared (OP–FTIR) and revealed a separated two-phase flow mechanism (CF model) implying differential gas transfer primarily accumulated in a shallow ponding zone at about 1.5 – 2 km under the crater (Allard et al., 2005).

I.3. Introduction to remote sensing techniques

Remote sensing, in the simplest words, means obtaining information about an object without touching the object itself. Human eye is the best example of such a remote data acquisition technique using passively natural electromagnetic waves scattered by surrounding objects to build a coloured image of our environment. *In situ* measurements of volcanic eruptions are one of the major challenges left in geophysical Volcanology. Bearing in mind obvious difficulties to study hazardous explosive eruptions, remote sensing techniques turn out to be a very powerful tool for direct observations and quantitative measurements inside eruptive jets. The volcanological community has rapidly perceived the great ability of remote sensing systems to the monitoring and risk assessment of dangerous volcanoes.

I.3.1. Satellite-based methods

Satellite-based remote sensing systems have been used abundantly for volcanic applications. Large spatial coverage is one of the main important advantages of satellite-based methods, which can be advantageously used for tracking the long range evolution of large ash plumes.

Bearing in mind the profusion of these systems, we just aim at giving some key example of satellite-based studies. Particularly infrared systems such as MODIS (Moderate Resolution Imaging Spectroradiometer), have a low earth polar orbit satellite with a good spatial resolution up to 250 m (e.g., Gu et al., 2003; Watson et al., 2004), and a poor temporal resolution inherent to its orbit. MSG (Meteosat second generation), has a high earth geosynchronous orbit with a low spatial resolution (2.5 km) and very high temporal resolution (1 image per 15 min) related to its geosynchronous orbit (Prata et al., 2007). Such systems are complementary and permit both the detailed analysis and real-time monitoring of large ash plumes dispersal.

In contrast, Ultra-violet systems such as TOMS (Total Ozone Mapping Spectrometer; Krueger, 1983; Bluth et al., 1993) or more recently OMI (Ozone Monitoring Instrument; Krotkov et al., 2007; Carn et al., 2008) are both low earth polar orbit satellite and are rather devoted to volcanic SO_2 retrieval.

However, these satellite-based methods operating at small wavelengths (ultra-violet to infrared) compared to radar techniques meet real difficulties for the quantitative assessment of ash and gas loading. Indeed, micrometric wavelengths are very sensitive to fine particles that constitute the earth's atmosphere, and hence the contribution of water vapour reflectivity for instance remains problematic for the estimation of volcanic products dispersed into the atmosphere. In addition, satellite-based techniques often fail to probe early eruptive processes or even low intensity eruption because of either low temporal or spatial resolutions, and hence they cannot be used easily routinely for early warnings.

I.3.2. Ground-based methods

Simultaneously to the development of satellite-based systems, a wide range of ground-based remote sensing devices had emerged. First we present a group of tools devoted to the determination of volcanic gas release and composition, based on the spectroscopic techniques. Then we give some details on radar techniques used particularly for determination of volcanic clasts loading and velocity.

I.3.2.1. Spectroscopic remote sensing techniques

Most of the spectroscopic methods are geared toward quantifying the SO_2 input into atmosphere because SO_2 is believed to be one of the most important volcanic gases and has a strong short-term influence on the global climate. The application of spectroscopic remote sensing techniques turns out to be a key tool for the monitoring of hazardous volcanoes. In addition to real-time capabilities, these techniques permit the thorough study of various volcanic gas species inside the eruptive jet providing stringent constraints on the state of the plumbing system.

COSPEC

The Correlation Spectrometer (COSPEC) is the first and most common spectroscopic remote sensing technique employed at volcanoes. This UV sensitive opto-mechanical instrument is able to measure slant or vertical SO_2 column, which is purely volcanic and NO_2 purely atmospheric. The retrieval of gas abundance is based on the comparison between blue-sky, calibration cell (without volcanic gas), and a volcanic plume scan. Gas flux can hence be

determined multiplying the integrated SO_2 cross-section by estimated plume transport velocity, derived from simultaneous measurements of wind speed and direction. However, the accuracy of gas velocity estimation is crucial for evaluating reliable volcanic gas fluxes. The uncertainty of the wind speed at high altitude contributes greatly to the error in the flux evaluation outlined by COSPEC users. The uncertainty (15–25% according to Caltabiano et al., 1994) does not invalidate remote COSPEC SO_2 measurements as flux variations are considered significant. For 30 years, the correlation spectrometer (COSPEC) has been the principal tool for remote monitoring of volcanic SO_2 fluxes, particularly at Mt. Etna (e.g., Haulet et al., 1977; Bruno et al., 2001). During this time, the instrument has played a prominent role in volcanic hazard assessment. Though innovative for its time, COSPEC is now outdated in several respects.

DOAS

The Differential Optical Absorption Spectroscopy (DOAS) is a proven method for accurate spectral analysis that has been recently applied to volcanic gas monitoring (e.g., McGonigle et al., 2002), and turns out to be a serious alternative to COSPEC instruments. There are a number of advantages to such spectrometers including the collection of broadband ultraviolet spectra, which gives the potential to sense other atmospheric trace gases and to model the radiative transfer. Furthermore, ultra-compact and light-weight mini-DOAS systems recently developed offers the possibility to obtain plume SO_2 measurements with the minimum of logistical support. Note that in some cases radars such as VOLDORAD can be used to provide an accurate transport speed of ash cloud and hence be coupled advantageously with DOAS for estimating SO_2 gas flux.

FTIR

The Fourier Transform Infrared (FTIR) spectroscopy is a technique that has first been widely used in laboratory analyses, and has provided excellent results in open path air for volcano monitoring (Francis et al., 1996). At Etna for instance, Allard et al. (2005) proved the emptying of a large gas bubble layer previously accumulated at about 1.5 km depth below the erupting crater. This technique represents an important step forward as it permits to obtain real-time measurements of absolute column abundances, and relative concentration ratio for different gas species. Indeed, OP-FTIR can determine the identity and molar path amount of a large range of gas species (H_20, CO_2, SO_2, N_2O, HCL, HF and CO) along the beam path

length from spectral absorption lines of the infrared radiation emitted by hot bodies (pyroclasts or lava flows), or simply from solar occultation.

Digital camera

Forward Looking Infrared Radiometer (FLIR) cameras offer a unique view of explosive volcanism by providing an image of calibrated temperatures. FLIR camera operates at typical temporal resolution up to 30 Hz. The FLIR is able to detect both ash plumes and coarse ballistic scoria, meet in various styles of eruptions (e.g., Patrick et al., 2007). In addition to temperature information, this technique also permits the estimation of particle and gas velocities.

More recently, a ultra-violet digital camera has been developed for imaging and quantification of volcanic plume SO_2 (Bluth et al., 2007). This camera utilizes a bandpass filter to collect photons in the ultra-violet (UV) region where SO_2 selectively absorbs UV light. SO_2 is quantified by imaging calibration cells of known SO_2 concentrations. Reliable images can be acquired from distances ranging from 4 to 16 km away from the volcanic target, with a temporal resolution of up to 6 images per minute. In addition to a very short set-up time capabilities, the camera can observe variable in-plume concentrations, and accurate plume speeds (or rise rates) can readily be determined by tracing individual portions of the plume within sequential images.

I.3.2.2. Acoustic measurements

A different technique, also based on the Doppler shift during acoustic sounding (SODAR) was used by Weill et al. (1992) who carried out measurements of eruption velocities at Stromboli Volcano. They measured more than 100 explosions from which vertical velocities close to the vent ranging from 20 to 80 m/s were determined. This technique allows continuous monitoring of volcanic eruption, but the weight (~500 kg) and high energy consumption of the antenna do not make this instrument easy to operate in difficult areas. In addition, the speed of sound is a strong function of the temperature; therefore its accurate knowledge is necessary for calculating eruption velocities.

I.3.2.3. Doppler radar systems

Radar (**Ra**dio **d**etection **a**nd **r**anging) is an active remote sensing system for the detection and location of reflecting objects. By contrast to passive remote sensing systems, radars operate by radiating their own electromagnetic source into space with a wavelength (Figure I.9) typically ranging from 1–8 cm (apart for VOLDORAD) for volcanic applications (X, C, or S-band). The spectral region investigated by radar systems permit the detection of solid particles as fine as few millimetres up to several dozens of centimetres thus covering the particle size range of typical volcanic eruptions. Systems are typically amplitude modulated (AM), based on short pulses of very high power. In addition to their capability to detect the amount of particle inside distinct sampling volumes (the so-called range gates), most radar systems utilize Doppler shift-based techniques to measure the velocity of moving targets. Such radar systems have long been employed for meteorological purposes, and utilized opportunistically for volcanic applications.

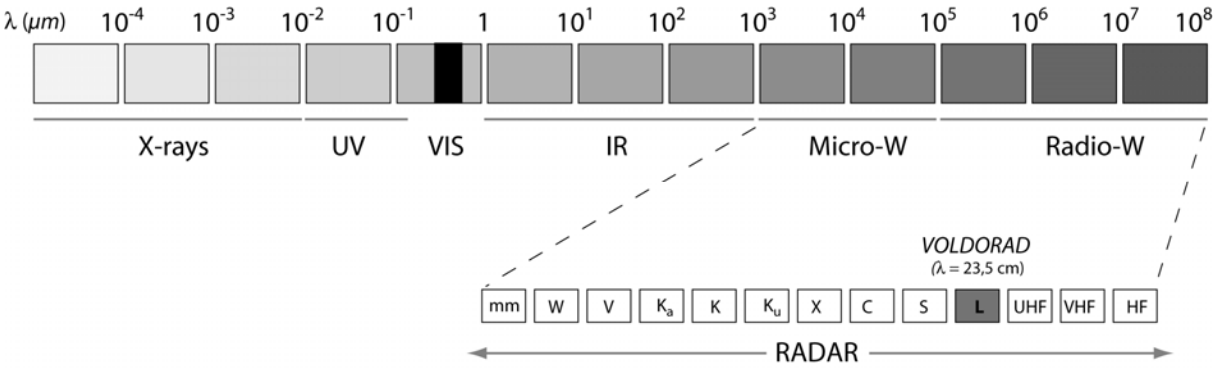

Figure I.9. Electromagnetic spectrum showing spectral bands of most common radars. Weather radars usually utilized for volcanic applications operate at wavelengths ranging typically from 1 – 8 cm (X, C, or S-band). We also focus on VOLDORAD system that operates at the singular wavelength of 23.5 cm (L-band), and specifically devoted to the sounding of explosive volcanic activity.

Weather radars

Since nearly three decades ground-based weather radars were used to track the long range evolution and some physical characteristics (ash plume velocity, ash concentration, geometrical extent of the volcanic plume) of large ash clouds derived from explosive eruptions of various volcanic targets, such as Mount St. Helens (e.g., Harris et al., 1981; Harris and Rose, 1983). But these radar systems are fixed and have to be used opportunistically in a maximum distance range of about 500 km to the target. At such a distance, the sampling volume resolution is low leading to some incapability to detect small

eruptive events and obtain accurate information on internal structure dynamics. Moreover, the earth curvature impedes weather radars to provide information on early ash plume component (Lacasse et al., 2004). Therefore, they just permit to probe the upper convective part of high eruption columns and provide information on fine ash only that ultimately constitute the distal volcanic products (Marzanno et al., 2006a,b). Most of all, considering their real-time capabilities, weather radar systems are devoted to the tracking of large ash clouds dispersal, valuable for the risk mitigation related to air transport for instance. In addition, some weather radars operate at small wavelength, lower than a centimetre (mm to X-band), and hence serious difficulties arise for the detection and quantification of ash particles loading under rainy conditions.

Volcanological Doppler radars

A major challenge is henceforth to measure physical parameters such as ash masses and velocities closer to the vent in order to retrieve directly the true source parameters that permit the understanding of the explosive dynamics.

In this aim, portable Doppler radar system has allowed a great step forward, providing velocities and mass estimates of pyroclasts right above the crater. Particularly, VERDEMOS (Hort and Seyfried, 1998; Seyfried and Hort, 1999) is a system constituted of a Doppler radar operating with a frequency-modulated continuous wave (FMCW) and working at 1.24 cm wavelength (K_u-band). Note that in this spectral region some difficulties related to the detection of volcanic ash may arise under harsh rain condition. Such radar systems give a very high velocity resolution (~0.2 m/s) but the location of the target is rendered much more difficult. Hort et al. (2003) have provided at Stromboli from Doppler radar measurements average velocities of 19 and 8 m/s for ascending and descending particles respectively, with a maximum vertical velocity of 60–70 m/s. Under some assumptions based on the terminal settling velocities of particles they obtain a mean particle size of 3 mm at Stromboli. Three coupled FMCW radar were also used at Erebus volcano to determine the directivity of Strombolian explosions (Gerst et al., 2008). Finally, another version of FMCW radar operating at about 3 cm wavelength was used at Merapi volcano for active lava dome monitoring (Voge and Hort, 2009).

Besides, VOLDORAD is a Doppler radar exclusively devoted to the study of volcanic activity. It operates with a pulsed wave at a 23.5 cm wavelength (L-band) that permits the detection of fine ash under any weather conditions. The resolution (~0.9 m/s) and maximum range (>1000 m/s) velocity of VOLDORAD is suitable, as well as the temporal resolution (>10 Hz), for the detailed analysis of explosive activity. Dubosclard et al. (1999, 2004) have provided initial particle velocities of 80–90 m/s and maximum particle radial velocity inside the beam of about 60 m/s at Etna during the eruption of October, 1998. Donnadieu et al., (2003, 2005) obtained maximum radial particle velocities of 90 m/s and 110 m/s for the eruption of July 13, and July 29, 2001 respectively. Gouhier and Donnadieu (2008) give mean particle diameter ranging from 1.3 to 1.6 cm and ejecta mass estimate between 60–200 tons for a typical Strombolian explosion at Etna during the eruption of July 4, 2001.

Portable ground-based Doppler radar techniques allow direct kinetic and loading measurements on volcanic gas and/or particles immediately above the vent. Therefore, in addition to their significant monitoring potential and early warnings, these radar systems permit us to study, under any weather conditions, explosions of lesser intensity barely imaged by satellites or weather radars, so as to retrieve physical source parameters.

CHAPTER II

VOLDORAD (Volcano Doppler Radar): technical characteristics and theoretical considerations

II.1. Presentation of VOLDORAD

We wanted to provide a chapter exclusively devoted to the thorough description of VOLDORAD as it was extensively utilized for the study of this thesis. After a detailed presentation of VOLDORAD and its derived parameters, we give some theoretical elements related the Doppler radar method.

II.1.1. VOLDORAD technical characteristics

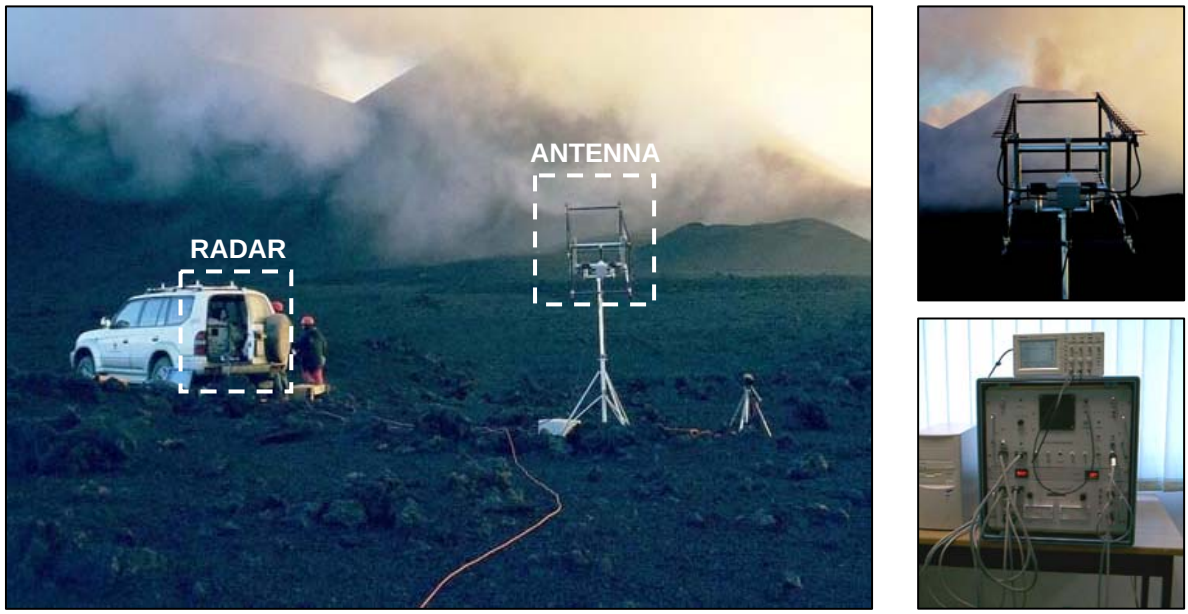

Figure II.1. Photograph of the sounding conditions during the radar acquisition campaign of July, 2001 at Mt. Etna SEC, and we provide close views of the 4-Yagi antenna array, and radar core.

VOLDORAD literally VOLcano DOppler RADar, belongs to the family of pulsed ground-based Doppler radars, and was developed by the Observatoire de Physique du Globe de Clermont-Ferrand (France), specifically for the remote sensing of volcanic jets and plumes. A first prototype was successfully used at Etna during the eruption of October 1998 (Dubosclard et al., 1999, 2004), operating at 1238 MHz (equivalent wavelength of 24.2 cm) with a high-power transmitter up to 1 kW. The second version of VOLDORAD, more compact, was used at Etna during the eruption of the Southeast crater (SEC) on July 4, 7, and 13, 2001 and at the Laghetto cone on July 29 and 31, 2001 (Figure II.1). This version works with a low-power transmitter (60W), and an array of 4 Yagi antenna with a beamwidth $\alpha = 9°$ for a total weight of about 70 kg. These improvements permit the radar to be set up easily in the field with a four-wheel-drive and supplied by an electric generator. The VOLDORAD antenna radiation

pattern, like typical Doppler radar, is not focussed such as a laser, but comprises a main lobe surrounded by several side lobes. The aperture angle is defined at -3 dB beamwidth of the main lobe (Figure II.2). However, side lobes may reach the slopes of the crater and hence be responsible for ground clutter echoes, readily eliminated with basic treatments.

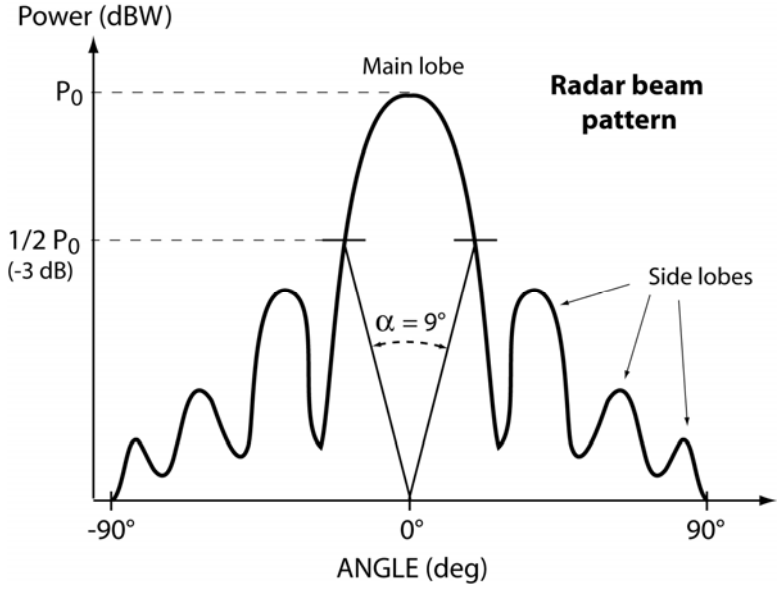

Figure II.2. Sketch of a typical radar beam pattern showing the multiple lobes, and the beam aperture angle (α=9°) as calculated from the beamwidth of the main lobe at -3dB of P_0.

VOLDORAD is designed to monitor all types of explosive volcanic activity of variable magnitude. It operates at a medium distance range (0.2 – 12 km), at a wavelength (λ) of 23.5 cm (equivalent frequency of 1274 MHz), and with a high sampling rate ≥10 Hz, which permit the sounding under any weather conditions and the detailed analysis of early eruptive processes. Note that the intensity of the scattered signal is a strong function of the particle size and can be separated into three regions of strictly different behaviour, depending on the relation of particle diameter (D) and the wavelength (λ) of the transmitted wave. In many cases the power of the scattered signal (P) is proportional to the number of particles in the volume, where scattering takes place. For $D>>\lambda$, the theory of geometrical optics is applicable, and the scattered power P is proportional to the square of the particle diameter ($P \propto D^2$). The range $D \approx \lambda$ is called the Mie region after the first theoretical approach to the complete scattering theory by Mie (1908). Here the scattered power P becomes a function of the transmitted frequency and the location around the particle (see Appendix B for more details). Rayleigh scattering takes place for $D<<\lambda$ with the scattered power being proportional

to the sixth power of the particle diameter ($P \propto D^6$). Bearing in mind the large wavelength used by VOLDORAD (23.5 cm), we show that for volcanic ejecta size in the millimetre range, mostly Rayleigh scattering occurs, and beyond a particle diameter threshold found to be around 6 cm, Mie scattering starts to become dominant (Gouhier and Donnadieu, 2006). Considering the wide range of particle sizes for Strombolian explosions exceeding the diameter threshold by far, the Mie scattering formulation is required for any modelling of the scattering field. Note that for smaller wavelengths, as it is the case for most of Doppler radars used for volcanological applications, the Rayleigh approximation validity limit arises at even lower diameter threshold.

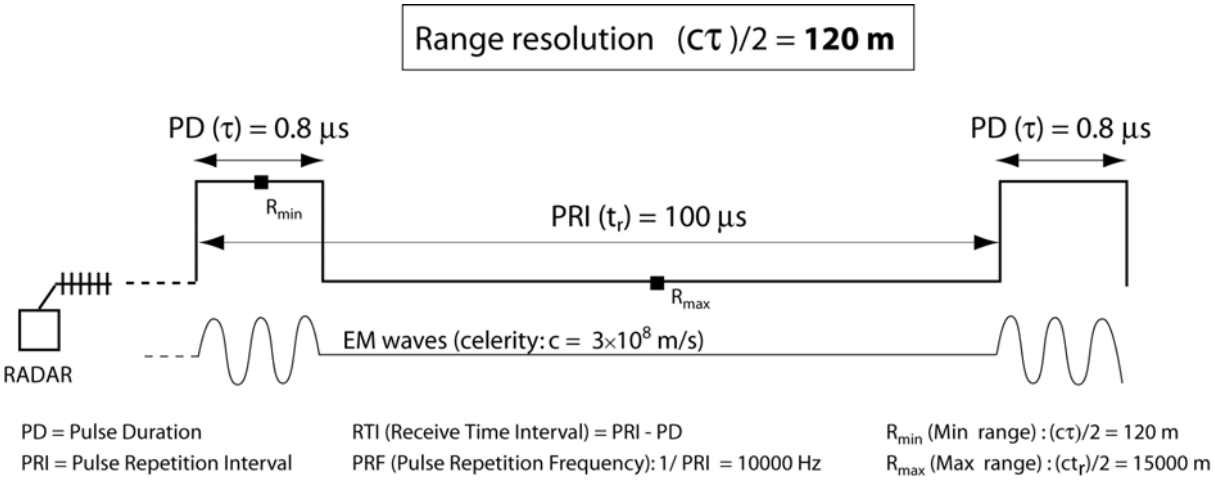

Figure II.3. Sketch showing the principle of emission/reception of an electromagnetic (EM) signal by a Doppler radar, and used for the characterization of the range resolution of the sampling volumes (range gates). The range resolution is directly defined by the pulse duration (PD) taken as τ = 0.8 μs at Etna, and corresponds to half the travel distance of the transmitted wave through the pulse duration $c\tau/2$ = 120 m. Actually the radar is able to record the backscattered signal only during the receive time interval PRI-PD, thus characterizing the minimum and maximum unambiguous distance range.

Pulsed Doppler radars also permit to define easily distinct sampling volumes (the so-called range gates), which make possible the localization of the plume inside the beam. The range resolution of successive sampling volumes can be determined directly from the pulse duration (τ). At Etna, the pulse duration was taken as 0.8 μs, which corresponds to a radial range resolution of 120 m, i.e., half of the travel distance of the transmitted wave through the pulse duration ($c\tau/2$), *c* being the celerity of light. The azimuthal and elevation range resolution depends on the aperture of the antenna beam (α) and hence varies with the distance

between the considered range gate and the antenna. At Etna, we defined a mean azimuthal range resolution of about 165 m at 1 km. Likewise, we characterize a minimum and maximum unambiguous range from the pulse duration (τ) and the pulse repetition interval (t_r) taken as 100 μs at Etna of 120 m and 15 km respectively (Figure II.3).

The pulsed repetition interval (t_r) and the number of coherent integrations (6 – 10) of radar pulses in the time domain selected at Etna permit to define a maximum radial velocity range of about 59 and 98 m/s from $V_{rad} = \lambda/(4N_c t_r)$, with a radial velocity resolution of 1.8 m/s and 3 m/s respectively. The principal technical characteristics of VOLDORAD are summarized in Table II.1.

Table. II.1. Technical characteristics of VOLDORAD version 2.

Technical characteristics of VOLDORAD 2	Symbols	Values
Transmitted frequency (MHz)	f_t	1274
Wavelength (cm)	λ	23.5
Peak power (W)	P_t	60
Pulse repetition interval (μs) *	t_r	100
Pulse duration (μs) *	τ	0.8
Radial range resolution (m) *	L	120
Mean azimuthal/elevation range resolution (m) *	H	165
Antenna beamwidth (°)	α	9

* Parameters set for the sounding at Etna SE crater on 4 July 2001.

II.1.2. VOLDORAD setting at Etna on July 4, 2001

VOLDORAD was set up at an altitude of about 3000 m, at a horizontal distance of 930 m to the centre of the crater, 280 m below the summit of the SEC, and with an antenna elevation angle θ = 23°. Moving particles were detected in successive range gates (G_1 to G_4) corresponding to a slant distance of 807-1167 m to the radar antenna with a mean gate width of 120 m and a gate height ranging from 127-184 m (Figure II.4). The centre of range gates G_1 and G_2 are located at 78° and 34° respectively to the south of the vertical axis, whereas range gate G_3 and G_4 are oriented at 23° and 43° respectively to the north of the vertical axis. The centre of the range gate G_3 is located at a horizontal distance of 54 m and an elevation of 127 m to the center of the crater. Note however that echo-power can be recorded as soon as particles enter the range gate G_3, i.e., about 40 m above the crater rims. In this configuration,

most of the volcanic material ejected is recorded in the range gate G_3. Geometrical parameters of the ranges gates G_1 to G_4 are summarized in the table II.2.

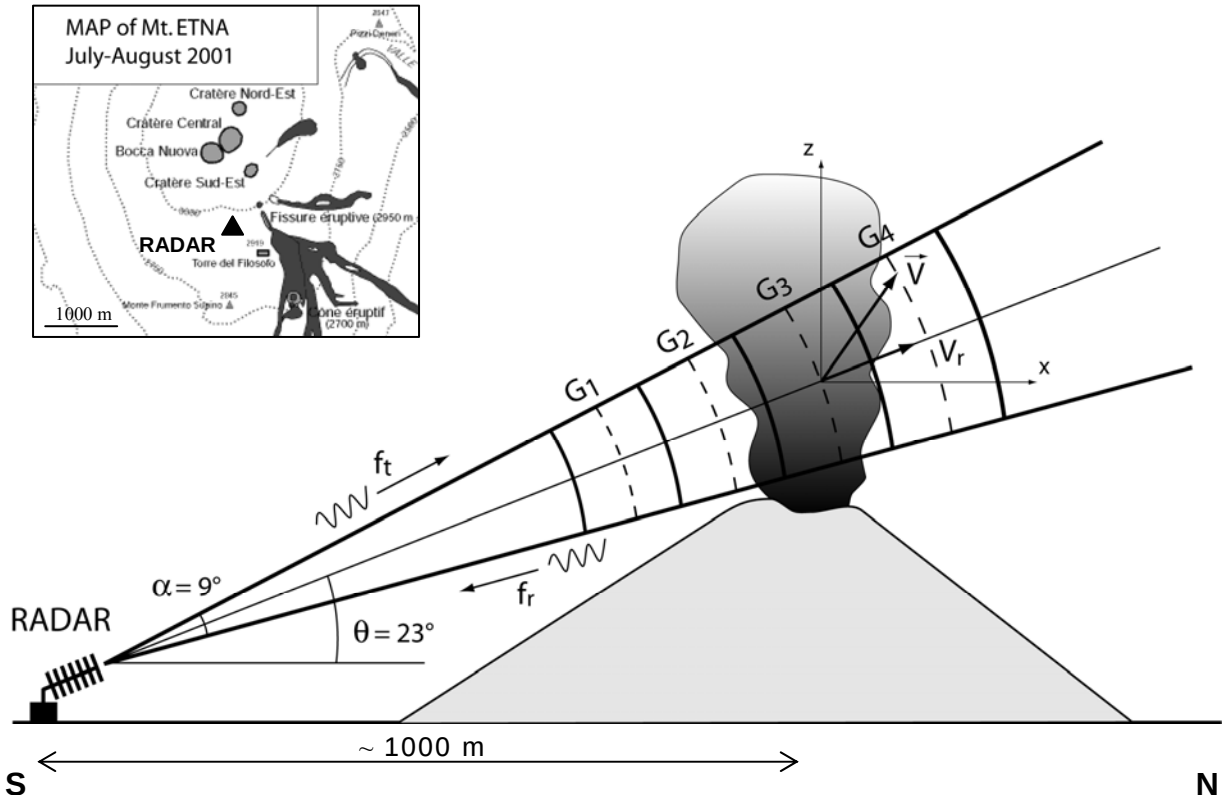

Figure II.4. Sketch of the radar sounding geometry used for the acquisition campaign on Mt. Etna, on 4 July, 2001.VOLDORAD was set up at an altitude of 3000 m, at a horizontal distance of 930 m to the crater rim, 280 m below the summit of the SE crater, and with an elevation angle of 23°. Note that the range G3 is centred above the vent and provides most of the echo-power. We also provide a map of the summit craters area during the July-August eruption showing the location of VOLDORAD.

Table II.2. Gate-centre coordinates (G_1 to G_4) for an antenna beam elevation angle of 23°.

Antenna beam elevation (θ =23°)	G_1	G_2	G_3	G_4
Gate angle to the vertical (°)	78	34	-23	-43
Slanting distance to the radar (m)	807	927	1047	1167
Horizontal distance to the crater (m)	-166	-56	54	165
Elevation above crater rim (m)	33	80	127	174
Gate height (m)	127	146	165	184

II.2. VOLDORAD parameters acquisition

II.2.1. Radar power and velocity

II.2.1.1. Recorded power

VOLDORAD is a Doppler radar, it means that it is able to record both the backscattered power and radial velocity of particles crossing the antenna beam axis, and sampled in successive range gates. The echo-power received to the radar is a complex function depending on the characteristic of the radar utilized (C_r), the physical properties (number, sizes shape, composition, etc.) of the targets (η), the distance (r) and attenuation (L) of the medium between the radar and the target (see section II.3 for more details).

$$\overline{P_r} = C_r L^2 \frac{\eta}{r^2} \tag{II.1}$$

For convenience, the radar reflectivity factor is often employed because it is a quantity characteristic of the targets only and hence permits the comparison measurements carried out by different radars with different characteristics.

$$Z = \frac{\eta \lambda^4}{\pi^5 \left| K^2 \right|} 10^{18} \tag{II.2}$$

The reflectivity factor Z is often expressed in logarithmic units as dBZ. For instance, we have found for 2 distinct typical Strombolian explosions at Etna, a reflectivity factor ranging from 85 – 94 dBZ. As a comparison, very harsh rain gives a maximum reflectivity of ~60 dBZ.

II.2.1.2. Recorded velocity

Doppler radars work by using the so called Doppler Effect, this physical phenomenon was discovered by Christian Doppler in 1842 from a study based on acoustic wave. The Doppler Effect (or Doppler shift) is the change in frequency of a wave received by an observer moving relative to the emitting source of the waves (Figure II.5). Such a physical phenomenon meets

fundamental applications in the domain of sound waves as well as in the domain of electromagnetic waves. The best illustration of both applications are first the variation of the pitch commonly heard when an object emitting sound is moving, such as the horn of firetrucks, and then the variation of colour when an object emitted light is moving such as stars (this example is often cited as evidence for an expanding universe).

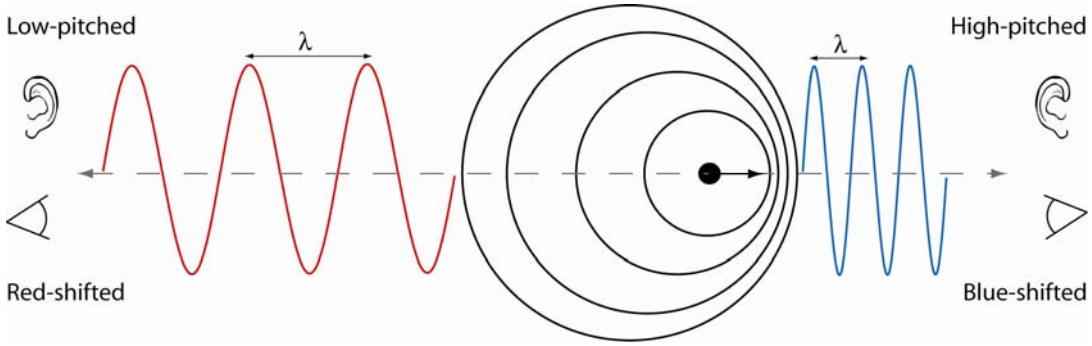

Figure II.5. Sketch showing the Doppler Effect principle: when a target moves away from the observer, wavelength of the emitted wave is increased, leading to lower pitch of the sound and red-shift of the light from the observer. At the opposite, when the target draws closer to the observer, the emitted wavelength is reduced, leading to higher pitch of the sound and blue-shift of the light from the observer position.

For volcanic application, when ejecta cross the radar beam, it generates radar echoes backscattered to the receiver with a frequency shift between the transmitted and the received signal that is related to the particle velocity along the beam axis. Therefore, the radial velocity (V_r) of a moving target can be determined from the Doppler frequency (f_d) and the wavelength of the transmitted wave as:

$$V_r = \frac{-f_d \lambda}{2} \qquad \text{(II.3)}$$

When the target moves away from the radar ($Vr>0$), the Doppler shift is negative. It is the opposite when the target draws closer (see section II.3 for more details).

II.2.2. Calculation of the spectral moments

II.2.2.1. Doppler spectra

Finally, echo-power data acquired from successive range gates are displayed in real time as Doppler spectra representing the power spectral density (y-axis) as a function of the radial velocity (x-axis) at every moment. We show in Figure II.6, an example of Doppler spectra recorded by VOLDORAD, as displayed in real time in the field for a Strombolian explosion, occurring at 2135:35 UT in July 4, 2001 at Etna SEC. Six successive range gates are reported here ranging from 567 to 1167 m.

Most of the signal is centred on the range gate at 1047 m (i.e., G_3), taking a maximum power value close to -80 dBW. The range gate G_3 is located right above the Southeast crater and present both positive (ascending particles) and negative (ascending and descending particles) radial velocities.

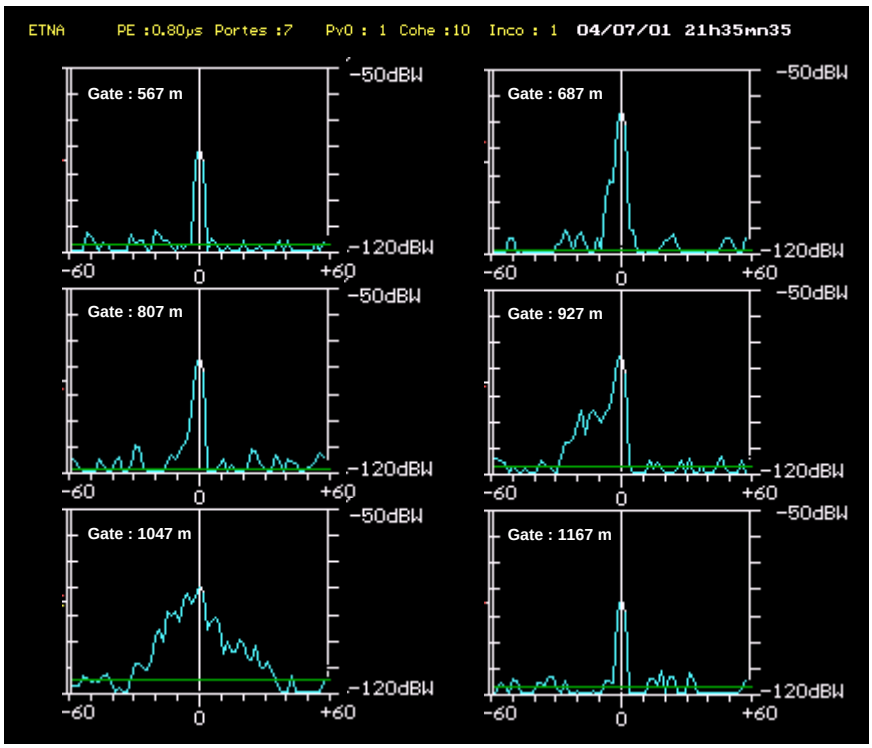

Figure II.6. VOLDORAD Doppler spectra occurring at 2135:35 UT on July 4, 2001 at Etna SEC, as displayed in real-time during the radar sounding. Each spectrum corresponds to the power backscattered by particles crossing the several successive sampling volumes of the antenna beam (so-called range gates), 120-m wide, ranging from 567 to 1167 m from the radar location.

From the processing of the series of Doppler spectra in the range gates above the crater and on either side of the jet axis, times series can be computed for three sets of positive (indexed +) and negative (indexed -) parameters corresponding theoretically to ascending and descending ejecta respectively (Figure II.7).

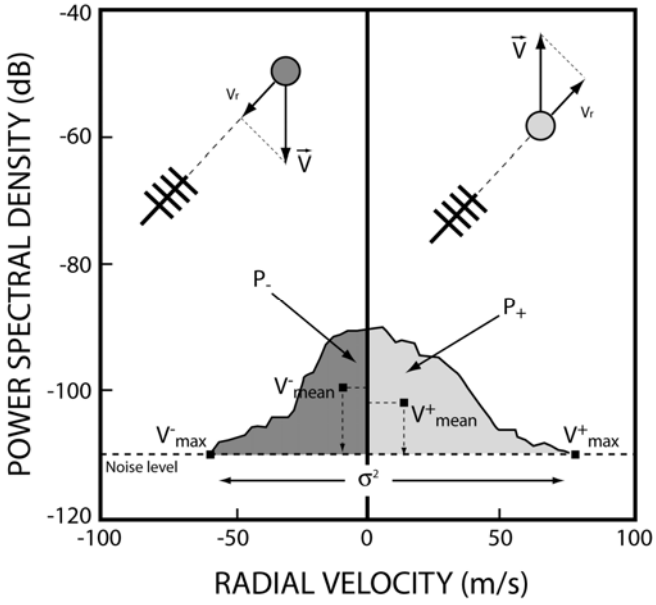

Figure II.7. Sketch of a typical volcano Doppler spectrum showing the spectral moments (power, maximum and mean radial velocity, and spectral width) as calculated from the power spectral density. They are indexed (+) and (-) for ejecta with the radial component of their velocity vector moving away and towards the antenna respectively, except for the spectral width that represents the standard deviation of the whole spectrum.

Firstly we characterize the maximum radial velocities where the power spectral density is equal to the background noise level. Therefore, we can define the spectral moment of order 0 that corresponds to the power backscattered by particles moving toward (P^-) or away (P^+) from the radar within the sampling volume. The backscattered power is derived from the integral of the power spectral density *S(v)* over the range of radial velocity intervals *dv*, i.e., from 0 to $V_{\max}^{+}$ for ascending particles and from $V_{\max}^{-}$ to 0 for descending particles:

$$P^{+} = \int_{0}^{V_{\max}^{+}} S(v)dv \qquad \text{and} \qquad P^{-} = \int_{V_{\max}^{-}}^{0} S(v)dv \tag{II.4}$$

Secondly, we define the spectral moment of first order that corresponds to the mean velocity $V_{mean}^{\pm}$ weighted by the power spectral density over the positive or negative velocity range.

$$V_{mean}^{+} = \frac{\int_{0}^{V_{\max}^{+}} vS(v)dv}{P^{+}} \quad \text{and} \quad V_{mean}^{-} = \frac{\int_{V_{\max}^{-}}^{0} vS(v)dv}{P^{-}} \tag{II.5}$$

Finally, we define the spectral moment of second order that represents the spectral width of the Doppler spectrum from $V_{\max}^{-}$ to $V_{\max}^{+}$, which can be described as the variance of the spectral distribution:

$$\sigma^2 = \int_{V_{\max}^{-}}^{V_{\max}^{+}} \left(v - V_{mean}^{\pm}\right)^2 S(v)dv \tag{II.6}$$

Originally, the spectral moments were characterised from weather-radar Doppler spectra. In meteorological applications, in particular, the backscattered power parameter provides an estimate of the amount of water droplet, which is related to the precipitation rate. The mean velocity parameter gives the average velocity of sinking water droplets, and the spectral width parameter is commonly used to assess the turbulence of the air, related for example to shear stresses caused by the wind. However, the study of Strombolian volcanic activity is far different and more localized, so that the interpretation of the spectral moments has to be considered cautiously, taking into account the radar sounding conditions, along with the complex kinematics and the wide range of volcanic particles sizes.

II.2.2.2. Time series

We show in Figure II.8 time series of the maximum radial velocity ($V_{\max}^{+}$) and the total power derived from the processing of the Doppler spectra during the eruptive episode of July 4, 2001 at Etna SEC. The total power is simply the sum of P^{-} and P^{+} over the whole range gates, and $V_{\max}^{+}$ is calculated from the range gate G_3 (1047 m). Time series have been calculated at a sampling rate of about 1 Hz and displayed with a 10-s running average. Both parameters show

the long range evolution of the eruption velocity and power, with alternating periods of quiescence and periods of intense activity.

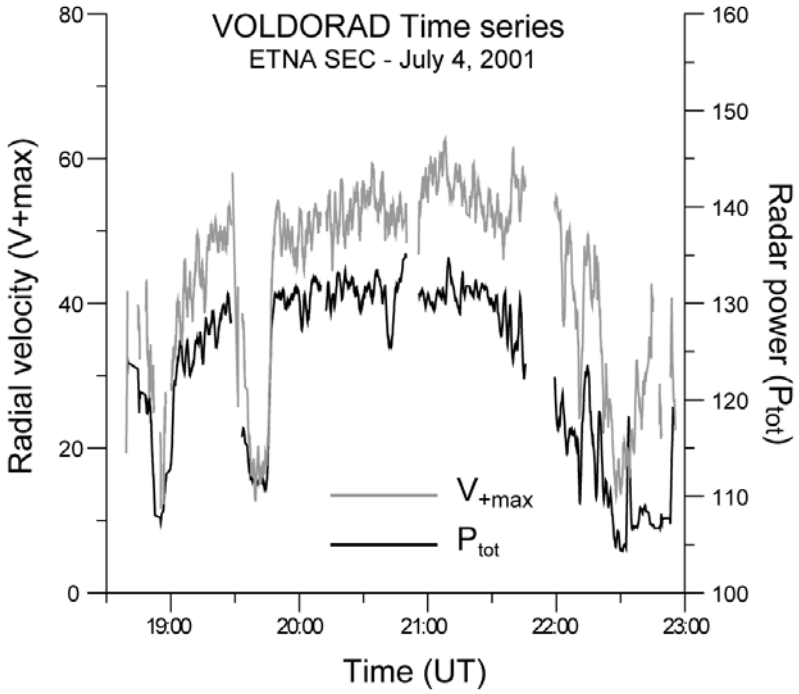

Figure II.8. Time series of the maximum radial velocity in gate G_3 (1047 m) and the total power integrated over the whole range gate during the eruption of July 4, 2001 at Etna SEC.

II.3. Doppler radar: theoretical considerations

II.3.1. Formulation of the radar equation

The radar equation expresses the relationship between the average power of the received signal and the properties of the scattering targets inside the sampling volume located at range r, as a function of the technical characteristics of the radar and the conditions of propagation between the radar and the target. We commonly assume that the target radiates isotropically the intercepted radar power, and hence can be characterized by its backscattering cross section σ. Note that the value of σ is different from the geometric cross section of the target, and depends on many factors: shape and dimension of the target, orientation, dielectric factor and conductivity of the material. If the target (σ) is in direction (θ, ϕ), at a distance r, the power flux density returned by the target and arriving at the reception antenna is (Sauvageot, 1992):

$$S_r = \frac{PtG_0 \left| f_n(\theta,\phi) \right|^2 L^2 \sigma}{\left(4\pi r^2\right)^2} \tag{II.7}$$

where P_t is the transmitted power, G_0 is the antenna gain and L being the attenuation on the radar-target path. f_n is the function that represents the power distribution in the main lobe (Figure II.2). The power of the echo collected by the antenna with effective aperture A_e is $P_r=A_eS_r$. Therefore, for a monostatic radar (i.e., the same antenna is used for emission and reception) the received power scattered by a single target is:

$$P_r = \left(\frac{P_t G_0^2 \left| f_n(\theta,\phi) \right|^2 \lambda^2 L_r}{(4\pi)^3} \right) L^2 \frac{\sigma}{r^4} \tag{II.8}$$

Where L_r is the attenuation due to the finite width of the pass band of the receiver, and λ is the radar wavelength. For a "distributed target" (i.e., consisting of a large number of scatterers simultaneously present in the same resolution volume V, randomly distributed and assumed homogeneous), the radar backscattering cross section is simply the summation made over the entire resolution volume as:

$$\sum_V \sigma_i = V \left(\sum_V \sigma_i / V \right) = V\eta \tag{II.9}$$

The quantity η is the average cross section of the target per unit volume, called the radar reflectivity and expressed in cm^{-1}. Using Equation II.8 for a distributed target we obtain:

$$\overline{P_r} = \left(\frac{P_t G_0^2 \lambda^2 L_r L^2 \eta}{(4\pi)^3} \right) \iint_V \frac{\left| f_n(\theta,\phi) \right|^2}{r^4} dV \tag{II.10}$$

In most cases we can assume that the distribution in the main lobe can be conveniently represented by a Gaussian function of the form:

$$\left| f_n(\theta,\phi) \right|^2 = \exp\left[-\left(\frac{\theta^2}{2\sigma_\theta^2} + \frac{\phi^2}{2\sigma_\phi^2} \right) \right] \tag{II.11}$$

where σ_θ and ϕ_θ are the standard deviations of the distribution. Under these conditions and neglecting side lobes we finally obtain:

$$\int_{\Omega} \left| f^4(\theta,\phi) \right|^4 d\Omega = \frac{\pi\theta\,\phi_0}{8\ln 2} \tag{II.12}$$

where θ_0 and ϕ_0 are the -3dB beamwidth, ln2 is the natural logarithm of 2, and $d\Omega$ is the element of solid angle of the antenna beam. When r is large compared to the resolution volume $c\tau/2$, we finally obtain:

$$\overline{P}_r = \left(\frac{P_t G_0^2 \lambda^2 \theta_0 \phi_0 (c\tau) L_r}{(4\pi)^3} \right) L^2 \frac{\eta}{r^2} \tag{II.13}$$

That is,

$$\boxed{\overline{P}_r = C_r L^2 \frac{\eta}{r^2}} \tag{II.14}$$

This form is convenient because it permits to identify easily each contributor to the received echo-power: C_r is the constant related to technical characteristics of the radar, L is related to the attenuation of the medium, η is characteristic to the properties of the scatterers and r is the distance between the radar and the targets.

II.3.2. Calculation of the radial velocity

Therefore, the Doppler Effect has been advantageously used by remote sensing techniques for the study of natural processes dynamics as volcanoes are. The transmitted pulse from the Doppler radar consists of a few thousands of oscillations with a frequency f_0, with a peak power reaching about 60W. The wave emitted by the antenna can be described as:

$$S(t) = A_t \cos \omega_0 t \tag{II.15}$$

Where A_t is the amplitude, and $\omega_0 = 2\pi f_0$ is the angular frequency and t is the time. For a point target at distance r, the instantaneous voltage of signal received by the radar can be written as:

$$e(t) = a\cos\left[\omega_0 t + \varphi(t)\right] \tag{II.16}$$

a is the amplitude and $\varphi(t)=2\pi(2r/\lambda)$ is the phase. For a monostatic radar (i.e., the same antenna is used for emission and reception of the signal) with a wavelength λ observing a point target at range r, the signal from the scattered field received by the antenna is a pulse of duration τ represented by equation (II.16). The phase of the received signal is then:

$$\varphi(t) = -\frac{4\pi r(t)}{\lambda} \tag{II.17}$$

Volcanic ejecta are moving targets, and hence cross the antenna beam generating radar echoes backscattered to the receiver with an angular frequency shift ($d\varphi/dt$) due to the Doppler Effect between the transmitted and received signal, that is related to the particle velocity along the beam axis.

$$\frac{d\varphi}{dt} = -\frac{4\pi}{\lambda}\frac{dr}{dt} = -\frac{4\pi}{\lambda}V_r \tag{II.18}$$

When the target moves away from the radar ($Vr>0$), the Doppler shift ($d\varphi/dt$) is negative. It is the opposite when the target draws closer. We can write:

$$\frac{d\varphi}{dt} = \omega_d = 2\pi f_d \tag{II.19}$$

It leads to the well-known relation between the Doppler frequency (f_d) and the radial velocity (V_r) of the considered target:

$$\boxed{f_d = \frac{-2V_r}{\lambda}} \tag{II.20}$$

II.3.3. Calculation of the power spectral density

The In-phase component *I(t)* and the quadrature phase component *Q(t)* of the received signal may be represented by the real and imaginary parts of the complex amplitude:

$$y(t) = A_0 e^{i\omega_d t} \tag{II.21}$$

with *I(t)* and *Q(t)* respectively:

$$\begin{aligned} I(t) &= A_0 \cos(\omega_d t) \\ Q(t) &= A_0 \sin(\omega_d t) \end{aligned} \tag{II.22}$$

The power spectral density *S(f)* can then be obtained from the complex autocorrelation function $R(\tau)$ of the complex amplitude of the signal arriving from a specific range and is defined by:

$$R_y(\tau) = \lim_{T\to\infty} \frac{1}{T} \int_{-T/2}^{T/2} y(t) y^*(t+\tau) dt \tag{II.23}$$

where τ is the autocorrelation interval and y^* is the complex conjugate quantity. *S(f)* is the Fourier transform of $R(\tau)$:

$$S(f) = \int_{-\infty}^{\infty} R(\tau) e^{-i\omega\tau} d\tau \tag{II.24}$$

Note that in the case of a finite-energy signal, the Fourier transform of the autocorrelation function is equal to the squared Fourier transform of the complex amplitude.

$$S(f) = \int_{-\infty}^{\infty}\int_{-\infty}^{\infty} y(t) y^*(t+\tau) e^{-j\omega\tau} dt d\tau = \left| \int_{-\infty}^{\infty} y(t) e^{-i\omega t} dt \right|^2 \tag{II.25}$$

Note that the radial velocity corresponds to the Doppler frequency via the Equation II.20 and leads to the following equivalence:

$$S(f)df \Leftrightarrow S(v)dv \tag{II.26}$$

FIRST PART

DOPPLER RADAR STUDY

RÉSUMÉ : PREMIÈRE PARTIE

Les explosions volcaniques constituent une source importante d'informations utiles à la compréhension de la dynamique éruptive. Compte tenu de la dangerosité des phénomènes éruptifs explosifs, ainsi que de la difficulté d'accès pour réaliser des mesures *in situ*, les méthodes de sondage à distance ce sont avérées êtres des outils indispensables à l'étude et à la surveillance des volcans actifs. Ainsi, depuis quelques dizaines d'années l'émergence de nouvelles technologies a permis de faire un vrai pas en avant quant à la compréhension des mécanismes qui contrôlent les éruptions volcaniques.

Dans cette thèse, et plus particulièrement dans la première partie du manuscrit, nous nous sommes intéressés à l'étude de l'activité volcanique de type Strombolien par le biais de la télédétection. De nombreux travaux concernant la détection des cendres et du gaz volcaniques ont été réalisés, à partir notamment de mesures satellites et provenant de radar météorologiques. Cependant, à cause notamment de la faible résolution spatiale de ces techniques, et compte-tenu de leur distance à la cible, ces méthodes ne permettent pas l'accès aux informations proches de la source d'émission, et ne peuvent donc pas apporter de contraintes solides sur les processus éruptifs précoces (vitesse de gaz et de particules avant le régime thermique, distribution de taille des particules avant ségrégation par sédimentation au sein du panache, etc.). Un des enjeux majeur actuel est de mesurer les paramètres physiques à la source d'émission (i.e., au niveau de l'évent).

Ainsi, nous avons utilisé un radar Doppler pulsé et portable, appelé VOLDORAD (Volcano Doppler Radar), pendant l'éruption du 4 juillet 2001 au cratère Sud-Est de l'Etna (SEC). Cet instrument a été développé par l'Observatoire de Physique du Globe de Clermont-Ferrand (France), exclusivement pour le sondage des jets et des panaches volcaniques. Ce système transportable permet d'effectuer des sondages au sein même du panache éruptif, juste au-dessus du cratère, permettant ainsi l'estimation quantitative de paramètres physiques sources. La technologie radar Doppler permet : (1) la détection des paramètres de vitesse et de charge de la cible (ex. panache volcanique constitué de gaz et de pyroclastes) et (2) la localisation de la cible.

L'objectif de cette première partie est donc de caractériser de manière quantitative la vitesse et la masse des différents composants (gaz et pyroclasts) d'un jet Strombolien, et d'obtenir des informations sur la géométrie du jet (angle d'éjection, isotropie, etc.). L'estimation quantitative de ces paramètres sources est cruciale pour améliorer notre connaissance des phénomènes éruptifs.

Dans le chapitre 3, on s'attache plus particulièrement à l'estimation des vitesses de gaz et de particules éjectés. Pour réaliser ce travail, nous avons choisi une approche multi-méthode. Tout d'abord nous avons exploité des images provenant de vidéos enregistrées simultanément au radar. Bien que des problèmes subsistent quant à l'exploitation de la vidéo, cette méthode permet malgré tout de calculer des vitesses de gaz et de particules que l'on peut ensuite comparer avec les vitesses radar. Cette approche nous a permis, notamment, de définir plus précisément les biais géométriques reliés aux mesures radar, et nous a aidé à faire la discrimination entre vitesses de gaz et vitesses de particules. Ensuite, nous avons utilisé une approche couplée, avec les données de vitesses radar et des données synthétiques de vitesses calculées à partir d'un modèle balistique. Cette approche nous a permis de remonter à des estimations minimum de vitesses initiales de gaz (c.à.d. au niveau de l'évent), à partir du paramètre radar V^{+}_{max}. On obtient, sur une moyenne de plus de 150 explosions analysées pendant le paroxysme du 4 juillet, une vitesse initiale de gaz minimum de 144 m/s. De même, nous donnons une estimation de la vitesse moyenne initiale des particules de 67 m/s, pour un diamètre moyen de 0.26 m. A partir de la vitesse initiale de gaz, nous pouvons donner une estimation des flux massiques et volumiques de gaz. On obtient un flux volumique de Q_g = 6.03x10^3 m^3/s et un flux massique de M_g = 2.4x10^3 Kg/s, moyennés sur une séquence de 17 minutes se déroulant pendant le paroxysme du l'éruption du cratère Sud-Est de l'Etna le 4 Juillet 2001, entre 21h29 UT et 21h46 UT.

Dans le chapitre 4, nous présentons une méthode dédiée à l'estimation des paramètres de charge du jet volcanique (masse, nombre, volume et concentration des particules notamment) par inversion des données de puissance du radar Doppler VOLDORAD. Dans l'algorithme d'inversion, nous utilisons la formulation complète de la diffusion électromagnétique de Mie (1908) par des cendres sphériques et homogènes pour calculer des puissances radar rétrodiffusées synthétiques. Cette étude a été réalisée sur 2 explosions stromboliennes typiques au cratère Sud-est de l'Etna le 4 juillet 2001. L'acquisition des paramètres de masse

et de vitesse nous a permis d'estimer d'autres paramètres directement reliés comme le flux de masse, l'énergie cinétique et thermique des particules. Tout d'abord nous proposons un modèle d'inversion basé sur une distribution de taille de particules dite « polydisperse », caractérisée par la fonction de Weibull. Le mode de cette distribution est calculé à partir de la vitesse terminale de chute des particules que l'on peut obtenir directement sur les spectres Doppler, pour chaque explosion. Ensuite, on a défini un facteur de forme de la distribution de Weibull (k = 2.3) basé sur des données de la littérature pour des explosions Stromboliennes typiques (Chouet et al., 1974). Le facteur de forme obtenu correspond à une distribution de taille de particule de type log-normal, comme il est souvent observé à partir d'études de dépôts Strombolien. Finalement, le modèle d'inversion polydisperse converge sur un facteur d'ajustement de la fonction de Weibull, caractérisant le meilleur « fit » entre la puissance synthétique et la puissance réelle, nous permettant ainsi de calculer les paramètres de charge. D'autre part nous présentons un modèle alternatif basé sur une distribution de taille dite « monodisperse », qui donne une estimation plus grossière des paramètres de charge mais permet un calcul beaucoup plus rapide. Ce modèle pourrait donc être utilisé avantageusement pour de la surveillance de l'activité volcanique en temps réel. Nous avons travaillé sur deux explosions Stromboliennes, une diluée et l'autre beaucoup chargée. Nous obtenons, à partir du model polydisperse, une estimation de masse totale de pyroclastes de 58 tonnes et 206 tonnes, ce qui correspond à un volume équivalent de magma de 22 m^3 et 76 m^3 respectivement.

Enfin, dans le chapitre 5 on s'intéresse à la géométrie des explosions Stromboliennes. C'est un domaine où les données sont plus rares, notamment parce que peu de méthodes sont vraiment adaptées à ce type d'étude. Jusqu'à présent, la principale technique utilisée était l'analyse photographique, cependant l'exploitation de cette méthode, bien que très précise, est extrêmement longue et fastidieuse, ce qui empêche toute analyse statistique et altère donc la représentativité des résultats. Dans cette étude, nous avons mis en évidence que la forme des spectres Doppler était un fort indicateur de la géométrie des explosions. Ainsi, en réalisant un modèle synthétique de spectre Doppler, nous avons pu contraindre la forme des spectres enregistrés et donner une interprétation en terme géométrique. Les spectres Doppler sont construits à partir du paramètre de puissance radar et de vitesse radiale. Ainsi, nous avons utilisé les deux modèles présentés précédemment pour obtenir des puissances radar et des vitesses radiales théoriques, afin de construire des spectres Doppler synthétiques.

Ainsi, nous avons testé notre méthode de caractérisation géométrique sur 2 cas particuliers et montré l'existence de deux signatures spectrales distinctes : une signature spectrale dite « top-hat », associée à l'éjection isotrope de particules, c'est-à-dire la même quantité de matière dans un cône d'éjection considéré. Puis, nous avons mis en évidence une signature spectrale dite « triangular », associée à une éjection anisotrope. A partir de là, nous avons réalisé une étude statistique et quantitative sur plus de 200 explosions. Nous avons montré que la distribution de matériel volcanique est isotrope dans un cône d'éjection de 30 – 40° de large centré verticalement. Enfin, nous avons calculé sur plus de 200 explosions Stromboliennes que 80 – 90% du matériel volcanique éjecté est concentré dans un cône d'émission de 30 – 40° de large centré verticalement.

CHAPTER III

Kinetic features of Strombolian jets: insight from coupled Doppler radar and numerical modelling approaches, and correlation with video data

III.1. Introduction

Volcanic surface processes are, potentially, important sources of information for understanding deep mechanisms at the origin of the dynamics of an eruption. The velocity of gas and pyroclasts is a particularly important parameter as it betrays directly the physical conditions under which Strombolian explosions occur. For evident safety reasons during field work near a volcanic erupting vent, velocity measurements are generally restricted to passive remote sensing methods such as photographic (Chouet et al., 1974; Blackburn et al., 1976; Ripepe et al., 1993), video (Sparks and Wilson 1982; Neuberg et al., 1994; Ripepe et al., 2001) or acoustic (Vergniolle et al., 1996; Ripepe et al., 1996) techniques. Recently, active remote sensors based on the Doppler radar principle have been successfully operated at Stromboli (Weill et al., 1992; Hort and Seyfried, 1998; Seyfried and Hort, 1999) and Mt. Etna volcanoes (Dubosclard et al., 1999; Dubosclard et al., 2004). These techniques permit to probe selectively inside a specific volume of the jet. Moreover they provide directly velocity measurements with a high temporal resolution and a good spatial coverage. Nevertheless, some difficulties remain about accurate measurements of velocities and particularly for the discrimination of gas and clasts velocities. In this chapter, we aim at improving the interpretation of Doppler radar (VOLDORAD) velocity measurements carried out at Etna Southeast crater (SEC) on July 4, 2001. For this purpose, we use a multi-method approach: first we exploit video measurements and then we use numerical modelling. Indeed, video sequences have been recorded simultaneously to the Doppler radar sounding. In addition, the video analysis portrays the surface activity and can hence be usefully compared to VOLDORAD's data to constrain velocity measurements from volcanic gas and clasts. Thus, we first compare the maximum radial velocity ($V_{\max}^{+}$) as given by the Doppler radar, i.e., without any geometrical correction, with video-derived velocities. Then, we use and enhance a ballistic numerical model originally developed by Dubosclard et al., (2004) in order to bring more stringent constraints on the decoupling of the gas phase and pyroclasts velocities considering the geometry of the sounding. Therefore, we are able to give a minimum estimate of the initial gas velocity (V_0^g), and we also provide the initial mean velocity ($\overline{V}_0^p$) of the particles (i.e., the velocity of a particle with mean diameter ($\overline{D}$).

III.2. Insight from video analysis method

III.2.1. Lava-bubble vs. lava-jet explosions

We have worked on 18 explosions occurring on July 4, 2001 between 2130:00 UT and 2145:00 UT, which corresponds to the paroxysm of the eruption. We have distinguished two types: (i) Lava-jets; which originate from a slug bursting beneath the crater rim (invisible on video snapshot), and producing a discrete explosion with a quite narrow particle ejection cone. (ii) Lava-bubbles; which originate from a slug bursting above the crater rim (visible on video snapshot), and producing a discrete explosion with a rather hemispherical ejection cone. Both types are related to the Strombolian activity as one discrete slug is at the origin of the ejection of pyroclasts. However, some differences of shallow physical processes exist and lead to these contrasted surface manifestations. We believe that the increase of the magma level that may partly fill the crater cavity can lead to the growth of a large gas bubble raising the overlying magmatic film that deforms and breaks subsequently into disconnected blocks ejected in all directions by the overpressurized gas release.

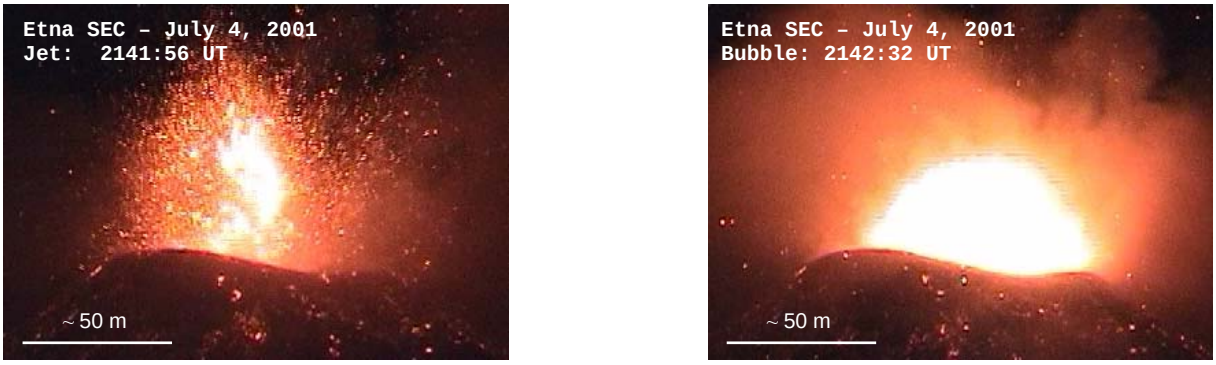

(a) **LAVA – JET TYPE** (b) **LAVA – BUBBLE TYPE**

Figure III.1. (a) Video snapshot of lava-jet type explosion occurring at 2141:56 UT during the July 4, 2001 eruption at Etna SEC. (b) Video snapshot of lava-bubble type explosion occurring at 2141:56 UT during the July 4, 2001 eruption at Etna SEC.

Other parameters may also control the formation of lava-bubbles, such as the size and the gas overpressurisation of the slug. The physical conditions under which such a lava-bubble may form are difficult to meet and hence this type of explosions is scarce. Indeed, during the considered period of time (~ 15 min) we have identified about 150 explosions and only 10 are bubble-type. Therefore, jet-type explosions are statistically more representative of typical

Strombolian activity in terms of geometry. We show on Figure III.1 a lava-jet explosion occurring at 2141:56 UT, and a very large lava-bubble type explosion occurring at 2142:32 UT.

III.2.2. Video-derived gas measurements

Therefore we have measured, from video snapshots acquired simultaneously to the radar, the cumulative distance covered by both (i) discrete solid blocks propelled upward and (ii) the luminous front propagating in the surrounding air. We assume that the luminous front represents the gas phase or at least fine particles such as ash, characterised by a very low inertia and hence that move (accelerate/decelerate) as the gas phase does. Such video measurements thus permit us to give a rough estimate of the gas velocity above the crater rim. However, finest particles are quickly cooled down and may not be seen at night; hence the real gas velocity might be slightly higher. The instantaneous velocity can finally be derived from finite difference calculations (eq. III.1), with *z* being the distance between each front or block displacement measured at each time step Δt. Note that the video temporal resolution permits a detailed analysis every 0.04 s.

$$V = \frac{dz}{dt} = \frac{z_{i+1} - z_i}{\Delta t} \qquad \text{(III.1)}$$

Figure III.2a shows an example of luminous front (i.e., gas phase) velocities measured on one Strombolian jet occurring at 2137:44 UT at Etna SEC. Practically, we have drawn the contours of luminous front propagating through time that gives, via a scale factor, the distance covered by the front at each time step. Some difficulties arise with this method, particularly for the detection of the front boundary as it is often rendered hazy by the scattering of light in the surrounding air. The pixel saturation of the video snapshot also makes difficult the accurate determination of the propagating front position, but relative interspaces might give satisfactory results. Moreover, the exploitation of a two-dimensional (2D) field of view may also induce some biases on video measurements that can virtually reduce real particle velocity, although we have tried to work on early trajectories, close to the vertical, so as to reduce this effect. We provide (Figure III.2b) the cumulative distance covered by the luminous front propagating upward and the corresponding time-derivative (*dz/dt*) that gives the instantaneous velocity of the gas phase expansion at each time step. We observe a

significant velocity decrease of the gas phase from 165 m/s right above the crater rim (z≈0) at t_0=0, until 75 m/s at about z≈110 m upright to the crater at t_f=0.8 s. We obtain a time-average gas velocity of 111 m/s for the Strombolian jet at 2137:44 UT.

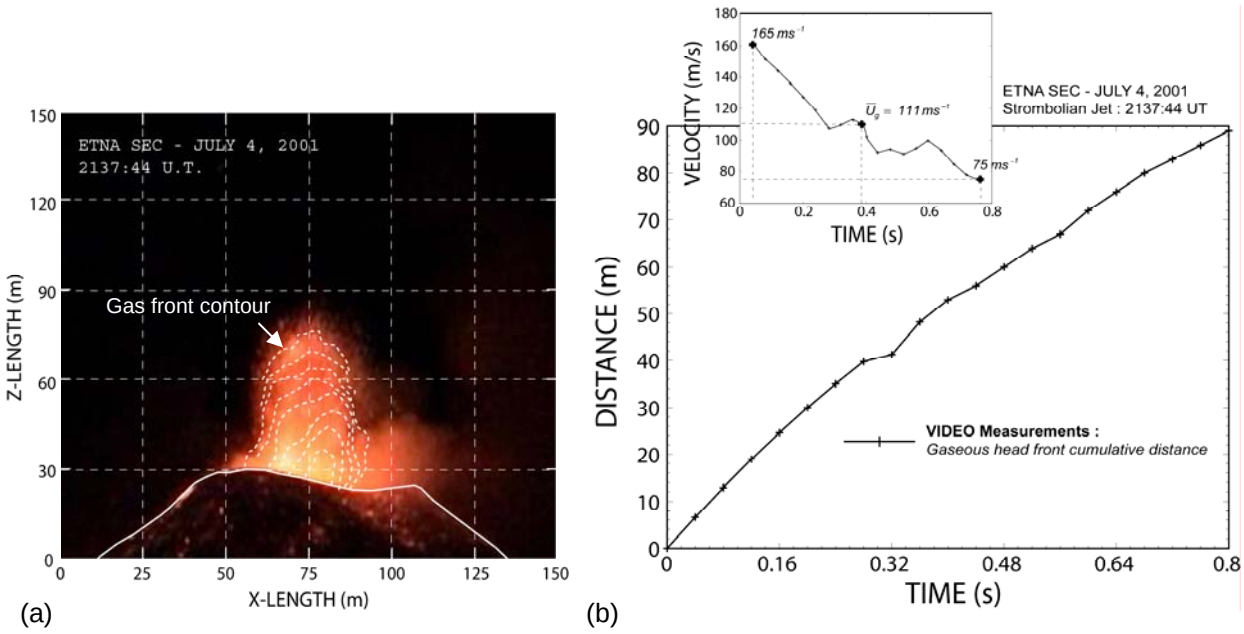

Figure III.2. (a) Video snapshot showing the expansion of the gas phase, with contours of each luminous front drawn in dashed line. (b) Plot of video-derived measurements of the lava-jet explosion occurring at 2137:44 UT on July 4, 2001 at Etna SEC, representing the cumulative distance covered by each luminous front rising upright through time sampled every 0.04 s, and the corresponding time-derivative that gives the instantaneous velocity of the gas at each time step.

III.2.3. Video-derived particles measurements

We show on Figure III.3a an example of displacement and velocity measurements on solid blocks for the same Strombolian jet occurring at 2137:44 UT at Etna SEC. In this case, we follow the trajectory of discrete particles travelling upward. Bearing in mind our objective to compare video-derived velocities with maximum radar velocity (V^{+}_{max}) we have selected the fastest blocks trajectories. We provide (Figure III.3b) the cumulative distance covered by one lava block ejected upward and the corresponding time-derivative (*dz/dt*) that gives the instantaneous velocity of the particle at each time step. We observe a low velocity decrease of the particle from 85 m/s at t_0=0 (z≈30) until 58 m/s at about z≈120 m above the crater rim at t_f=1.12 s. Note that if we consider the potential bias related to the 2D field of view, then, the velocity decrease could even be lower. Finally we obtain a time-averaged particle velocity of

70 m/s for the Strombolian jet at 2137:44 UT. We were not able to achieve particle displacement measurements right above the crater rim as the gas phase is too dense in the very first tenths of meters, which impedes individual blocks to be visible below z=30 m. In this example, the velocity of the gaseous front is much higher than that of particles, and we observe that the velocity decrease of particles is much lower than that of the gas. Indeed, the ratio between the first and the last gas velocity measurement is 165/75=2.2 over a distance of 90 m within 0.8 s against a ratio of 85/58=1.47 over the same distance of 90 m within 1.12 s for the particle velocity measurements. This can be easily explained by the high inertia of large particles, first propelled slower than fine ash by the gas phase, and then, not as much slowed down by the gas velocity decrease.

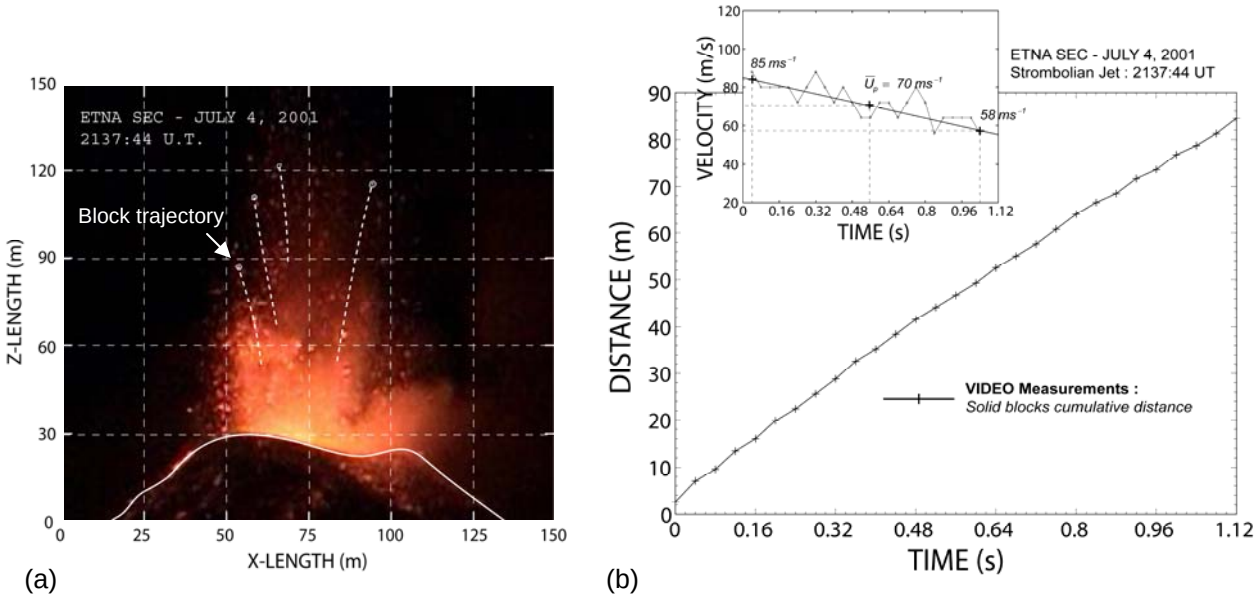

Figure III.3. (a) Video snapshot showing the trajectories of four large lava blocks ejected almost vertically. (b) Plot of video-derived measurements of the lava-jet explosion occurring at 2137:44 UT on July 4, 2001 at Etna SEC, representing the cumulative distance covered by a single lava block rising through time, sampled every 0.04 s, and the corresponding time-derivative that gives the instantaneous velocity of the particle at each time step.

Consequently, the maximum velocity recorded by the Doppler radar at a given elevation above the emission source is related to the competition between both kinetic regimes. In order to exemplify that issue, if we assume that measurements were carried out right above the emission source (i.e., vent), the maximum velocity recorded would clearly be related to the gas phase expansion. On the other hand, if measurements were carried out at a few hundreds

of meters above the vent, the maximum velocity recorded would most likely be related to the particle ejection. Actually, the competition between both regimes is a continuum and hence, the maximum velocity recorded strongly depends on the size of particles and on the measurement elevation. The same video measurements have been carried out on large lava-bubble explosions. However, in this case the luminous front is related to the nose of the lava-bubble before breaking, and hence, velocity measurements do not correspond to the gas velocity, but rather to the expansion rate of the expanding slug at the magma-air interface prior to bursting. Then, we will only provide instantaneous velocities of discrete lava blocks propelled hemispherically after the bursting of the gas slug; these can be compared to radar velocities. Note that during the considered period of time (~ 15 min) we have identified about 150 explosions and only 10 are bubble-type explosions. Therefore, jets-type explosions are statistically more representative of typical Strombolian activity in terms of geometry. In the next section, we attempt to give more constraints on the origin (particles or gas) and accuracy of velocities measured by the Doppler radar VOLDORAD.

III.2.4. Radar/video correlations of particles velocities

Velocity measurements have been carried out on 8 lava-jet and 10 lava-bubble explosions occurring on July 4, 2001 between 2130:00 UT and 2145:00 UT. Figure III.4 and Figure III.5 show the positive maximum radial velocities ($V^{+}_{\max}$) recorded by VOLDORAD that is calculated as the right most abscissa of the Doppler spectrum for which the echo-power is superior to the noise level. These maximum radar-derived velocities are then compared with: (i) particles velocities ($U^{p}_{z\approx 100m}$) inferred from video measurements for both lava-jet (Figure III.4a) and lava-bubble (Figure III.4b) explosions, and then (ii) compared with gas velocities ($U^{g}_{z\approx 100m}$) inferred from video measurements of lava-jets only (Figure III.5). In order to make these comparisons as relevant as possible, all video-derived velocity values have been selected at a same elevation of about z=100 m, which is moreover roughly consistent with the radar measurements elevation. Note however that it is not a critical issue for particle measurements in particular, because of their low velocity decrease in the first hundred meters (Figure III.3).

III.2.4.1. Lava-jet explosions

We obtain, as shown in Figure III.4a, a positive maximum radial velocity $V^{+}_{\max}$ =56 m/s and a particle velocity, at an elevation of 100 m, of $U^{p}_{z\approx 100m}$=60 m/s averaged on the 8 lava-jet explosions. We observe that radar-derived and video-derived mean velocity values are very similar, which may suggest that $V^{+}_{\max}$ measurements are consistent with particles velocities. However, by examining in detail each explosion individually, we point out some significant discrepancies between radar-derived and video-derived velocities. We also stress the variation of velocities of the radar and video measurement series themselves.

Firstly, for lava-jet explosions (Figure III.4a), we show a large dispersion of $V^{+}_{\max}$ values with a standard deviation of 13.9 m/s (i.e., 25%). The dispersion of Doppler radar measurements could simply be related to the natural variation of particles or gas velocities between each explosion; however, other reasons can also be invoked.

(1) Radar data have been acquired with a velocity range up to 60 m/s, although faster particle velocities can nevertheless be recovered if the radar signal is not too much deformed by aliasing. Indeed, in some cases Doppler spectra are too distorted for the automatic processing to retrieve correct values, and velocity measurements can hence be biased. However, for the velocities given in this section, all measurements have been cautiously checked directly on each Doppler spectrum and can be considered as correct.

(2) VOLDORAD records radial velocities, i.e., the component along the radar beam axis, inclined at 23° from the horizontal. So, real velocities are potentially underestimated if the particle trajectory is not parallel to the radar beam axis. In addition, the variability of particles trajectories from one explosion to another may also account for the dispersion of radar-derived measurements. The geometrical framework of the radar sounding has then to be defined cautiously.

The dispersion of particles velocities derived from video measurements is far lower, with a standard deviation of 5.9 m/s (i.e., only 10% of the mean value). Remind that we have selected on video snapshots the fastest particles so as to make a comparison with maximum velocities recorded by VOLDORAD.

Secondly, although the correlation between mean velocity values derived from video and radar measurements are very good, we show that the difference of velocity (ΔV) between

individual explosions can reach a maximum close to |ΔV|=30 m/s for explosion at 2137:36 UT, whereas explosion at 2136:21 UT gives very similar values with |ΔV|=1.6 m/s. Note that ΔV takes alternatively positive ($V^{+}_{\max} > U^{p}_{z\approx 100m}$) and negative values ($V^{+}_{\max} < U^{p}_{z\approx 100m}$). By using the root mean square coefficient (RMS), we obtain a mean velocity difference between radar and video measurements on 8 lava-jet explosions of ΔV_{RMS}=12.7 m/s. This disparity is not so large bearing in mind that methodological approach of velocity retrieval is very different.

III.2.4.2. Lava-bubble explosions

Lava-bubble explosions are geometrically very different from lava-jet explosions as the gas slug bursts above the crater rim and hence propels particles hemispherically with ejection angles ranging from vertical to almost horizontal trajectories. This singular feature, if not representative of the common Strombolian explosions encountered at Etna during the July 4, 2001 eruption, may nevertheless be used advantageously to point out some crucial evidence.

Very comparable mean values are found for lava-bubble explosions (Figure III.4b) with values of $V^{+}_{\max}$=55 m/s and $U^{p}_{z\approx 100m}$=59 m/s averaged on 10 events. Once again, this similarity may suggest that $V^{+}_{\max}$ measurements are consistent with particles velocities.

Note that mean velocity values are found to be equivalent for both lava-jet (Figure III.4a) and lava-bubble (Figure III.4b) explosions, which stresses that an analogous physical mechanism of particle ejection is at work. Indeed, we think that for both type of explosions, the bursting of an overpressurized gas slug reaching the magma-air interface is at the origin of the fragmentation and ejection of disconnected particles in the surrounding air. Obviously, some differences still exist, such as the depth of bursting, the gas slug geometry and overpressurisation, and probably the fragmentation. The latter seems (from visual observations) to be less efficient in the case of lava-bubble explosions generating larger particles.

For lava-bubble explosions (Figure III.4b), the dispersion of $V^{+}_{\max}$ values is found to be far smaller than for lava-jet ones, with a standard deviation of 6.9 m/s (i.e., 12.5%). One of the main obvious reasons that may explain this low dispersion lies on the trajectories of ejected particles. Indeed, we have clearly observed from video snapshot analysis (Chapter V) that for

the case of lava-bubble explosions, particles are ejected hemispherically with quite homogeneous velocities. Therefore, a significant amount of pyroclastic matter is always ejected with an angle close to that of the radar beam axis, and hence gives a better estimate of particle velocities because it is less biased by the geometrical effect.

On the other hand, the dispersion of particles velocities derived from video measurements is also low with a standard deviation of 7 m/s (i.e., 12%), and close to that of lava-jet explosions. It confirms the consistency and accuracy of video-derived measurements. Most interestingly, the correlation of velocities derived from both radar and video measurements between each individual explosion turns out to be also pretty good, with particularly, a mean velocity difference of ΔV_{RMS} =7.6 m/s.

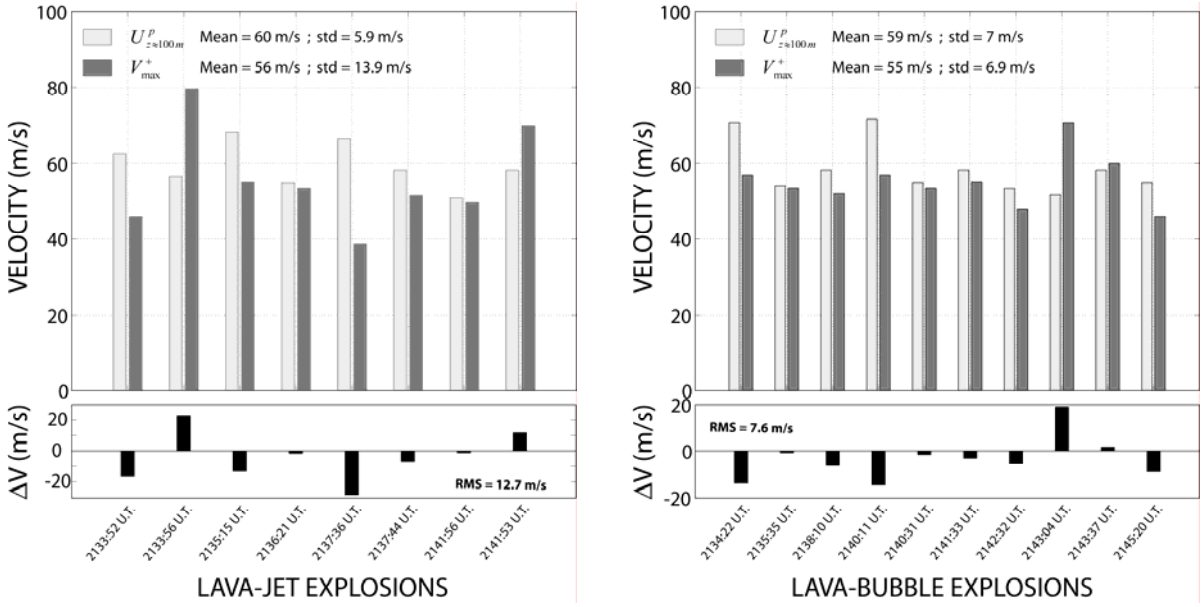

Figure III.4. Plot of the particle velocity ($U^{p}_{z\approx100m}$) derived from video measurements carried out at an elevation of about 100 m above the crater rim, and compared to maximum radial velocity (V^{+}_{max}) recorded by VOLDORAD in the radar range G_3, for (a) lava-jet explosions and (b) lava-bubble explosions.

We have shown that video-derived velocities are reliable, and give similar values for lava-jet and lava-bubble explosions, with for both, a low standard deviation. On the other hand, we have shown that radar-derived velocities are more variable, although in fairly good agreement with video-derived velocity in average, and probably quite sensitive to the geometry of the particle ejection. As a consequence, bearing in mind the very large number of lava-jet explosions constituting the July-4 Strombolian activity, we assume that a geometrical

correction must be taken into account on V^{+}_{max} measurements. The results obtained in this section suggest that radar measurements of maximum velocity (V^{+}_{max}) are consistent with velocities of lava blocks.

III.2.5. Radar/video correlations of gas velocities

The gas velocity can be roughly estimated from video measurements of the luminous front propagating upward as explained previously (Section III.2.2). In this section, video-derived gas velocities ($U^{g}_{z\approx 100m}$), taken at an elevation of about 100 m above the crater rim, are compared with radar-derived velocities (V^{+}_{max}). Although previous results have shown that V^{+}_{max} may be consistent with particles velocity, we investigate the possibility that fine ash, roughly behaving like the gas phase, may be endowed of a higher velocity, and hence be recorded as V^{+}_{max} by VOLDORAD.

Figure III.5 gives a mean value of gas velocity derived from video measurements of $U^{g}_{z\approx 100m}$=72 m/s at an elevation of 100 m above the crater rim, and a maximum radial velocity recorded by VOLDORAD of V^{+}_{max}=56 m/s, averaged on 8 lava-jet explosions. These values are relatively similar and point out that V^{+}_{max} values may be consistent at first order with gas velocities. Note however, bearing in mind the high decrease of gas velocity, that the elevation chosen (z=100) for video-derived gas measurement can be critical for the comparison of both methods. Accordingly, the dispersion of video-derived gas measurements is higher than for particles, reaching a standard deviation of 16.5 m/s (i.e., 21%). This larger dispersion has also to be attributed to the technical difficulties to make accurate measurements on the luminous front of video snapshots. The dispersion of radar-derived measurements is also quite large with a standard deviation of 13.9 m/s (i.e., 25%), due to the possible geometrical and technical biases mentioned previously.

Consequently, the difference of velocity (ΔV) between each individual explosion is also not very good, with a maximum velocity difference that can reach |ΔV|=40 m/s for explosion at 2137:36 UT, and a mean velocity difference averaged on 8 lava-jet explosions of ΔV_{RMS} =27.8 m/s.

This disparity is not so large bearing in mind the difficulties to measure gas velocity on video snapshots. Moreover, note that velocities recorded by VOLDORAD, on lava-jet explosions particularly, underestimate real velocity values owing to the possible geometrical bias. A geometrical correction on $V^{+}_{\max}$ would clearly make radar measurements closer to the gas velocity video measurements. Moreover, some tests on the minimum detectable signal threshold carried out according to the sounding characteristics at Mt. Etna clearly show that a small amount of very fine ash (about 11 particles of 1 mm per m^3) can be detected by VOLDORAD.

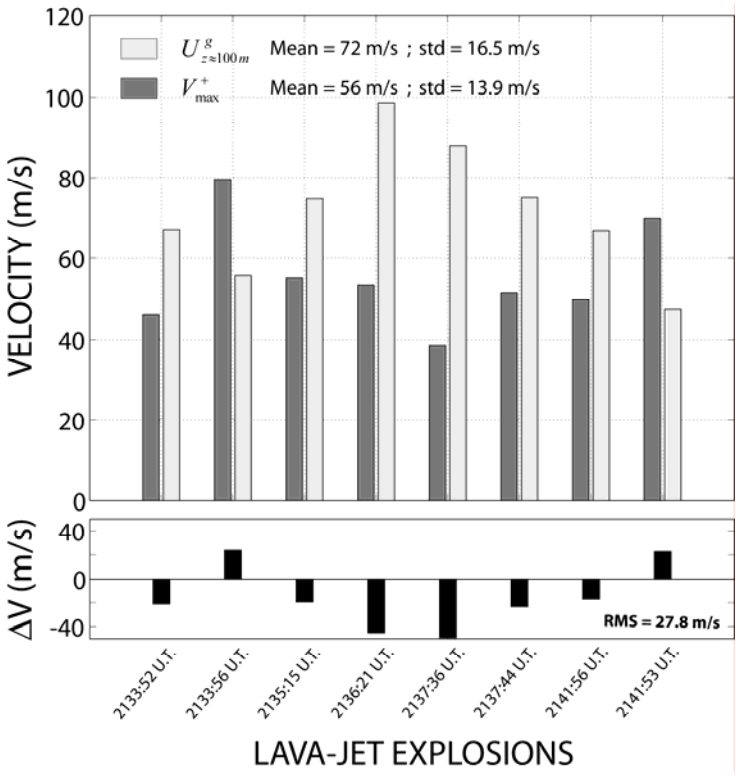

Figure III.5. Plot of the gas velocity ($U^{g}_{z\approx100m}$) derived from video measurements carried out at an elevation of about 100 m above the crater rim, and compared to maximum radial velocity ($V^{+}_{\max}$) recorded by VOLDORAD in the radar range G_3, for lava-jet explosions.

Finally, we have shown from radar and video correlations that maximum velocity $V^{+}_{\max}$ recorded by the Doppler radar may be in agreement with both particle and gas velocities, although large individual discrepancies remain. The contribution of large particles and fine ash in the velocity estimate is difficult to evaluate. Indeed, the velocity recorded at a given elevation above the emission source is related to the competition between both kinetic regimes, i.e., high-inertia regime represented by large particles, and low-inertia regime

represented by the gas phase or at least very fine ash. Considering the geometrical characteristic of the sounding, we suspect that the distance between the emission source and the radar range gate G_3 corresponds to the limit between both kinetic regimes. In the next section, we thus aim at giving some constraints on kinetic regimes at work.

III.3. Insight from numerical ballistic model

III.3.1. Ballistic model definition

The theoretical evolution of the gas velocity with height and the corresponding velocity decrease of particles can be assessed from numerical modelling. The objective is to bring additional constraints on both kinetic regimes, and give a better insight on the origin (particles or gas) of the maximum velocities recorded by VOLDORAD. These kinetic features are calculated by the numerical ballistic model, presented in appendix A, on the basis of equations of motion, assuming that the two forces acting on each particle are the drag force, and the gravitational force. We first define, particularly, the initial velocity of a particle with diameter D (Steinberg and Babenko, 1978):

$$V_0^p(D) = V_0^g - k\sqrt{D} \qquad \text{(III.2)}$$

where k is a constant, taken as 150 as inferred from previous studies (Chouet et al., 1974, Ripepe et al., 1993), and then, the gas velocity is defined as a function of height (Blackburn et al., 1976) by using:

$$V_g(z) = V_0^g \exp\left(\frac{-\gamma z}{z_{ref}}\right) \qquad \text{(III.3)}$$

where γ is a constant taken as 4.6 (Dubosclard et al., 2004) and z_{ref} is the height above the vent such as $V_g(z_{ref}) = 0.01V_0^g$. The constant z_{ref} was chosen by Dubosclard et al., (2004) at 1200 m, but we show from video measurements (Figure III.6) that this value is too high for the July-4 eruption at Mt. Etna. In the next section we thus try to better constrain this constant.

III.3.2. Parametric constraints

In order to better constrain the decrease coefficient (z_{ref}) of the gas velocity, we used the gas velocity measurements inferred from direct video observations, extrapolated at the emission source (i.e., at the vent level) at t_0 =0 s and averaged on 8 lava-jet explosions (Figure III.6). Then, we have searched out the best height reference coefficient (z_{ref}) such as equation III.3 fits at best the observed trend. We have found a best match for a coefficient z_{ref}=850 m. Note that the constant γ is taken as 4.6, and cannot be constrained from our video measurements. Some uncertainties on this constant may probably induce a small error on the velocity decrease law.

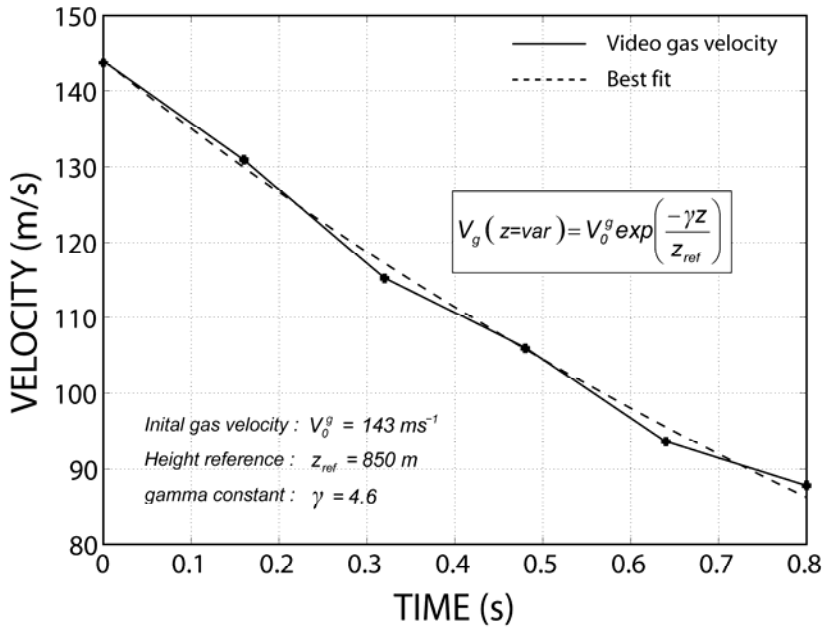

Figure III.6. Time series of the gas velocity derived from luminous front measurements on video snapshots averaged on 8 lava-jet explosions. The velocity decrease curve has been extrapolated at the emission source level (t_0). We give the best height reference coefficient z_{ref}=850 m such that equation III.3 (Blackburn et al., 1976) fits at best the averaged video-derived trend.

III.3.3. Gas vs. particles velocities

By using the numerical ballistic model, we are able to describe the evolution of the gas velocity with height and the corresponding velocity decrease of particles. We give on figure III.7 the theoretical velocity decrease of a gas parcel from equation III.3 with an initial gas

velocity V_0^g=100 m/s, a constant γ=4.6 and a reference elevation z_{ref}=850 m. The corresponding velocities of particles for different sizes are then calculated by a fourth order Runge-Kutta algorithm, until an elevation of z=180 m. Finally, we show for example that a particle with diameter D=0.01m launched at about 85 m/s by a gas phase with initial velocity of 100 m/s, becomes faster than the gas phase after about 40 m travelling upright. At the opposite, a particle with diameter D=0.06 m propelled initially at about 66 m/s by a gas phase with initial velocity of 100 m/s never becomes faster than the gas within about two hundreds of meters above the vent. The bottom of the radar range gate G_3 is located at about 75 m upright to the vent of the SE crater, but we show hereinafter that the maximum radial velocities ($V_{\max}^+$) recorded by VOLDORAD correspond to particle trajectories inclined at 55°, that represents the boundary of the sampling volume. Therefore, it gives a slanting distance between the radar range gate and the emission source of about 120 m. Under these conditions, we show that maximum velocities recorded by VOLDORAD inside the range gate G_3 are related to particle with diameters inferior to 0.06 m.

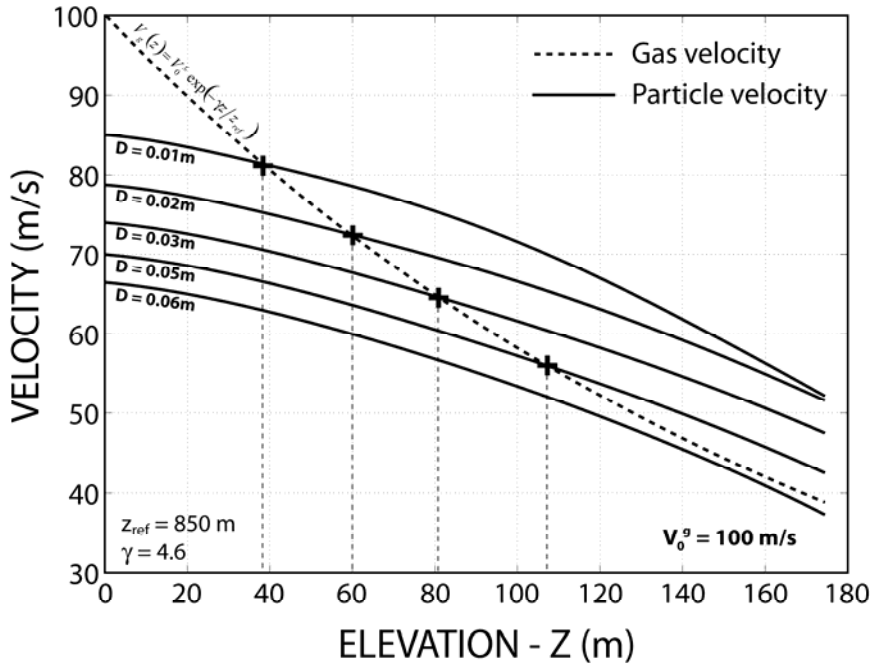

Figure III.7. Plot of the evolution of the theoretical gas velocity with height, for an initial gas velocity of 100 m/s, a height reference coefficient z_{ref}=850 m, and a constant γ=4.6. We provide the corresponding particle velocity for different particle sizes, calculated from a Runge-Kutta algorithm developed in the ballistic model.

This result points out that maximum velocities recorded by VOLDORAD are consistent with small particles of a few centimetres or less, and hence that $V_{\max}^{+}$ measurements can give a first order estimate of the gas velocity at the elevation of the range gate G_3. From this statement, we will aim in the next section at estimating, particularly, the initial gas velocity, i.e., at the vent, considering some geometrical corrections related to the sounding characteristics.

III.4. Source parameters retrieval method

In this section we present a method to retrieve initial kinetic parameters, such as the initial gas velocity and the average initial particle velocity from radar data. We have shown previously from coupled video and numerical analysis that the gas velocity can be assessed from direct radar measurements of the maximum radial velocity ($V_{\max}^{+}$). On the other hand, we will define the positive mean radial velocity (V_{mean}^{+}) that can be used advantageously for the estimation of mean particle velocity with median diameter $\overline{D}$. We first apply the retrieval method developed hereinafter on a single typical Strombolian explosion and then we extend this method to long sequences of Strombolian activity.

III.4.1. Initial gas velocity retrieval

Maximum radial velocities ($V_{\max}^{+}$) recorded by VOLDORAD are related to small particles possibly ranging from fine ash to particles of a few centimetres. We thus assume reasonably that $V_{\max}^{+}$ may represent a minimum estimate of the gas velocity at the range gate elevation. In order to recover the initial gas velocity (V_0^g) from $V_{\max}^{+}$ measurements, the geometrical setting of the radar sounding and the geometry of the SE crater must be known accurately (Figure III.8.).

VOLDORAD was located at a slanting distance of 1047 m to the centre of the range gate G_3, with a central antenna beam elevation of θ=23°. The centre of the considered range gate was positioned at a distance of about L_{SA}=150 m upright (φ=90°) to the vent. However, VOLDORAD measures radial velocities on the component of the antenna beam axis, therefore maximum radial velocities recorded by VOLDORAD corresponds to particles with trajectories the most inclined. Considering the limited extent (120m-wide and 160m-height)

of the range gate G_3, we define a maximum inclination of φ=55° that corresponds to a slanting distance of about L_{SB}=120 m from the emission source to the bottom right corner of the range gate G_3. In these calculations, the depth of the crater was taken at about 50 m as inferred from direct visual information (personal communication with Charles Rivière). Note, that the antenna beam is conic, and having an aperture angle α=9°, the elevation of its bottom part can be defined as θ-α/2=18.5°.

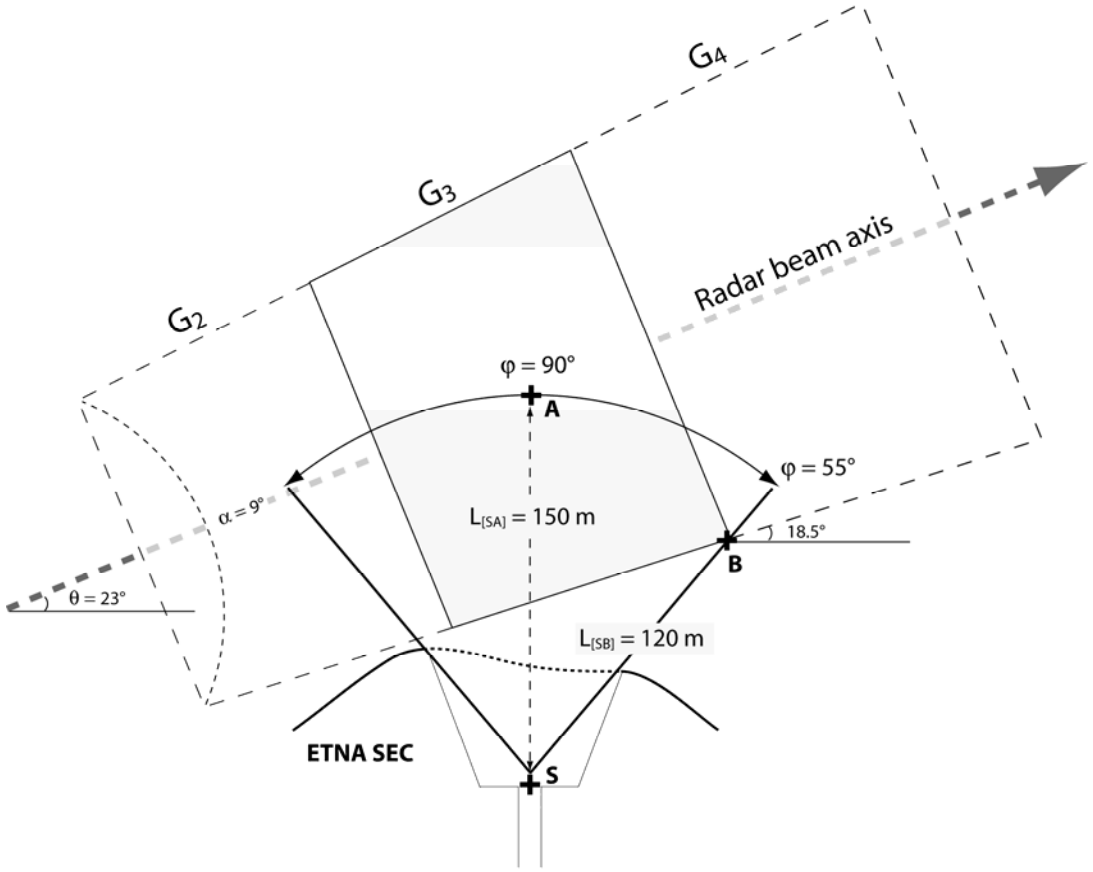

Figure III.8. Sketch of the geometrical setting for the radar sounding carried out at Etna SEC, on July 4, 2001. VOLDORAD was located at a slanting distance of 1047 m to the centre of the range gate G_3, with a central antenna beam elevation of θ=23°, and an aperture angle of α=9°. The distance between the vent (S) and the centre of the radar range gate G_3 (A) is estimated at about $L_{[SA]}$=150 m with an angle φ=90°. The distance between the vent (S) and the bottom right corner of the range gate G_3 (B) is estimated at about $L_{[SB]}$=120 m for a maximum inclination of φ=55°.

Two corrections have to be applied on the maximum radial velocity ($V^{+}_{\max}$) recorded by VOLDORAD to recover the initial gas velocity (V^{g}_{0}): (i) The geometrical correction (C_{φ}), related to the maximum inclination of the particle trajectory, can be expressed by a simple trigonometric relation; and (ii) the elevation correction (C_L) due to the slanting distance

between the source of gas emission and the gate corner can be inferred from a decrease exponential law of the gas velocity as a function of height (Blackburn et al., 1976):

$$C_{\varphi} = \frac{1}{\cos[\varphi - (\theta - \alpha/2)]} \qquad \text{and} \qquad C_L = \exp\left(\frac{\gamma L}{z_{ref}}\right) \tag{III.4}$$

Finally the initial gas velocity (V_0^g) is simply the product of the maximum radial velocity ($V_{\max}^+$) with the two correction coefficients, and can be expressed as:

$$V_0^g = V_{\max}^+ C_{\varphi} C_L = V_{\max}^+ \frac{\exp(\gamma L / z_{ref})}{\cos(\varphi - (\theta - \alpha/2))} \tag{III.5}$$

Under the geometrical characteristics of the sounding at Etna SEC during the July-4 eruption we define a slanting distance between the source of gas emission and the range gate corner of L=120 m, for a maximum inclination φ=55°. The velocity decrease constants are taken as γ=4.6 and z_{ref}=850 m, and the antenna beam elevation is θ =23° with an aperture angle α=9°. Therefore we obtain a geometrical correction coefficient of $C_{\varphi=55°}$=1.2 and an elevation correction coefficient of $C_{L=120m}$=1.9.

III.4.2. Initial particle velocity and mean diameter retrieval

In the previous section we used the maximum radial velocity ($V_{\max}^+$) recorded by VOLDORAD to retrieve the initial gas velocity. $V_{\max}^+$ is defined as the right most abscissa (i.e., radial velocity) of Doppler spectra for which the power stands above the noise level (Figure III.9). We have shown particularly, that the maximum radial velocity may correspond both to the finest particles and to the most inclined trajectories crossing the bottom right corner of the radar range gate G_3.

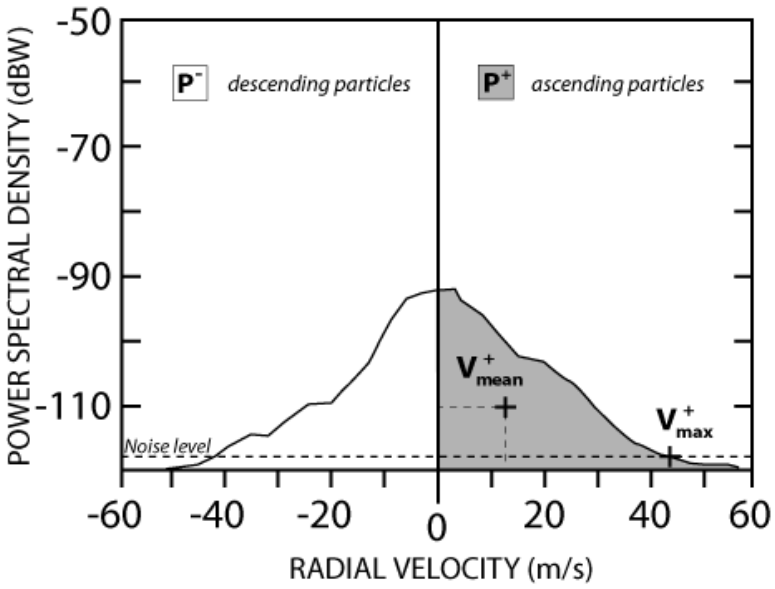

Figure III.9. Sketch of a radar Doppler spectrum showing the positive maximum radial velocity ($V^{+}_{\max}$) recorded by VOLDORAD that corresponds to the right most radial velocity for which the power stands above the noise level (dashed line). The positive mean velocity (V^{+}_{mean}) corresponds to the velocity weighted by the power spectral density over the whole positive velocity range. In the geometric configuration of the sounding carried out at Etna SEC in July 4, 2001, the positive index (+) is mainly related to ascending particles in the range gate G_3 located above the crater.

Now, we use the positive mean velocity (V^{+}_{mean}) measured by VOLDORAD, that corresponds to the mean velocity weighted by the power spectral density over the whole positive velocity range (Figure III.9). As shown in chapter V, a volcanic Doppler spectrum can be characterised completely using a particle size distribution (PSD), and an ejection angle distribution (EAD). Firstly, V^{+}_{mean} may represent the mean velocity of all particles sizes, ranging from finest ash to largest blocks, and can hence be defined as the velocity of particles with mean diameter $\overline{D}$. Secondly, V^{+}_{mean} should take into account all ejection trajectories, integrated in the considered sampling volume. However, on the basis of statistical analyses carried out on a large number of typical Strombolian explosions in Chapter V, we assume reasonably that most of particles are distributed symmetrically along the vertical axis within a narrow ejection cone. Therefore, V^{+}_{mean} may correspond at first order to the velocity of particles with mean diameter $\overline{D}$ (i.e., monodisperse distribution) ejected mainly vertically (i.e., mono-angle distribution) at the centre of the radar range gate G_3.

Since we know the value of initial gas velocity (V_0^g), that is the driving force for particle motion, we can estimate the mean initial particle velocity ($\overline{V}_0^p$) with diameter ($\overline{D}$). However, in this case we cannot give accurate analytical solution of the equations of motion and then we need to employ the numerical approach based on the fourth order Runge-Kutta algorithm described in the ballistic model (Appendix A). Practically, at the input to the model we have to define (i) the initial gas velocity (V_0^g), which varies between each explosion, (ii) the distance between the emission source and the centre of the radar range gate G_3 (L=150 m) and (iii) the angle of particles trajectories (φ=90°). Finally, the mean diameter ($\overline{D}$) is a variable parameter that is incremented in the recursive loop of the inversion procedure until the synthetic mean velocity V_{mean}^{+synt} match the recorded mean velocity (V_{mean}^{+}). Eventually, we obtain both the mean diameter ($\overline{D}$) and the mean initial particle velocity ($\overline{V}_0^p$).

III.5. A case study: explosion at 2141:56 UT

We worked on a single explosion occurring at 2141:56 UT during the paroxysm of the eruption on July 4, 2001 at Etna SE Crater. This explosion is typically Strombolian; the particle ejection is centred rather vertically, and the duration of particle emission lasts about 2 s. We have selected one Doppler spectrum corresponding to the range gate G_3 that gives the maximum radial velocity ($V_{\max}^{+}$) and the mean radial velocity (V_{mean}^{+}) at the onset of the explosion (Figure III.10a). Note that both parameters can be acquired either visually from the Doppler spectrum picture, or automatically from the computation of spectral moments. This last option will advantageously be used for the processing of long sequences of Strombolian explosions. As a comparison, we provide (Figure III.10b) a video snapshot of the explosion at 2141:56 UT, displayed at the maximum brightness intensity so as to show the magnitude of the explosion.

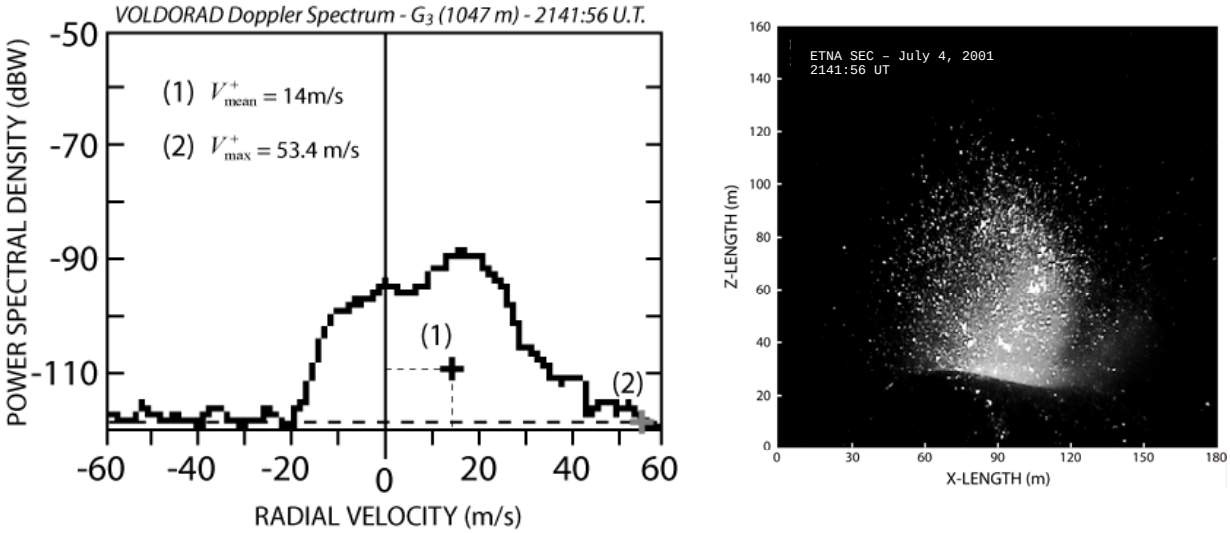

Figure III.10. (a) Plot of VOLDORAD Doppler spectrum recorded in the range gate G_3 on July 4, 2001 at Etna SEC, at the onset of the explosion at 2141:56 UT. We give the maximum radial velocity ($V^+_{\max}$) and the mean radial velocity (V^+_{mean}). (b) Video snapshot of the explosion occurring at 2141:56 UT displayed at the maximum brightness intensity.

III.5.1. Initial gas and particles velocities

The initial gas velocity (V_0^g) is obtained directly from the analytical approach using the maximum radial velocity ($V^+_{\max}$=53.4 m/s) recorded by VOLDORAD on the explosion at 2141:56 UT, with the geometrical correction coefficient $C_{\varphi=55°}$=1.2 and the elevation correction coefficient $C_{L=120m}$=1.9.

$$V_0^g = V^+_{\max} \times C_{\varphi=55°} \times C_{L=120m} = 122 \text{ m/s} \qquad \text{(III.6)}$$

We give for the explosion at 2141:56 UT a minimum estimate of the initial gas velocity of V_0^g=122 m/s. Note that the gas velocity inside the sampling volume, at the elevation of the bottom right corner of the range G_3 is equal to 64 m/s.

The mean diameter ($\overline{D}$) is obtained by best fit matching of the synthetic mean radial velocity (V_{mean}^{+synt}) with the recorded mean radial velocity (V_{mean}^{+}) using the ballistic numerical model. The mean radial velocity recorded by VOLDORAD is found to be V_{mean}^{+}=14 m/s for the explosion at 2141:56 UT, and assumed to be the velocity of particles with mean diameter $\overline{D}$ at the centre of the radar range gate G_3, about 150 m upright to the vent. We thus obtain a mean diameter $\overline{D}$=0.13 m with an initial mean particle velocity of $\overline{V}_0^{\,p}$=66 m/s. Note that the mean particle velocity at the centre of the range gate G_3 is found to be 36 m/s. Theses values are summarized in table III.1.

Table III.1. Values of initial gas velocity (V_0^g), average particle diameter ($\overline{D}$), and initial particle velocity (V_0^p), obtained for the explosion at 2141:56 UT on July 4, 2001 at Etna SEC.

	Gas velocity		Mean diameter		Particle velocity	
INPUT	$C_{\varphi=55°}$	1.2	φ *(deg)*	90	φ *(deg)*	90
	$C_{L=120m}$	1.9	*L (m)*	150	*L* (m)	150
	$V_{\max}^{+}$ (m/s)	53.4	V_{mean}^{+} (m/s)	14	V_{mean}^{+} (m/s)	14
OUTPUT	V_0^g (m/s)	122	$\overline{D}$ (m)	0.13	V_0^p (m/s)	66

Our values fall in the wide range of values given in the literature for Strombolian activity. Chouet at al. (1974) gave estimations of gas velocity of about 94–112 m/s and mean particle velocities of 15–26 m/s at Stromboli from photoballistic measurements on two explosions.
Steinberg and Babenko (1978) derived from calculations the gas velocity by using the particles size distribution at Etna and Stromboli, giving values of about 95 m/s and 70 m/s respectively. Ground deposits studies carried out at Etna Northeast Crater by McGetchin et al., (1974) have given an estimate of particle diameters ranging from 0.1–0.3 m. They also derived from calculations based on observed particle diameters a mean particle velocity of about 51 m/s. Acoustic measurements realized at Etna SEC during the same period (July, 2001) have provided average particle diameters around 0.1 m (Vergniolle and Ripepe, 2008). Note however that most of the velocity data given in the literature are not values taken at the emission source and are therefore hardly comparable.

III.5.2. Comparison of radar/video initial gas velocities

In the previous section we have tested our source parameters retrieval method on one Strombolian explosion.

Now, we will calculate and compare the initial gas velocities retrieved from both radar and video measurements for 8 lava-jet explosions. The initial gas velocity (V_0^g) derived from Doppler radar measurements is calculated as previously, by using the two correction coefficients ($C_{\varphi=55°}$, $C_{L=120m}$) applied on the maximum radial velocity ($V_{\max}^+$) recorded by VOLDORAD. Note that the elevation correction coefficient (C_L) is derived from the equation of gas velocity decrease (eq. III.3), where the constant z_{ref} has been defined by best fit matching of video-derived velocity measurements averaged on the 8 lava-jet explosions. Therefore, the initial gas velocity derived from video analysis can be calculated by using the same elevation correction coefficient (C_L) but with the suitable distance between the vent and video measurements elevation. In section III.1, gas velocities were given at an elevation of about 100 m above the crater rim, whereas the vent is estimated at about 50 m beneath the crater rim. Therefore we define an elevation correction coefficient of $C_{L=150m}$=2.2 for video-derived measurements. Note that the geometrical correction is not needed since video measurements were carried out directly according to the trajectory of the particle or gas parcel.

We thus provide on figure III.11 the initial gas velocity (V_0^g) inferred from radar measurements with a mean value of 127 m/s and a standard deviation of 30 m/s (i.e., about 24% of the mean value). On the other hand, we give the initial gas velocity (U_0^g) inferred from video measurements, with a mean value of 143 m/s and a standard deviation of 33 m/s (i.e., about 23% of the mean value). These values are relatively similar in average but have a quite large dispersion. Indeed, individual explosions can have a large discrepancy, reaching a maximum of about $|\Delta V|=|V_0^g - U_0^g|$=85 m/s for explosion at 21h37:36 UT. The mean difference between both sets of data is given by the root mean square coefficient as ΔV_{RMS} =50 m/s.

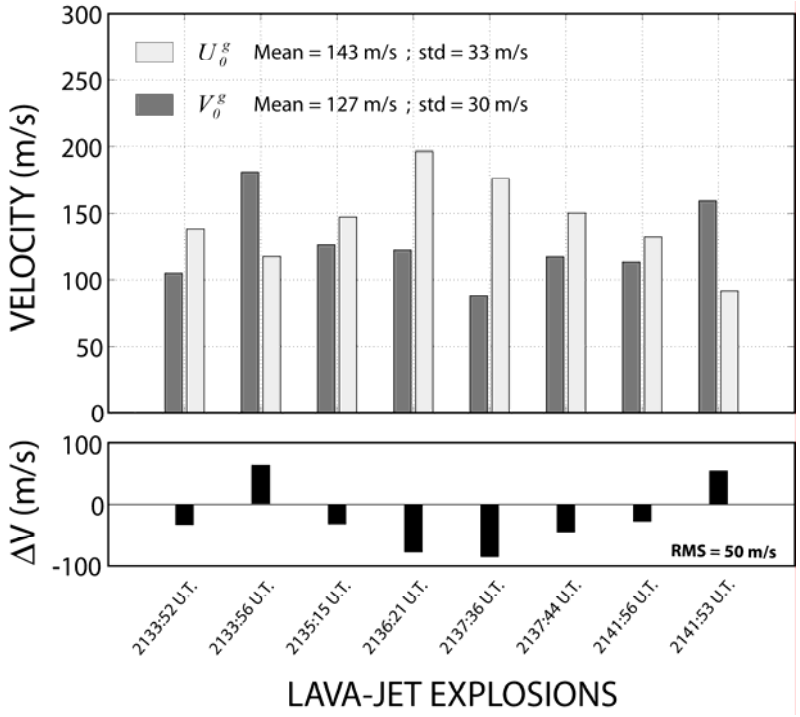

Figure III.11. Plot of the initial gas velocity (U_0^g) derived from video measurements carried out on 8 lava-jet explosions during the eruption of July 4, 2001 at Etna SEC, and compared to initial gas velocity (V_0^g) inferred from VOLDORAD measurements in the radar range G_3.

This difference is relatively large and can be due to some errors on radar or video measurements as mentioned previously in section III.1. Nevertheless, we can observe that most of initial gas velocity (V_0^g) estimates inferred from radar measurements are lower than initial gas velocity derived from video measurements (U_0^g). Indeed, the sum of the differences ΔV on 8 lava-jet explosions is strongly negative, reaching a value of -135 m/s. We suppose, in spite of some technical errors on both measurements, that maximum velocities recorded by VOLDORAD are rather related to very fine particles that move slower than the gas phase. Therefore V_0^g has to be regarded as minimum initial gas velocity estimates. Velocity data inferred from radar and video measurements are summarized in Table III.2.

Table III.2. Summary of values inferred from radar and video measurements on 8 lava-jet explosions occurring during the paroxysm of July 4, 2001 eruption at Etna SEC.

LAVA-JET	RADAR		VIDEO		
	$V_{\max}^{+}$ (m/s)	V_0^g (m/s)	$U_{z\approx 100m}^{p}$ (m/s)	$U_{z\approx 100m}^{g}$ (m/s)	U_0^g (m/s)
2133:52 UT	46	104,9	62,5	67,2	134,3
2133:56 UT	79,6	181,5	56,7	55,8	111,6
2135:15 UT	55,2	125,9	68,3	74,7	149,5
2136:21 UT	53,4	121,8	55	98,6	197,3
2137:36 UT	38,6	88	66,6	87,8	175,7
2137:44 UT	51,5	117,4	58,3	75	150
2141:53 UT	49,7	113,3	50,8	66,9	133,8
2141:56 UT	70	159,6	58,3	47,3	94,6
Mean values	**56**	**127**	**59**	**72**	**144**

III.5.3. Gas velocity decrease: insight from radar and video methods

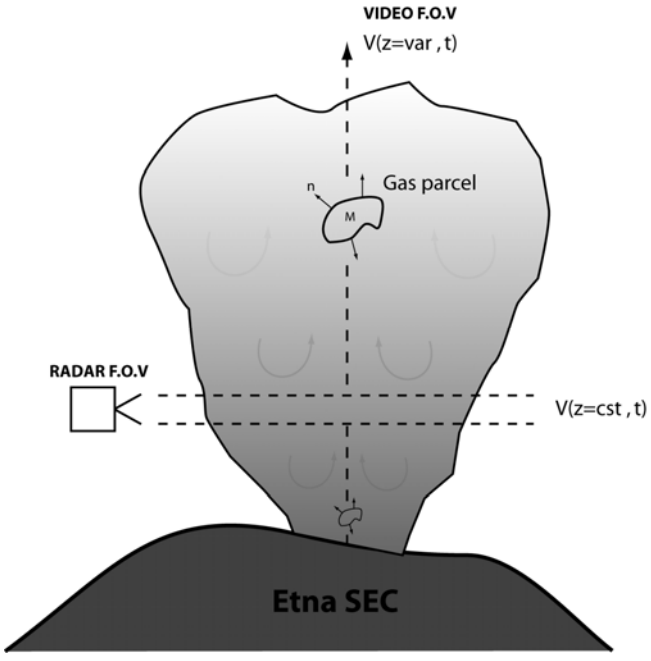

Figure III.12. Sketch showing the difference of radar and video field of view (F.O.V) during measurements of gas velocities. Video-derived measurements have been carried out by following the displacement of a single gas parcel moving upward and slowing with height: this approach is related to the Lagrangian description. Radar-derived measurements of several successive bodies (gas parcels) crossing a fixed sample volume at a given elevation: this approach is related to the Eulerian description.

Radar and video methods of velocity data acquisition are quite different and may also account, to some extent, for the discrepancy between both sets of data. Indeed, video

measurements have been carried out by following the displacement of a single gas parcel moving upward and slowing with height. This approach is related to the Lagrangian description, which gives physical information on a given body travelling trough time and space. On the contrary, VOLDORAD provides measurements of several successive bodies (gas parcels or particles) crossing a fixed sample volume at a given elevation. This approach is related to the Eulerian description, which gives physical information on the whole jet dynamic through time, but at a constant elevation (Figure III.12).

Punctual gas velocity measurements carried out from both methods at the same elevation are of course comparable, and are representative of the velocity of a gas parcel at a given instant and elevation of the lava-jet flow. However, the temporal evolution of radar and video velocity measurements are significantly different. We think that the temporal evolution of video-derived measurements portrays the velocity decrease of a single gas parcel rising upright and slowing down with height. At the opposite, we suppose that the temporal evolution of radar-derived measurements describes the velocity decrease of the jet flow, waning through time until the gas release be depleted.

We provide on Figure III.13a the time series of gas velocity decrease derived from video analysis extrapolated at the emission source at t_0 =0 s and averaged on 8 lava-jet explosions. As shown previously (section III.3.1), the velocity decrease of a gas parcel follows the law predicted by Blackburn et al., (1976) given by equation III.3, for a height reference coefficient z_{ref}=850 m, a constant γ=4.6 and a mean initial gas velocity U_0^g=143 m/s. On the other hand, Figure III.13b shows the time series of gas velocity derived from VOLDORAD measurements ($V_{\max}^+$), and extrapolated at the emission source level by using the retrieval method described previously (section III.4). The radar-derived velocity decrease curve also represents the average of 8 lava-jet explosions. We thus define a simple exponential expression that fit radar-derived velocities with a decrease coefficient β=1/2 and a mean initial gas velocity V_0^g=127 m/s

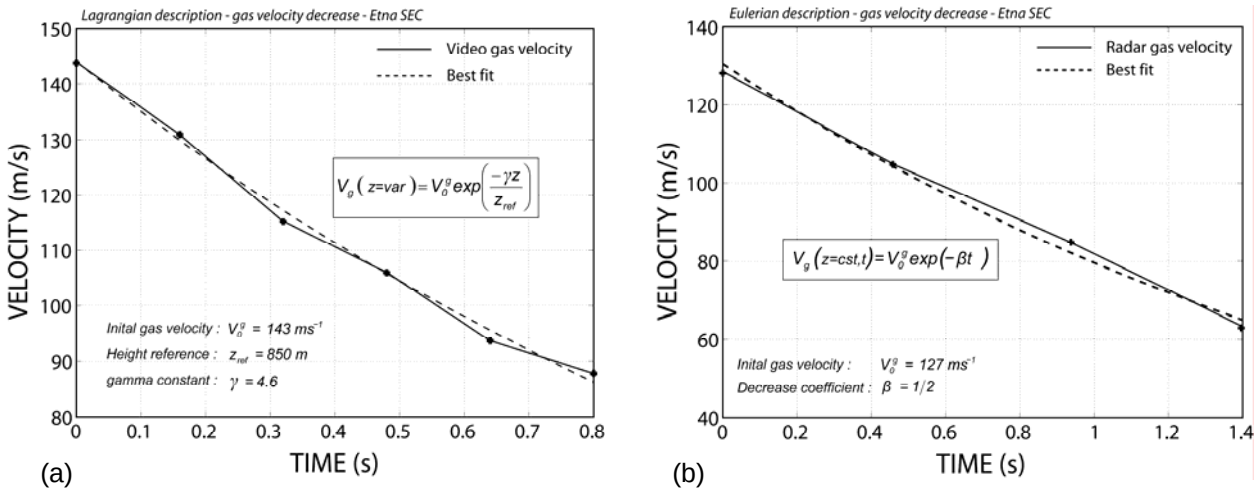

Figure III.13. (a) Time series of the gas velocity derived from luminous front measurements on video snapshots averaged on 8 lava-jet explosions (see fig.III.6 for details). (b) Time series of the gas velocity calculated from Doppler radar measurements averaged on 8 lava-jet explosions, and extrapolated at the emission source level by using the retrieval method described previously (section III.4)

In order to better compare both velocity decrease trends, we provide the slope of each curve as they were straight-lines at first order. We obtain a slope of -70 m.s^{-2} for video-derived values, and a slope of -50 m/s^{-2} for radar-derived values. Thus, we deduce that the velocity decrease of a gas parcel slowing down with height (as portrayed by video-derived measurements) is higher than the gas velocity decrease related to the lava-jet flux depletion at the vent level, during about one second (as portrayed by radar-derived measurements). However, bearing in mind possible technical errors inherent to radar and video measurements and assumptions ventured in the source parameters retrieval model, this result has to be regarded as preliminary work. We aim here at pointing out some important methodological differences between radar and video, which may provide complementary information on the lava-jet dynamics.

III.6. Long sequence analysis of Strombolian activity

III.6.1. Doppler radar data

The thorough study of discrete isolated events is obviously fundamental to understand shallow physical processes such as bubble bursting, magma drainage or gas release mechanisms. However, the analysis of volcanic processes integrated on longer periods of time is also essential to understand eruptive mechanisms occurring on larger time and space scales. In this section we give a set of kinetic parameters, for a 17-min sequence of Strombolian activity that occurs during the paroxysm of July-4 eruption from 2129:00 UT to 2146:00 UT at Etna SEC. The activity at the SE crater was intense, consisting of a series of Strombolian explosions occurring every 5 s in average. From the computation of the spectral moments from Doppler radar measurements, we provide time series of the maximum radial velocity ($V^{+}_{\max}$) and the mean radial velocity (V^{+}_{mean}) in the range gate G_3, at a sampling rate of about 2.5 Hz (Figure III.14).

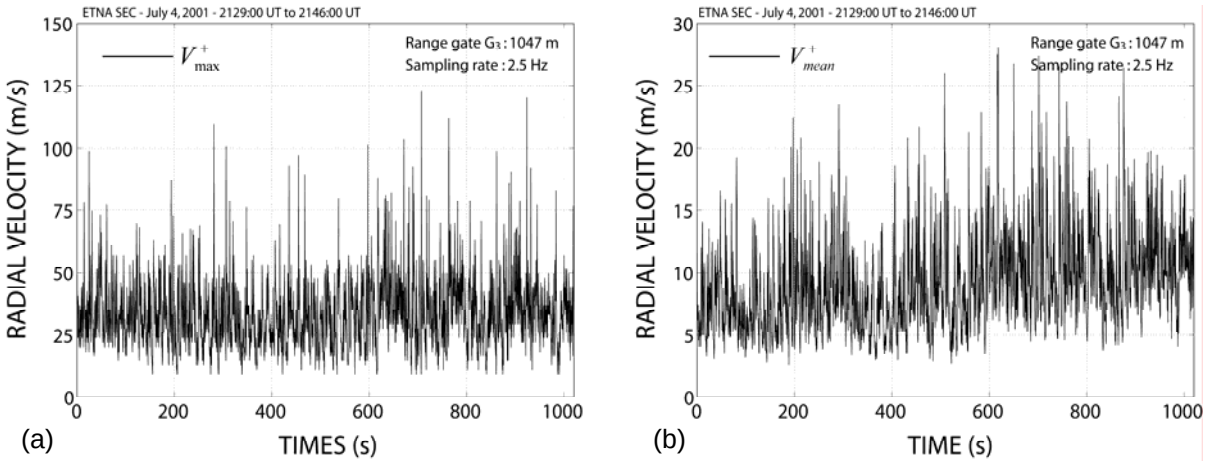

Figure III.14. Time series of (a) maximum radial velocities and (b) mean radial velocities, recorded by VOLDORAD in the range gate G_3, sampled at about 2.5Hz, during the paroxysm of July-4 eruption from 2129:00 UT to 2146:00 UT.

III.6.2. Kinetic parameters retrieval

Firstly, the initial gas velocity (V_0^g) is calculated from the maximum radial velocity ($V_{\max}^+$) for the whole sequence, applying the geometrical correction factor $C_{\varphi=55°}$=1.2 and the elevation correction factor $C_{L=120m}$=1.9. Importantly, in order to retrieve the initial gas velocity at the onset of each discrete explosion, we only take into account the peak values. We obtain, for 157 explosions, a mean initial gas velocity of V_0^g=144 m/s with a maximum value of 269 m/s and a minimum of 79 m/s. The standard deviation of V_0^g reaches 40 m /s, which represent a dispersion of about 28% of the mean, value (Figure III.15a).

Secondly, we calculate the mean particle velocity $V_{G_3}^p$ from the mean radial velocity (V_{mean}^+) at the elevation of the range gate centre by using the geometrical correction $C_{\varphi=90°}$=2.56. Similarly to the initial gas velocity calculation, we focus on peak values only. We find an average value of the mean particle velocity at the centre of the range gate G_3 of $V_{G_3}^p$=41 m/s with a maximum of 72 m/s and a minimum of 18 m/s. The standard deviation of $V_{G_3}^p$ reaches 11 m /s, which represents a dispersion of about 27% of the mean value (Figure III.15b).

The variability of both sets of data is relatively large; although geometrical or technical errors may arise on radar-derived measurements, the statistical number of explosions analysed should balance these effects. Therefore, we assume that most of the dispersion observed is related to the natural variability of gas velocities.

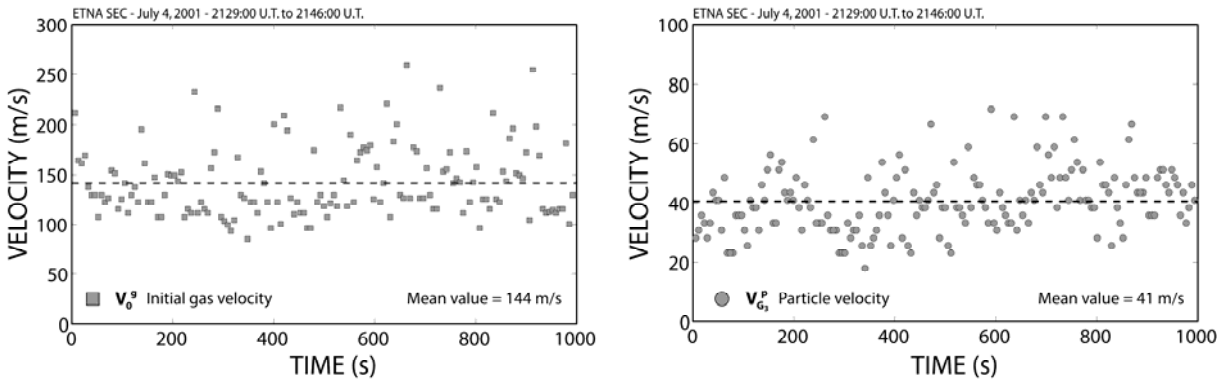

Figure III.15 (a) Initial gas velocity calculated for 157 explosions at Etna SEC on July 4, 2001 between 2129:00 UT and 2146:00 UT. (b) Mean particle velocity at the centre of the radar range gate G_3 calculated in the same conditions.

In order to retrieve the mean diameter ($\overline{D}$) and the initial mean particle velocity (V_0^p) of each discrete explosion, we would need to run an inversion on each explosion. Instead, we calculate $\overline{D}$ from time-average values of the initial gas velocity (V_0^g) and mean particle velocity at the range gate level ($V_{G_3}^p$). Therefore, we obtain, for 157 explosions, average values for a mean diameter of $\overline{D}$=0.26 m and initial mean particle velocity of V_0^p=67 m/s.

III.6.3. Loading parameters retrieval

Finally, the flux and the total volume of gas released during this sequence of Strombolian activity can also be deduced from the time series of initial gas velocities. In our case, the time series has been calculated on 1020 s, and the gas flux can be expressed as the product of the vent section with the mean initial gas velocity of all values recorded at a sampling rate of 2.5 Hz.

$$Q_g = \frac{\pi r^2}{n} \sum_{i=1}^{n} V_0^g$$

where r is the radius of the vent at Etna SEC, which is taken equal to r=5 m (Vergniolle and Ripepe, 2008), and *n*=2478 is the number of initial gas velocity values in the time frame of the sequence studied. We obtain an average gas flux of Q_g=6x10^3 m^3/s. The total volume released during the 17-min sequence of Strombolian activity can hence be estimated easily from the product of the gas flux (Q_g) and the duration of the activity (*t*):

$$W_g = Q_g t$$

We obtain a total gas volume of W_g=6.1x10^6 m^3. Considering that H_2O commonly represents more than 90% of the gas released during Strombolian eruptions (Allard et al., 2005), we assume for the calculation of the total mass of gas that H_20 is the only magmatic gas specie. We obtain, with a water vapour density $\rho_{H_2O}^{vap} \approx 0.18$ kg/m^3 at 3300 m elevation, a gas mass flux of about M_g=1x10^3 Kg/s and a total gas mass of about 1.1x10^6 kg during the 17-min

sequence studied. All values related to the study of the 17-min sequence occurring on July 4, 2001 are summarized in Table III.3.

Table III.3. Summary of kinetic and loading values inferred from radar measurements for a 17-min sequence of Strombolian activity that occurs during the paroxysm of July-4 eruption from 2129:00 UT to 2146:00 UT at Etna SEC.

Kinetic parameters				**Loading parameters**			
V_0^g (m/s)	144	V_0^p (m/s)	67	Q_w^g (m^3/s)	$6x10^3$	Q_M^g (Kg/s)	$1x10^3$
$V_{G_3}^p$ (m/s)	41	$\overline{D}$ (m)	0.26	W_g (m^3)	$6.1x10^6$	M_g (Kg)	$1.1x10^6$

III.7. Discussion

This study has permitted the detailed analysis of kinetic features, which provides crucial initial kinetic parameters retrieved routinely from Doppler radar measurements. Particularly, VOLDORAD enable initial gas velocity assessment (i.e., at the emission source), and gives first order estimate of the mean initial particle velocity and mean diameter. In addition, the acquisition of source kinetic parameters has permitted us to calculate velocity-derived parameters such as gas masses and volumes released during the Strombolian eruption occurring on July 4, 2001 at Etna SEC.

Obviously some difficulties remain on the estimation of such parameters, particularly regarding assumptions included in the ballistic model. At the input of the model, two fundamental relations are used the model (i) the gas-dependence of particle velocity and (ii) the gas velocity decrease law. The first one is defined with the constant k, taken as 150 as found in the literature from studies carried out at Stromboli volcano. But this value may vary from one explosion to another as well as between different volcanoes. The particle velocity also depends on the gas behaviour; however, the gas velocity decrease law is also poorly constrained. Indeed, it is defined with two decrease coefficient $\gamma = 4.6$ and $z_{ref} = 850$ m. The height reference coefficient (z_{ref}) has been constrained in this study from video measurements, on which some uncertainties also remain, and taken as constant throughout the whole sequence studied.

Photoballistic measurements have been carried out from the analysis of video snapshots recorded simultaneously to the radar. Some difficulties arise with this method, particularly for the detection of the front boundary that prevents accurate determination of the propagating gas front position. Note that in this study, the luminous front has been considered as being the gas phase propagating upward. However, we suppose that only fine particles can be seen from our video recording, which can slightly biased video-derived velocities interpretations. Ultra-Violet or Infrared measurements, such as ground-based UV camera or FLIR method, would probably be better adapted for the gas phase analysis. Moreover, the exploitation of a two-dimensional field of view may also induce some biases on video measurements that can virtually reduce real gas or particle velocity values.

Some assumptions formulated in the source parameters retrieval method can also be discussed, particularly regarding the geometrical correction coefficients of the analytical procedure. Indeed, for all explosions studied, we assume that the maximum radial velocity ($V^{+}_{\max}$) recorded by VOLDORAD stands for particles ejected with an inclination of about 55° in average. This value is not arbitrary, as it corresponds to the physical boundary of the radar range gate G_3 located right above the vent. Theoretically, highest radial velocities are indeed measured in the bottom right hand corner of the gate G_3, however, we assume in that study that all jets studied hold enough particles (to emerge from the radar noise level) ejected within a dispersion cone sufficiently large to meet such radial trajectories (55°).

In this study, the mean radial velocity (V^{+}_{mean}) recorded by VOLDORAD and calculated as the first spectral moment (i.e., the mean velocity weighted by the power spectral density over the whole positive velocity range) is used to derive the average particle velocity corresponding to the velocity of particles with mean diameter ($\overline{D}$). However, the interpretation of V^{+}_{mean} is actually more complex. Indeed, the particle size distribution is not monodisperse, and hence the total echo-power recorded is the result of multiple-size particles backscattering to the radar. But we know that the scattering law that gives the relation between the reflectivity and the size of particles is strongly not linear, particularly for large diameters. Therefore the use of V^{+}_{mean} has for effects to underestimate the mean particle velocity and overestimate the mean diameter.

CHAPTER IV

Loading features of Strombolian jets: insight from inversion of Doppler radar measurements

See also Appendix C:

Gouhier, M., and F. Donnadieu (2008), Mass estimations of ejecta from Strombolian explosions by inversion of Doppler radar measurements, J. Geophys. Res., 113, B10202, doi:10.1029/2007JB005383.

Mass estimations of ejecta from Strombolian explosions by inversion of Doppler radar measurements

Mathieu Gouhier[1] and Franck Donnadieu[1]

Received 13 September 2007; revised 25 June 2008; accepted 23 July 2008; published 4 October 2008.

[1] We present a new method for estimating particle loading parameters (mass, number, volume) of eruptive jets by inversion of echo power data measured using a volcano Doppler radar (VOLDORAD) during typical Strombolian activity from the southeast (SE) crater of Mount Etna on 4 July 2001. Derived parameters such as mass flux, particle kinetic and thermal energy, and particle concentration are also estimated. The inversion algorithm uses the complete Mie (1908) formulation of electromagnetic scattering by spherical particles to generate synthetic backscattered power values. In a first data inversion model (termed the polydisperse model), the particle size distribution (PSD) is characterized by a scaled Weibull function. The mode of the distribution is inferred from particle terminal velocities measured by Doppler radar for each explosion. The distribution shape factor is found to be 2.3 from Chouet et al.'s (1974) data for typical Strombolian activity, corresponding to the lognormal PSDs commonly characteristic of other Strombolian deposits. The polydisperse model inversion converges toward the Weibull scale factor producing the best fit between synthetic and measured backscattered power. A cruder, alternative monodisperse model is evaluated on the basis of a single size distribution assumption, the accuracy of which lies within 25% of that of the polydisperse model. Although less accurate, the monodisperse model, being much faster, may be useful for rapid estimation of physical parameters during real-time volcano monitoring. Results are illustrated for two explosions at Mount Etna with contrasted particle loads. Estimates from the polydisperse model give 58,000 and 206,000 kg as maxima for the total mass of pyroclasts, 26,400 and 73,600 kg s^{-1} for mass flux rates, 38 and 135 m^3 (22 and 76 m^3 equivalent magma volume) for the pyroclast volumes, and 0.02–0.4 and 0.06–0.12 kg m^{-3} for particle concentrations, respectively. The time-averaged kinetic energy released is found to be equal to 4.2×10^7 and 3.9×10^8 J, and thermal energy is estimated at 8.4×10^{10} and 3×10^{11} J.

Citation: Gouhier, M., and F. Donnadieu (2008), Mass estimations of ejecta from Strombolian explosions by inversion of Doppler radar measurements, *J. Geophys. Res.*, *113*, B10202, doi:10.1029/2007JB005383.

IV.1. Introduction

Volcanic explosions are important sources of information for understanding eruption mechanisms. The masses and velocities of gas and pyroclasts are particularly important parameters controlling the dynamics of an eruption as they define crucial parameters such as mass fluxes, kinetic and thermal energies released by an explosion. In order to better understand the dynamics of explosive eruptions, satellite imagery, and ground-based weather radars particularly have been used for the sounding of volcanic ash plumes from large eruptions [*Harris et al.*, 1981; *Harris and Rose*, 1983; *Weill et al.*, 1992; *Dean et al.*, 1994; *Dehn et al.*, 2000; *Lacasse et al.*, 2004]. These techniques probe the upper convective parts of high eruption columns and provide information primarily on the small particles that ultimately constitute the distal volcanic products. A major challenge is now to measure physical parameters, such as ejecta velocities and masses, close to the vent in order to retrieve directly the true source parameters. A first approach to measure jet velocities was used at Stromboli with an acoustic Doppler sounder (sodar) [*Weill et al.*, 1992]. Other techniques that potentially provide information on both velocity and mass parameters are ground-based portable Doppler radar, either pulsed such as VOLDORAD (Volcano Doppler Radar) [*Dubosclard et al.*, 1999; *Dubosclard et al.*, 2004] or frequency-modulated such as VERDEMOS [*Hort and Seyfried*, 1998; *Seyfried and Hort*, 1999]. These techniques allow direct measurement of particle velocities and reflectivities immediately above the vent. In addition to their significant monitoring potential, these radar systems allow us to study, under any weather conditions, explosions of lesser intensity barely imaged by satellites or weather radars.

VOLDORAD was used to record several eruptive episodes at Etna in July 2001, ranging from mild Strombolian activity to paroxysmal lava fountains [*Donnadieu et al.*, 2005]. A new method based on inversion of echo-power data measured using VOLDORAD is now presented for estimating the masses of pyroclasts ejected during individual explosions. The method also provides first-order estimates of mass-related parameters such as mass flux, ejecta volume, particle concentration, thermal and kinetic energy at the vent. The method was applied to two Strombolian explosions with contrasted particle loads that occurred during an eruptive episode of Mt. Etna southeast (SE) crater on 4 July, 2001. Firstly, an algorithm is developed to simulate radar echoes from pyroclasts of various sizes, using the complete

electromagnetic scattering formulation [*Mie*, 1908]. This approach provides synthetic data of power backscattered by particles (P_{synth}) at the particular wavelength employed by VOLDORAD. Secondly, as an input to the model, a scaled-Weibull function [*Weibull*, 1939] is used to characterize the particle size distribution (PSD). The general shape of the Weibull distribution is constrained from published data for typical Strombolian activity [*Chouet et al.*, 1974], and the mode of the PSD is estimated from our own radar velocity measurements for each explosion. All Weibull parameters characterizing a polydisperse (multiple particle size) distribution, such as shape, shift and scale factors, can then be deduced and used to compute synthetic values of backscattered power. Lastly, a recursive inversion algorithm is applied in order to obtain a PSD such that the synthetic power (P_{synth}) best fit the measured radar power (P_{mes}). The mass of ejected material and related parameters are then deduced. An alternative model is proposed, based on a monodisperse (single particle size) PSD, which turns out to be an acceptable approximation of the polydisperse model. This approach reduces computing time, making it useful for real-time quantitative assessment of ejected mass during volcano monitoring.

IV.2. Acquisition of radar power parameters

Data from successive range gates are displayed in real time as Doppler spectra representing the power spectral density versus radial velocity. From the processing of the series of Doppler spectra, two sets of parameters are directly retrieved for ascending (positive parameters indexed +) and descending (negative parameters indexed -) ejecta crossing the successive range gates above, or on either side of, the eruptive jet axis: (1) velocity information, in particular maximum radial velocity ($V^{+}_{max,}$ V^{-}_{max}) and; (2) power (P_{+}, P_{-}) backscattered by particles contained in the sampling volume at a given instant [*Dubosclard et al.*, 2004]. In the aim of loading estimations we will mainly focus on the radar power parameters

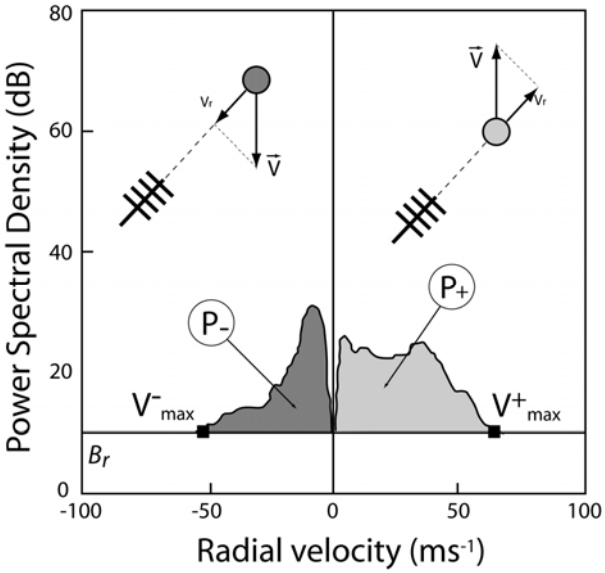

Figure IV.1. Sketch of a typical Doppler spectrum obtained by VOLDORAD. The power spectral density is displayed as a function of the radial velocity in a given range. The horizontal line (B_r) corresponds to the background noise level. Total echo power, maximum and mean velocities can be deduced from Doppler spectra. They are indexed (+) and (-) for ejecta with the radial component of their velocity vector moving away and towards the antenna respectively.

The received echo power from the particles can be defined by the integral of the spectral power density *S(v)* in a velocity interval between *v* and *v+dv*, from 0 to V^{+}_{max} for ascending particles and from V^{-}_{max} to 0 for descending particles. The power measured in the Doppler spectra has been calibrated in the laboratory by means of an input signal, the power of which was known, delivered by an external frequency generator.

$$P_{+} = \int_{0}^{V^{+}_{max}} S(v)dv \qquad P_{-} = \int_{V^{-}_{max}}^{0} S(v)dv \tag{IV.1}$$

Maximum radial velocities in the directions toward and opposite to the radar, V^{-}_{max} and V^{+}_{max} respectively, are defined where *S(v)* is equal to the background noise level B_r (Figure IV.1).

IV.3. Electromagnetic scattering model

The aim of this study is to estimate masses of volcanic ejecta from two Strombolian explosions with contrasted particle loads by inversion of the Doppler radar measurements. For this purpose, a comparison between the backscattered power measured by the radar (P_{mes}) and

the synthetic (i.e., calculated) backscattered power (P_{synth}) is needed (see § 4. for more details on the inversion method). In this section, we first describe how to retrieve P_{mes}, and then we derive P_{synth} using the electromagnetic scattering theory of *Mie* [1908]. As shown by Figure IV.1, processing of the Doppler spectra yields the total backscattered power ($P_{tot} = P_{-} + P_{+}$). Raw power values (P_{mes}) can then be deduced directly from the radar conversion constant (C_c) that depends on technical characteristics of the radar acquisition line.

$$P_{mes} = P_{tot} C_c \tag{IV.2}$$

On the other hand, P_{synth} can be derived from an electromagnetic scattering model. A good approximation for small particles is the Rayleigh scattering theory, the validity limit of which depends on the radar wavelength [*Sauvageot,* 1992]. This method is commonly used in meteorology, because the typical diameter of water droplets is small compared to the wavelengths of meteorological radars. In our case (λ = 23.5 cm), the Rayleigh theory can only be applied for particles of diameter (D_L) smaller than $\lambda/4$, which corresponds to ~5.9 cm [*Gouhier and Donnadieu*, 2006]. However, considering the wide range of particle diameters characterizing volcanic activity, the complete scattering theory is required to account for the effects of larger particles. A general solution of electromagnetic wave scattering was given by *Mie* [1908]. This approach applies Maxwell's equations for plane waves scattered by compositionally homogeneous particles (Appendix A). For application to volcanic eruptions, we focus on waves scattered at a large distance by spherical particles, which we assume are homogeneously distributed in space. Theoretically, the power backscattered to the radar by a population of such particles in a given range gate is proportional to their radar reflectivity (η). The synthetic power can then be defined as:

$$P_{synth} = \frac{C_r V_s \eta}{R^4} \tag{IV.3}$$

where C_r is the radar constant, V_s, the sampling volume, and R, the slant distance between the radar and the target. The radar constant is defined by a set of technical parameters related to the radar configuration. The radar constant has been calibrated using a classical method comparing the reflectivity of rainfalls probed by the radar and the reflectivity calculated from the drop size distribution and velocity of the falling hydrometeors measured simultaneously with a disdrometer [*Pointin et al.*, 2005]. The radar reflectivity (η) is the sum of the

backscattering cross sections (σ_{bks}) of the individual particles per unit volume. The reflectivity factor (Z) is defined by Sauvageot (1992) as:

$$\eta = \sum_{i=1}^{n} \frac{\sigma_{bks(i)}}{V_s} \tag{IV.4}$$

and

$$Z = \frac{\eta.\lambda^4}{\pi^5 |K|^2} 10^{18} \tag{IV.5}$$

Z (commonly confused with η in the literature) is often expressed in logarithmic units as dBZ and is related to η through the radar wavelength λ, and the particle complex dielectric factor $K = (m^2\text{-}1)/(m^2\text{+}2)$. Scattering and attenuation by compositionally homogeneous spheres are significantly influenced by the complex refractive index (m). VOLDORAD transmits power through a square array of four Yagi antennas, such that the incident electromagnetic wave is polarized parallel to the scattering plane. Being a monostatic radar (i.e., the same antenna is used for transmission and reception), we define a backscattering cross section (σ_{bks}) for horizontal linear polarization:

$$\sigma_{bks} = \frac{\lambda^2}{4\pi} \left| \sum_{n=1}^{\infty} (-1)^2 (2n+1)(a_n - b_n) \right|^2 \tag{IV.6}$$

where a_n and b_n are the complex scattering coefficients (so-called Mie coefficients). Examples of Mie vs. Rayleigh scattering patterns of an electromagnetic wave scattered by homogeneous spheres of four different sizes are shown in Figure IV.2 for a signal at the wavelength used by VOLDORAD (λ = 23.5 cm) and with the complex dielectric factor of volcanic ash ($|K|^2$ = 0.39) [*Adams et al.*, 1996]. These patterns illustrate the large discrepancy between the Rayleigh and Mie formulations for particle diameters larger than a few centimeters at 23.5 cm wavelength. Note that, at smaller radar wavelengths, this discrepancy occurs at even smaller particle diameters, making the complete Mie formulation absolutely necessary for studies of volcanic ejecta from radar measurements.

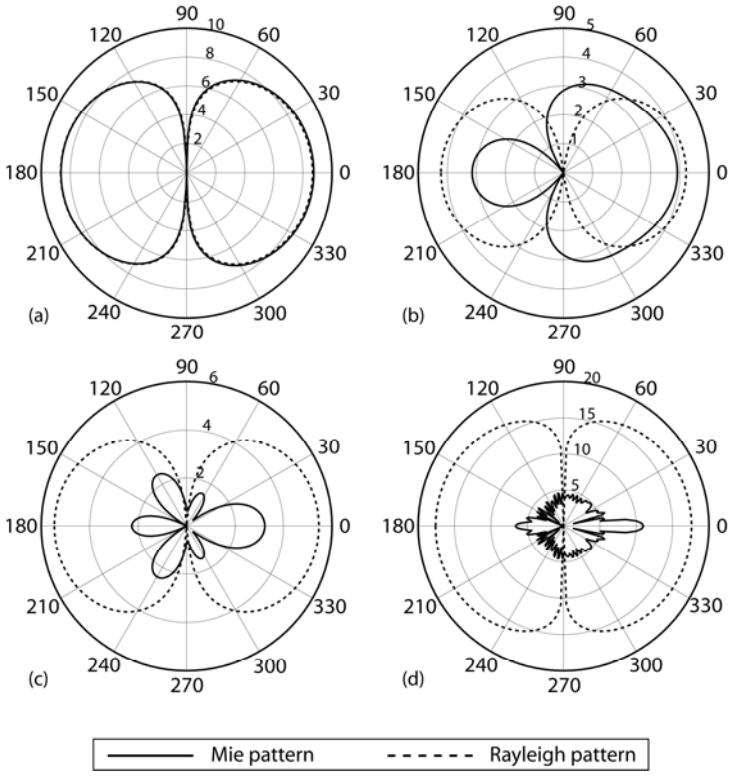

Figure IV.2. Mie vs. Rayleigh scattering patterns of an electromagnetic wave, parallel polarized, scattered by a single homogeneous sphere with the complex dielectric factor of volcanic ash, $|K|^2$ = 0.39 [*Adams et al.*, 1996], and λ = 23.5 cm. The wave arrives from the left, and the particle is situated at the centre of the pattern. Irradiance amplitude is normalized to that of Mie and expressed on a logarithmic scale. (a) Example of a small particle of diameter 2 cm. The Rayleigh and Mie scattering patterns are identical and symmetrical. Irradiance intensity is the same in front of and behind the particle. (b) Particle of diameter 14 cm. The Rayleigh and Mie scattering patterns are now significantly different. The Mie pattern still has two main lobes, but is strongly asymmetric, as the backscattered intensity is lower than the forward-scattered intensity. (c) Particle of diameter 20 cm. The Rayleigh pattern is still symmetrical whereas the Mie pattern is divided into several lobes and shows much lower values of irradiance. (d) For a diameter of 2 m, the Mie (true) scattering pattern becomes very complex, and shows always much lower values of irradiance than the Rayleigh approximation.

Figure IV.3 shows the reflectivity factor (Z) as a function of particle diameter, using both the Mie and Rayleigh formulations for a wavelength of 23.5 cm. Note the overestimation of Z when computed using the Rayleigh approximation for particle diameters greater than ~ 5.9 cm.

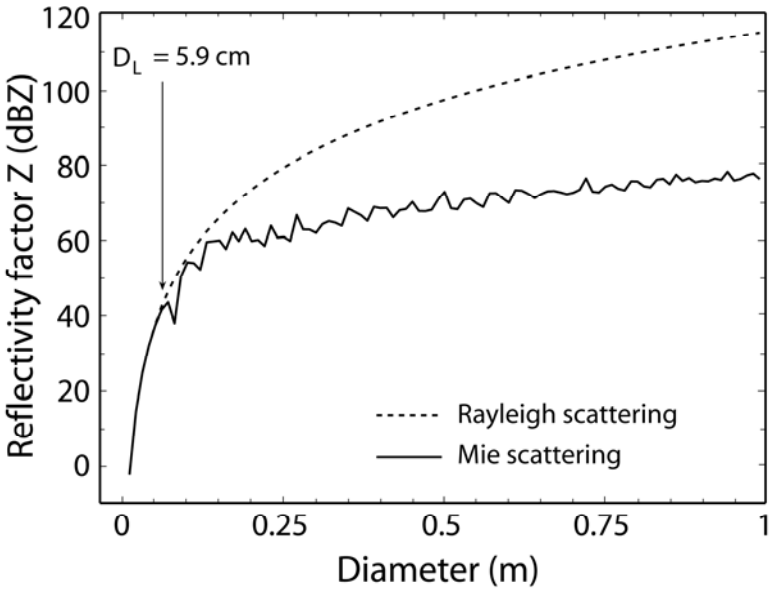

Figure IV.3. Synthetic reflectivity factor (*Z*, expressed in dBZ) as a function of particle diameter. Note the large overestimation of Z for large diameters when computed using the Rayleigh approximation. The validity domain depends on the radar wavelength. In the case of VOLDORAD (λ = 23.5 cm), the validity limit (D_L) lies close to 5.9 cm, i.e., ~λ/4 [*Gouhier and Donnadieu*, 2006].

IV.4. Inversion method

Model inversions are frequently used in geophysics to recover initial parameters and boundary conditions from observed data of natural phenomena. In this case, backscattered power values (P_{mes}) are retrieved from radar measurements, and synthetic power data (P_{synth}) are determined from the forward electromagnetic-scattering model. The inversion algorithm thus seeks the best correlation between P_{mes} and P_{synth}, providing the optimum variable input parameters defined by the vector (X) that characterizes the PSD. Physical parameters such as particle mass and volume are then deduced from the PSD. The model takes into account two main classes of parameters: (1) constant parameters describing the geometry of the system, the technical characteristics of the radar or material physical properties; (2) the vector of variable input parameters (*X; see below*) defining the Weibull function of the PSD. A least-square estimation method is used, based on the minimization function *S(X)* characterized by the squared residual between radar measured data and synthetic data:

$$S(X) = \sum \left[P_{mes} - P_{synth}(X) \right]^2 \qquad \text{(IV.7)}$$

Finally, a comparison criterion between radar-measured (P_{mes}) and synthetic (P_{synth}) power data is used to stop the recursive loop when the fitting criterion is reached. The successive steps of the inversion algorithm are summarized below.

- ***Step 0****: Attribution of initial values for estimation of the input parameters :*
  $X_j \equiv \left[X_1, X_2, ..., X_n \right]$
- ***Step 1:*** *Resolution of the direct model (Mie scattering):*
  $X \rightarrow P(X)_{Synth}$
- ***Step 2:*** *Calculation of the minimization function:*
  $S(X) = \sum \left[P_{mes} - P_{synth}(X) \right]^2$
- ***Step 3:*** *Characterization of the iterative comparison criterion:*
  $\Delta P(X^i) = S(X^{i-1}) - S(X^i)$
- ***Step 4:*** *Testing of the fitness criterion:*
  $\Delta P(X) < 0$

where $\Delta P(X)$ is the fitness criterion, and indices i and j refer respectively to the step of the iterative procedure and the number of variable parameters. When a satisfactory solution is reached, the iterative procedure stops. The computational procedure is summarized in Figure IV.4.

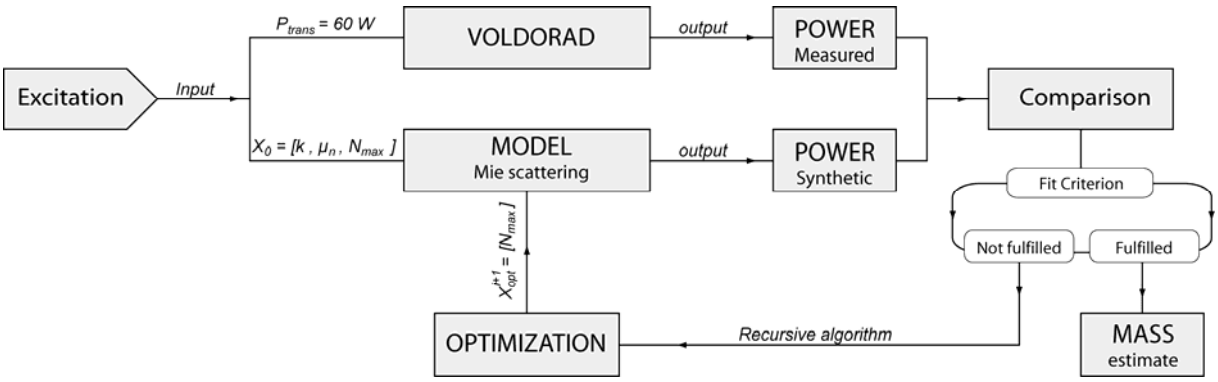

Figure IV.4. Sketch of the inversion approach. Synthetic radar power data (P_{synth}) are provided from the theoretical model (Mie formulation) and compared to the power data measured (P_{mes}) by VOLDORAD. If the fit criterion is met, the procedure stops and gives the best result. Otherwise, the input parameters (X) are optimized in the recursive loop, and the calculation is repeated.

IV.5. Polydisperse particle size model

IV.5.1. Particle size distribution

Solving the inverse problem consists of estimating the shape of the PSD by best-fit matching of synthetic and observed data. Various PSDs have been used in, or inferred from, previous studies of volcanic ejecta: exponential [*Ripepe et al.*, 1993], log-normal [*Sheridan*, 1971; *Chouet et al.*, 1974; *McGetchin et al.*, 1974; *Self et al.*, 1974], Rosin Rammler [*Kittleman*, 1964; *Spieler et al.*, 2003], Weibull [*Nakamura*, 1984; *Marzano et al.*, 2006(a); *Marzano et al.*, 2006(b)], polymodal [*Sheridan et al.*, 1987; *Riley et al.*, 2003] and SFT (Sequential Fragmentation/Transport) [*Wohletz et al.*, 1989]. However, there is still a lack of consensus on which PSD best characterizes Strombolian activity, particularly for the largest particle diameters. For this reason, a scaled-Weibull function is used, because its overall shape may be varied widely from exponential to Gaussian by means of only 3 factors: shape (k), shift (Λ), and scale (N_{max}). The PSD can then be adjusted easily during the optimization phase of the data-inversion procedure. The scaled-Weibull distribution S_w is defined through a probability density function f_w of particles with diameter D:

$$S_w(D;k,\Lambda,N_{\max}) = \frac{f_w(D;k,\Lambda)}{\max\left[f_w(D;k,\Lambda)\right]} N_{\max} \tag{IV.8}$$

with

$$f_w(D;k,\Lambda) = \left(\frac{k}{\Lambda}\right)\left(\frac{D}{\Lambda}\right)^{(k-1)} \exp\left(\frac{-D}{\Lambda}\right)^{k} \tag{IV.9}$$

The shape factor (k) allows us to choose from an exponential (k=1) to Gaussian (k=3) distribution, along with all intermediate log-normal distributions (1<k<3).

The shift factor (Λ) directly depends on the mode (μ_n) of the PSD and on the shape factor (k). It can be defined by using:

$$\Lambda = \mu_n \left(\frac{k-1}{k}\right)^{-\frac{1}{k}} \tag{IV.10}$$

N_{max} is the maximum number of particles of diameter μ_n in the scaled-Weibull distribution (Figure IV.5a). It is the dominant term in the computation of the synthetic power because it strongly influences the estimate of particle mass.

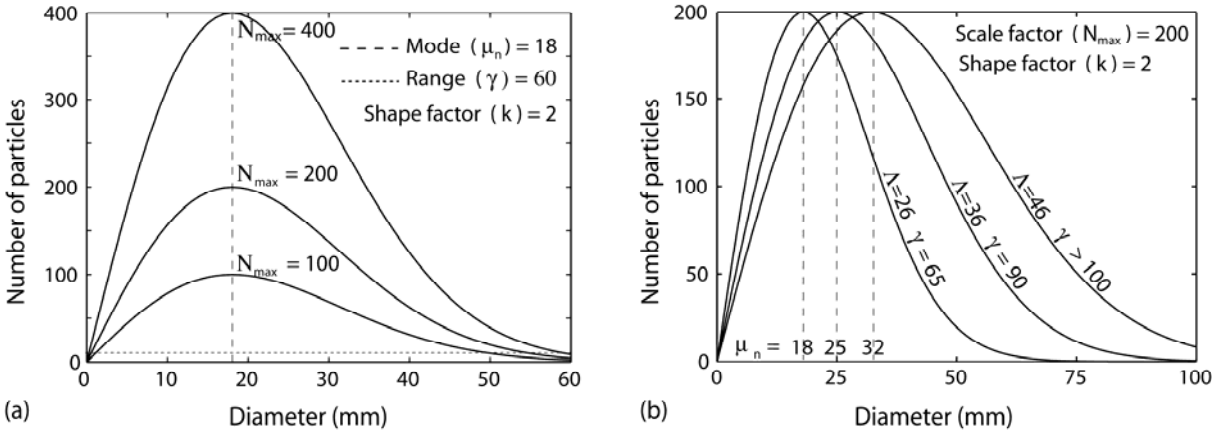

Figure IV.5. Evolution of the particle size distribution (PSD) for different values of shift (Λ) and scale factors (N_{max}). For both examples, the shape factor is constant at k=2. (a) The scale factor (N_{max}) represents the maximum number of particles with diameter μ_n, and therefore directly controls the total number of particles. (b) The mode (μ_n) and range (γ) of the distribution evolve jointly with the shift factor.

The three variable parameters (k, μ_n, N_{max}) controlling the PSD make up the vector X of input parameters to the model. However, in order to obtain a unique solution to the inverse problem, the number of variable parameters is reduced. This also increases the efficiency and speed of the algorithm. Parameters k and μ_n are constrained from the following assumptions argued in subsequent sections: (1) the PSD of Strombolian explosions can be characterized on average by a single shape factor k; (2) the mode of the PSD (μ_n) can be determined from mean particle terminal velocity estimated from the radar measurements. These assumptions then reduce the optimization procedure to a single free parameter (N_{max}).

IV.5.2. Parameter constraints

IV.5.2.1. Shape factor, k

Data on Strombolian PSDs are scarce in the literature. However, *Chouet et al.* [1974] gave an exhaustive description of two explosions at Stromboli Volcano by photoballistic analysis. They made an estimate of the PSD for inflight ejecta (which is what a radar records), and determined the modes, ranges, numbers and sizes of particles for two explosions. They also deduced eruptive parameters such as number, mass and volume of ejected particles, and found that one explosion contained a number and mass of particles about 17 times greater than the other (Table IV.1). We use this study, where all output parameters are already known, to determine the input parameter (k) that best describes the two Strombolian explosions observed by *Chouet et al.* [1974]. With this aim, we first calculate the "equivalent" radar power corresponding to the total ejected mass estimated by *Chouet et al.*'s [1974] observations for two Strombolian explosions. Then synthetic radar powers are computed for different values of shape factor k. Finally, the recursive procedure stops when synthetic radar powers match the equivalent radar power and when synthetic particle loading parameters (number, mass, volume) correspond to those described by *Chouet et al.* [1974]. Note that an alternative method would have been simply to determine k from a best fit function of the *Chouet et al.* [1974] PSD. However, our chosen approach had the advantage of additionally testing our inversion algorithm.

Table IV.1. Comparison between values observed by *Chouet et al.* [1974] on two explosions at Stromboli and synthetic values calculated by the inversion algorithm. Note that the best fit for both sets of data is reached for the same shape factor k = 2.3 (log-normal particle size distribution).

		Explosion 1: Sept. 1971		Explosion 2: Sept. 1971	
		Observed data	Synthetic data	Observed data	Synthetic data
Number of particles	(N)	2588	2588	146	144
Mode (m)	(μ_n)	0,022	0,022	0,025	0,025
Range (m)	(γ)	?-0,06	0,004-0,06	?-0,06	0,001-0,06
Volume (m^3)	(V)	0.033	0.035	0.002	0.0027
Mass (Kg)	(M)	51	53	3	4.1

The best fit between the observed and synthetic PSDs is reached in both cases for the same value of k = 2.3, which describes a log-normal distribution. The equivalent synthetic power achieved is about 3.3×10^{-9} mW and 3.2×10^{-10} mW for explosions 1 and 2 respectively, and corresponds to equivalent reflectivity factors (Z) of 61 dBZ and 51 dBZ. The inversion procedure yields three parameters (number, mode and range) characterizing the synthetic PSDs, from which two eruptive parameters (mass and volume) are directly deduced (Table IV.1). The agreement between observed and synthetic parameters is very good and validates our inversion algorithm. Shape factor estimation can then be used afterward with reasonable confidence. Furthermore log-normal PSDs have also been inferred from deposits of Strombolian activity on other volcanoes, like Etna [*McGetchin et al.*, 1974] and Heimaey [*Self et al.*, 1974]. Although k may vary between individual explosions on Stromboli, as well as between Strombolian eruptions at different volcanoes, we assume in what follows that the value k = 2.3, found for both explosions at Stromboli, represents a suitable average value for Strombolian PSDs and use it as input to the model. Moreover, sensitivity tests reveal a limited dependence of the total ejected mass on k, varying only by a factor of two for values of k ranging from 2.0 to 2.6.

IV.5.2.2. Shift factor, Λ

The shift factor (Λ) is linked to the mode (μ_n) and range (γ) via the shape factor (k) (Figure IV.5b). The mode of the distribution is estimated directly from radar measurements using the terminal settling velocities of ejected particles. Indeed, under the assumptions of vertical trajectories, no wind influence, and terminal fall velocity, an average particle diameter D_p can be deduced from the mean negative radial velocity weighted by the power spectral density [*Rogers and Yau*, 1989; *Hort et al.*, 2003].

$$D_p = \frac{C_s}{P_-}\sum_{V_{\max}^-}^{0} S(v)\left(\frac{V_r}{\sin\theta}\right)^2 \qquad \text{(IV.11)}$$

where $S(v)$ is the spectral power in a velocity interval. P_- refers to the power backscattered mainly by descending particles (left part of the Doppler spectrum), and θ stands for the antenna beam elevation angle. C_s is the shape coefficient, which for a spherical particle is:

$$C_s = \frac{3}{4} C_d \frac{\rho_a}{\rho_p g} \qquad \text{(IV.12)}$$

with C_d being the drag coefficient, g the gravitational acceleration and ρ_a, ρ_p the densities of air and particles respectively. Importantly, the interpretation of D_p retrieved from Doppler radar spectra differs significantly from μ_n (the mode of the PSD). Indeed, μ_n corresponds to the particle diameter that is most represented in the particle size distribution, i.e., the top of the curve. In radar meteorology, D_p is approximately equal to μ_n because the size distributions of atmospheric water droplets are typically Gaussian and very narrow. In a volcanic jet however, the power spectrum is much wider [e.g., *Dubosclard et al.,* 1999], and the physical interpretation of D_p is therefore more complex. D_p and μ_n are offset by a factor based on the dependence of the reflectivity (calculated at a given radar wavelength) on the number (N) and diameter (D) of particles. Thus μ_n is obtained from D_p using a scattering formulation adequate for the range of particle sizes characterizing explosive volcanic activity [*Woods and Bursik*, 1991; *Gouhier and Donnadieu*, 2006]. Once k and μ_n are obtained, the shift factor Λ can be calculated from equation 10.

IV.5.2.3. Scale factor, N_{max}

By assuming that k and μ_n are constant throughout the inversion procedure, the parameter vector X then becomes dependent on just a single free parameter, the scale factor, N_{max}. This characterizes the maximum of the scaled-Weibull distribution curve (S_w) and evolves during the optimization phase of the algorithm. It describes, along with k and μ_n, the total number of particles ejected during the explosion, and hence controls the erupted mass estimation. The accuracy of the results depends on the step chosen between two successive values of N_{max} in the recursive loop. However, although a small step leads to a more accurate estimation, it increases considerably the computing time.

IV.6. Monodisperse particle size model

An alternative data-inversion model based on a monodisperse PSD approximation is now presented. In this model, the single particle size equals μ_n, as well as D_p. Figure IV.6 shows that the number of small particles required to generate a given reflectivity can be up to several orders of magnitude larger than the number of corresponding large particles. Because of this huge difference in particle number, the fraction of small ejecta contributes most to the total estimated mass. For example, a reflectivity of 95 dBZ requires 8.8×10^6 kg of 0.01-m particles compared to 6.4×10^4 kg of 1-m particles, a difference of two orders of magnitude. This result illustrates that large blocks are not so important in first-order estimations of total ejected mass. This monodisperse PSD model significantly reduces computing time and ensures fast synthetic power calculations. Mass estimations are provided in Figure IV.7 for a wide range of realistic values of D_p and Z. Since these parameters are derived directly from the Doppler spectra, the corresponding mass can be retrieved instantaneously without any computing phase. This alternative method is valuable because a first-order mass estimate of ejected pyroclasts can be obtained in real time and used for volcano monitoring.

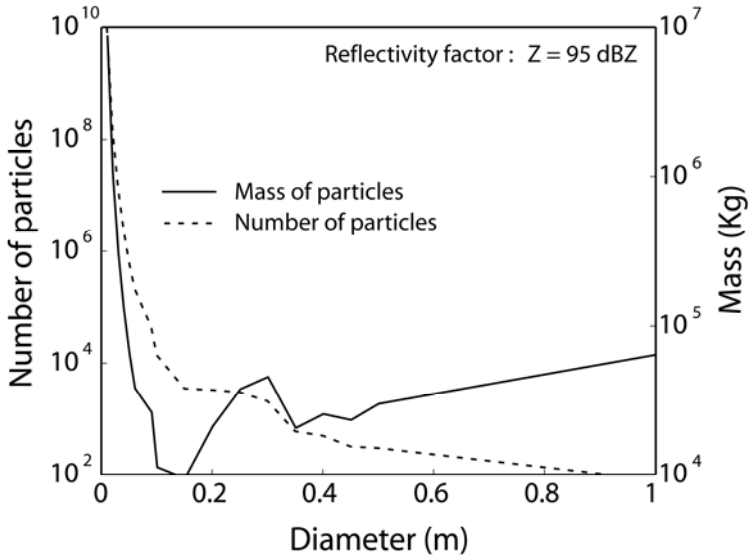

Figure IV.6. Plot of the total mass and number of particles as a function of their diameter in the monodisperse model for a reflectivity factor Z = 95 dBZ. Small particles contribute the most to the total ejected mass, for example 8.8×10^6 kg for a diameter of 0.01 m, compared to 6.4×10^4 kg for a diameter of 1 m; i.e., a difference of two orders of magnitude.

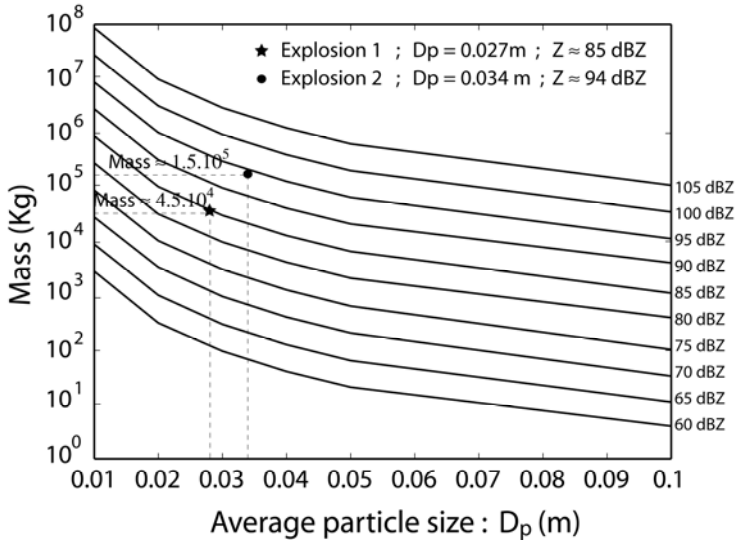

Figure IV.7. Mass estimate as a function of average particle size (D_p) retrieved from the power spectral density using the monodisperse model, for different reflectivity factors (Z) of ejected particles. First-order mass assessments can be given simply from the reflectivity factor (Z) and the average particle size (D_p) determined directly from the Doppler spectra, without any computation phase. Masses of 4.5×10^4 kg and 1.5×10^5 kg are roughly estimated for explosions 1 and 2, respectively.

IV.7. Radar data

Strombolian explosions and lava fountains were monitored with VOLDORAD for several hours during eruptive episodes of the SE crater on 4, 7 and 13 July, 2001. We focus on data acquired during two explosions that occurred at 21:41'53'' and 21:41'56'' U.T. during the eruption of 4 July. The two explosions were each short-lived, with durations of about 3 s. Temporal series (Figure IV.8) of radar power are computed from the power spectral density *S(v),* and sampled at a high frequency (10 Hz) suitable for such short-lived explosions.

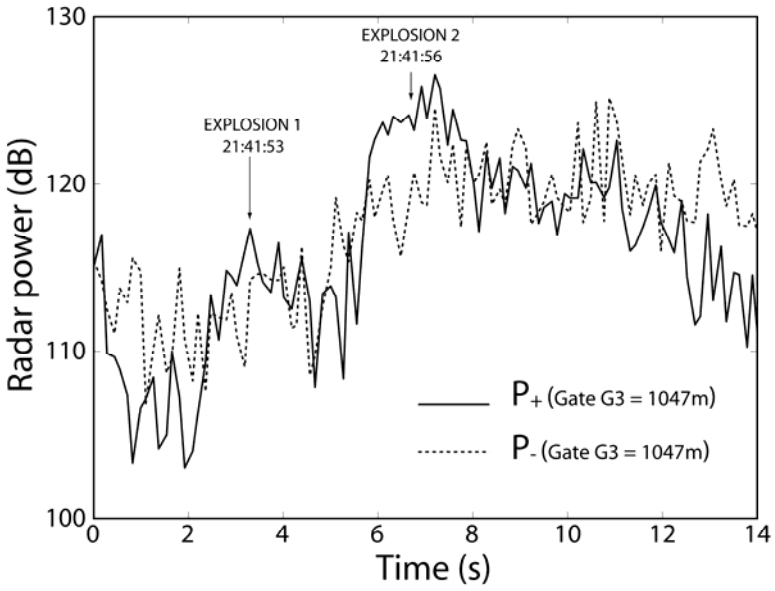

Figure IV.8. Temporal evolution of radar echo power during the two explosions studied at Mt. Etna on 4 July, 2001, sampled at 10 Hz. Both echo powers of particles moving away from (P_+) and towards (P_-) the antenna are plotted in order to infer the total power at a given instant, in the range gate (G_3) located above the vent. Both explosions are brief, lasting 2.2 s and 2.8 s respectively. The second explosion is much more powerful (125 dB and 123 dB for P_+ and P_- respectively), than the first (117 dB and 115 dB).

It is important that the power used as input to the inversion model be defined carefully. First, it is essential to ensure that the total power at a given instant is the sum of P_{tot} across the different range gates along the beam axis. Were the jet wider than the width of a single range gate (120 m), it would be necessary to integrate across several range gates in order to obtain the total reflected power. However, in the cases studied here, both jets were sufficiently narrow as to fit within a single range gate (G_3). This is deduced from (1) visual inspection of video snapshots, (2) and from the lack of echo-power signal from neighbouring range gates (G_2 and G_4). Integration along the beam axis is therefore unnecessary.

The second requirement is that the reflected power be integrated throughout the entire duration of the explosion as the jet passes vertically across the range gate concerned (G_3). In this case, two situations can be envisaged, as shown schematically in Figure IV.9. To explain these two cases, we consider two time durations: Δt_{jet}, the duration of jet production, and Δt_{cross}, the time necessary for the jet to traverse vertically the given range gate. In the first case (Figure IV.9a), $\Delta t_{jet} < \Delta t_{cross}$ and the jet is thus short enough for most of the particles to be recorded at the same instant inside a single sampling volume. The peak of radar echo power can therefore be considered as representative of the entire jet and the input parameters to the

model can be derived on the basis of a single Doppler spectrum. When $\Delta t_{jet} \geq \Delta t_{cross}$ (Figure IV.9b), the jet is never entirely contained within a single range gate, and the peak of echo power represents only a fraction of the constituent particles. Integration over the duration of the jet (Δt_{jet}) is therefore essential. Note that for lava fountaining sustained over longer periods of time at a relatively steady rate, the mean residence time of ejecta inside the range gate would need to be taken into account. This could be inferred from velocities measured by the radar and from the sounding geometry, leading to estimation of the mass flux. The total mass of lava ejected could then be calculated using the duration of the lava fountain.

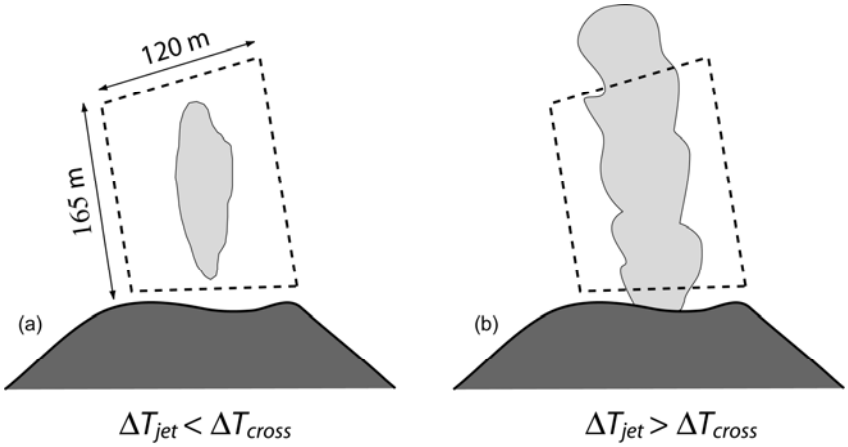

Figure IV.9. Sketch illustrating the two hypotheses made in the calculation of total power. Δt_{jet} is the duration of jet production, and Δt_{cross} is the time necessary for the jet to traverse vertically the range gate. (a) Example of a short-lived jet ($\Delta t_{jet} < \Delta t_{cross}$): the jet is short enough to be wholly enclosed in the sampling volume. A single Doppler spectrum can then be used for the calculation of total power. (b) Example of a long-lived jet ($\Delta t_{jet} > \Delta t_{cross}$): the jet is too long to be contained entirely in the sample volume at a given instant. The maximum radar echo power represents only a fraction of the total amount of ejected particles, and several Doppler spectra have to be taken into account for the calculation of the total power. The two explosions jets of 4 July, 2001 at Mt. Etna studied in this paper were both short-lived.

In the explosions considered here , the average time Δt_{cross} taken by the jet to cross the range gate (G_3) is 4.7 s at an average velocity of 38 m.s^{-1} for explosion 1, and 2.9 s at 62 m.s^{-1} for explosion 2. By comparison, Δt_{jet} is estimated from videos and radar time series at 2.2 s and 2.8 s for explosions 1 and 2 respectively. In both cases, therefore, $\Delta t_{jet} < \Delta t_{cross}$; no time integration is necessary, and data analysis can be based on a single Doppler spectrum. Moreover, the explosion jets commonly become depleted in blocks, and proportionally richer in gas toward the waning stage of their emission, so that the relevant values for Δt_{jet} might actually even be lower.

IV.8. Results

Results of the polydisperse and monodisperse models are shown in Tables IV.2 and IV.3. The fitness between observed and synthetic power data is very good, with 98.7% and 97.8% for explosions 1 and 2 respectively.

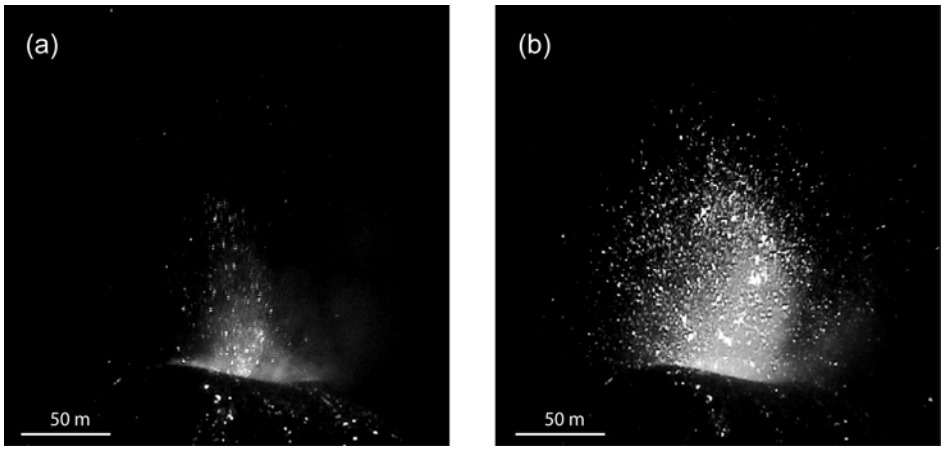

Figure IV.10. Snapshots of the two explosions from the SE crater of Mt. Etna on 4 July, 2001. Images are shown at maximum brightness, corresponding to the highest radar reflectivity from lava fragments. (a) The first explosion, occurring at 21:41'53'' U.T., displays a low quantity of lava fragments and lasts 2.2 s; (b) the second explosion, occurring at 21:41'56'' U.T., displays a much higher number of lava fragments and lasts 2.8 s.

IV.8.1. Particle loading parameters

Using the more accurate polydisperse model, the total mass of pyroclasts ejected by the first explosion is estimated at 58400 kg, corresponding to a volume of 38 m^3 assuming a pyroclast density of 1530 $kg.m^{-3}$ [*McGetchin et al.*, 1974] and a reflectivity factor of 85 dBZ. The equivalent magma volume (DRE), for a density of 2700 $kg.m^{-3}$ [*Williams and McBirney*, 1979] is 22 m^3. The second explosion (Table IV.3) yields higher values of the different parameters, with an ejecta mass of 206000 kg, a pyroclast volume of 135 m^3, a reflectivity factor of 94 dBZ, and a magma volume of 76 m^3. The difference between the reflectivity factors of the two explosions is 9 dBZ, meaning that the second explosion jet is about 8 times more reflective than the first, and the ejecta volume and mass are consequently about 3.5 times higher. This agrees with visual observations which show clearly that the first explosion involved a smaller quantity of incandescent lava clots than the second explosion (Figure IV.10).

Table IV.2. Results using both the polydisperse particle size distribution model and the monodisperse approximation, for explosion 1 (21:41'53'' U.T.) at Mt. Etna SE crater, 4 July 2001

		Synthetic results monodisperse PSD	Synthetic results polydisperse PSD	Model parameters Input / output		Explosion 1 Characteristics	
Number of particles	*(N)*	2.75×10^{6}	13.9×10^{6}	μ_n	0.0129	Date	04/07/01
Mode (m)	(μ_n)	0.027	0.013	D_p	0.027	Time (U.T.)	21:41'53''
Volume (m^3)	*(V)*	28.4	38.2	Λ	0.0165	t_{jet} (s)	2.2
Mass (Kg)	*(M)*	43.4×10^{3}	58.4×10^{3}	k	2.3	V^{+}_{max} (m/s)	60
Concentration ($Kg.m^{-3}$)*	*(C)*	0.01-0.2	0.02-0.4	γ	0.01 – 0.056	$\overline{V}^{+}_{max}$ (m/s)**	37.9
Reflectivity factor (dBZ)	*(Z)*	85.16	85.13	N_{max}	8.00×10^{5}	*Z* (dBZ)	85.12
Power (mW)	(P_{synth})	8.14×10^{-7}	8.08×10^{-7}	*Fit* (%)	98.68	P_{mes} (mW)	8.10×10^{-7}

* Concentration parameters are poorly constrained and have to be regarded as rough approximations (see text for details).
** The parameter $\overline{V}^{+}_{max}$ is the time-averaged maximum velocity and differs from the mean velocity calculated by the radar.

Particles numbers, masses and volumes estimated using the monodisperse model lie within ~25% of those of the polydisperse model for both explosions (Tables IV.2 and IV.3). This underestimation is accounted for by small particles that are not considered in the monodisperse model, but that in reality contribute most to the total mass, owing to the great particle number required to match a given reflectivity.

It is instructive to compare the measured reflectivity factors of the two Etna explosions with those theoretically calculated at Stromboli from the *Chouet et al.* [1974] observations. Recall that reflectivity factor (*Z*) is a positive function of the number (*N*) and diameters (*D*) of ejected particles. The two explosions at Stromboli give reflectivity factors of 61 dBZ and 51 dBZ (Table IV.1), whereas the two explosions at Etna give 85 and 94 dBZ (Tables IV.2 and IV.3). Thus, even a small explosion at Etna is over 250 times more reflective than a large one at Stromboli, and involves a mass of ejecta 3 orders of magnitude higher (Table IV.1). For comparison, very heavy rainfall induces maximum reflectivity factors of ~60 dBZ [*Sauvageot*, 1992].

Table IV.3. Results using both the polydisperse particle size distribution model and the monodisperse approximation, for explosion 2 (21:41'56'' U.T.) at Mt. Etna SE crater, 4 July 2001

		Synthetic results Monodisperse PSD	Synthetic results Polydisperse PSD	Model parameters Input / output		Explosion 2 Characteristics	
Number of particles	*(N)*	5.00×10^{6}	23.3×10^{6}	μ_n	0.0164	Date	04/07/01
Mode (m)	(μ_n)	0.034	0.016	D_p	0.034	Time (U.T.)	21:41'56''
Volume (m^3)	*(V)*	102.9	134.7	Λ	0.021	t_{jet} (s)	2.8
Mass (Kg)	*(M)*	157×10^{3}	206×10^{3}	k	2.3	V^{+}_{max} (m/s)	100
Concentration ($Kg.m^{-3}$)*	*(C)*	0.05-0.1	0.06-0.12	γ	0.01 - 0.072	$\overline{V}^{+}_{max}$ (m/s)**	61.6
Reflectivity factor (dBZ)	*(Z)*	93.78	93.77	N_{max}	1.05×10^{6}	*Z* (dBZ)	93.83
Power (mW)	(P_{synth})	5.92×10^{-6}	5.87×10^{-6}	*Fit* (%)	97.82	P_{mes} (mW)	6.00×10^{-6}

* Concentration parameters are poorly constrained and have to be regarded as rough approximations (see text for details).
** The parameter $\overline{V}^{+}_{max}$ is the time-averaged maximum velocity and differs from the mean velocity calculated by the radar.

IV.8.2. Derived parameters

The mean mass fluxes of ejecta, estimated from the duration of each explosion (Tables IV.2 and IV.3), reach 26400 kg.s^{-1} and 73600 kg.s^{-1} for explosions 1 and 2 respectively. These represent time-averaged values, and are not expected to be constant over the duration of each explosion.

We have also attempted to estimate particle concentrations in the two explosion jets at Etna. This is difficult since, although the radar data provide estimates of total particle mass, the jet volumes are poorly constrained. One possibility is to make the assumption that each jet filled completely and homogeneously the range-gate volume. In this case, concentration estimates have to be regarded as minima. Using the volume of range gate (G_3) above the crater yields values of 0.02 kg.m^{-3} and 0.06 kg.m^{-3} for explosions 1 and 2 respectively. However, inspection of video footage (Figure IV.10) shows that this assumption is probably not realistic. The other option is to make an estimate of the jet volume from video snapshot analysis, but two difficulties are inherent in this approach: first, the jets are spatially heterogeneous, and, second, only large lava clots are visible and the volume occupied by ash and small laplli cannot be estimated. However, taking limiting edges on video snapshots yields that the jets of explosions 1 and 2 represent approximately 5% and 50% respectively of the range-gate volume. Using these values gives maximum particle concentrations estimates of about 0.4 kg.m^{-3} and 0.12 kg.m^{-3} for explosion jets 1 and 2 respectively (Tables IV.2 and IV.3). Note that these concentrations represent spatially averaged values over the estimated jet volume; however, much higher ejecta concentrations can be found locally especially close to the vent.

The high data-sampling rate (~10 Hz in the configuration used for this study) allows VOLDORAD to measure rapid signal fluctuations on the timescale of an individual explosion. It is therefore possible to calculate an average ejecta velocity, and hence a mean kinetic energy for an explosion, using:

$$E_k = \frac{1}{2} M \left(\frac{1}{N_t} \sum_{i=1}^{n} V^{+}_{\max}(i) \right)^2 \qquad \text{(IV.13)}$$

where M is the total ejected mass given in Tables IV.2 and IV.3, and V^{+}_{max} is the maximum radial velocity of each Doppler spectrum (i) recorded in the sampling volume. N_t is the total number of Doppler spectra acquired during a given explosion. A mean kinetic energy of 4.2×10^7 J is obtained for a time-averaged maximum radial velocity ($\overline{V}^{+}_{max}$) of 38 m.s^{-1} for

explosion 1 and 3.9×10^{8} J for 62 m.s^{-1} for explosion 2. These values can be compared with the thermal energies of explosions 1 and 2 from equation 14, which are estimated at 8.4×10^{10} J and 3×10^{11} J, respectively, assuming a magma temperature T of 1373 K [*Francalanci et al.*, 1989] and a magma specific heat capacity, C_p, of 1050 J.kg^{-1}.K^{-1} [*Vosteen and Schellschmidtb*, 2003]:

$$E_T = MTC_p \tag{IV.14}$$

The thermal energies of the two explosions therefore exceed the kinetic energies by approximately three orders of magnitude. Note that the kinetic and thermal energies of the gas phase are not taken into account in these calculations.

IV.8.3. Possible effects of outsized particles

The numerical approach to the inverse problem requires us to define a continuous theoretical function for the PSDs characterizing the explosions. In reality, however, explosion-generated PSDs might contain a coarse tail of large, discrete blocks which, although relatively small in number, could have a non-negligible effect on the mass estimation. For example, the PSDs estimated photoballistically by *Chouet et al.* [1974] at Stromboli contained such coarse tails of blocks. Large blocks ejected during Strombolian explosions at Mt. Etna have also been documented by *McGetchin et al.* [1974]. In the present study these have been neglected because they cannot be described by the type of continuous PSD function required by our automatized inversion algorithm. Manual runs have therefore been carried out to assess the sensitivity of mass calculations to an additional fraction of large particles. We define a composite PSD with a continuous part and an additional discrete part that constitute respectively the lower and upper ranges of the natural PSD (Figure IV.11). The coarse tail, consisting of 85 discrete blocks, is represented by an exponential distribution from 0.1 to 1 m in diameter with a median size of 0.23 m, i.e., close to that observed by *McGetchin et al.* [1974] at the NE crater of Mt. Etna (~0.2 m). Although numerically less abundant by more than five orders of magnitude than the smaller particles constituting the continuous PSD (Figure IV.11), the blocks of this coarse tail account for ~10% of the total reflectivity. This composite PSD is probably a more realistic representation of the explosion ejecta, and gives a total mass of 187000 kg for explosion 2, in comparison to 206000 kg for the continuous PSD

lacking a coarse tail. We conclude that neglecting large blocks results in overestimation of the mass by only 9 % for this explosion. This is because the total mass of pyroclasts is mostly controlled by the large number of small particles, as shown in Figure IV.6. As a result, all the mass-related parameters listed in Tables IV.2 and IV.3 can be regarded as maxima.

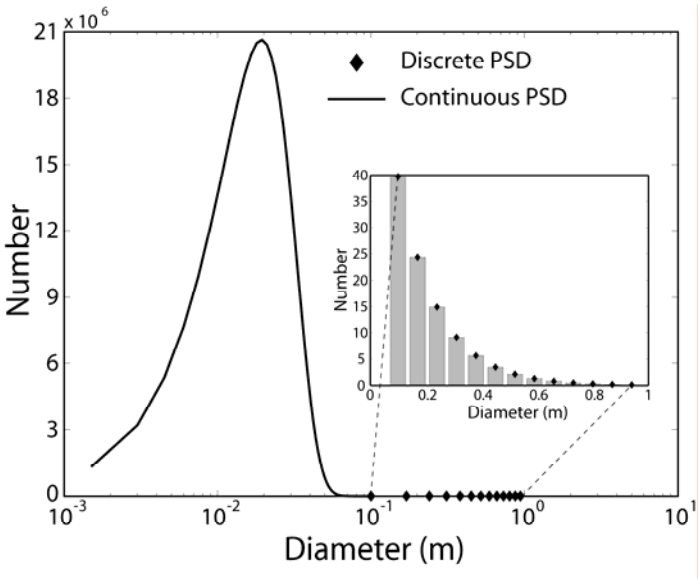

Figure IV.11. Composite particle size distribution comprising a continuous function to describe the smaller end of the PSD, with an additional coarse tail of large, discrete blocks. The continuous part refers to the PSD of explosion 2 calculated from our algorithm. The coarse tail is constrained from the data of *McGetchin et al.* [1974]; it consists of a total of only 85 blocks with a median size of 0.23 m, but that represents about 10% of the total reflectivity.

IV.9. Discussion

A Doppler radar (VOLDORAD) has been used to estimate for the first time a wide range of physical parameters characterizing Strombolian explosions at Mt. Etna. In addition to the velocity data routinely provided by Doppler radar [*Donnadieu et al.*, 2005], the results yield estimates of particle loading (number, mass and volume), as well as derived parameters such as mass flux, time-averaged particle kinetic and thermal energies and, more approximately, particle concentration in the eruptive jet.

Our approach in estimating particle loading, and the parameters derived from it, involves certain assumptions. For example, the electromagnetic scattering model assumes that all particles are smooth, spherical and compositionally homogeneous, which is not the case for

pyroclasts. However, bearing in mind the statistical effects of a very large number of rough and complexly shaped particles, as well as our objective of first-order estimation, these simplifications seem reasonable. Another assumption concerns the particle size distribution (PSD) used for data inversion. The inversion procedure involves three physical parameters: two constants defining the PSD (mode and shape factor), and the third being the number of particles corresponding to the mode that evolves during the optimization phase of the inversion procedure. In the present study the mode was constrained from the radar measurements at Mt. Etna. On the other hand, the shape factor was constrained independently using published photoballistic data of *Chouet et al.* [1974] from explosions at Stromboli, and was assumed to be representative of the explosion ejecta at Mt. Etna. Many problems are inherent in this approach. For example, the photoballistically-derived PSD of *Chouet et al.* [1974], while not skewed by atmospheric or depositional processes, is inadequate to describe the fine tail of the distribution, particles of which are too small to be detectable on photographs. On the other hand, *McGetchin et al.* [1974] constructed a PSD at Mt. Etna from grain-size measurements of Strombolian deposits, but this method also failed to take into account the smallest particles, which are dispersed far from source by the wind. Other difficulties involved in determining PSDs from deposits may also arise from bomb agglutination or from block breakage on impact. In addition, such studies probably fail to sample volumes of ejecta large enough to be statistically representative of real amounts of large blocks. Both photoballistic and ground-deposits methods therefore fail to take into account small particles, whose contribution to the total mass is important. In contrast, UV satellite methods such as TOMS or more recently OMI [*Carn et al.*, 2008; *Krotkov et al.*, 2008], succeed in imaging gas (particularly SO2), ash and aerosols released by volcanic eruptions. The IR satellite methods such as Meteosat or MODIS [*Watson et al.*, 2004] are further able to provide estimates of the distal ash content of large eruptive clouds far from the emission source that are mainly composed of small particles. But these satellite-based methods fail to image the larger size fractions segregated earlier during plume ascent. These methods might also be biased by atmospheric effects on particles, such as water vapor content and ice formation. Nevertheless, the comparison of near-source estimates of ejecta mass from ground-based Doppler radar with the mass of distal fine ash estimated by satellite-based methods could bring valuable constraints on the particle segregation from ash clouds through space and time and hence on models of ash dispersal. In order to obtain more accurate values of the mass of ejecta, a more thorough knowledge must be acquired of total source granulometries of volcanic explosions, and of their variability for different eruptive regimes.

Insights into such source PSDs could be gained for instance by high-resolution imagery and remote sensing methods working at different wavelengths. Such methods should target regions of the eruptive jet close to the vent in order for all ejected particles to be included. Their combination with ground ash collectors would bring even more stringent constraints. Knowledge acquired on PSDs would additionally provide further valuable insights into fragmentation and explosion processes during volcanic eruptions.

By fixing the explosion source PSD shape factor independently, and by determining the PSD mode using the radar measurements, we obtain a way of estimating the particle loading parameters to a first approximation. Neglecting the inevitable coarse tail of large blocks appears justified on the basis of our calculations. The two PSD assumptions used in this paper each have different advantages. The polydisperse model requires an inversion procedure that takes a long time to compute, but which results in mass estimation to a reasonable first-order accuracy. This approach is probably best adapted to studies of eruption dynamics, where the most accurate possible parameter estimates are required. The monodisperse PSD model, on the other hand, does not require any computing phase, so that mass estimation is fast and straightforward. The disadvantage of this method is that it underestimates the particle loading. This monodisperse model is most suitable for volcano monitoring, where the eruptive parameters could be calculated automatically in real-time from the Doppler spectra, but where a lower degree of accuracy could probably be tolerated.

This study has shown that Doppler radar is a powerful, as yet under-exploited, tool for quantitative studies of eruptive dynamics. The wide range of physical parameters accessible is potentially valuable for testing mathematical models of eruption jets and plumes. VOLDORAD is also well suited to the routine monitoring of active volcanoes. It can be sited at distances of up to 12 km from the vent, making it useful for the monitoring of large, highly explosive edifices. It functions under harsh weather conditions and has a data-sampling rate suitable for the study of explosive activity. The relatively low energy consumption allows us either to set up the system quickly in the field with a small power generator for a limited period of time, or to run the radar continuously at a site supplied with electric power. In addition to classical continuous records of temporal series, VOLDORAD has a “trigger” mode, in which sequences of raw data can be recorded at high sampling rate, without basic processing and hence visualization. The system can be activated either on command of the operator [*Dubosclard et al.*, 2004], or by an eruptive seismic signal of some pre-defined threshold potentially linked to an alarm system. This option is useful when monitoring isolated explosions interspersed with long intervals of quiet activity, as characteristic of many

volcanoes. In addition to the immediate benefits for operational surveillance, the long-term deployment of such radar on active volcanoes would enable to document the variability of eruptive behaviors and to build databases potentially useful for future eruptions. Combination with other ground-based methods, such as visual and infrared imagery, broadband seismic, ultrasound detection and gas analysis would shed light on the complex interactions among various eruptive processes. Thermal video such as Forward Looking Infrared Radiometer (FLIR) would be particularly helpful for the study of Strombolian activity. Its capacity to detect both fine ash plumes and large blocks can bring additional constraints on PSDs. This method can also provide further insights on Strombolian source conditions [*Patrick et al.*, 2007]. Besides, our methodology of particle loading estimation could be extended to the study and monitoring of volcanic ash plumes. With this aim, the coupling of multi-channel satellite imagery with ground-based radar measurements would be particularly relevant for the mitigation of risks related to ash clouds and for the investigations on ash plume dynamics.

CHAPTER V

Geometrical features of Strombolian jets: insight from numerical modelling of Doppler-radar spectra

V.1. Introduction

Geometrical features of a volcanic explosion visible at the surface of a volcano often betray deeper mechanisms at the origin of the eruptive dynamics. Therefore, the acquisition of quantitative data on geometrical characteristics of Strombolian jets turns out to be an important source of information for the understanding of Strombolian eruption particularly. Nevertheless, such quantitative estimates are scarce in the literature. Acquisition of geometrical data is made difficult because of the complexity of multiple parameters involved in the mechanism of particle ejection. We call particularly attention to the particles size distribution (PSD) that may widely vary from one explosion to another, and which is in addition very difficult to assess precisely. Moreover, volcanic ejecta are moving targets requiring suitable analysis tools, such as remote sensing methods. Photoballistic measurements have first been carried out at Etna (McGetchin at al., 1974) and Stromboli (Chouet et al., 1974). They give some quite accurate geometrical data, but on a very small number of explosions. Indeed, such photoballistic analyses request a heavy and tedious work that prevent statistical analysis on long sequences of Strombolian explosions. Active remote sensing tools such as Doppler radars turn out to be a good alternative for the systematic study of Strombolian jets. Indeed, Doppler radar measurements permit the detailed analysis of the eruptive activity at a high sampling rate during long sequences of time. However, some difficulties remain on the understanding of Doppler radar signal.

The aim of this chapter is to bring more stringent constraints on Doppler spectra recorded by VOLDORAD, in order to be better interpreted for particularly the understanding of geometrical processes. The study of Doppler spectra is very complex, as it integrates a lot of diverse information related for instance to the ejection angle distribution, the velocity of ejecta, and the particle size distribution. Thus, the thorough inspection of recorded Doppler spectra only is not sufficient to put constraints on the dynamics of Strombolian jets. For this reason, we modelled synthetic Doppler spectra from both ballistic model and electromagnetic scattering model presented in chapter III and IV respectively.

We then make the analysis of two contrasted Strombolian explosions as characteristic tests of the method developed here for geometrical properties retrieval. Eventually, we give a statistical set of geometrical features for a large number of characteristic Strombolian explosion at Etna SEC during the eruption of July 4, 2001.

V.2. Recorded volcano Doppler spectra (VOLDORAD)

V.2.1 Data acquisition with VOLDORAD

VOLDORAD is a pulsed Volcano Doppler Radar that permits recordings of backscattered power and radial velocity of particles crossing the antenna beam axis, and sampled in successive range gates. The width of each radar range gate is fixed at about 120 m and is defined by the pulse duration taken here as τ=0.8μs. The height directly depends on the aperture angle of the antenna beam (α=9°) and on the distance between the centre of the gate and the antenna array. For the range gate G_3, located at slanting distance of 1047, we obtain a mean height of 165 m (see Chapter II for more details)

Both parameters (backscattered power and radial velocity) are then used to build Doppler spectra in each sampling volume, and displayed in real-time on the screen of the computer controlling data acquisition and storage (Figure V.1). The acquisition rate of one set of Doppler spectra depends on the number of incoherent integrations, taken as inco=1 in the configuration of this sounding, which leads to a sampling frequency of about 10 Hz. The maximum radial velocity (Eq. V1) that can be recorded by the Doppler radar depends on the number of coherent integrations taken here as Cohe=10, which leads to a velocity range up to about 60 m/s, with a spectral resolution of the velocity axis of 0.9 m/s.

$$\left|v_{\max}\right| = \frac{\lambda}{4 \times t_r \times Cohe} \qquad \text{(V.1)}$$

Where λ is the radar wavelength equal to 23.5 cm and t_r is the pulsed repetition interval taken as 100 μs. Each Doppler spectrum represents the power spectral density *S(v)* over the range of radial velocities *(v)* measured at a given instant in a given range gate. The high resolutions in the time-domain and frequency-domain, along with the relatively good spatial resolution allow the detailed analysis of the pyroclasts trajectories and the study of their kinematics inside the eruptive jet

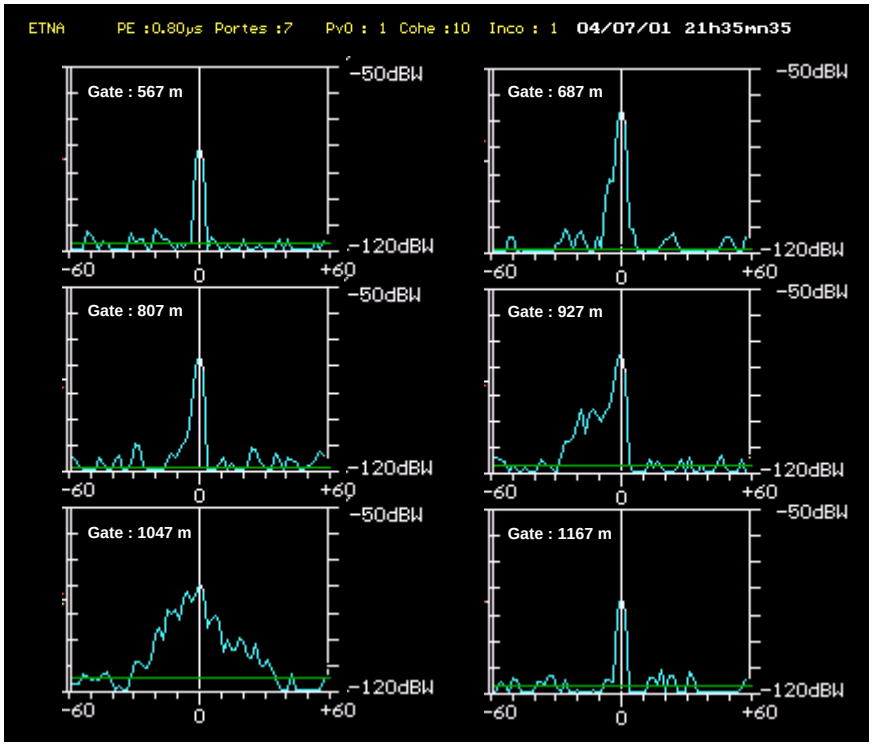

Figure V.1. VOLDORAD Doppler spectra occurring at 2135:35 UT on July 4, 2001 at Etna SEC, as displayed in real-time during the radar sounding. Each spectrum corresponds to the power backscattered by particles crossing the antenna beam, divided into several successive sampling volume (so-called range gates) 120-m wide, and ranging from 567 m to 1167 from the radar location.

Figure V.1 is a print-screen of Doppler spectra recorded by VOLDORAD on a Strombolian explosion, occurring at 2135:35 UT in July 4, 2001 at Etna SEC, as displayed in real-time in the field. Six successive range gates are reported here, ranging from 567 to 1167 m. Most of the signal is centred on the range gate at 1047 m (called G_3), taking a maximum power value close to -80 dBW. The range gate G_3 is located right above the Southeast crater and present both positive and negative radial velocities. Range gates located closer to the radar give mainly negative velocities, particularly for the gates at 687 m, 807 m, and 927 m. At the opposite, range gates located farther to the radar give mainly positive values, particularly for the gate at 1167 m. Because of the beam inclination, in typical Strombolian activity most ascending particles have a radial component of motion away from the radar in the range gates above the vent [*Dubosclard et al.*, 2004]. They generate echoes with, by convention, positive velocities and appear on the right side of the spectrum. Reciprocally, falling particles generally have a radial component of motion toward the radar inducing signal with negative

velocities on the left side of the spectrum. Figure V.2 shows the geometric characteristics of the sounding at Etna SEC during the eruption of July 4, 2001, with particularly the position of the radar range gates G_1 to G_4, and the nomenclature of ejection angles as used in the following study.

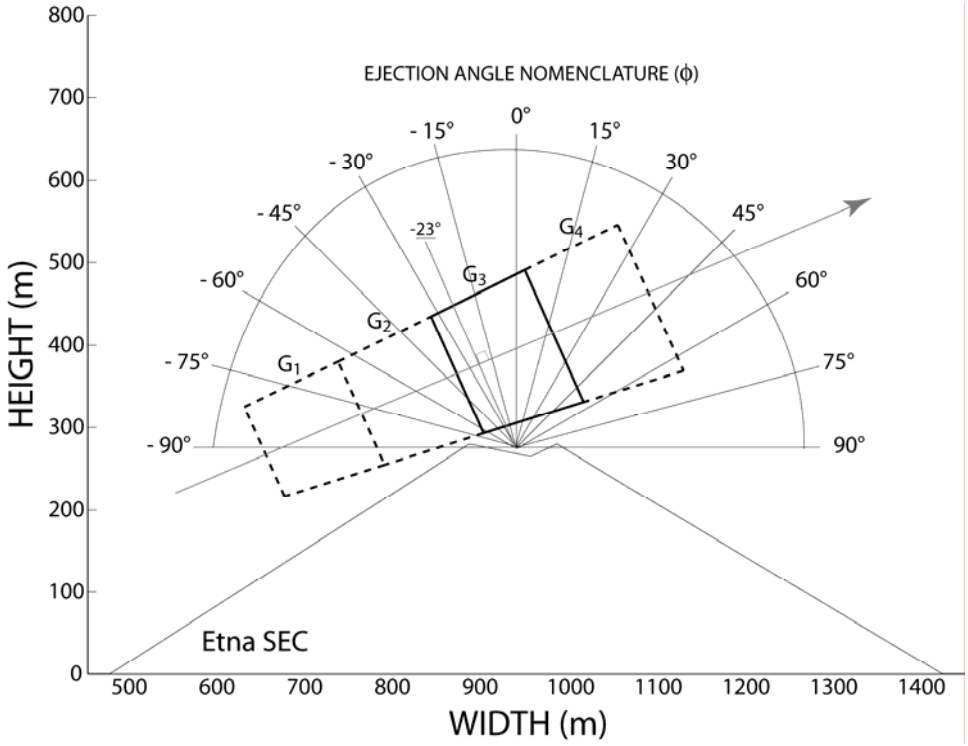

Figure V.2. Sketch of the radar sounding geometry at Etna SEC during the eruption of July 4, 2001, showing the location of 4 range gates (G_1 to G_4). In this study we focus on the gate G_3, positioned right above the crater. We present the ejection angle (ϕ) nomenclature as used in the following, with the vertical axis taken as 0°. Particles ejected toward the radar are indexed minus, and particles ejected away from the radar are indexed plus.

V.2.2. Spectral moment calculations

From the processing of the series of Doppler spectra in the range gates above the crater and on either side of the jet axis, times series can be computed for three sets of positive (indexed +) and negative (indexed -) parameters corresponding respectively to ascending and descending ejecta.

Firstly, we define the spectral moment of order 0 that corresponds to the power backscattered by particles moving toward (P^-) or away (P^+) from the radar within the sampling volume. The

backscattered power is derived from the integral of the power spectral density *S(v)* over the range of radial velocity intervals *dv*, i.e., from 0 to $V_{\max}^{+}$ for ascending particles and from $V_{\max}^{-}$ to 0 for descending particles:

$$P^{+} = \int_{0}^{V_{\max}^{+}} S(v)dv \qquad \text{and} \qquad P^{-} = \int_{V_{\max}^{-}}^{0} S(v)dv \tag{V.2}$$

Secondly, we define the spectral moment of first order that corresponds to the mean velocity $V_{mean}^{\pm}$ weighted by the power spectral density over the positive or negative velocity range (Eq. V.3). Note that because reflectivity is not a linear function of particle diameters and because the shape of the spectrum is strongly controlled by the jet geometry, the physical meaning of $V_{mean}^{\pm}$ is complex and likely different from the average particle velocity.

$$V_{mean}^{+} = \frac{\int_{0}^{V_{\max}^{+}} vS(v)dv}{P^{+}} \qquad \text{and} \qquad V_{mean}^{-} = \frac{\int_{V_{\max}^{-}}^{0} vS(v)dv}{P^{-}} \tag{V.3}$$

Finally, we define the spectral moment of second order that represents the spectral width of the Doppler spectrum from $V_{\max}^{-}$ to $V_{\max}^{+}$, which can be described as the variance of the spectral distribution:

$$\sigma^{2} = \int_{V_{\max}^{-}}^{V_{\max}^{+}} \left(v - V_{mean}^{\pm}\right)^{2} S(v)dv \tag{V.4}$$

Remind that maximum radial velocities are defined where the power spectral density *S(v)* is equal to the background noise level. In the particular case where positive and negative patterns of the Doppler spectrum are symmetrical, the spectral width can be obtained simply by:

$$\sigma^{2} = 2 \times V_{\max}^{+} \tag{V.5}$$

This method can be advantageously used, by assuming that most of Strombolian jets are roughly symmetric, because the negative part of the Doppler spectrum represents both ascending and descending particles, whereas the positive part of the Doppler spectrum is only related to ascending particles. Therefore, the contribution of ascending pyroclasts only, related to the ejection stage in the left part of the Doppler spectrum is difficult to determine. This effect would bias any estimate of the spectral width based on both negative and positive velocities.

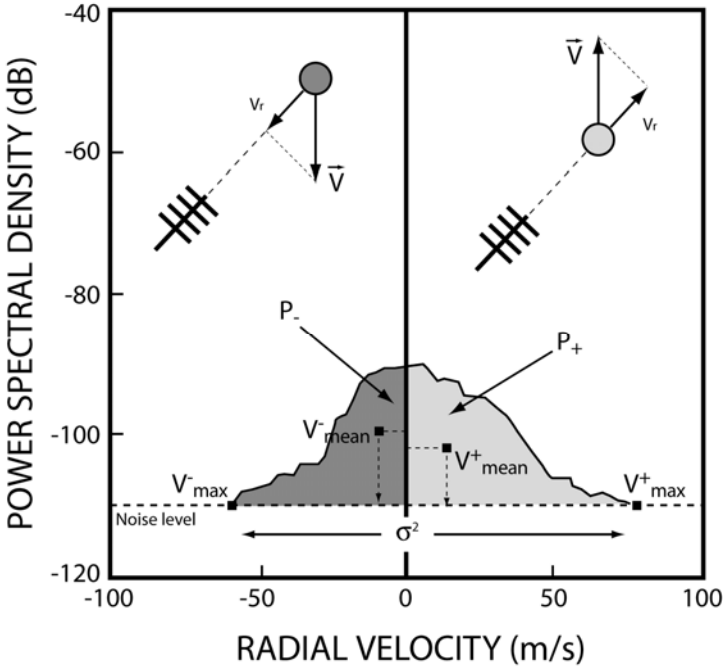

Figure V.3. Sketch of a typical volcanic Doppler spectrum, showing the spectral moments (power, maximum and mean radial velocity, and spectral width) as calculated from the power spectral density. They are indexed (+) and (-) for ejecta with the radial component of their velocity vector moving away and towards the antenna respectively, except for the spectral width that represents the standard deviation of the whole spectrum.

Originally, the spectral moments were characterised from weather-radar Doppler spectra. In meteorological applications, in particular, the backscattered power parameter provides an estimate of the amount of water droplet, which is related to the precipitation rate. The mean velocity parameter gives the average velocity of sinking water droplets, and the spectral width parameter is commonly used to assess the turbulence of the air, related for example to shear stresses caused by the wind. However, the study of Strombolian volcanic activity is far different and more localized, so that the interpretation of the spectral moments has to be considered cautiously, taking into account the radar sounding conditions, along with the

complex kinematics and the wide range volcanic particles sizes. In the present study, we aim at improving our interpretation of volcano Doppler spectra in order to retrieve quantitative information on the geometrical properties of Strombolian jets.

V.3. Synthetic volcano Doppler spectra (numerical modelling)

The understanding of Doppler spectra from Strombolian volcanic jets turns out to be very difficult, particularly because of the very large particle size distribution (PSD), ranging from submillimetric ash to metric blocks. Indeed, the decoupling of ash-sized particles entrained by expanding gases from larger blocks following ballistic trajectories leads to a wide range of ejecta speeds, and to large dynamic of the power spectral density spanning several orders of magnitude. Also, the jet geometry, characterized by ejection angle distribution (EAD) at each instant, strongly controls the shape of Doppler spectra and varies largely from an explosion to another.

The thorough inspection of recorded Doppler spectra only is therefore not sufficient to put constraints on the dynamics of Strombolian jets. This is the reason why we have developed a complete model that generates synthetic Doppler spectra under controlled geometric conditions. Recorded Doppler spectra are constructed from radial velocities and the backscattered power of particles crossing the antenna beam axis. Therefore, in order to build synthetic Doppler spectra, we need to define (1) the radial velocities from the ballistic model developed for the kinetic parameters estimate (Chapter III), and (2) the synthetic backscattered power calculated from the electromagnetic scattering model developed for the loading parameters assessment (Chapter IV). In the next two sections we present very briefly both models that have already been introduced.

At the input of the models we have the possibility to define (1) the particle size distribution (PSD), the one can be chosen as monodisperse (single size particle) or polydisperse (multiple sizes particles), the latter following uniform, Gaussian, log-normal or exponential distribution. (2) The ejection angle distribution (EAD) can also be widely varied, from mono-angle to poly-angles, the latter following isotropic (i.e., uniformly distributed) or anisotropic distribution. (3) We define for each explosion modelled the initial gas velocity that is the driving force of the particle ejection and finally (4) the number of particles to launch.

Figure V.4. shows the schematic representation of various PSD and EAD configuration that can be used at the input of our models.

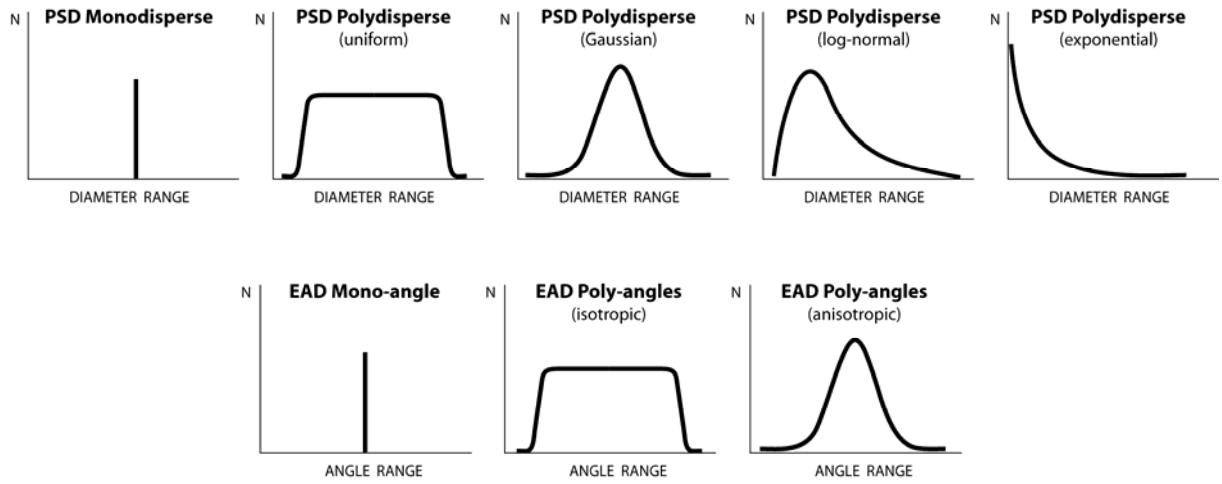

Figure V.4. Sketch of the of particle size distribution (PSD) being monodisperse or polydisperse, which can follow uniform, Gaussian, log-normal or exponential law. We also present the schematic representation of ejection angle particle (EAD) being mono-angle or poly-angles, the latter being isotropic or anisotropic.

V.3.1. Ballistic model

To simulate the ejection of pyroclasts during a Strombolian explosion, we use the two-dimensional ballistic model initiated by Dubosclard et al. (2004) and developed in this work (Appendix XX). Kinetic features are then calculated on the basis of equations of motion, assuming that the two forces acting on each particle are the drag force, and the gravitational force. We define particularly, the initial velocity of a particle with diameter *D* (Steinberg and Babenko, 1978):

$$V_0^p(D) = V_0^g - k\sqrt{D} \qquad \text{(V.6)}$$

where *k* is a constant, taken as 150 as inferred from previous studies (Chouet et al., 1974, Ripepe et al., 1993), and the gas velocity as a function of height (Blackburn et al., 1976):

$$V_g(z) = V_0^g \exp\left(\frac{-\gamma z}{z_{ref}}\right) \quad \text{(V.7)}$$

where γ is a constant taken as 4.6 (Dubosclard et al., 2004) and z_{ref} is the height above the vent such as $V_g(z_{ref}) = 0.01 V_0^g$, and taken as z_{ref}=850 m as inferred from video measurements (Chapter III).

We have modelled here (Figure V.4) a test explosion with a uniform polydisperse PSD ranging from 0.01 m to 0.1 m, and with an anisotropic poly-angles EAD ranging from -45° to +45°, centred on the vertical axis. In this test explosion, 4520 particles were instantaneously propelled upward from the vent, located approximately 50 m beneath the crater rim, by a gas phase of initial velocity V_0^g =100 m/s.

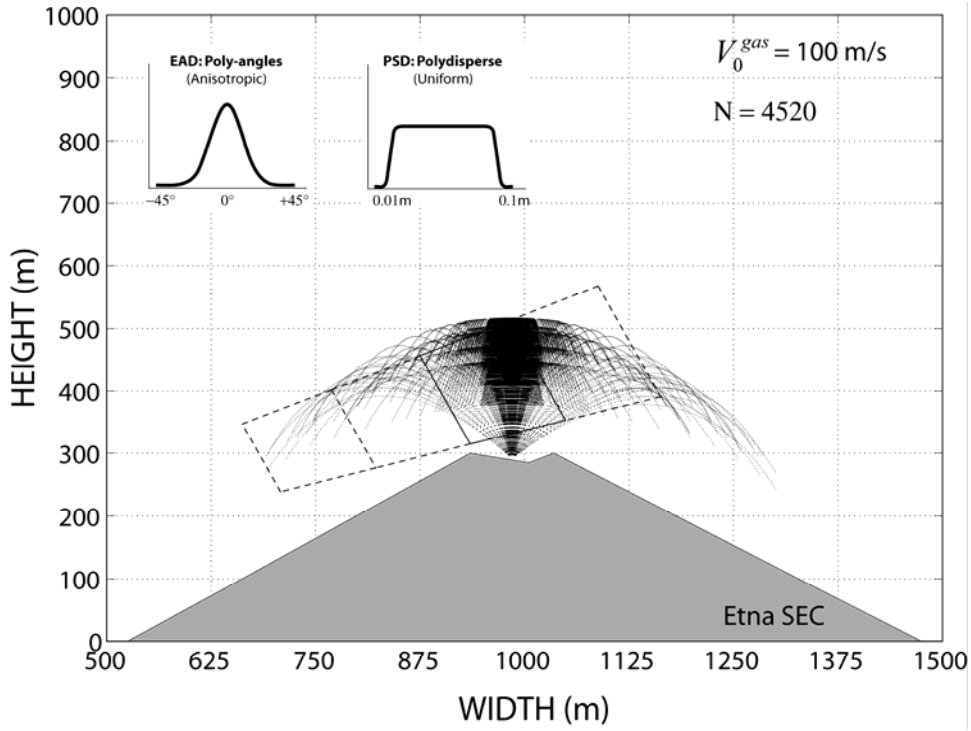

Figure V.5. Visual representation of one test explosion modelled from the ballistic model. At the input we imposed a uniform polydisperse PSD ranging from 0.01 to 0.1 m, nad a poly-angles EAD following an anisotropic distribution ranging from -45 to +45°. The initial gas velocity is taken as 100 m/s, with 4520 particles launched.

The velocity of each particle is calculated from the numerical integration of the equations of motion at each time step and its radial component is readily obtained. We show in Figure V.6 the temporal evolution of the mean and maximum radial velocity in the radar range gate G_3 and G_4, located respectively at 1047 m and 1167 m to the radar, for the test explosion as calculated by the ballistic model. Importantly, the mean radial velocity calculated here represents the real average velocity of all particles, whereas the maximum radial velocity corresponds to the velocity of the fastest particle, both calculated inside the considered range gate, along the antenna beam axis at each time step.

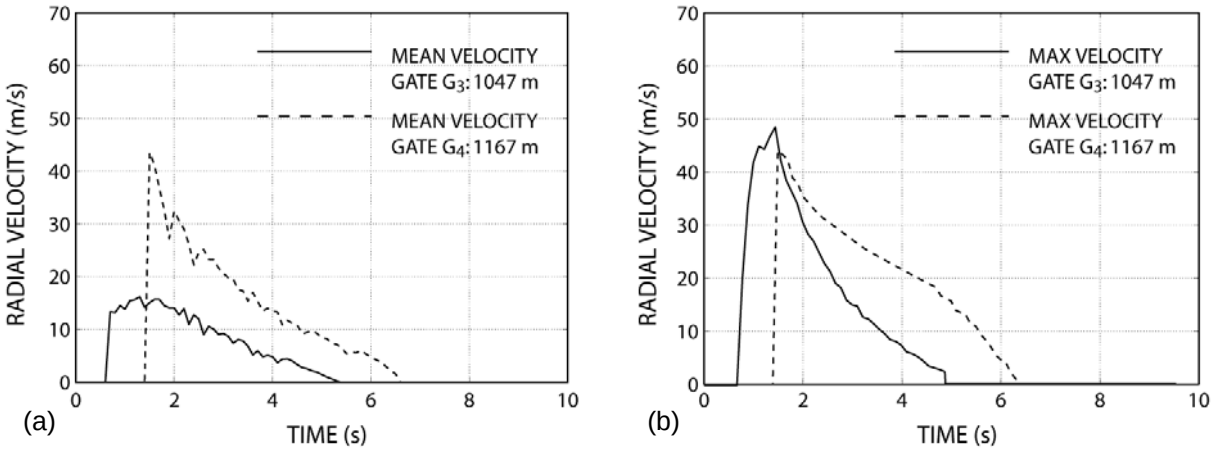

Figure V.6. Time series inferred from the ballistic model for the test explosion modelled previously. (a) We provide the mean radial velocity in range gates G3 and G4, representing the average velocity of all particles in a given range gate at each time step. (b) We give the maximum radial velocity in the same two range gates, representing the velocity of the fastest particle in a given range gate, at each time step.

We find that the patterns for mean and maximum velocities are rather similar in the range gate G_4, whereas they differ significantly in the range gate G_3, located right above the vent These differences come from the radar sounding geometry, in particular the lateral offset of the range gate G_4 to the vent and the inclination of the beam axis (θ=23°). The radial component of velocity (i.e. along the beam axis, as measured by the radar) becomes lower as particle trajectories depart from the beam axis, and ultimately reaching zero when the particle trajectory is perpendicular to the beam axis (i.e., = 90°+θ).

Most particles in the range gate G_3 (above the vent) have a trajectory with a strong vertical component; therefore the average of all particle radial velocities (17m/s) largely underestimates the real mean velocity of the whole jet at this instant. At the opposite, particles

trajectories in the range gate G_4 become much more tangent to the beam axis as particles incline during the ballistic flight, giving better estimate of the real mean velocity (43 m/s). Note however, that velocities of particles inside the gate G_4 have already slowed down because of the large distance covered from the emission source.

Also, in the configuration of our radar sounding, the maximum value of the radial velocity in gate G_3, peaking at 47 m/s in Figure V.6b, leads to a slight underestimation of about 20% of the real maximum velocity (56 m/s). This difference is related to the ejection angle of the particle that is never parallel to the antenna beam axis in the range gate G_3. Indeed, if we take the bottom right hand corner of this range gate as maximum inclination (55°), we obtain from equation V.7 a geometrical correction coefficient of about 1.2, which is fully consistent with the ratio of real maximum velocity with radial maximum velocity.

$$V_{real} = \frac{V_{rad}}{\cos(55 - \theta)} \tag{V.7}$$

Finally, the peak value of the maximum radial velocity calculated in the range gate G_4 is slightly lower (44 m/s) than the one inferred from range gate G_3. This difference can be easily explained by the natural speed decrease of particles with height. Note that very rapidly, the maximum radial velocity in range gate G_4 becomes faster than in the range gate G_3, actua
lly, it is a competition between both effects, i.e., the distance covered by the particle and the angle of its trajectory).

V.3.2. Electromagnetic scattering model

The power backscattered by particles is derived from the electromagnetic wave scattering theory of Mie (1908), using the complete set of equations applied to our specific case given in Gouhier and Donnadieu (2008). A good approximation can be obtained with advantageous computing time applying the Rayleigh analytical solution, but only for particles of diameter smaller than $\lambda/4$, i.e. ~5.9 cm in our case (Gouhier and Donnadieu, 2006). However, considering the wide range of particle diameters characterizing Strombolian activity, the Mie scattering theory is required to account for the effects of larger particles.

Theoretically, the power backscattered to the radar by a population of such particles in a given range gate is proportional to their radar reflectivity (η). The echo-power can then be defined as:

$$P = \frac{C_r V_s \eta}{R^4} \qquad \text{(V.8)}$$

where C_r is the radar constant, V_s, the sampling volume, and R, the slant distance between the radar and the target. The radar constant is defined by a set of technical parameters related to the radar configuration. The radar reflectivity (η) is the sum of the backscattering cross sections of the individual particles per unit volume (see Appendix B for more details)

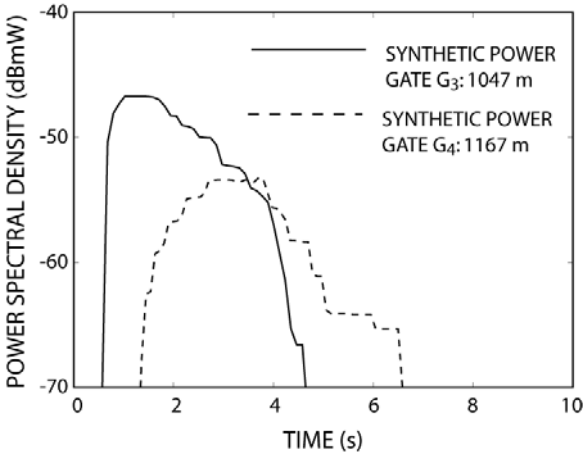

Figure V.7. Time series inferred from the electromagnetic scattering model, for the test explosion modelled previously. We provide the synthetic power calculated from the complete Mie formulation that corresponds to the echo-power backscattered by particle in range gate G_3 and G_4 at each time step.

The backscattered power of each particle is calculated from the electromagnetic scattering model at each time step. We show in Figure V.7 the temporal evolution of synthetic power in the radar range gate G_3 and G_4, located respectively at 1047 m and 1167 m to the radar, for the same test explosion. The synthetic echo power signal in the gate G_3 gives higher values, peaking at -47 dBmW, and last shorter than in the gate G_4. Both features can be explained by the fact that a majority of emitted particles cross the closest gate (G_3), the one located right above the vent. Then, particles enter the next range gate (G_4) with a delay related to the time for particles to cross the gate G_3. Moreover, their velocities have significantly decreased and hence the resident time in the gate G_4 is longer.

V.3.3. Synthetic Doppler spectra

From the acquisition of both radial velocities and power values derived from the ballistic and the electromagnetic scattering models respectively, we are able to construct synthetic Doppler spectra. A time step of 0.1 s was chosen to correspond approximately to the acquisition rate of Doppler spectrum by VOLDORAD (~10 Hz). The velocity range in the synthetic Doppler spectrum (abscissa) can be adapted according to the conditions of the modelled explosion, and is commonly taken at ±60 m/s with a spectral resolution of 1m/s, i.e., 120 velocity classes over the whole spectrum range, each associated with the power backscattered by particles having a radial velocity falling in the class under consideration. The distribution of power among the velocity classes defines the power spectral density, expressed in dBmW (mW in Log_{10} scale).

In figure V.8 we show a synthetic Doppler spectrum in the range gate G_3 (1047 m) calculated from the test explosion described above. We observe that the synthetic Doppler spectrum is quite triangular and roughly symmetric around its mode at about 15 m/s. Indeed, most of the signal is centred on the positive part of the Doppler spectrum, which is due to the geometry of the radar sounding. Note that in what follows, we will not take into account the quantitative measurements of the power parameter. Indeed, bearing in mind the huge amount of particles necessary to reproduce real Strombolian explosions and the long related time to compute, we will only model smaller explosions of a few thousands of particles. However, quantitative measurements of kinetic parameters are not affected by this simplification and can be deeply exploited. Also, considering the logarithmic scale of power values, the global shape of Doppler spectra is preserved, and can be compared with the ones derived from Doppler radar measurements.

Then, we are able to calculate the synthetic spectral moments from equations given in section V.2. We obtain a synthetic maximum positive radial velocity of $V_{\max}^{+synth} = 47$ m/s, note that in the case of modelled Doppler spectrum there is no noise level, and hence even one very fine particle can lead to the calculation of the maximum velocity. Moreover, we point out that the peak of maximum radial velocity obtained from the Doppler spectrum analysis (i.e., in the same way as the radar), is equal to the maximum jet velocity observed in the time series. This result emphasises that maximum velocities are not biased by the power

distribution. We find a synthetic mean radial velocity of V_{mean}^{+synth} = 11 m/s. Remind that the mean velocity parameter, inferred from Doppler spectrum calculation (moment of order 1), is weighted by the power spectral density over the whole positive or negative range. Therefore, this value differs from the mean radial particle velocity (17 m/s) as calculated from time series from Figure V.6. As a consequence, in addition to the geometric bias on the estimation of real velocities, this result stresses the influence of the power distribution among the different velocity classes, and hence of the particle sizes on the assessment of the mean velocity, as calculated from radar data.

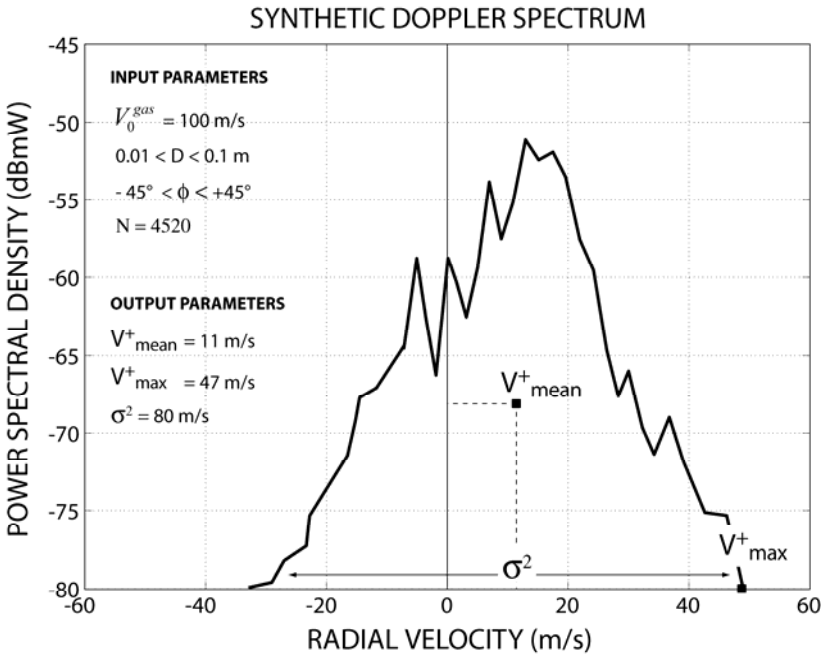

Figure V.8. Synthetic Doppler spectrum of the test explosion modelled from the ballistic and electromagnetic scattering model, showing the power spectral density as a function of radial velocity. Spectral moments (spectral width, maximum and mean velocities) are calculated in the same way as VOLDORAD.

V.4. Parametric tests

Any volcanic Doppler spectrum is potentially a great source of information on the explosion dynamics, particularly from the study of its shape and its spectral moments. Simple parameter comparisons made in previous sections show the complexity in the analysis of volcanic Doppler spectra. Henceforth, we identify two main factors influencing the spectral patterns (1) the sounding geometry strongly controls measured radial velocities, and (2) the numerous particle sizes additionally account for the variability of ejecta speeds. In the following (Figure V.9), we carry out simple parametric tests to assess the contribution of both potential biases in the Doppler-radar measurements.

V.4.1. Ejection angle vs. particle sizes distribution sensitivity

Figure V.9a shows a synthetic Doppler spectrum with a single peak at v=30 m/s resulting from the simplistic case of a single particle of diameter D=0.03 m (monodisperse PSD) launched vertically at ϕ=0° (mono-angle EAD).

In Figure V.9b, a narrow Doppler spectrum (spectral width <10 m/s) is modelled with particles ejected also vertically (mono-angle EAD), but using a uniform polydisperse PSD with diameter ranging from 0.003 m to 0.06 m. Therefore, we show that a wide PSD does not account for a large dispersion of radial velocities recorded on Doppler spectra.
Contrastingly, we modelled in Figure V.9c an explosion with a monodisperse PSD with a diameter D= 0.03 m, launched with an isotropic poly-angle EAD ranging from -45° to +45° of the vertical. We observe a top-hat Doppler spectrum with a large spectral width, close to 80 m/s. This clearly emphasizes the overall influence of the aperture of the ejection cone on measured radial velocities.

A more realistic simulation is shown in Figure V.9d, where particles were launched over a wide range of ejection angles (-45° to +45°) following an isotropic EAD, for two distinct particle size distributions: (1) the first one, ranging from 0.003m<D<0.03m, aims at representing the fine particles, and (2) the second one stands for larger particles, ranging from 0.03m<D<0.06m. The Doppler spectrum corresponding to fine particles have a lower spectral density, which is easily explained by the fact that small particles scatter dramatically less than

large particle. For instance, the power backscattered by particles with D=0.06 m is proportional to their diameter to the power of sixth (Rayleigh domain). Moreover, the spectral width of the fine particle Doppler spectrum is larger due to the fact that small particles, having a low inertia, are propelled with higher initial velocities, close to that of the gas, enlarging the range of measured radial velocities. Despite large geometrical effects on the shape of spectra, we can nevertheless identify qualitatively power and velocities variations due to changes in particle size.

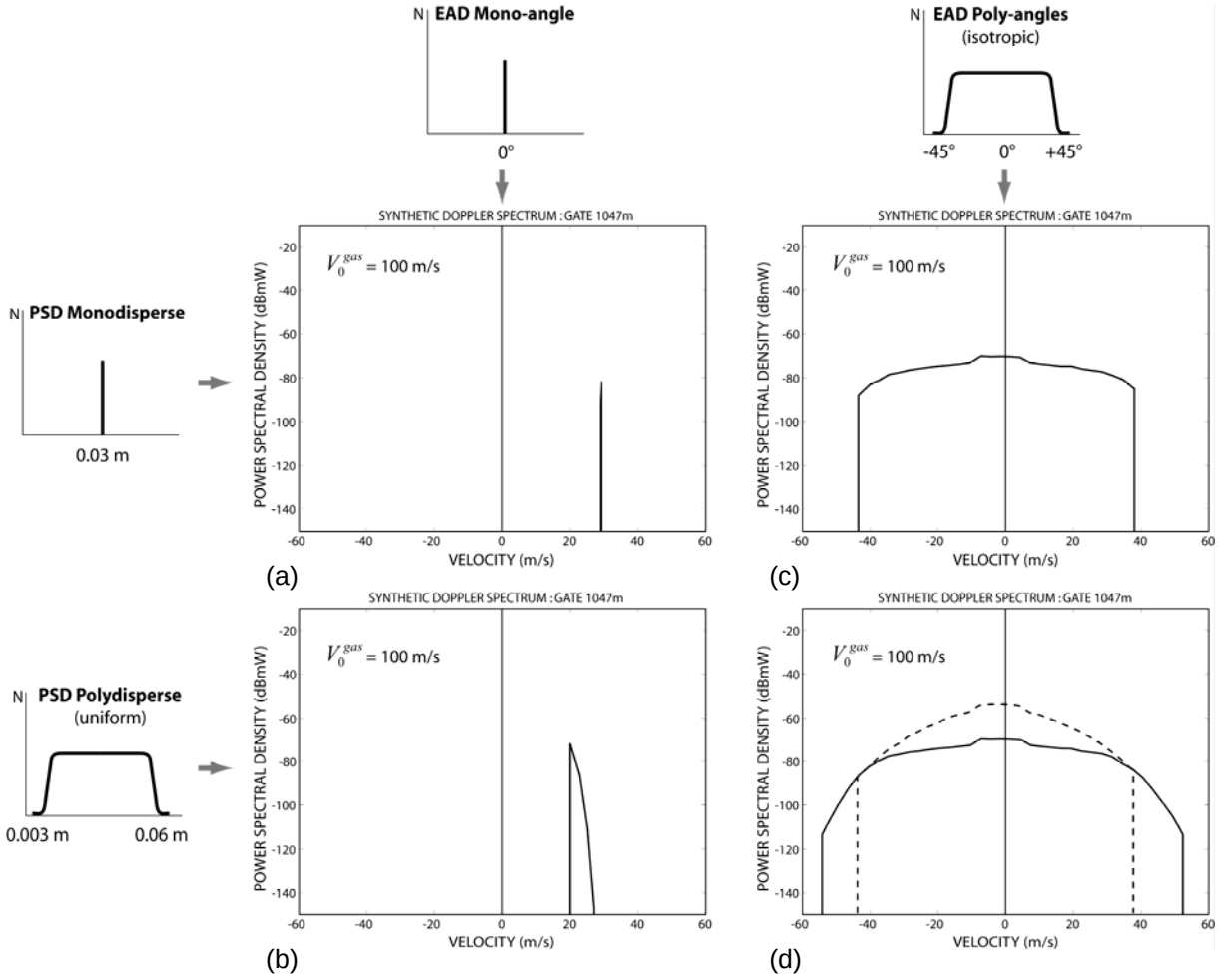

Figure V.9. Plot of some parametric tests showing the contribution of ejection angle distribution (EAD) and particle size distribution (PSD) on the variability of volcanic Doppler spectrum. (a) Both PSD (D=0.03m) and EAD (ϕ=0°) are monodisperse. (b) EAD is still monodisperse (ϕ=0°) but with a uniform polydisperse PSD ranging from 0.003m<D<0.06m. (c) At the opposite, we provide a monodisperse PSD (D=0.03m) with an isotropic poly-angles EAD ranging from -45<ϕ<+45 and centred vertically. (d) We provide a Doppler spectrum with both polydisperse PSD (0.003m<D<0.06m) and poly-angles EAD (-45<ϕ<+45).

V.4.2. Ejection angle anisotropy

Lots of other parametric tests have been carried out in order to refine our interpretation on radar Doppler spectra. We do not aim at presenting all of them exhaustively, but just to sum up the main characteristics that may control the shape of Doppler spectra. We have shown previously the dominant role played by the ejection geometry and, to a lower extent, by the range of particle sizes. However, all explosions modelled so far were isotropic. We now investigate how sensitive is the shape of a Doppler spectrum to the ejection angle distribution (EAD) variability.

In figure V.10, two explosions are modelled with different poly-angles EAD and a fixed monodisperse PSD with diameter D=0.01m. For each explosion tested, the maximum power is the same (P_{max} = -96 dBmW), as well as the maximum positive radial velocity ($V^{+}_{\max}$ = 50 m/s); only the curvature of the Doppler spectrum turns out to be variable. Two main shapes can be identified: top-hat and triangular Doppler spectra.

The first explosion (figure V.10a) follows an isotropic poly-angles EAD, ranging from -45° to +45°. It means that the same amount of volcanic material is included in a wide range of ejection angle. This feature can be directly interpreted from the Doppler spectrum plateau ranging from about -15 m/s to 30 m/s, and leads to a top-hat Doppler spectrum. Henceforth, we make the distinction between the plateau spectral width (σ_p^2=45 m/s) and the total spectral width (σ_t^2 = 70 m/s).

At the opposite, the second explosion (figure V.10b) follows an anisotropic (Gaussian) poly-angles EAD, ranging from -45° to +45°. It means that the amount of volcanic material dramatically decrease for high angle values (from the vertical). This characteristic is clearly seen on the Doppler spectrum by a severe decrease of the power spectral density with increasing radial velocities from the single peak power value. Indeed, there is no plateau component, and we define this Doppler spectrum as triangular. Thus we only give an estimate of the total spectral width, found to be the same as for explosion one (σ_t^2 = 70 m/s). Remind that in the case of Doppler spectra recorded by VOLDORAD, we do not use the negative part of the Doppler spectrum for the total spectral width measurement (see section V.2 for details). As a comparison, by using the alternative equation V.5, the total spectral width is taken as twice the maximum positive radial velocity (i.e., 100m/s), which fairly differs from the first calculation.

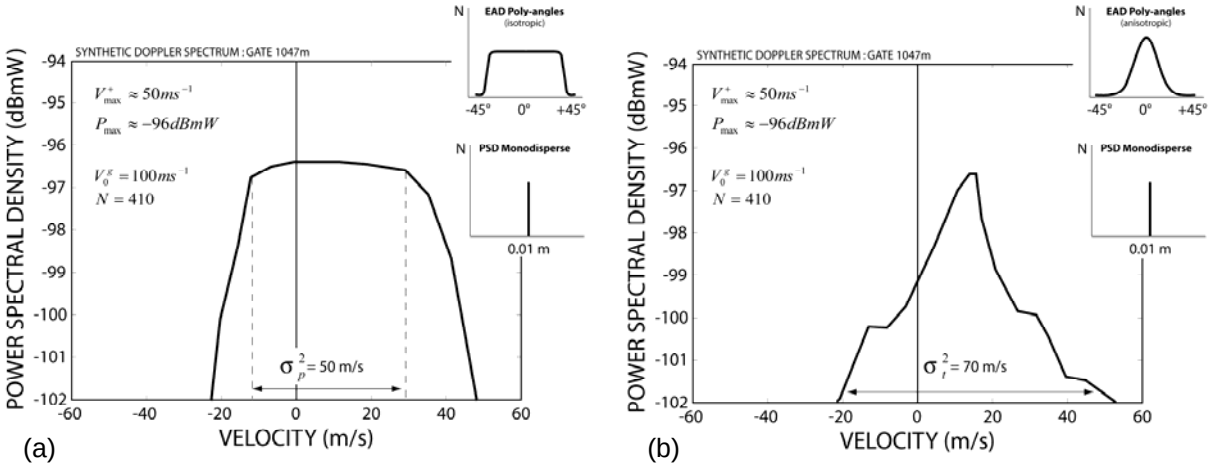

Figure V.10. Plot of parametric tests showing the effect of an anisotropic ejection angle on the shape of Doppler spectra. We point out two distinct shape: (a) Top-hat-shaped Doppler spectrum related to the isotropic EAD, and (b) triangular-shaped Doppler spectrum related to the anisotropic EAD.

V.4.3. Mean ejection angle inclination

We have finally carried out some parametric tests to assess the sensitivity of Doppler spectrum shape to the jet inclination. Figure V.11 shows four Spectra modelled by following an anisotropic (Gaussian) EAD inclined at 20°, 0°,-20°, and -40° to the vertical. Note that all Doppler spectrum patterns are triangular as expected from such an ejection angle distribution. All Doppler spectra are modelled with a monodisperse PSD using a diameter of 0.01 m, and with an initial gas velocity of 100 m/s.

Interestingly, qualitative information on the jet inclination can be retrieved from the mode of the Doppler spectra, i.e. the radial velocity corresponding to the maximum power. In these examples, power mode values fall respectively at 45 m/s, 25 m/s, 0 m/s, and -30 m/s. Remarkably, the vertically oriented jet induces a power mode at a singular radial velocity $V_{\phi=0}$ = +25 m/s with the initial conditions chosen previously. Consequently, jets inclined away from the radar ($\phi>0°$) generate a power mode above this threshold radial velocity, whereas jets inclined toward the radar ($\phi<0°$) generate a power mode below $V_{\phi=0}$. Note that the power mode is found at 0 m/s when the main jet axis is perpendicular to the beam, that is to say inclined toward the radar at about -θ relative to the vertical (i.e., ϕ= -23°).

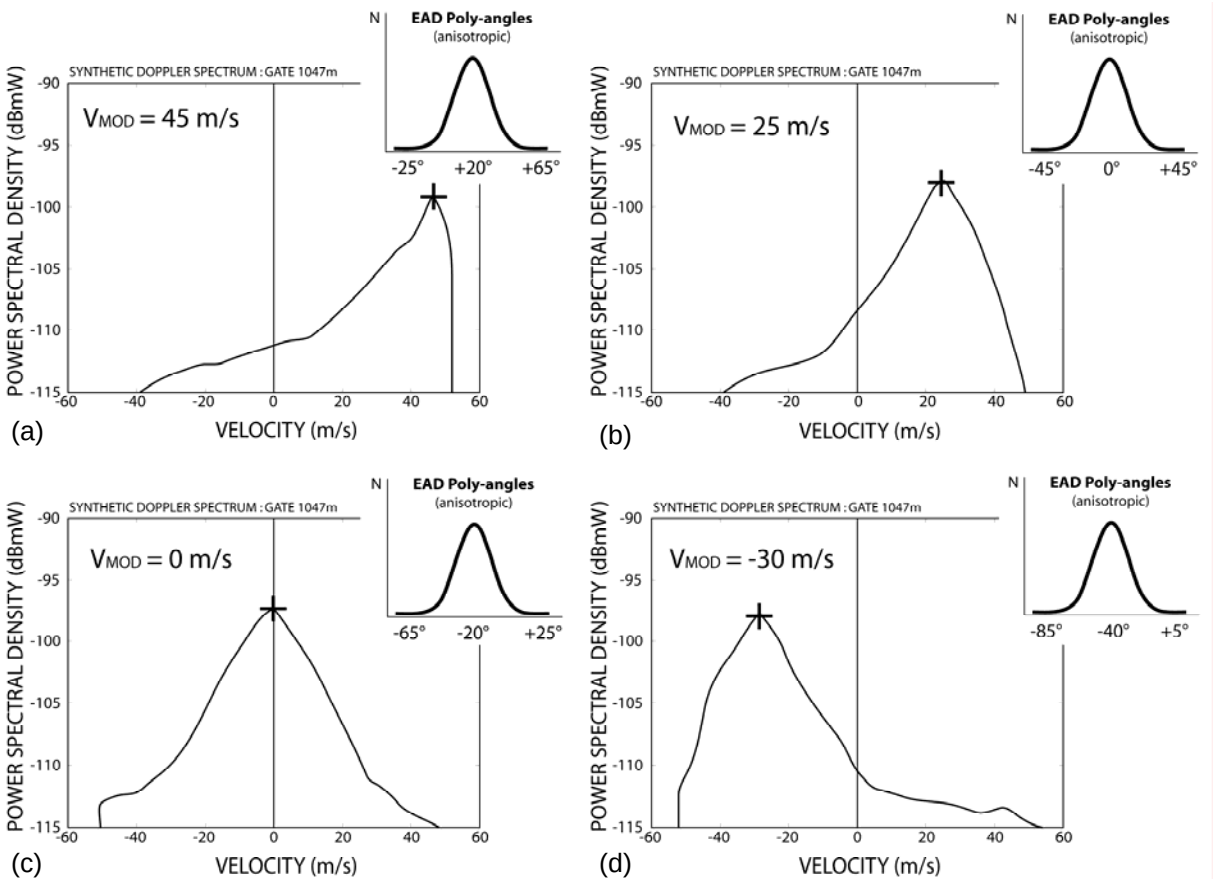

Figure V.11. Plot of parametric tests showing the sensitivity of Doppler spectrum shape to the jet inclination. The PSD is monodisperse (D=0.01m) and all EAD are anisotropic and poly-angles, only the mode of the distribution changes taking values of (a)+20° (b) 0°, (c) -20°, and (d) -40°.

Parametric tests achieved in this section point out the potential information held in Doppler-radar spectra for understanding the dynamics of volcanic jets. We show in the following sections that some of these singular characteristics can be used advantageously on Doppler spectra recorded by VOLDORAD at Mt. Etna, to retrieve geometric parameters characterizing eruptive jets.

V.5. Geometrical properties of two contrasted Strombolian explosions

In this section, we characterize the geometrical aspects of Strombolian jets produced by Mt. Etna SEC. Typical Strombolian activity consists of a series of large bubbles rising from depth, and bursting at the surface of the magma column (Vergniolle and Brandeis, 1996). The bubble overpressure release is then responsible for the ejection of fine ash to large disconnected blocks above the vent, finally crossing the radar beam. The dynamics of Strombolian explosion is fairly complex, and the study of the geometrical characteristics of such volcanic jets should bring constraints on the physical source mechanisms at work. We focus here on two particular explosions occurring on July 4, 2001, showing contrasted geometrical features.
The analysis of Doppler spectra recorded by VOLDORAD brings out two main distinct shapes: top-hat and triangular. In what follows, we aim at reproducing the shape of recorded Doppler spectra for two distinct explosions occurring at 2143:04 UT and 2139:34 UT showing top-hat and triangular shape respectively. In order to build synthetic Doppler spectra, we need to define three types of variable input parameters: (i) the initial gas velocity, (ii) the ejection angle distribution (EAD) and (iii) the particle size distribution (PSD).
The PSD is defined by the number N of particles with diameter D, the distribution being monodisperse or polydisperse. An EAD is defined by the range of ejection angles, the direction of the main jet axis (inclination) and the spacing between angles. The latter reflects the particle concentration among the different angles and characterise the jet isotropy or anisotropy within the dispersion cone. These parameters have been adjusted so as to best fit the shape of the recorded Doppler spectrum, without trying to match the real power amplitude.

V.5.1. Top-hat-shaped spectra

In Figure V.12, we have reproduced an explosion that occurred on July 4, 2001 at 2143:04 UT during the paroxysm of the eruptive episode. In this example, the overall shape of the recorded Doppler spectrum is typically top-hat, with two distinct parts: (1) a large plateau characterised by a spectral width of σ_p^2=35 m/s, and bordered by (2) a sub-vertical slope reaching the noise level at $V_{\max}^{+}$=38 m/s. The corresponding video snapshot shows the uprising of a very large bubble expanding above the crater rim, whose bursting ejects lava

clots in all directions within a hemispherical ejection cone, suggesting an isotropic concentration of particles moving radially from the vent and ejected with quite homogeneous velocities.

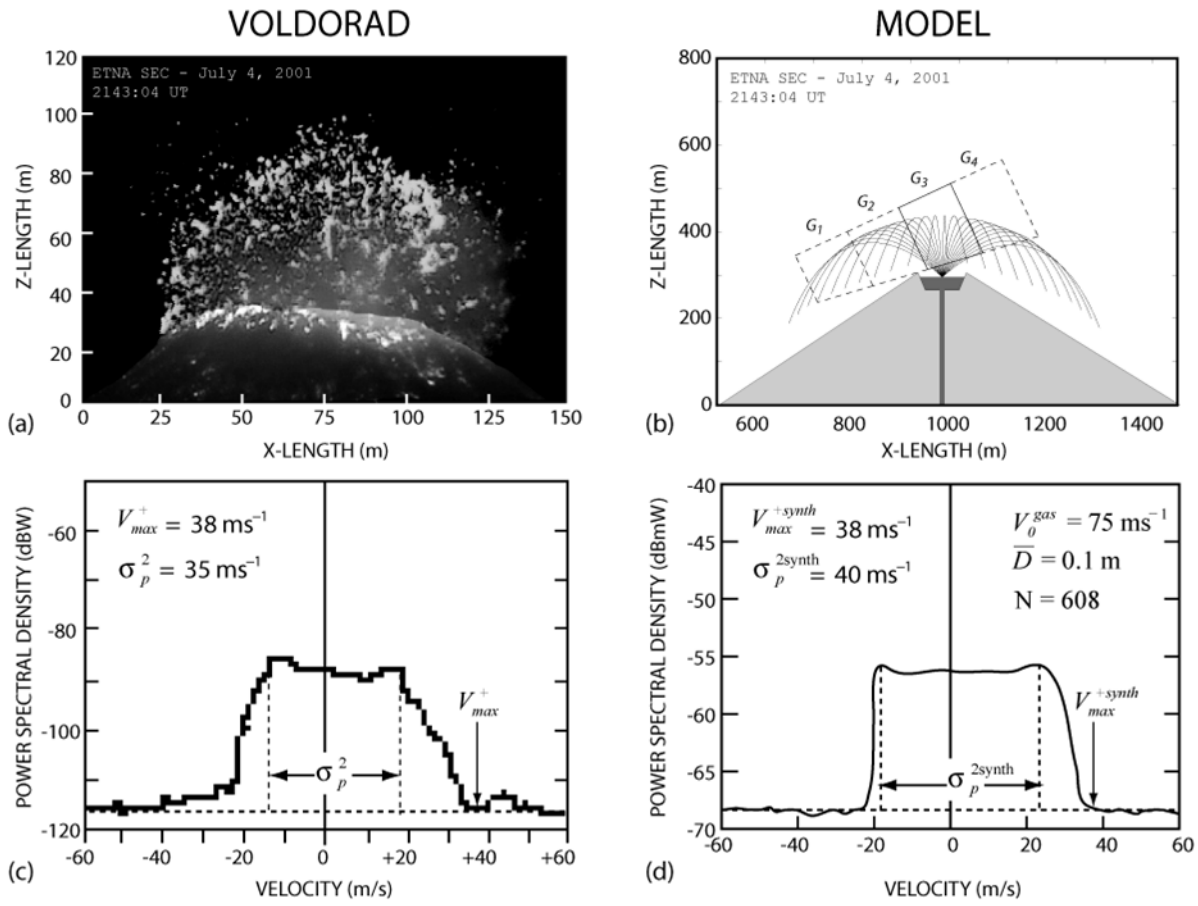

Figure V.12. (a) Video snapshot of the explosion occurring at 2143:04 UT at Etna SEC during the eruption of July 4, 2001. (b) Visual representation of this explosion modelled from the ballistic model. (c) VOLDORAD Doppler spectra recorded at 2143:04 UT; note that ground-echoes have been removed. (d) Corresponding synthetic Doppler spectra modelled from both ballistic and electromagnetic scattering models. This example is related to the top-hat-shaped Doppler spectrum (see text for more details).

Previous photoballistic studies at Etna have shown for one explosion of the North-East Crater, in June 1969, that 50% of ejecta have a size between 0.1 m and 0.4 m (McGetchin et al., 1974). Ground deposits studies have also pointed out similar sizes of scoria blocks produced by Strombolian activity at Etna on July 25-31, 2001 (Metrich et al., 2004). Modelling of acoustic waves at Etna have provided a characteristic thickness of the magmatic film

overlying the gas bubble right before its rupture, assumed to be on the order of the average size of the blocks formed thereafter of about 0.1 m (Vergniolle and Ripepe, 2008).

These constraints on the particle sizes at Etna led us to run our model on this explosion (Figure V.13a) with a load of single-sized particles of diameter D=0.1m (monodisperse PSD) ejected (Figure V.13b) over a wide range of angles (-45°<ϕ<45°) covering the whole gate G_3, with an isotropic distribution (isotropic poly-angles EAD). Note that this kind of event is not the most common, occurring mainly during the paroxysmal phase when the magma level in the conduit is high and partly fills the crater cavity.

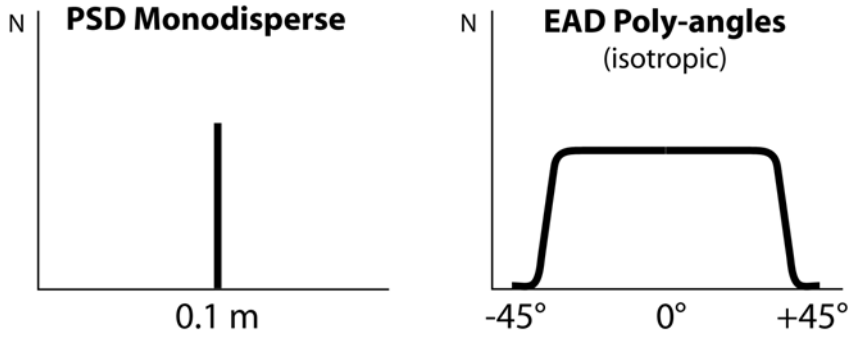

Figure V.13. Input characteristics for the modelling of explosion at 2143:04 UT. (a) PSD following a monodisperse distribution (D=0.1m) and (b) EAD following an isotropic poly-angles distribution ranging from -45° to+45° an centred vertically.

We have successfully reproduced in figure V.12d a top-hat shaped Doppler spectrum with a large plateau, with a spectral width slightly superior (σ_p^{2synth} = 40 m/s) and a slope somewhat steeper, but, most importantly, with an equivalent maximum radial velocity ($V_{\max}^{+synth}$ =38 m/s). Note that we did not aim at reproducing real power values, although this could easily be achieved by increasing the number of particles, because the computing time would be too long. This however by no way interferes with quantitative results related to geometrical or velocimetric parameters. This result confirms that the top-hat Doppler spectrum is therefore typically representative of an isotropic distribution of ejecta emitted mainly radially from the source vent.

Rigorously, the spectral width of the plateau directly corresponds to a range of ejection angles bearing a similar amount of ejecta, i.e. the isotropic part of the jet. For a spectral width plateau

of about σ_p^2 = 35 m/s, we deduce an isotropic ejection cone about 90° wide (-45° to +45°), spreading entirely over the radar range gate G_3. The resulting initial gas velocity found with a single-sized class of particles of diameter 0.1 m is about V_0^g = 75 m/s. On the other hand, the slope of the observed Doppler spectrum is not strictly vertical, unlike the synthetic spectrum. The likely explanation is twofold: (1) the particle size distribution is more likely polydisperse to some extent, including particularly additional smaller particles that contribute to a weak amount of power over the full spectrum. This effect is overprinted by the large amount of power backscattered by large blocks within their characteristic range of radial velocities (plateau) and, as small particles are entrained faster, can only be seen on the outer part of this range, leading to the non-vertical slope of the spectrum. (2) The concentration of ejecta (distribution of ejection angles or of amount of particles) might depart from purely isotropic at high angles, with less particles emitted laterally. This depletion of ejecta is commonly observed on the sides of other jet types and this might also occur to some extent for large bubble outbursts and contribute to non-vertical slopes of the spectra. Both effects are most likely at work, even though they are not preponderant in the generation mechanism of top-hat Doppler spectra.

V.5.2. Triangular-shaped spectra

We have also modelled a second type of explosion that occurred on July 4, 2001 at 2139:34 UT (Figure V.14). This brief Strombolian explosion (emission time interval ≈ 2 s) is typical of a dense Strombolian jet, caused by the bursting of an overpressurized bubble at the top of the magma column. In this case, the magma column is lower in the conduit, and probably does not fill the crater. The bubble bursting then occurs under the crater rim level within a more confined space, and partially constrained vertically by the crater walls or the conduit.

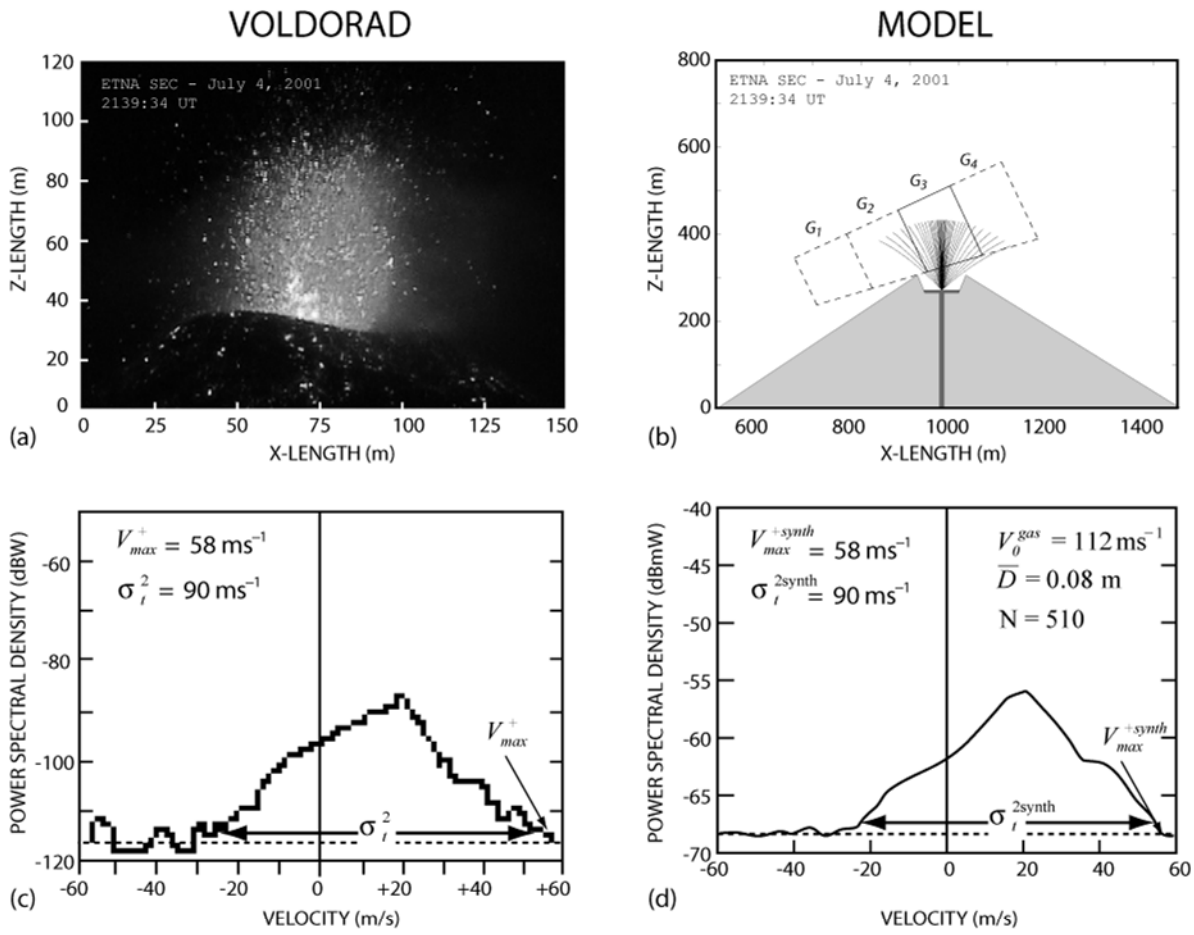

Figure V.14. (a) Video snapshot of the explosion occurring at 2139:34 UT at Etna SEC during the eruption of July 4, 2001. (b) Visual representation of this explosion modelled from the ballistic model. (c) VOLDORAD Doppler spectra recorded at 2139:34 UT; note that ground-echoes have been removed. (d) Corresponding synthetic Doppler spectra modelled from both ballistic and electromagnetic scattering models. This example is related to the triangular-shaped Doppler spectrum (see text for more details).

The video analysis reveals that the jet is mainly vertical, with a higher concentration of particles in the inner core, as indicated by the higher intensity of light scattered. The mean size of ejecta seems also smaller than that of the explosion at 2143:04 UT. From these observations we assume here again a monodisperse PSD, with diameter D=0.08 m and an anisotropic EAD, having a maximum concentration along the vertical axis (ϕ=0) and decreasing sideways.

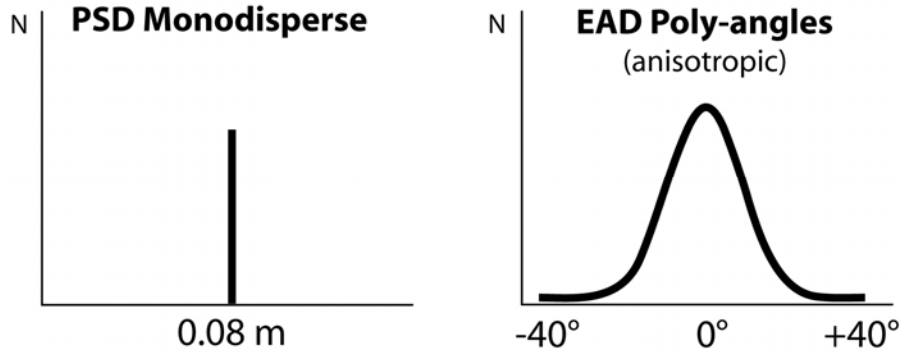

Figure V.15. Input characteristics for the modelling of explosion at 2139:34 UT. (a) PSD following a monodisperse distribution (D=0.08m) and (b) EAD following an anisotropic poly-angles distribution ranging from -40° to+40° an centred vertically.

The recorded triangular-shaped Doppler spectrum is representative of many Strombolian lava jets, and differs from a top-hat spectrum in that it does not have any plateau component. It only comprises two non-vertical slopes, generally straight but sometimes slightly concave in its right part (v>0), with a single power maximum at V_{MOD}. In this example, $V_{MOD} \approx$ 20 m/s and the right slope reaches the noise level at $V_{\max}^{+}$=58 m/s, and the total spectral width is found to be σ_t^2=90 m/s (or 116 m/s if calculated as $2\times V_{\max}^{+}$). Using the input parameters summarized in Table V.1, and ignoring possible effects of a polydisperse particle size distribution, the triangular-shaped Doppler spectrum can nevertheless be satisfactorily reproduced. We obtain the same values of synthetic maximum radial velocities ($V_{\max}^{+synth}$=58 m/s) and total spectral width ($\sigma_t^{2\,synth}$=90 m/s).

We are thus able to give an interpretation of such triangular-shaped Doppler spectra, in terms of parameters controlling the geometrical features of Strombolian lava jets. In the case of explosion occurring at 2139:34 UT, we find that the particle concentration profile must be strongly anisotropic (taken here as Gaussian) to account for the observed spectrum. We have calculated that about 80% of the total amount of particle are ejected within a dispersion cone 20° wide centred on the vertical axis, the remaining 20% being distributed between this inner cone and the limit of the range of ejection angles (from -40° to -10° and from +40° to +10°). The important depletion of particles on the sides of the jet, i.e. at high ejection angles, explains the slanted slope of the triangular Doppler spectrum.

Note that the explosion gives most of the signal in the right positive part of the Doppler spectrum as V_{MOD} = +20 m/s. This result is characteristic of a lava-jet explosion ejected mainly vertically, and confirms that information on the jet inclination can be retrieved directly from Doppler spectra. Finally, we obtain an initial gas velocity for this explosion of V_0^g = 112 m/s.

Table V.1. Input parameters of the forward model for explosion 1 (21h43:04 UT) and 2 (2139:34 UT).

	V_0^g	PSD		EAD	
		Particles	monodisperse	Range	Inclination
Explosion 1	75 m/s	N=608	0.1 m	Isotropic: -45° to +45°	0°
Explosion 2	112 m/s	N = 510	0.08 m	Anisotropic: -40° to +40°	0°

V.6. Statistical analysis of geometrical features for a large number of characteristic Strombolian explosions

The detailed analysis of two particular Strombolian explosions has pointed out the close relationships between the Doppler spectrum shape and the geometry of the volcanic jet. We have shown particularly that under the assumption of a monodisperse PSD, we are able to retrieve the concentration of particles along the angular profile. Therefore, some quantitative estimates of geometrical parameters are given in this section for more than 200 Strombolian explosions.

V.6.1. Relationship between radial velocity and ejection angle

In order to provide statistical results on a large number of events relatively quickly, we have constructed abacus (Figure V.16) so as to retrieve the aperture of the dispersion from the measured radial velocity range.

Figure V.16a shows the relation between radial velocities and ejection angles for different values of initial gas velocities ranging from 60 to 160 m/s, and for a constant particle diameter taken as D = 0.1 m, as defined previously as the best average value. We observe that the variability between each curve is relatively important, however, bearing in mind the initial gas velocity values obtained from both explosions studied previously (75 and 112 m/s), we choose an average value of V_0^g=100 m/s as reference initial gas velocity. Note that for a vertical ejection angle, as it is the case for most of particles ejected within lava-jet explosions,

we obtain a low radial velocity of 12 m/s. Moreover we notice that a radial velocity of 0 m/s is measured for an ejection angle of -18.5° from the vertical, i.e., perpendicular to the lower boundary axis of the antenna beam.

Inversely, figure V.16b shows the relation between radial velocities and ejection angles for different diameters ranging from 0.01 to 0.2 m, and for a constant initial radial velocity taken as V_0^g=100 m/s, as defined for the reference value. The variability is lower in this case, and the choice of the reference diameter looks less critical. Therefore, we select an average value of D = 0.1 m as reference diameter, for the reasons mentioned in section V.5. In the following, we thus take into account for the statistical analysis, values relative to the curve with D = 0.1 m and V_0^g = 100 m/s.

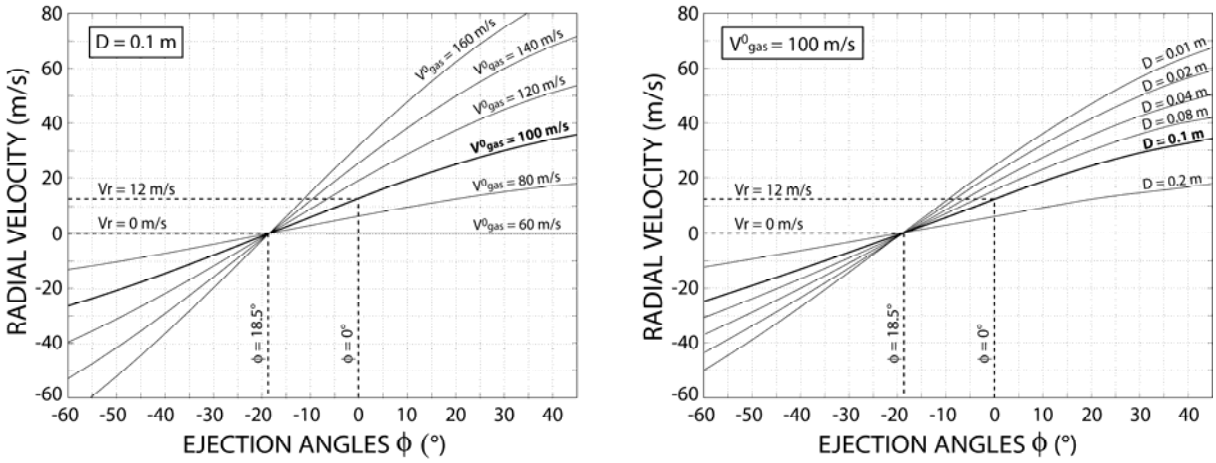

Figure V.16. Abacus showing the relationship between the radial velocity and the particles ejection angle (a) for different initial gas velocities and constant diameter (D=0.1m) and (b) for different diameters and constant initial gas velocity (100 m/s).

V.6.2. Statistical analysis of isotropic distributions

In this study, we carried out measurements on about 200 explosions that took place between 21:00 U.T. and 21:45 U.T. during the paroxysmal phase of the eruption of July 4, 2001 at Etna SE Crater. The detailed analysis of the explosion at 2143:04 UT has pointed particularly the close relationships between the plateau spectral width (σ_p^2) and the geometry of the volcanic jet. The statistical analysis of Doppler spectra, once the ground echoes have been removed, gives only 8% of explosions with a typical top-hat-shaped spectrum, comprising a large plateau bordered by sub-vertical slopes. Then 34% of Strombolian events have a purely

triangular-shaped spectrum (without plateau) and are thus characterised by a single power maximum. The majority (58%) of the explosions studied have a spectrum shape intermediate between both end-members described above. They are characterised by a plateau bordered by non-vertical slopes.

We show in figure V.17 the proportion of Strombolian explosions as a function of the range of ejection angles with similar amount of ejecta (isotropic dispersion cone), as measured from the plateau spectral width from explosions having purely or intermediate top-hat-shaped spectra. They represent 66% of the total of explosions studied. We show that 70% of these top-hat-shaped spectra (i.e. 45% of the total jet) present an isotropic distribution of ejecta within a cone $\phi_w \leq 35°$ wide. Then, 90% (i.e. 60% of the total jet) present an isotropic distribution of ejecta within a cone $\phi_w \leq 50°$ wide. Finally, only 10% (i.e. 7% of the total jet) of top-hat-shaped spectra have an isotropic distribution $\phi_w \geq 50°$.

These results show the variability of geometrical features of Strombolian jets within a one hour time scale, and hence the variation of the physical source conditions at the origin of their formation. We observed particularly an augmentation of top-hat-shaped Doppler spectrum events between 21h30 U.T. and 21h45 U.T., which corresponds unsurprisingly to the moment where the magma column was the highest and partly filled the crater. One can suppose that, in this configuration, overpressurized bubbles reaching the top of the magma column could expand more easily in the large magma-filled crater and then burst without physical constraints from the crater or conduit boundaries, leading to the quite hemispherical ejection of pyroclasts often seen over the crater rim.
At the opposite, when the level of the magma column is lower, gas slugs burst out deeper in the conduit, promoting vertical rather than lateral gas expansion near the surface, thus limiting the ejection of lava fragments sideways. The lava drainage is then mainly vertical, leading to narrower oriented Strombolian jets. These results are consistent with deductions from previous photoballistic studies at Etna North-East Crater. McGetchin et al. (1974) showed for one explosion that the ejection angles are distributed uniformly (i.e., isotropic) within a dispersion cone 30° wide.
We find for 50% of the total of explosions studies, representing more than 100 Strombolian explosions, that ejection angles are distributed uniformly within a dispersion cone of about $\phi_w = 40°$ wide in average. The fact that similar results were reached by totally independent

methods and on different Strombolian eruptions suggests that 30-40° might be a statistically representative value for the isotropic ejection cone of lava jets, at least at Etna. Note that particles are also present outside this cone, although at concentrations decreasing sideways.

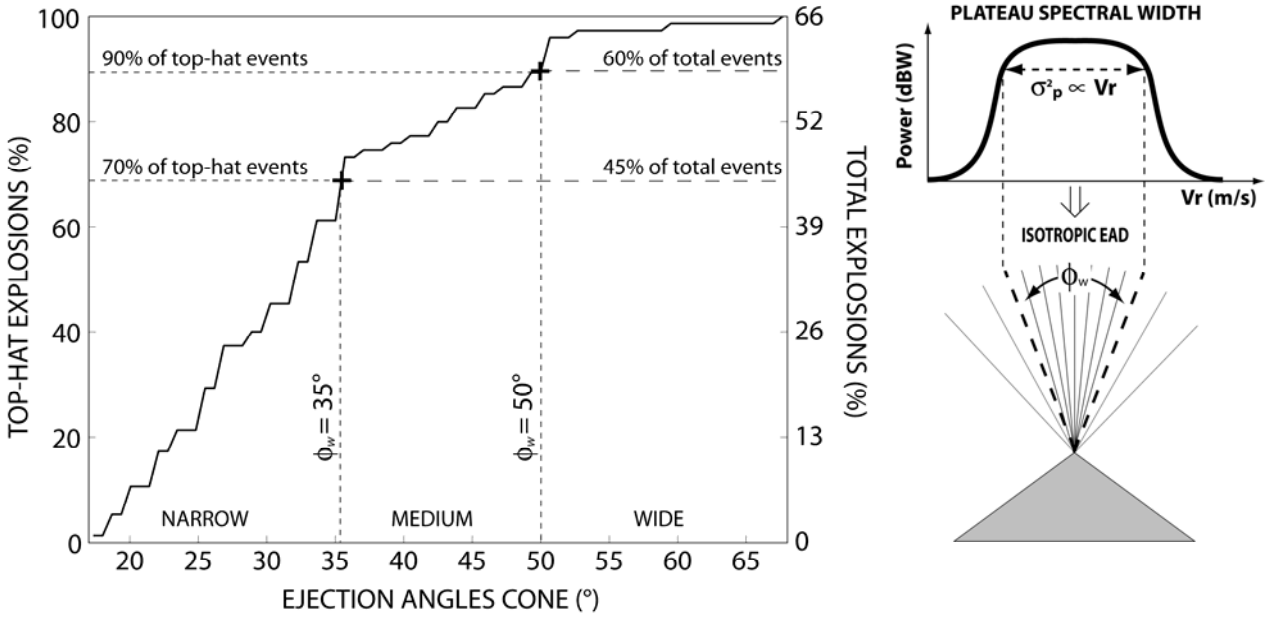

Figure V.17. (a) Plot showing the proportion of top-hat and total Strombolian explosions as a function of the range of ejection angles with similar amount of ejecta (see text fore more details). (b) Sketch showing the conceptual correspondence between the plateau spectral width and the isotropic dispersion cone.

V.6.3. Ejecta concentration inside the dispersion cone

In this section, we examine the proportion of particles inside the jet for all explosions studied. Remind that the power backscattered by particles is related to the number (N) of particles crossing the radar beam and their diameter (D) to a certain power *x* ($P \propto ND^x$) that depends on the scattering domain (Rayleigh or Mie). Keeping our assumption that the ejecta sizes can be represented by a unique diameter (monodisperse PSD), the backscattered power recorded by VOLDORAD can be used advantageously to retrieve a relative concentration estimate of single-sized particles within the ejection angle profile. We focused in what follows, on the concentration of particles comprised within a dispersion cone of ϕ_w=35° wide, because it is a reference aperture angle of typical Strombolian explosions as shown previously.

Figure V.18 shows that 50% of all Strombolian explosions studied (i.e., representative of the typical Strombolian explosion) are found to have ≥83% of the particle load within a dispersion cone 35° wide, whereas only 20% of all Strombolian explosions have over 90% of the total particle load within an ejection cone 35° wide. Comparatively, a photoballistic study carried out on one explosion at Stromboli in September 1971 [*Chouet at al*., 1974] has shown that 90% of the total of particle load was ejected within a dispersion core 37° wide. These values are also in agreement with the ones inferred from our Doppler spectra analysis, which illustrate that typical Strombolian explosions have most of their pyroclastic material (80–90 %) within a relatively narrow dispersion cone (30–40°).

Also, these results illustrate the variability of the Strombolian activity at Etna, which is related to the variation of physical source conditions. We speculate that the level of the magma column, and hence of the bubble bursting, is the predominant source of variability, although other mechanisms may play a role. For instance, the PSD is polydisperse in real jets and fragmentation conditions may also vary from one explosion to another, likely accounting for differences in particle size distribution and hence, on the dynamics of Strombolian jets.

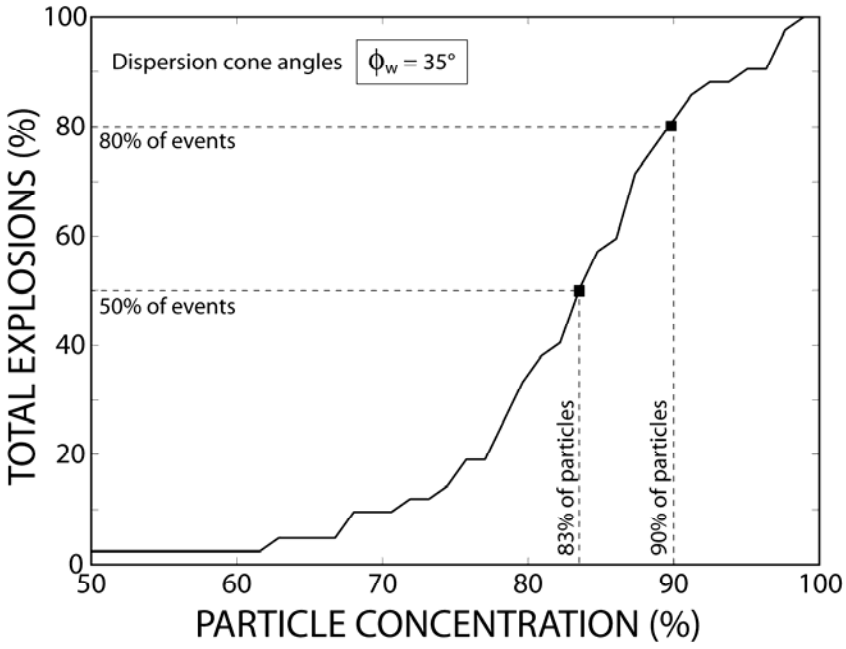

Figure V.18. Plot showing the proportion of particles inside the jet for a dispersion cone 35° wide, taking into account all explosions studied.

V.7. Discussion

This study has provided some interesting geometrical features on typical Strombolian jets. Particularly, we point out two distinct signatures: Top-hat-shaped Doppler spectrum related to isotropic ejection angle distribution (EAD), and Triangular-shaped Doppler spectrum related to anisotropic ejection angle distribution. In addition we were able to give statistical quantitative information on geometrical features carried out on a large number of typical Strombolian explosions. Particularly we find that 30-40° might be a statistically representative value for the isotropic ejection cone of Strombolian lava jets, at least at Etna, and we search out that typical Strombolian explosions contain most of their ejecta (80–90%) within a relatively narrow dispersion cone (30–40°) centred vertically.

However some uncertainties remain, and assumptions included into the models can be discussed. For instance, the gas velocity decrease law included in ballistic model is poorly constrained. The decrease coefficient z_{ref} has been defined from video measurements (Chapter III) and taken as constant. The gas velocity decrease law could probably be better constrained from infrared measurements. In addition, bearing in mind the complexity of the scattering processes, the electromagnetic scattering model carries some simplifying assumptions: particularly, we assume particles to be compositionally homogeneous, spherical, and homogeneously distributed inside the sampling volume. Nevertheless, these effects are most likely balanced by the large statistical number of particles comprised in a range gate. Some problems may also arise from technical difficulties related to the radar, such as aliasing of the signal, or ground echo-power. However these questions can be easily avoided, or even treated from automatic procedures.

One of the most disputable points is related to the assumption formulated in the statistical analysis. Indeed, we have given geometrical results based on the theoretical relation between radial velocities and jet aperture angles; the one strongly depends on the initial gas velocity and the particle size. Because of the large (>200) number of explosions to analyse, calculations have been carried out using a mean initial gas velocity (100 m/s) and a mean diameter (0.1 m). We know that the initial gas velocity, especially, varies widely from one explosion to another, and hence could account for a small bias in the analysis of geometrical data.

In the same way, we point out that synthetic Doppler spectra do not reproduce the echo-power values given by VOLDORAD because the computing time would be too long. Note however that it could easily be achieved by increasing the number of particles to model.

SECOND PART

MULTI-METHOD APPROACH

RÉSUMÉ : DEUXIÈME PARTIE

Dans cette deuxième partie nous nous sommes intéressés à l'étude des mécanismes qui sont à l'origine de l'émission du matériel volcanique en surface. Comme on l'a vu précédemment, l'activité éruptive des volcans basaltiques est essentiellement de type Strombolien, au moins à l'Etna. Le mécanisme de ces éruptions est associé à la remontée de grandes poches de gaz qui se forment en profondeur par coalescence d'une mousse riche en bulles de gaz qui s'effondre sur elle-même de manière cyclique. Pendant sa remontée dans le conduit, la bulle de gaz surpressurisée (slug) se décomprime et grandit corrélativement jusqu'à son arrivée à la surface où la bulle se dilate en soulevant une fine épaisseur de magma qui se fragmente en blocs de lave pendant l'éclatement de la bulle, eux-mêmes éjectés par le relâchement du gaz surpressurisé.

Dans le chapitre 6, nous avons focalisé notre attention sur les tous derniers stades de l'ascension de la bulle : depuis sa rapide expansion au sommet de la colonne magmatique jusqu'à son éclatement. Nous avons réalisé ce travail à partir de données acoustiques et vidéo sur des explosions Stromboliennes se produisant pendant le paroxysme de l'éruption du 4 Juillet 2001 au cratère Sud-est de l'Etna. Depuis longtemps, des mesures acoustiques sont réalisées pour « écouter » les sons volcaniques. En fait, cette méthode permet d'obtenir de précieuses informations sur les mécanismes superficiels pouvant générer une surpression dans l'air (ex. vibration, éclatement, circulation de fluides, etc.) et donc souvent invisible par d'autres méthodes. Les mesures de pression acoustique enregistrées au cours d'une phase d'activité éruptive Strombolienne montrent l'émergence de pulses de pression pouvant atteindre 100 Pa à près de 1 km de la source volcanique. L'origine précise de ces pulses de pression et les mécanismes associés restent difficiles à comprendre et rarement documentés par des observations directes.

Pendant le paroxysme de l'éruption du 4 Juillet, le niveau de magma était monté suffisamment haut pour remplir en partie la cavité du cratère Sud-est et permettre aux larges bulles de gaz de se développer à la surface de la colonne magmatique, puis de gonfler au delà des bordures du cratère, et ainsi d'être visibles sur les enregistrements vidéo. Ainsi, les données vidéo ont permis l'analyse de l'évolution de 4 grandes bulles avant, pendant, et après éclatement. En particulier, nous avons travaillé sur l'évolution du rayon de la bulle, ce qui nous a permis de calculer des formes d'ondes théoriques de pression acoustique (c.à.d. les pulses de pression) à partir des données d'observations, afin de les comparer avec les formes

d'ondes acoustiques enregistrées par le capteur de pression. Puis, cette analyse nous a permis d'observer les mécanismes associés à la rupture de la membrane de magma qui enveloppe la bulle. Finalement, cette étude vidéo a été utilisée pour contraindre, grâce à des mesures dérivées d'observations directes, les mécanismes de génération du son volcanique.

Nous avons montré à partir de ces corrélations que l'oscillation d'une bulle surpressurisée à la surface de la colonne magmatique est bien le mécanisme principal à l'origine du son enregistré par le capteur acoustique pendant une éruption Strombolienne. Enfin, nous avons montré que le mécanisme de rupture de la membrane magmatique est initié par le développement d'instabilités à l'interface bulle-magma. Suite à ces résultats, nous avons pu utiliser un modèle de vibration de bulle théorique qui nous permet, par ajustement de la forme d'onde synthétique avec la forme d'onde enregistrée, d'obtenir des paramètres physiques quantitatifs sur la source sonore : la bulle. Ainsi, nous avons obtenu une estimation quantitative moyenne de la surpression initiale de la bulle, c'est à dire lors de son arrivée à la surface, de $\Delta P = 0.36$ MPa. Puis nous donnons une estimation moyenne de la pression et du volume de la bulle juste avant éclatement : $P_g = 0.23$ MPa and $V_g = 1.6\times10^3$ m^3 respectivement.

Dans le chapitre 7, on s'est intéressé aux corrélations entre les méthodes acoustique et radar. Cette comparaison est intéressante car l'acoustique nous délivre des informations sur les mécanismes (vibration et éclatement de bulles) à l'origine des phénomènes de surface enregistrés par le radar (éjection du gaz et des pyroclasts).

Tout d'abord nous avons pu montrer une bonne corrélation temporelle entre les signaux de pression acoustique et de vitesse radiale, aussi bien de pic à pic que sur de longues périodes d'activité éruptive. Cette corrélation n'est pas étonnante compte-tenu de la relation qu'il existe entre les deux mécanismes étudiés. Cette corrélation est confirmée par des mesures de pression acoustique et de vitesses radiales de particules effectuées sur plus de 80 explosions Stromboliennes. En effet, on montre qu'il existe une relation de puissance du second degré entre ces deux paramètres. Enfin, des estimations de vitesses initiales de gaz on pu être réalisées à partir du calcul de la puissance acoustique, que l'on a comparé avec les vitesses de gaz initiales calculées avec le radar. On a obtenu des valeurs d'environ 40 à 50 m/s à partir des mesures acoustiques, contre des valeurs plus de deux fois plus élevées, allant de 95 à 118 m/s, à partir des mesures radar.

CHAPTER VI

Acoustic-video correlations: the last steps of a Strombolian bubble approaching the top of the magma column

VI.1. Introduction

Basaltic volcanoes activity is typically characterized by periodic fire fountains (Hawaiian activity) or discrete explosions (Strombolian activity). Both eruptive mechanisms are driven by large gas pockets formed at depth by the coalescence of a foam layer collapsing cyclically at the roof of the magma chamber (Jaupart and Vergniolle, 1988, 1989). For very fluid magma, the foam layer totally collapses leading to a phase that develops into annular flow and produces fire fountains at the surface. For more viscous magma, only a portion of the foam layer collapses leading to a phase that develops into slug flow and produces Strombolian explosions at the surface. The similarity between these large bubbles and fire fountaining episodes, added to the continuous transition between both regimes, suggests that both have the same origin (Vergniolle and Ripepe, 2008). FTIR measurements have shown, particularly, that fire fountains at Etna (Italy) form at depth of about 1.5 km (Allard et al., 2005). Mount Etna, a volcano laboratory, turns out to be a first-rate candidate for our investigations. We worked on the July 4, 2001 episode that clearly shows a Strombolian activity at the summit of the Southeast crater (SEC) where large bubbles expand as they rise through the conduit until breaking at the surface of the magma column.

Acoustic measurements have long been carried out on volcanoes, and three main models have been developed for volcanic acoustic signals. The first class of acoustic models associates the frequency and amplitude of acoustic signals with resonant modes of the shallow volcanic conduit (Buckingham and Garcès, 1996; Garcès et al., 2000; Hagerty et al., 2000). The second class of acoustic models suggests that the sound is produced when the volcano is suddenly uncorked after reaching a critical pressure threshold (Uhira and Takeo, 1994; Johnson et al., 1998; Johnson and Lees, 2000). In contrast, the third class of acoustic models interprets the radiated sound mainly to the strong vibration of a large bubble expanding at the surface of the magma column prior to bursting (Vergniolle and Brandeis, 1994, 1996; Vergniolle et al., 2004; Vergniolle and Ripepe, 2008).
Acoustic measurements are commonly used to constrain the radius and length of the bubble reaching the top of the magma column. Then, fundamental parameters such as overpressure and volume of the bubble before breaking can hence be estimated. Previous studies at Stromboli volcano (Italy) have been carried out with similar acoustic measurements, where characteristic values of bubble overpressure (≈ 0.1 MPa) and radius (≈ 1 m) were found. In

the present study, we provide quantitative estimates of similar parameters for a set of large bubbles bursting at the surface of the lava column at Etna SEC on July 4, 2001.
However, the main interest of this work is centred on the study of the processes developing prior and during the bubble breaking associated to the radiated sound waves, by using coupled acoustic and video measurements. Although the video can provide very strong constraints, visual observations of bubble rising above the crater rims are scarce. During the paroxysm of the July-4 eruption, we observe only 9 large bubbles and only four of them are really exploitable. Moreover, video snapshots analysis cannot give information prior the very last stage of bubble rise. In this study we provide quantitative estimates of physical parameters (radius, velocity, and acceleration of the bubble membrane) derived from the video analysis on four large bubbles. These measurements permit us to build video-derived acoustic waveforms, subsequently compared with recorded acoustic waveforms in order to better interpret the processes prior to the bubble breaking at the vent.

VI.2. Setting and material

After more than 8 months of minor activity (slow lava flows, degassing, light ash emission, and low-level Strombolian activity) at Etna volcano (Sicilia), a new episode of vigorous activity began on May 9, 2001. About fifteen eruptive episodes have been reported, occurring in average every 3-5 days, until the eruption turned to a major flank eruption on 17 July, 2001. We focus in this study on the activity at the Southeast crater and not to that of the flank eruption. Each eruptive episode before the flank eruption lasted a few hours, involving multiple Strombolian explosions and sometimes lava fountaining. The whole eruptive episode of July 4, 2001 lasts about 5 hours from 1800:00 UT to 2300:00 UT. At the beginning, explosions are infrequent, occurring only every few minutes, but after one hour, the activity becomes noisy and frequent, every several seconds. The paroxysm takes place during the third hour, between 2100:00 UT and 2200:00 UT, and provides close series of violent Strombolian explosions that punctually develop into quasi fire fountains activity. At the end of the paroxysm, the magma level increased, and then partly filled the crater cavity. Large bubble developing at the top of the magma column can thus be observed, and analyzed from video recording. Acoustic pressure was recorded for the whole duration of the July 4, 2001 eruptive episode (Vergniolle and Ripepe, 2008). The acoustic sensor, set at a distance of about 950 m from the vent, is an infrasonic microphone (Bruel Kjaer 4193) amplified by

Nexus (Bruel Kjaer), and has a wide frequency range, from 0.1 Hz to several kHz. Recording was performed on a digital acquisition station (Vibra4, Tad) at a sampling frequency of 1200 Hz and a dynamical range of 8 bits.

VI.3. Acoustic and video observations data

VI.3.1. Description of video data

Video data was acquired during the whole eruption of 4 July 2001 at Etna SEC and permits us a detailed analysis of the eruptive activity at the summit crater during 4 hours. The paroxysm of this eruption takes place between 2100:00 UT and 2200:00 UT, and the magma layer increased significantly in the crater, leading large bubbles to grow and expand over the crater rims. We thus were able to pick up a series of four large bubbles that can be easily observed from the video field of view (Figure VI.1). Most of these kinds of explosions appear between 2135:00 UT and 2145:00 UT, but we count no more than about 10 bubbles during the paroxysm period. It means that conditions that permit large bubble to form and expand over the crater rims are not commonly encountered. Bubbles shapes are mainly spherical but we are only able to observe the upper part of the rising bubble on video snapshots, as shown in Figure VI.1. Large bubbles can hence be divided into two half a sphere; the upper one (visible on video snapshots) moving freely in the surrounding air, and the lower one, immersed into the magmatic liquid, thus having a restricted displacement.

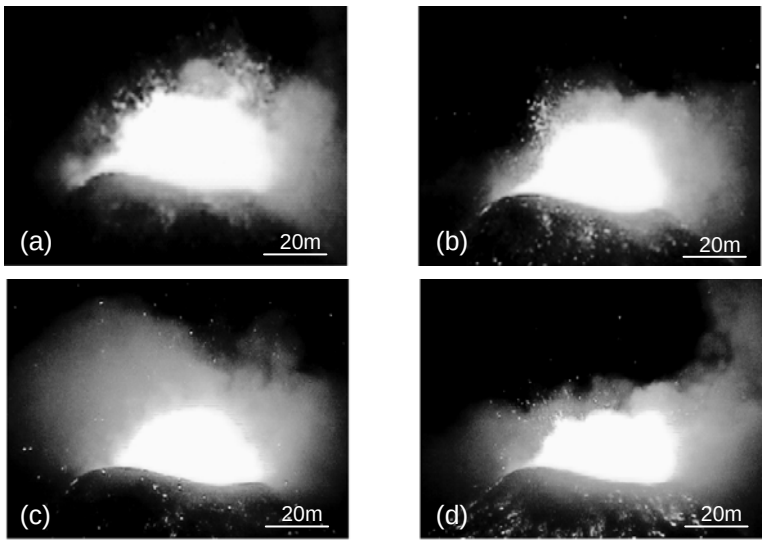

Figure VI.1. Video snapshots of four large bubbles occurring at Etna SEC during the eruption of July 4, 2001, at (a) 2135:35 UT,(b) 2138:10 UT, (c) 2142:32 UT, and (d) 2143:04 UT.

VI.3.1.1 Bubble radius measurement procedure

The video of each large bubble was broken up into a series of images at a sampling rate of 25 frames per second, which corresponds to one image every 0.04 s. This temporal resolution is satisfactory bearing in mind the characteristic time of the physical process at issue. Afterwards, bubble contours have been traced out by an automatic procedure every 0.04 s realised with Matlab software, by selecting a reference pixel value intensity that corresponds to the edge of the luminous bubble (Figure VI.2). Note that it was also cautiously checked from visual observation directly on video snapshots.

Nevertheless, some uncertainties can remain on such video analysis: (1) the scattering of light in the surrounding gas can interfere with the bubble edge limitation and hence induce a bias on the bubble radius measurements. (2) The scale factor of images is based on the crater diameter which is not accurately known, and a potential error on the absolute measurement of the bubble radius can also be assumed. (3) Finally, measurements realised from 2D field of view snapshots can also lead to an underestimation of radius values.

Figure VI.2 shows an example of the automatic procedure used for the calculation of bubble radius measurements. In this case we provide bubble contours at a time step of 0.2 s for the explosion occurring at 2142:32 UT. The radius can hence be calculated at each time step (0.04 s in reality) from the displacement of each successive contour. The real spatial scale is recovered from the width of the crater from rim to rim. Note that this scale factor is not accurately known and may also induce an additional bias in the radius calculations.

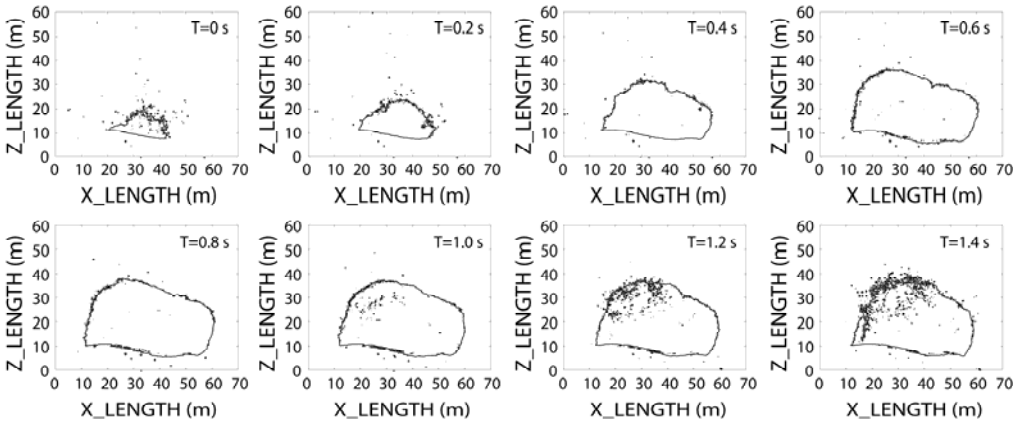

Figure VI.2. Plot of bubble contours from the automatic procedure, for the explosion occurring at 2143:32 UT at Etna SEC on July 4, 2001. Contours are traced out at a time step of 0.2 s in this example. Radius values of expanding bubbles are estimated from the cumulative distance measurement between each contour at each time step (i.e., 0.04 s in reality).

In reality bubbles are not purely hemispherical, therefore, the radius estimate depends on the profile considered, i.e., the direction in which radius measurements are carried out. We give in Figure VI.3 radius measurements realised from three different profiles: vertical, horizontal-right and horizontal-left, for the bubble occurring at 2142:32 UT, with a sampling rate of 25 Hz (i.e., with a time step of 0.04 s). The main trend is conserved for the three profiles but some significant discrepancies also occur more locally. This result stresses first the heterogeneity of bubbles growths, and point out that further results based on radius measurements may also depend on the profile chosen. In what follows, each profile has been systematically measured for the four large bubbles studied in order to check potential unexpected discrepancies. We finally choose the vertical profiles as reference for radius measurements.

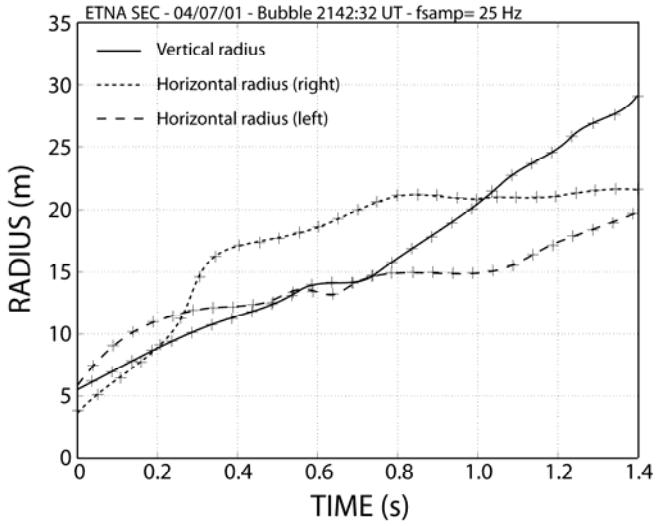

Figure VI.3. Time series of radius measurements given for 3 profiles (vertical, right, and left) from video snapshot analysis of bubble at 2142:32 UT acquired at a sampling rate of 25 Hz.

VI.3.1.2 Instabilities on the magma-air interface

The detailed analysis of this large bubble on video snapshots has pointed out the very existence of instabilities occurring at the surface bubble.

Importantly, the area between bubble and air can be described as the sequence of interfaces: (1) the first one to be considered is the interface between the bubble and the overlying magma layer, (2) the second one is the interface between the magma layer and the air. In the case of a plane surface, an interface is stable only when the acceleration ($\ddot{R}$) is directed from the liquid (L) to the gas phase (G_i), therefore the sign of the acceleration is determining (Figure VI.4). When the acceleration is positive ($\ddot{R}>0$) the bubble-magma interface (G_1 to L) is unstable

whereas the magma-air interface (L to G_2) is stable. This is the opposite when the acceleration of the magma layer is negative ($\ddot{R}$ <0).

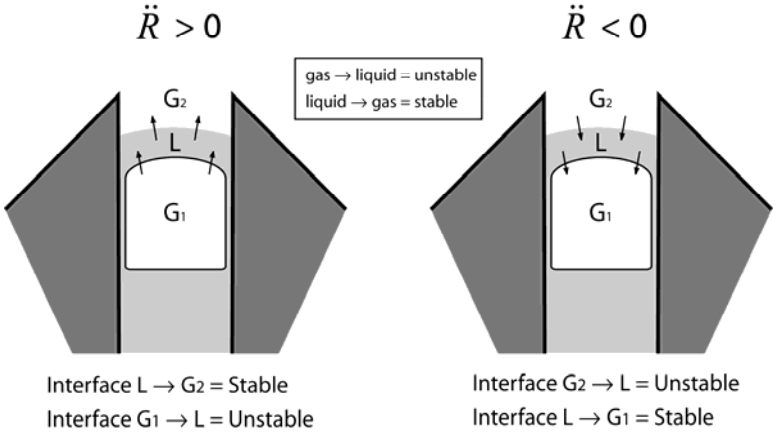

Figure VI.4. Sketches showing the development of instabilities on bubble-magma and magma-air interfaces as a function of the sign of the bubble membrane acceleration

Note that from visual observation, we only access to information on the magma-air interface. At the beginning of the bubble expansion (Figure VI.5a), we clearly observe an unstable magma-air interface that looks rippled showing successive crests and dents. A few tenths of second later (Figure VI.5b), the bubble has largely expanded over the crater rims, and shows a very stable and smooth magma-air interface. This first order qualitative observation is fundamental because it illustrates almost certainly that the bubble oscillates.

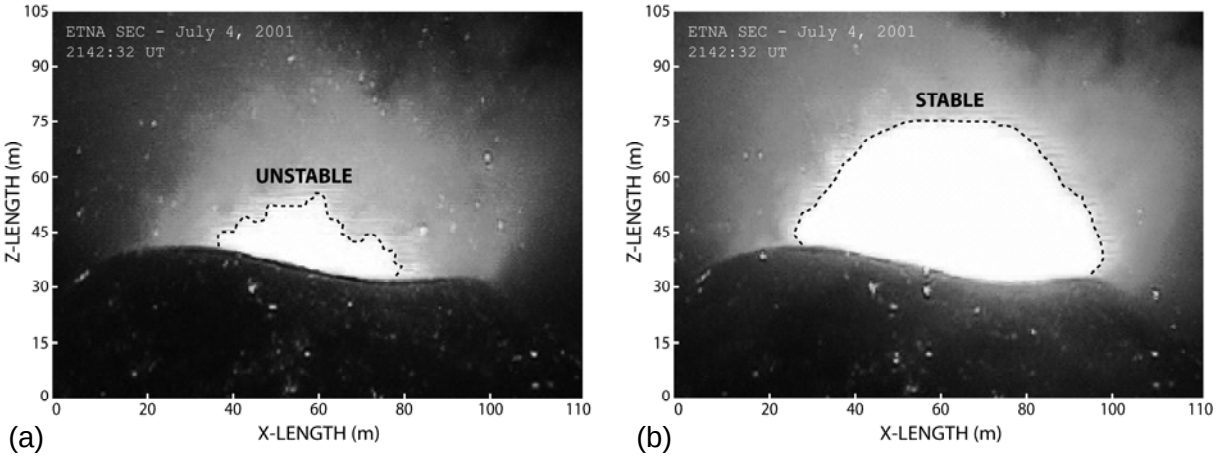

Figure VI.5. Video snapshot of the bubble at 2142:32 UT showing the development of (a) instabilities on the visible magma-air interface occurring at beginning of the bubble expansion, and (b) vanishing of these instabilities that leads to a stable magma-air interface.

VI.3.1.3. Bubble vibration mode

The deformation of interfaces does not occur arbitrarily of course, then the thorough analysis of instabilities may bring important constraints on the bubble behaviour, and hence on the origin of sound radiated. We show particularly (Figure VI.6) on bubble at 2143:04 UT, the long-range deformation of the magma-air interface, which corresponds to vibration mode equal to 3 on half a sphere, it means an even vibration mode of 6 on the whole sphere.

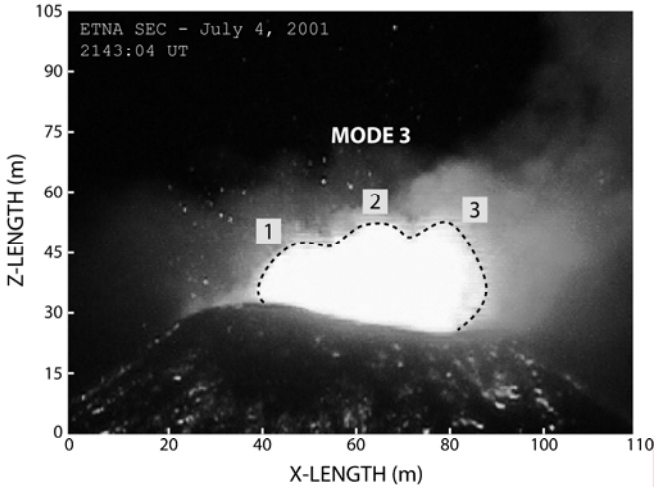

Figure VI.6. Video snapshot of the bubble at 2143:04 UT prior to bursting, and showing a long-range deformation that reveals a bubble vibration mode of order 3 on half sphere.

VI.3.1.4. Magmatic film rupture

Figure VI.7 shows the breaking mechanism of the magmatic film occurring on bubble at 2142:32 UT, after about one second of expansion above the crater rim. The initiation of rupture looks relatively localized on the top left side of the bubble. Sideways, the magma-air interface appears not very deformed, which suggests that it is not involved into the membrane rupture. At this stage, we suppose that the bubble-magma interface should be highly distorted and hence may be responsible for the membrane rupture. Immediately after the localized rupture, the bubble punctures all over the membrane, leading to the fragmentation of the overlying magmatic film into relatively large disconnected blocks subsequently propelled radially.

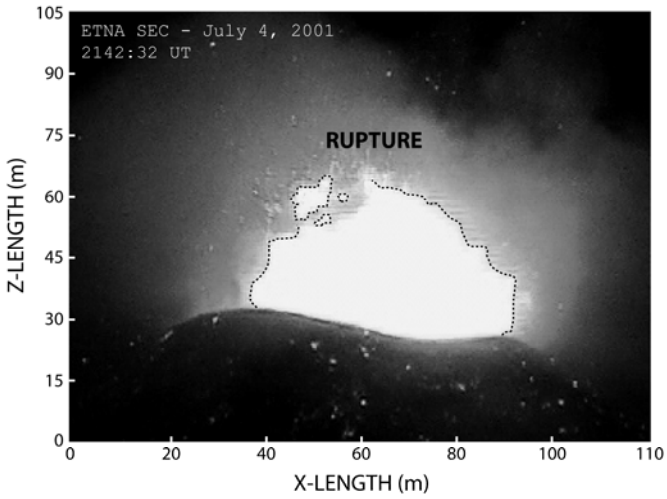

Figure VI.7. Video snapshot of the bubble at 2142:32 UT showing the magma-layer rupture locally punctured by instabilities developing most likely at the bubble-magma interface.

This preliminary analysis of video snapshots has permitted to shed light on crucial processes related to bubble expansion and bursting. Particularly, the existence of instabilities developing and vanishing at the magma-air interface strongly suggests that oscillations of such bubbles can be at the origin of sound radiated in the surrounding air.

VI.3.2. Description of acoustic data

Acoustic pressure was successfully recorded during the four hours of intense activity at Mount Etna SEC on July 4, 2001. The acoustic pressure signal shows a series of pulses, whose intensity is variable and can reach a maximum of 100 Pa. The occurrence of these pulses fairly changes in time, but the average interpulse duration is typically around a few seconds. The occurrence and intensity of explosions increase during the third hour of recording (2100:00 UT and 2200:00 UT). Note that Strombolian explosions at Etna have a waveform very similar to explosions at Stromboli and Shishaldin volcanoes. In this section we just aim at describing some basic features (amplitudes and frequencies) of acoustic signals generated by Strombolian explosions.

VI.3.2.1 Acoustic waveforms of typical Strombolian explosions

Acoustic measurements were realised at Etna Southeast Crater (SEC) during the eruption of July 2001, where the recorded acoustic pressure variations clearly show the existence of an oscillating source. The Strombolian activity at Mount Etna consists of a series of explosions caused by the breaking of large and overpressurized bubbles at the surface of the magma column. The spectral content analysis has pointed out that the whole explosion process, typically about 20 seconds from the bubble generation at depth to its bursting at the surface, is characterized by 3 different parts with particular frequencies which are related to specific mechanisms.

We show in Figure VI.8 the acoustic pressure signal recorded during the explosion occurring at 2135:35 UT lasting about 20 s. We point out three distinct parts showing very different acoustic features. (1) In the first part, lasting about 8 s, we observe three similar waveforms peaking at an acoustic pressure < 20 Pa. The duration of each event is short and fairly constant around 0.7 s, (equivalent frequency is ~1.4 Hz), but the time interval between each acoustic peak of the precursory part can be much more longer and may widely vary from about 2 to 4 s in this case (equivalent frequency is ~0.5 – 0.25 Hz) . The second part shows a single waveform with a high compressive component (positive peak) and a rarefaction component (negative peak) reaching in both cases an acoustic pressure of about ±100 Pa. A slight second positive peak can be observed but with very low acoustic pressure (~ 20 Pa). The total duration of this acoustic waveform is about 0.9 s, which corresponds to an equivalent frequency of 1.1 Hz. Finally, we can observe in part three, an acoustic waveform occurring about 8 s after the acoustic main pulse peaking at 30 Pa for the positive component and -40 Pa for the negative one. This event is typically low frequency (0.6 Hz), lasting about 1.7 s. Acoustic waveforms of the first part are assumed to be related to gravity waves generated at the surface of the magma column by a deeply rooted oscillating source. The main acoustic pulse meet in the second part is thought to be due to the vibration of large bubble reaching the magma-air interface. The third part, rather uncommon on acoustic signals, may be due to the gravity waves that develop at the bottom of the bubble. These interpretations are deeply discusses in section VI.4.1.

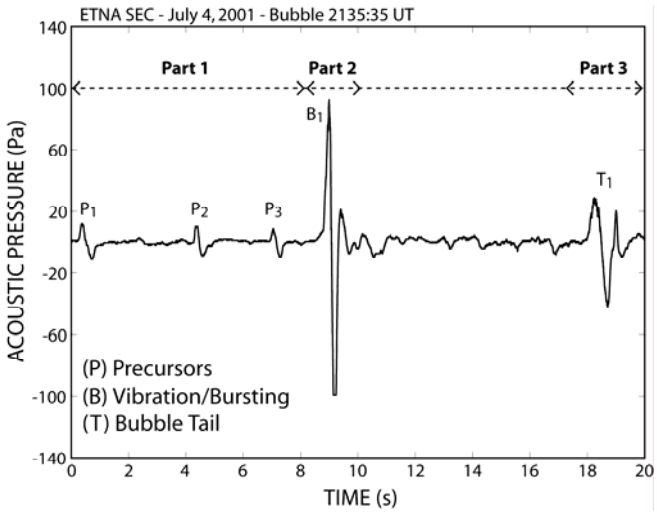

Figure VI.8. Acoustic pressure signal recorded at Etna SEC on July 4, 2001 on bubble at 2135:35 UT. We show three different parts corresponding to (part 1) precursors, (part 2) bubble vibration/bursting and (part 3) bubble tail.

VI.3.2.2. Detailed analysis on 9 large bubbles

We picked up a series of 9 large overpressurized bubbles during the paroxysm. We focused the spectral analysis on the main acoustic pulse (part 2, Figure VI.9) and its related precursors (part 1, Figure VI.10). Each bubble has in average two to four precursory waveforms that lead to about 30 values for the spectral content analysis of precursor events.

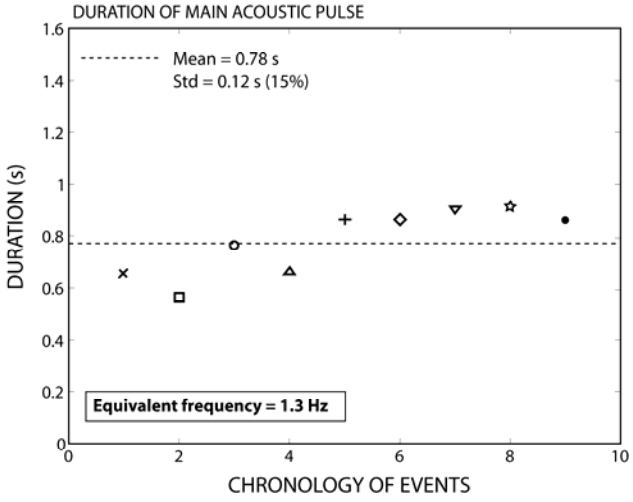

Figure VI.9. Characteristic duration and equivalent frequency of the acoustic main pulse for 9 large bubbles during the eruption of July 4, 2001 at Etna SEC, giving in average 1.3 Hz.

The characteristic duration of the acoustic main pulse (Figure VI.9) is found to be about 0.78 s that corresponds to an equivalent frequency of 1.3 Hz. The dispersion of duration data is relatively low, as we find a standard deviation of 0.12 s, i.e., a variability of about 15 % of the mean duration value.

We first characterize (Figure VI.10a) the duration between each acoustic peak of waveforms arising in part 2, which could correspond to a cyclic mechanism. We thus found a characteristic duration of about 1.83 s that corresponds to an equivalent frequency of ≈ 0.55 Hz. The dispersion of these duration data is higher for case of gravity waves with a standard deviation of 0.39 s, i.e., a variability of about 21% of the mean duration value.
Finally, the characteristic duration of precursor events (Figure VI.10b) is about 0.65 s that corresponds to an equivalent frequency of 1.54 Hz. The dispersion is larger, with a standard deviation of 0.16 s, i.e., a variability of about 24% of the mean duration.

The dispersion of the durations (or equivalent frequencies) of acoustic waveforms measured on recorded signal is most likely the result of natural variability of physical mechanisms at work. However, we note a significant difference between the variability of data of part 1 and 2. We suppose that the deeply rooted source of oscillations related to surface gravity waves in part 1, may also account for a larger dispersion. Indeed, first the recorded signal is lower (<20Pa), and the oscillation occurring at depth and transmitted to the surface is probably affected by additional processes leading to a larger variability in the signature of the source mechanism.

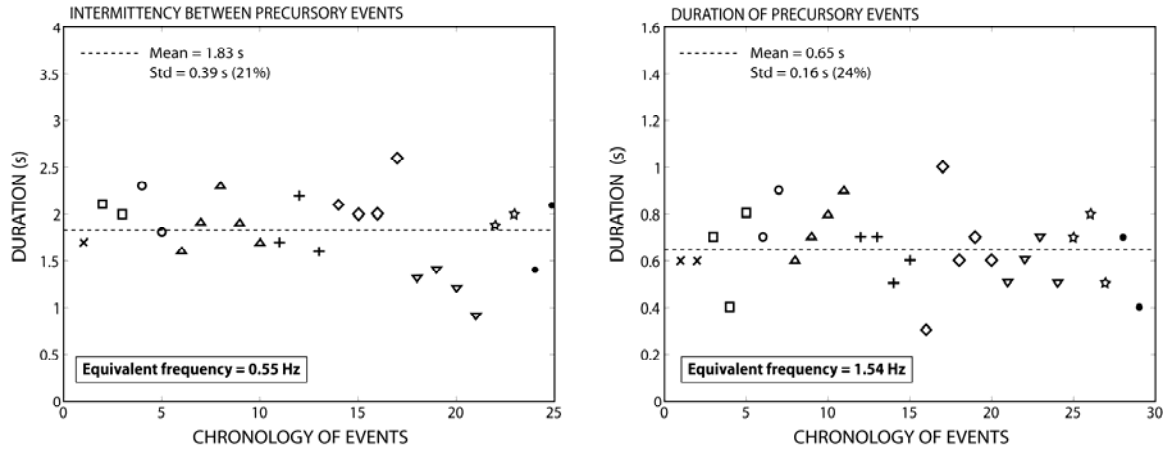

Figure VI.10. (a) Characteristic duration and equivalent frequency of intermittency between precursory events. (b) Characteristic duration and equivalent frequency of precursory events.

VI.3.2.3. Bubble depth estimate corresponding to the first acoustic precursor

The first acoustic precursor event (part 1) occurs in average 7 seconds before the acoustic main pulse (part 2). The latter corresponding to the bubble expansion at the surface of the magma column (z=0) we can deduce, if we know the bubble rise velocity, the maximum depth at which the bubble can generate surface waves. The rise velocity (U_s) of a slug in an infinite liquid can be theoretically estimated from (Wallis, 1969):

$$U_s = 0.345(g2R)^{1/2} \quad \text{(VI.1)}$$

where R is the conduit radius taken as 5 m at Etna SEC (Vergniolle and Ripepe, 2008), and g is the acceleration of gravity. Finally, we can estimate the equilibrium pressure inside the bubble from the lithostatic pressure corresponding to the thickness of the magma column above the bubble plus the atmospheric pressure, and calculated as (Vergniolle and Jaupart, 1990; Vergniolle et al., 1996):

$$P_g(t) = \rho_{liq} g\left(H_{liq}^0 - U_s t\right) + P_{air} \quad \text{(VI.2)}$$

H_{liq}^0 is the thickness of the magma layer at time t = 0, P_{air} is the atmospheric pressure ≈ 10^5 Pa, and ρ_{liq} is the density of magma (2700 kg/m^3).

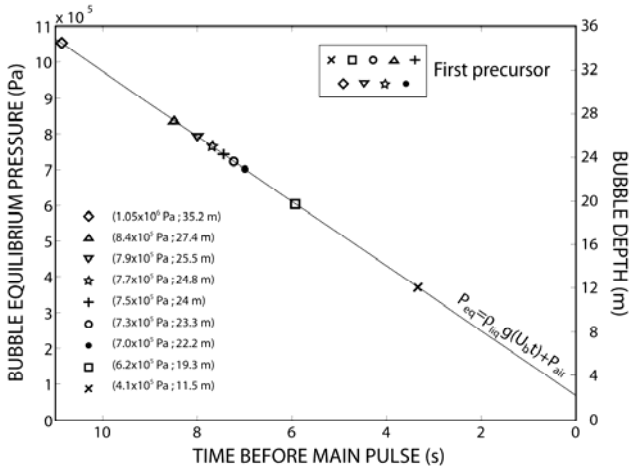

Figure VI.11. Estimation of bubble depth at the moment where the first sloshing event is recorded at the surface from theoretical bubble rise velocity U_s in an infinite liquid. We thus deduce the lithostatic pressure corresponding to the equilibrium pressure inside the bubble at a given depth for the first sloshing events of 9 large bubbles bursting at the surface of the magma column.

For a mean conduit radius of 5 m, we obtain a characteristic bubble rise velocity of 3.45 m/s. We are thus able to provide in Figure VI.11 the depth and equilibrium pressure of the 9 large bubbles studied. We obtain a mean bubble depth of 24 m under the surface of the magma column, with a maximum value of 35.2 m and a minimum value of 11.5 m. We give a mean corresponding bubble equilibrium pressure of 7.4×10^5 Pa, with a maximum value of 1.05×10^7 and a minimum value of 4.1×10^5. This result stresses that each bubble does not generate first surface waves from the same depth. This effect may be due to the natural difference of overpressure between each bubble, acquired more deeply, when the foam collapses.

VI.3.2.4. Spectral content analysis on a 300-s sequence

Fast Fourier Transforms of the acoustic pressure signal have been carried out over a period of 300 seconds at the end of the paroxysm between 2155:00 UT and 2200:00 UT. During this period, the activity consists in small frequent explosions with typical acoustic pressure around 20 Pa, interspersed by larger events typical of large bubbles studied in this work, and reaching acoustic pressure >40 Pa (Figure VI.12a).

Two main frequencies emerge from the spectral analysis (Figure VI.12b). We find out a peak between 1-2 Hz (1.35 Hz at maximum amplitude) that is compatible with frequencies of the acoustic main pulse (part 2, 1.54 Hz in average). It is the most energetic one, with a maximum acoustic pressure of 0.9 Pa. The peak at about 0.6 Hz is rather compatible with the frequency of precursory events (part 1, 0.55 Hz in average). Note that the amplitude of these two characteristic frequencies evolves jointly through time, suggesting that both mechanisms may be induced by the behaviour of the same rising bubble from depth to the surface.

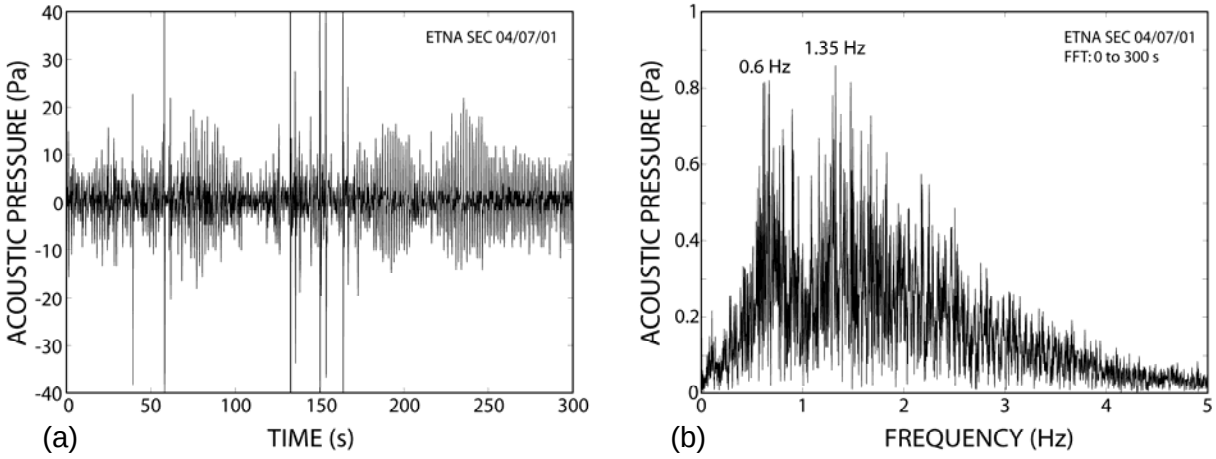

Figure VI.12. (a) Time series of acoustic pressure during 300 s of Strombolian activity occurring at 2155:00 UT at Etna SEC during the eruption of July 4, 2001. (b) Spectral content analysis from Fast Fourier Transform on the same period of 300 s. We show two main frequency peaks at about 0.6 Hz and 1.35 Hz, the latter having the maximum acoustic pressure at 0.9 Pa.

VI.4. Theoretical features

VI.4.1 Possible sources of sound generation

VI.4.1.1 Acoustic precursors: bubble vibration at depth

The first part (P_1), occurring in average a few seconds before the acoustic main pulse is assumed to be gravity waves (Vergniolle et al., 1996) generated at the surface of the magma column. The origin of these surface waves is related to the existence of a deeply rooted oscillating source. Indeed, gas pockets are formed at depth by the coalescence of a foam layer and overpressurized by the release of surface tension from numerous small bubbles. When the foam collapses at the roof of the magma chamber, a large bubble is generated, where its overpressure will force it to grow and oscillate in an infinite liquid. Because of the small finite-diameter of the conduit, the rising bubble cannot expand in width and thus develops as a gas slug, leading to longitudinal oscillations. The magma layer above the bubble follows passively its motion, and may be considered as a mass attached to a vertically oscillating spring. The resulting acoustic pressure recorded at the magma-air interface (i.e. at the surface) both arises from (1) the volume-mode and (2) the gravity-mode.

Firstly, the volume-mode is related to the oscillation of the bubble at depth, inferred from its variation of internal pressure. Assuming small oscillations and no damping as Vergniolle and Brandeis (1994), the radian frequency is the ratio between generalized stiffness and inertia, both derived from potential and kinetic energies respectively (Lighthill, 1978). We assume for simplicity that the bubble is a cylinder (i.e., a slug) of length L with a radius R pushing a layer of magma thickness H_{liq} at a density ρ_{liq}. The volume mode frequency f_v of the oscillator assuming isothermal heat transfer inside the gas at pressure P_g is therefore:

$$f_v = \frac{1}{2\pi}\sqrt{\frac{\gamma P_g}{\rho_{liq} L_{eq} H_{liq}}} \qquad \text{(VI.3)}$$

Where γ is the ratio of specific heats, equal to 1.1 for hot gas (Lighthill, 1978). Importantly, this calculation is a rough approximation because, in particular, the magma layer gets thinner as the bubble rises and hence increases in length by decompression. Setting P_g at the mean bubble equilibrium pressure (lithostatic + air) of 7.4×10^5 Pa corresponding to a mean bubble depth of 24 m, we obtain a mean characteristic frequency of 0.56 Hz. Note that it correspond to a bubble length of about 5 m (i.e. on the order of the conduit radius) close to the magma-air interface according to the adiabatic decompression relation (Equation VI.12.).

Secondly, the gravity-mode is related to the weight of the magma layer above the bubble. Considering the large thickness of this column of magma at the beginning of bubble ascent, we assume that gravity waves can develop at the magma-air interface and then generate both fragmentation and sound. In a tube, gravity waves may develop with a wavelength λ, for which the frequency f_g is:

$$f_g = \frac{1}{2\pi}\sqrt{\frac{g}{\lambda}} \qquad \text{(VI.4)}$$

The wavelength λ is on the order of the conduit radius. The theoretical frequency of the gravity waves is about 0.23 Hz for a radius of 5 m. Bearing in mind the approximation of these theoretical features, both volume-mode and gravity-mode give an estimate of characteristic low-frequency, lower than one hertz, and characteristic to the physical mechanism involved. As a comparison, frequencies inferred from acoustic analysis on the

precursors of the 9 large bubbles give values of 0.55 and 1.54 Hz for intermittency and duration of acoustic precursors respectively. Theoretical values of frequencies given in this section are rather consistent with the ones inferred from the intermittency between precursors.

VI.4.1.2. Main acoustic pulse: bubble nose vibration at the magma-air interface

The second part (P_2) represents the bubble nose vibration and its bursting at the magma-air interface; it is the most energetic event of the acoustic signal, and it can reach 100 Pa on the sensor, at about 1000 m from the source. At this stage the bubble can be commonly considered as a slug, with a cylindrical tail of length L and a bubble nose of initial radius R_0. However, in some cases, the magma level can increase and partially fill the crater. Then, the bubble form may change into a spherical cap of radius R without tail. The duration of the bubble vibration and the transition to its bursting are mechanisms hardly modelled and also difficult to observe. Indeed the spectral content of the oscillation of a large overpressurized bubble is expected to be lower than the one of a bubble bursting, and characteristic times of both physical processes are also expected to be different as well as their amplitudes. These problems are deeply discussed in the subsequent section. Because of the large difference in viscosity between air and magma, the motion of the immersed part of the gas slug is restricted; then, the bubble vibration is mostly concentrated into its hemispherical cap. The oscillating source, (i.e. overpressurized bubble) is the same than the one of part 1; however, in this case the slug is not moving in an infinite liquid, and its motion is not restricted by the conduit wall.

The vibration of the bubble-magma interface is transmitted radially through the thin layer of magma and reaches the magma-air interface. The sound velocity in magma is above 2500 $m.s^{-1}$ (Rivers and Carmichael, 1987; Kress and Carmichael, 1991) and the magma is largely incompressible for the radial motions considered here. Therefore, no energy is lost by the transmission through the thin layer of magma (Pierce, 1981): the magma-air interface vibrates as the bubble does. A bubble vibrating at such a boundary layer presents three modes of vibration. The first one is related to the surface tension, the second one is associated to the gravity waves and the third one is only due to volumes changes. Vergniolle and Brandeis (1996) showed that, for a large bubble with a thin overlying magma-layer, the energy released will go preferentially into the volume mode, directly driven by overpressure. We can obtain the frequency of the volume mode for a slug, from the kinetic and potential energy for a liquid

film of thickness *h* small before the initial bubble radius R_0 (Lighthill, 1978; Vergniolle and Brandeis, 1994) by using:

$$f_v = \frac{1}{2\pi}\sqrt{\frac{2}{2+3(L/R_0)}}\sqrt{\frac{3\gamma P_g}{\rho_{liq} h R_0}} \qquad \text{(VI.5)}$$

When the bubble is at the surface, the equilibrium pressure can be taken equal to the atmospheric pressure only. We thus obtain a characteristic frequency of about 1.4 Hz for a bubble radius of 5 m (i.e., on the order of the radius conduit) and a bubble length of 7 m. This frequency value is in agreement with the ones inferred from measurements of the main acoustic pulse carried out on 9 large bubbles (1.3 Hz).

After about a cycle of oscillation, the bubble usually bursts caused by the fragmentation of the thin magma-layer inferred from the development of instabilities on interfaces. Indeed, the stability of a spherical surface depends both on its acceleration and velocity; therefore instabilities can develop on both interfaces (i.e. bubble-magma and magma-air), particularly in the case of large bubbles, and lead to the fragmentation of the surrounding magma layer into disconnected ballistic pyroclasts. Bursting of a bubble is related to the rupture of its overlying membrane. We can consider two main cases: a short-time rupture and a long-time rupture. Firstly, we can make the analogy with a balloon bursting due to overpressure. In this case the characteristic time of the rupture is short, and the membrane punctures from a single hole inferred from located instabilities. The frequency of the sound generated by such a mechanism can be estimated by the following relation:

$$f_b = \frac{c}{2R_0} \qquad \text{(VI.6)}$$

For a sound velocity in air of 340 m/s and an initial bubble radius of 5 m as is assumed at Etna Southeast Crater (SEC), we obtain a frequency of about 34 Hz. The sound generated by such a mechanism is low amplitude and hence may not emerge from the raw acoustic signal. Secondly, in the case of a long-time rupture, the problem is much more complex, the energy repartition among the acoustic mode is different and the amplitude of the acoustic signal

would decrease. Note that the thickness and viscosity of the membrane can particularly account for the duration of the rupture time.

VI.4.1.3. Last acoustic event: bubble bottom vibration

The last part (P_3) corresponds to gravity waves that develop at the bottom of the bubble. Indeed, the lateral film of magma travelling downward along the conduit wall after bubble bursting can be transmitted at the bottom of the bubble, and generate oscillations at the surface of the new air-magma interface. The sound produced by this mechanism has been recorded on the acoustic signal as a single peak of relatively high amplitude and low frequencies. The frequency of these kinematic waves depends particularly on the viscosity of the magma and can be deduced from:

$$f_k = \left[\frac{0.9^6 n^3}{8\pi^3} \frac{\rho_l g^2}{\mu} \right]^{\frac{1}{3}} \qquad \text{(VI.7)}$$

Any change in the geometry of a hemisphere can be described by the superposition of various modes *n*. The fundamental mode corresponds to a volume change, and is expected to be odd. Then, for n = 1 and with a viscosity of 10 Pa.s, we obtain a characteristic frequency of about 2-3 Hz. Simultaneously, high frequencies with low amplitude are overlaid on the bubble tail signal most likely corresponding to the ejection of ballistic pyroclasts. These frequency values significantly differ from the one given from the analysis of explosion at 2135:35 UT (0.6 Hz). Note however that the comparison on a single example is not representative, but this kind of event is rarely recorded. The delay of a few seconds between acoustic signals generated by the bubble nose and the bubble bottom may give an estimate of the bubble length if we assume that the bubble bottom is still rising at its equilibrium velocity U_s.

VI.4.1.4. Summary of possible mechanisms at work

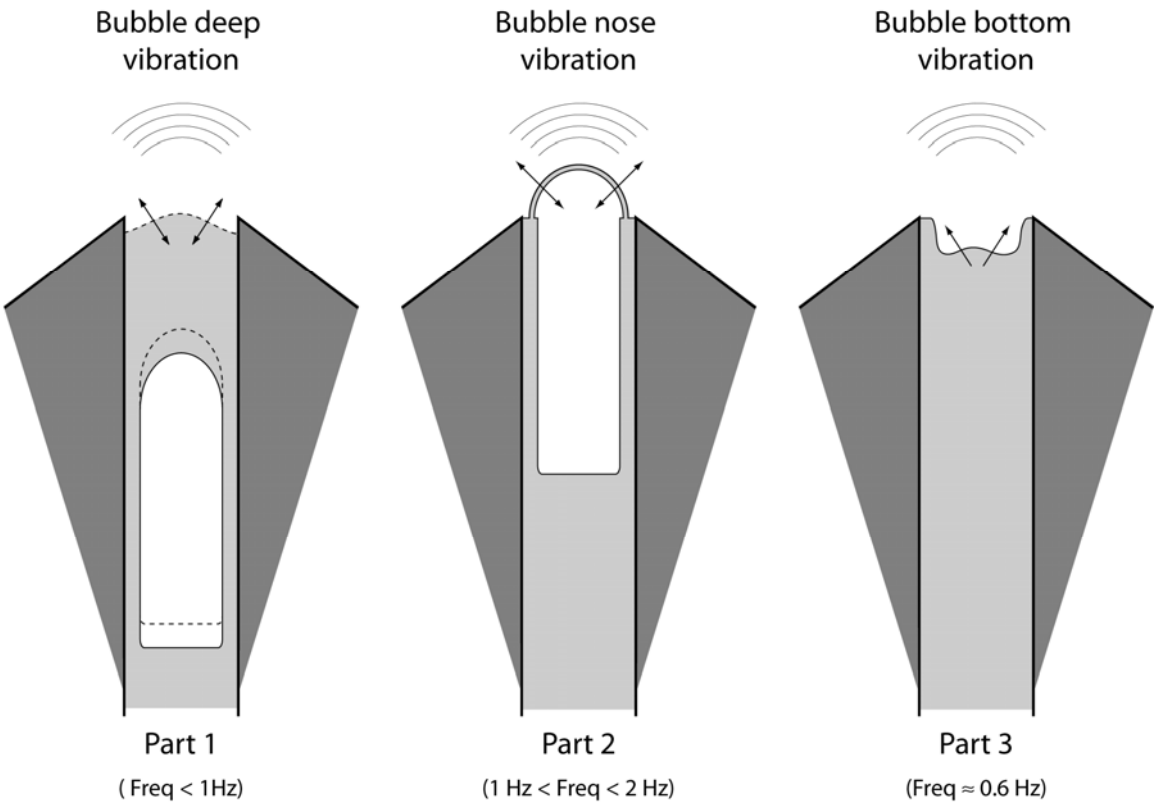

Figure VI.13. Sketches showing the different mechanisms at work during the whole bubble development since its growth at depth to its bursting at the surface, and generating characteristic frequencies measured during part 1, 2 and 3.

We provide in Figure VI.13 a summary of possible mechanisms assumed to be at work and constrained from both observation data (video and acoustic) and the theoretical analysis. The first part of the acoustic signal generated most likely by gravity waves is related to the oscillation at depth of an overpressurized bubble producing typical frequencies <1Hz. We suggest that the second part of the acoustic signal is related the oscillation of the bubble nose reaching the top of the magma column prior to bursting. We obtain typical frequencies ranging from 1-2 Hz. The third part is presumed to be related to the oscillation of the bubble bottom after bursting. However, frequencies inferred from observations significantly differ from the ones calculated theoretically, that suggest strong uncertainties on the validity of this interpretation.

VI.4.2. Synthetic modelling of acoustic waveform

We now focus on the waveform of the main acoustic pulse recorded during Strombolian explosions (part 2). High-amplitude oscillations results in the radiation of sound waves, and we assume in this case that the oscillations are set up by a sudden overpressure inside the bubble reaching the magma-air interface. We approximate the bubble shape by a hemispherical nose and a cylindrical tail, as expected in slug-flow. We propose that the sound generated at Etna is produced by the vibration of a shallow plurimetric bubble prior to bursting rather than the popping noise, by analogy to the balloon bursting problem. Any bubble in an infinite liquid oscillates easily: inertia causes the bubble to overshoot its equilibrium radius and the compressibility of gas, through the internal gas pressure, acts such as a restoring force (Batchelor, 1967; Leighton, 1994). If the lava is close to the surface, as it is the case during the paroxysm of 4 July 2001 at Etna, no external limitation exists on bubble growth when the bubble reaches the surface and breaks; and then, the resulting distortion of sound propagation inside the crater is likely to be low.

The source of sound is a thin layer of magma pushed by a variation of internal pressure inside the bubble (Vergniolle and Brandeis, 1996; Vergniolle et al., 2004). The thickness h of the magma layer is of the order of magnitude of the average diameter $\bar{D}$ of the ejecta, which are usually of the order of ($h_{eq} \approx R/100$) a few centimetres, i.e. much smaller than the radius, and hence can be considered as a membrane. It has been shown for Stromboli volcano that the source is a monopole as its amplitude decrease inversely proportional to the distance between the microphone and the vent (Vergniolle and Brandeis, 1994). Analogous analysis is possible at Etna, considering the type of activity studied here, and the extreme similarity between both acoustic waveforms. Therefore, the propagation of pressure waves is radial, and in that case the source is a simple one. The excess pressure can be described from the linear theory of sound, and in that case depends on the rate of mass outflow from the source, $\dot{q}$ (Lighthill, 1978). Acoustic pressure P_{ac} emitted at the source at time t will reach the microphone at time $t + r/c$, where r is the distance from the vent and c is the sound velocity in air. For such a monopole source, the excess pressure P_{ac}-P_{air} at time t is:

$$P_{ac} - P_{air} = \frac{\dot{q}(t - r/c)}{4\pi r} = \frac{d^2}{dt^2}\left[\frac{4\pi R^3 (t - r/c)}{6}\right]\frac{\rho_{air}}{2\pi r} \qquad \text{(VI.8)}$$

where P_{air} and ρ_{air} are respectively atmospheric pressure and air density. Finally we obtain the excess pressure in air:

$$P_{ac} - P_{air} = \left[2\dot{R}^2(t - r/c) + R(t - r/c)\ddot{R}(t - r/c)\right] \times \frac{\rho_{air} R(t - r/c)}{r} \quad \text{(VI.9)}$$

where $\dot{R}$ is the radial velocity and $\ddot{R}$ is the radial acceleration of the hemispherical bubble nose. This equation relates the variations in acoustic pressure to the bubble vibration. Thus, in order to express these variations in acoustic pressure, we model the bubble motions in response to a sudden overpressure. The bubble vibrates as a thin membrane of thickness *h*; its head grows but remains spherical with a radius *R* and the cylindrical tail has a length *L*. The total volume V_g of the bubble is simply the sum of both parts:

$$V_g = \frac{2\pi R^3}{3} + \pi R_o^2 L \quad \text{(VI.10)}$$

All the equations given in this section are related to the slug geometry (bubble nose and cylindrical tail). For the hemispherical cap geometry, the length *L* of the cylindrical tail has simply to be taken equal to zero in equations 10 and 14. Note that in the following, indexes o, g and eq refer to initial conditions, gas and equilibrium values, respectively. The high viscosity of the magma impedes any significant drainage by gravity of the magma above the bubble during the short time allowed for the bubble to vibrate. The volume of magma above the bubble is then conserved and the liquid stretches, following the variations in the bubble radius.

$$R^2 h = R_{eq}^2 h_{eq} \quad \text{(VI.11)}$$

Because heat transfer inside large bubbles is adiabatic (Plesset and Prosperetti, 1977), the pressure P_g inside the bubble follows the variations of its volume V_g:

$$P_g V_g^{\gamma} = P_{g.eq} V_{g.eq}^{\gamma} \quad \text{(VI.12)}$$

where γ is the ratio of specific heats, equal to 1.1 for hot gases (Lighthill, 1978). For a thin layer of magma, the contribution of its weight to the equilibrium pressure inside the bubble is small, and the equilibrium pressure $P_{g\ eq}$ can be considered as equal to the atmospheric pressure P_{air}. The temperature is homogeneous inside the gas during the vibration (Prosperetti, 1986) and obeys the law of perfect gases. It will passively follow variations in volume and pressure. Suppose that the bubble, initially at rest at the magma-air interface, is overpressurized by an amount ΔP. The bubble starts to grow and vibrate in response to that pressure change. Pressure and volume follow the adiabatic law; hence we can calculate their variations. The bubble radius R can be expressed by its variation around the equilibrium radius R_{eq} calculated from initial conditions and the adiabatic law (Vergniolle and Brandeis, 1996):

$$R = R_{eq}\left(1+\varepsilon\right) \tag{VI.13}$$

with

$$R_{eq} = \left\{\frac{3R_o^2}{2}\left[\left(\frac{2R_o}{3}+L\right)\left(1+\frac{\Delta P}{P_{air}}\right)^{1/\gamma} - L\right]\right\}^{1/3} \tag{VI.14}$$

where ε is a dimensionless bubble radius. The motion of the bubble is possible through an exchange between the kinetic energy of its hemispherical nose and the potential energy inside the gas. The general equation for the bubble vibration is:

$$\ddot{\varepsilon} + \left(\frac{12\mu}{\rho_{liq}R_{eq}^2}\right)\dot{\varepsilon} + \frac{P_{air}}{\rho_{liq}R_{eq}h_{eq}}\left[1-\left(\frac{V_{eq}}{V_g}\right)^{\gamma}\right]\left(1+\varepsilon\right)^2 = 0 \tag{VI.15}$$

where the gas volume Vg is a function of ε (Vergniolle and Brandeis, 1996). The first initial condition to be specified is the initial value of the dimensionless radius ε_o. The second initial condition is the initial radial acceleration $\ddot{\varepsilon}_o$, which depends on the initial force applied to the layer of magma. Assuming that the bubble, at rest at the magma-air interface, is suddenly

overpressurized by an amount ΔP, this force is directly related to the bubble overpressure. Therefore, the initial conditions are:

$$\varepsilon_o = \frac{R_o}{R_{eq} - 1} \tag{VI.16}$$

$$\ddot{\varepsilon}_o = \frac{\Delta P R_o^2}{\rho_{liq} R_{eq}^3 h_{eq}} \tag{VI.17}$$

Radial acceleration is maximum when the strong vibration starts and the initial radial velocity is equal to zero. These initial conditions correspond to a bubble close to its minimum radius

VI.4.3 Video-derived modelling of acoustic waveform

From the bubble nose radius R measured on the four large bubbles from video snapshots, we can calculate the resulting excess pressure P_{ac} in air by using the Rayleigh-Plesset relation that depends particularly, on the velocity $\dot{R}$ and the acceleration $\ddot{R}$ of the thin magma layer above the bubble. These two parameters are simply the first and second derivative of the bubble radius, respectively. They can be determined from finite difference calculations:

$$\dot{R} = \frac{\partial R}{\partial t} = \frac{R_{i+1} - R_i}{\Delta t} \tag{VI.18}$$

$$\ddot{R} = \frac{\partial^2 R}{\partial t^2} = \frac{R_{i+1} - 2R_i + R_{i-1}}{\Delta t^2} \tag{VI.19}$$

Then we calculate the stability factor of the bubble magma interface which depends mostly on the acceleration of the magmatic film. Although the bubble nose is only half a sphere, we apply the stability analysis for a sphere by using the stability factor C_{RT} that is related to the bubble-magma interface.

$$C_{RT} = \frac{(n-1)(n+1)(n+2)\sigma}{\rho_{liq} R_0^3} - \frac{3\dot{R}^2}{4R_0^2} - \frac{(2n+1)\ddot{R}}{2R_o} \tag{VI.20}$$

where σ is the surface tension and n is the wavenumber. If the stability factor is greater than zero, it means that the bubble-magma interface is stable and hence we deduce that the magma-air interface is unstable. It is the opposite when the stability factor C_{RT} is negative. The surface tension term, with $\sigma \approx 0.1$ kg.s^{-2} for a basaltic magma at 1200°C and 0.1 MPa (Proussevitch and Kutolin, 1986; Proussevitch and Sahagian, 1996), can be ignored for bubbles as large as a few meters. The perturbation of a spherical surface would remain small for $1 \geq R/R_{max} \geq 0.2$ and will become violent for $R/R_{max} \leq 0.1$.

VI.5. Results: Comparison between measured, synthetic and video-derived acoustic waveforms

VI.5.1. Bubble vibration as a source of sound

In this section we first compare the synthetic acoustic waveform with the measured acoustic waveform of the main acoustic pulse (part 2) on four large bubbles. The synthetic waveforms are calculated from the bubble vibration model at the magma-air interface using equations given in section VI.4.2. The objective is to fit both waveforms so as to validate the bubble vibration model, and to give some quantitative estimates on physical parameters such as magma thickness, radius, length, and overpressure of the bubble.

Afterwards, from the synthetic waveforms defined from the best fit of acoustic data, we can derive the temporal evolution of the radius, velocity, acceleration and stability factor on each large bubbles studied until bursting. We thus compare these parameters with the ones inferred from video-derived calculation, based on the equation presented in section VI.4.3.

Finally, we are able to calculate the temporal evolution of acoustic pressure, and generate the acoustic waveform corresponding to the bubble motion before bursting. This waveform is then compared with the one inferred from acoustic measurements.

VI.5.1.1. Synthetic vs. measured acoustic waveform comparison

Each explosion at Etna can be modelled by the vibration of a large bubble, induced by the residual overpressure left in the bubble approaching the top of the magma column. Similarly to Stromboli volcano, the low-frequency content of the high amplitude acoustic event would discard a mechanism of bubble bursting if solely based on a balloon bursting model.

At the input of the model we use particularly the mass of the oscillator that is related to the thickness h of the magma layer above the bubble. This parameter, poorly constrained, is assumed to be equal to the mean size of ejecta. Photoballistic studies at Etna show, for one explosion of the North-East Crater in June 1969, that 50% of ejecta have a size between 0.1 and 0.4 m (McGetchin et al., 1974). Ground deposit studies have pointed out similar results at Etna, from scoria blocks produced by Strombolian activity on July 25-31, 2001 (Metrich et al., 2004), making this diameter range characteristic of ejecta at Etna. Previous studies on acoustic modelling at Etna have shown that the best magma-layer equilibrium thickness h_{eq} lies around 0.1 m.

At the output of the model, the best fit between measured and synthetic waveforms provides three fundamental parameters: (1) the bubble nose radius, (2) the length of the bubble tail and (3) the bubble overpressure. A previous study on the time evolution of the source parameters at Etna SEC during the July 4, 2001 eruption gives a characteristic initial bubble radius R_o equal to 5 m. Bubble length L and overpressure ΔP are estimated on average at about 15 m and 0.22 MPa. In the present study, we worked specifically on the four large overpressurized bubbles both recorded by the acoustic sensor and the video camera. The output parameters carried out by the acoustic model are in agreement with the ones given by Vergniolle and Ripepe (2008). Indeed the best fits between measured and synthetic acoustic data give an initial radius of 5 m with a bubble length ranging from 6.5 m to 17 m and a bubble overpressure lying from 0.29 MPa to 0.45 MPa. These values are summarized in Table VI.1.

Table VI.1. Characteristic parameters for 4 large bubbles at Etna SEC on July 4, 2001, inferred from best fit of the synthetic vibration model.

		Bubble 2135:35	Bubble 2138:10	Bubble 2142:32	Bubble 2143:04
Magma thickness (m)	h_{eq}	0,1	0,08	0,1	0,15
Initial radius (m)	R_o	5	5	5	5
Length (m)	L	11	7	6,5	17
Overpressure (MPa)	ΔP	0,45	0,29	0,34	0,35

The fit between measured and synthetic acoustic waveforms is always very good for about half a cycle (Figure VI.14). Afterwards, we assume that the development of instabilities at the interfaces leads the oscillations of the magma layer to move apart from a purely steady oscillating regime represented by the acoustic model. As shown by the bubble at 2143:04 UT in Figure VI.14, the amplitude of the first positive peak of the measured acoustic pressure is perfectly matched by the synthetic model and reaches ≈ 60 Pa. By contrast, the negative peak

and the second positive peak are not well fitted. Indeed, acoustic pressures inferred from the synthetic model reach about -135 Pa and 60 Pa, against -90 Pa and 30 Pa for the measured acoustic pressures. On this example, the discrepancy between both acoustic signals occurs just before the maximum negative pressure.

We also observe on the measured signal a slight augmentation of the acoustic pressure a few tenths of a second before the strong increase of the first positive peak. This small increase, lower than 10 Pa, is not taken into account by the acoustic model, but we presume that it corresponds to the onset of the bubble expansion at the surface of the magma column. The oscillating frequency inferred from the synthetic waveform is in agreement with the one of the measured waveform over the whole cycle duration, i.e. about 1.1 Hz, and will permit the quantitative and temporal comparison with acoustic waveform calculated from video analysis.

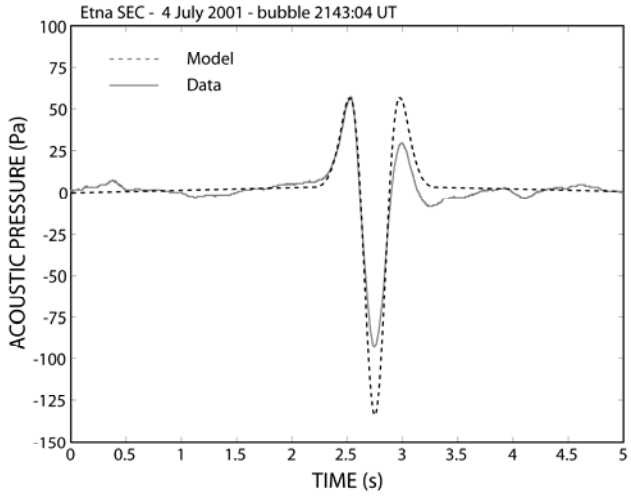

Figure VI.14. Best fit between the synthetic acoustic waveform (model) generated from the oscillation bubble equations and measured acoustic waveform (data) for the bubble at 2143:04 UT.

VI.5.1.2. Synthetic vs. video-derived acoustic waveform comparison

In this section, we compare video-derived parameters with synthetic parameters inferred from best-fit synthetic waveforms calculated theoretically from the bubble vibration model (Figure VI.14). We focused, particularly, on the bubble radius (R), the magma layer velocity ($\dot{R}$) and acceleration ($\ddot{R}$), and on the stability factor C_{RT} of the interfaces.

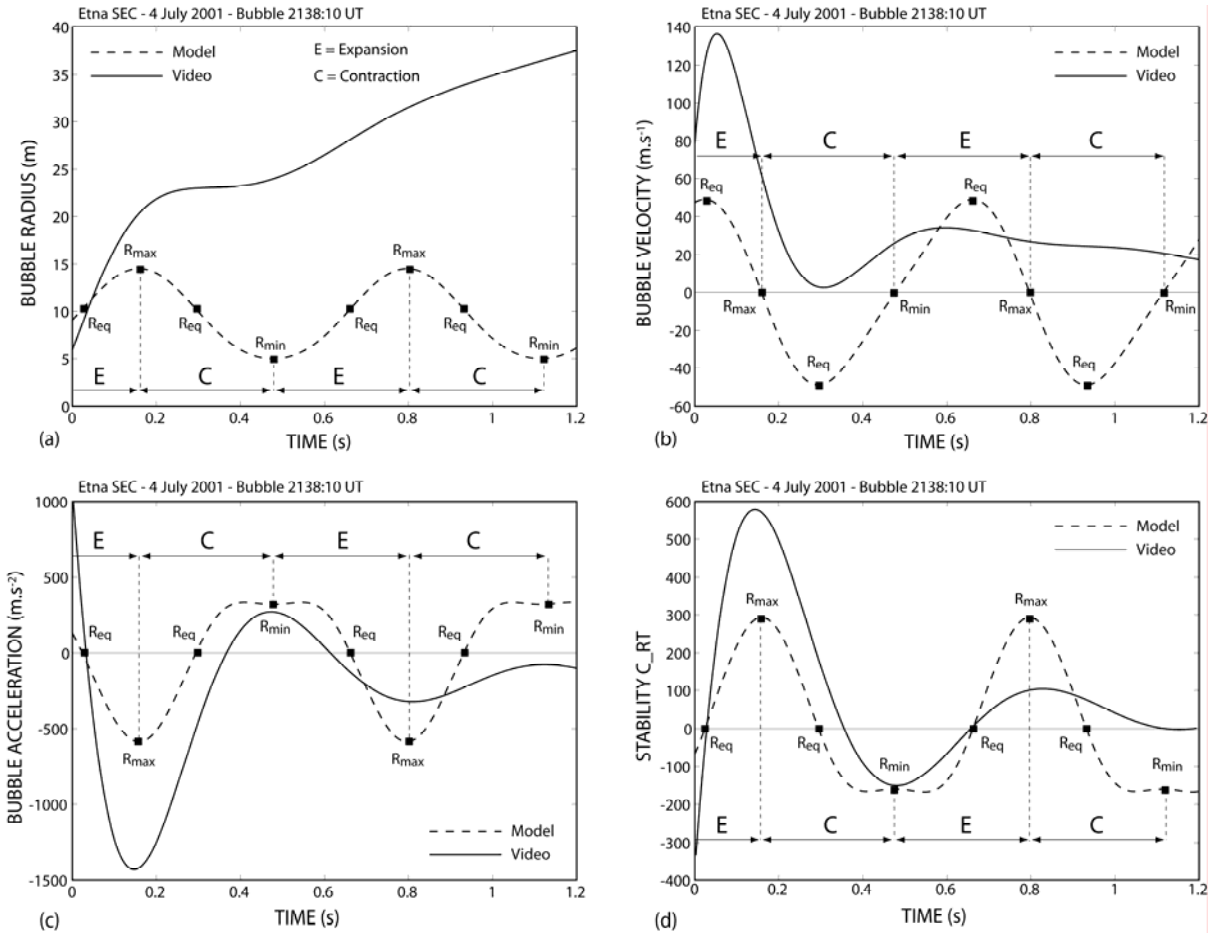

Figure VI.15. Evolution of the physical properties, (a) radius, (b) velocity, (c) acceleration and (d) stability factor, at Etna SEC on July 4, 2001 for the bubble at 2138:10 UT derived from both video measurements and synthetic bubble vibration model (see text for details).

We show on bubble at 2138:10 UT that the evolution of the radius (Figure VI.15a) has not a linear trend, particularly at the beginning of the time series (t=0 s to t=0.6 s), where we can observe a mild oscillation of the bubble radius. This tendency discards ballistic regime mechanisms of discrete fragmented pyroclasts, and is thus compatible with the fact that the bubble has not burst yet. Moreover, about 0.5 second after the onset of the video recording, visual observations from video snapshots show that the magma-air interface is still not fragmented.

In the following, we will thus mainly focus on this first half-second of video analysis. At the onset of the video recording (t=0 s), we assume that the bubble is not at its minimum radius (R_{min}) because it has probably begun to grow into the crater at the surface of the lava column. The first snapshot thus arises most likely a few tenths of a second later when the bubble membrane rises above the crater rims. Our measurements give a bubble radius ranging from

about 9 m at the equilibrium radius (R_{eq}) to about 20 m at the maximum radius (R_{max}). These values differ slightly from the synthetic data that give an equilibrium radius of about 11 m and a maximum radius of about 15 m. After R_{min}, i.e. about 0.5 second after the beginning of the video recording, the radius inferred from video measurements departs dramatically from the theoretical purely no-damped vibration model.

This discrepancy can be explained from two distinct effects. (1) At this moment, instabilities of the bubble-magma interfaces are at the maximum (Figure VI.15d) and can disorder the steady oscillations. (2) The global expansion of the rising bubble is most likely a predominant mechanism that adds up to the basic oscillation of the vibrating bubble. This effect makes the bubble radius grow faster, and may account for at least 20% of the bubble radius value. Remind, we have previously shown (Figure VI.14) that the synthetic waveform also does not fit very well the measured acoustic waveform a few tenths of a second after the onset of the bubble expansion. (3) The membrane may have punctured at this stage, leading to a sub-linear trend of the bubble radius corresponding to the ballistic trajectories of disconnected blocks propelled radially in the surrounding air.

The velocity (Figure VI.15b) and acceleration (Figure VI.15c) of the magma layer above the bubble are determined from finite difference calculation of the radius, and both bring out a high-amplitude oscillation pattern. The bubble membrane reaches its maximum velocity, of about 140 m/s, at the very beginning of the video time series, close to the equilibrium radius as expected theoretically. The synthetic model gives a lower estimate of the maximum velocity. This difference can be easily explained, in addition to error margins related to video measurements, by the global expansion effect that may increase the total resulting velocity of the bubble membrane. The velocity then decreases rapidly to its minimum value, i.e. close to 0 m/s, near the second equilibrium radius as expected theoretically, but never becomes negative. Indeed, the global bubble expansion effect impedes the bubble membrane to retract enough in its contraction stage, in spite of the restoring force owing to the compressibility of gas inside the bubble acting at the opposite of the steady bubble expansion. As a consequence, the magma layer above the bubble never moves back and leads only the bubble to slow down. We thus cannot observe negative velocity. However, we show that the characteristic frequency of the velocity oscillations is in agreement with the one of the synthetic pattern, in the time frame of about half a cycle. After this point, the development of instabilities may affect the fundamental bubble oscillation cycle.

The acceleration parameter, even more sensitive to the radius variations than the velocity parameter, clearly shows the different stages of expansion and contraction taking alternately positive and negative values. The difference in amplitude of the first negative peak between synthetic and video data can be explained by the same bubble expansion effect detailed above for the velocity. The maximum negative and positive acceleration occur at R_{max} and R_{min} respectively, as expected theoretically. The frequency of the bubble oscillation inferred from video measurements is also in agreement with the one calculated theoretically from the synthetic model.

The factor C_{RT} is related to the stability of the bubble-magma interface. It is stable during the cycle R_{eq}-R_{max}-R_{eq} when $C_{RT} > 0$ and becomes unstable at R_{eq}-R_{min}-R_{eq} for a stability factor $C_{RT} < 0$. The stability factor calculated from video measurements is in agreement with the one derived from the synthetic model. We show that the bubble-magma interface is stable at the beginning of the video recording and becomes unstable at the equilibrium radius R_{eq}, at about 0.35 second. This result corroborate the fact that radius, velocity and acceleration patterns significantly move apart from the theoretical model patterns after about half a cycle of bubble vibration. Visual observations suggest that bubbles bursting arise a few tenths of a second later, at about 0.6 s after the beginning of the video recording. However, we cannot be more accurate because of technical hitches related to the video method, such as light scattering and pixel saturation. We show nevertheless that the fragmentation of the magma layer above the bubble most likely occurs into the cycle R_{eq}-R_{min}-R_{eq} corresponding to the instability phase of the bubble-magma interface. At this instant, the magma-air interface is observed stable from video snapshots (Figure VI.5b) and show that membrane rupture is most likely controlled by the bubble-magma interface instabilities. Note that when the bubble-magma interface is stable, at the beginning of the video recording that corresponds to the cycle R_{eq}-R_{max}-R_{eq}, we observe on video snapshot (Figure VI.5a) that the magma-air interface is unstable, as expected by the theory.

We also point out that the bubble breaks during the expansion stage, after the minimum radius, and close to the maximum instability level of the bubble-magma interface. We assume that the expansion/contraction cycle during which the magma layer breaks, partly controls the ejection velocity of fragmented pyroclasts. However, the state of pressurisation of the bubble, at the moment where the magma-layer breaks, is also very important, and should mostly control the ejection velocity of pyroclasts through the gas release velocity. The combination

of both effects may thus be responsible for the large range of ejecta velocity encountered. In the case of an overpressurized bubble, bursting during the expansion stage, we assume that ejecta are expelled with high velocity. At the opposite, in the case of an underpressurized bubble, bursting during the contraction stage, the velocity of pyroclasts is assumed to be low.

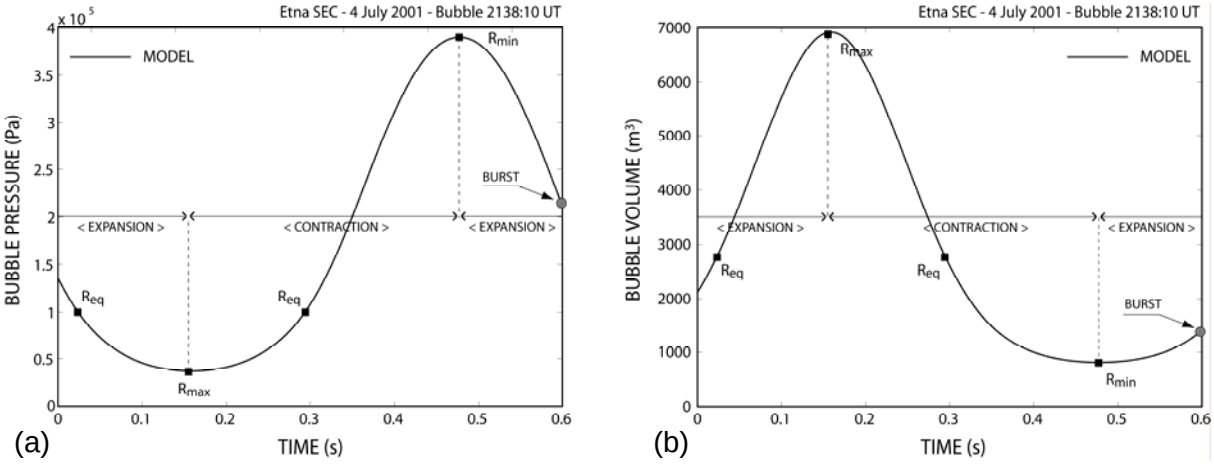

Figure VI.16. Evolution of the internal bubble (a) pressure and (b) volume inferred from the synthetic waveform best-fit on the bubble at 2138:10 UT during successive expansion/contraction stages of the vibrating bubble prior bursting.

The internal bubble pressure (Figure VI.16a) and volume (Figure VI.16b) at the moment where the bubble is assumed to burst can be estimated from the theoretical model by using Equation VI.12. For the bubble at 2138:10 UT detailed above, the magmatic film breaks around 0.6 s after the beginning of video measurements, during the expansion stage, and with an internal bubble pressure of 2.1×10^5 Pa and a volume of 1416 m^3. This bubble is thus overpressurized when it bursts, i.e., with an internal pressure higher than the atmospheric pressure ($P_{air} = 1\times10^5$). Results on the phase (expansion/contraction), pressure and volume are given for the four large bubbles at the bursting time and summarized in Table VI.2.

Table VI.2. Quantitative estimates of internal pressure and volume on four large bubbles derived from the synthetic bubble vibration model.

	Bubble 21h35'35''	Bubble 21h38'10''	Bubble 21h42'32''	Bubble 21h43'04''
Phase (E/C)	Expansion	Expansion	Expansion	Contraction
Bubble pressure (Pa)	3.1×10^4	2.1×10^5	4.1×10^5	2.8×10^5
Bubble volume (m^3)	1537	1416	773	2508

VI.5.1.3. Video-derived vs. measured acoustic waveform comparison

Finally, we calculate the excess of acoustic pressure from video-derived parameters detailed above (radius, velocity and acceleration), by using the Rayleigh-Plesset equation. We compare the resulting acoustic waveform with the one inferred from acoustic measurements recorded by the sensor on the bubble occurring at 2142:32 UT (Figure VI.17).

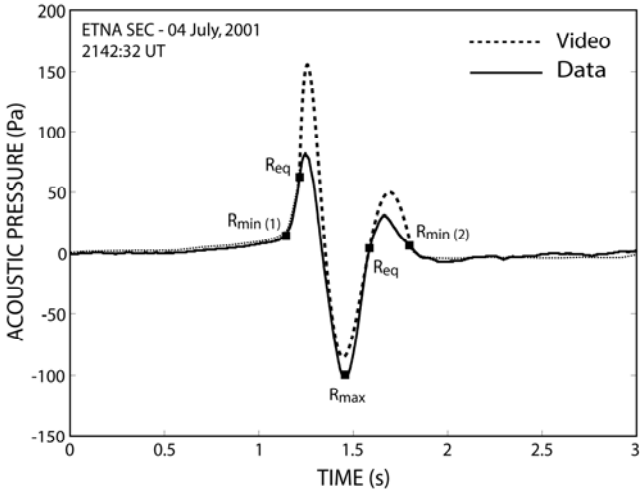

Figure VI.17. Comparison between video-derived acoustic waveform (video) and measured acoustic waveform (data) on bubble at 2142:32 UT.

We show that amplitudes are fairly in agreement (Table VI.3) which confirms that such bubble oscillations are able to generate high-amplitude acoustic pressure. Frequencies are observed between 1 – 2 Hz in average for both measured and video-derived waveforms. This result is compatible with bubble vibration mechanism as a source of sound. These values are also in agreement with the results of Vergniolle and Ripepe (2008) at Etna SEC on July 4, 2001, and consistent with a source radius-conduit of about 5 m. As a comparison, bubble oscillation frequency at Stromboli lies between 7 Hz and 9 Hz and hence corresponds to a smaller source radius-conduit of about 1 m. The video-derived acoustic signal starts between $R_{min(1)}$ and R_{eq}, at the middle of the expansion phase. That is well-explained by the fact that bubble begins to grow beneath the crater rim, at the surface of the magma column, and reaches the video field of view only a few tenths of a second later. The first positive acoustic peak occurs right after R_{eq}, during the expansion phase. The negative acoustic peak occurs at R_{max}, as expected theoretically, and point out the beginning of the contraction stage. Finally, the oscillation stops shortly after $R_{min(2)}$ in the expansion phase, with a high bubble internal

pressure (4.1×10^5). The rupture of the thin magma-layer most likely arises at this moment, after about a cycle of the bubble oscillation.

Table VI.3. Summary of the spectral content (frequency, duration and amplitudes) of the acoustic main pulse on the four bubbles inferred from both the visual analysis of recorded acoustic time series and video-derived measurements at Etna SEC on July 4, 2001.

	Bubble 21h35'35"		Bubble 21h38'10"		Bubble 21h42'32"		Bubble 21h43'04"	
	Video	Acoustic	Video	Acoustic	Video	Acoustic	Video	Acoustic
Frequency (Hz)	2,5	1,1	1,61	1,79	1,37	1,32	1,18	1,06
Duration (s)	0,4	0,9	0,62	0,56	0,73	0,76	0,85	0,94
Amplitude max (Pa)	130	94	490	54	150	82	129	57
Amplitude min (Pa)	-60	-100	-500	-85	-82	-100	-121	-92
Amplitude ratio	2,1	0,94	0,98	0,64	1,83	0,82	1,07	0,62

VI.5.2 Alternative mechanism: balloon bursting model

We have shown previously that the amplitude of the volume mode of the bubble is sufficient to generate the recorded level of sound intensity. The video-derived analysis of acoustic waveform has also provided some evidence of the bubble oscillation as being a possible source of sound. However, the potential impulse nature of the bubble bursting mechanism makes it an intuitive candidate to explain the main pulse in acoustic pressure. We now consider the likelihood of the bubble bursting as the source of the main pulse of acoustic pressure, keeping in mind the major role played by the dimensions of the source.

The balloon bursting model remains a possible mechanism of bubble bursting. The characteristic frequency of the popping noise generated by this mechanism can be easily calculated from Equation VI.6. This relation only depends on the sound velocity in air, supposed constant in the time scale considered here, and on the radius of the bubble at bursting time.

The instant of bubble breaking is not accurately known, but rough estimates of the bubble radius at bursting time (R_{burst}) can nevertheless be given from video-derived calculation carried out in previous section. We obtain a mean radius on the four large bubbles just before bursting of $R_{burst} \approx 28$ m, which gives a mean theoretical frequency derived from the balloon bursting model of $f_b = 6.1$ Hz. As a comparison, the theoretical frequency calculated on the basis of the volume mode (vibration bubble model), gives a mean value on the four large bubbles of $f_v = 1.2$ Hz. Detailed values for each bubble are given in Table VI.4.

Table VI.4. Summary of the spectral content inferred from the detailed analysis of Fast Fourier Transform carried out on 10 s for 4 larges bubbles at Etna SEC on July 4, 2001.

	Bubble 2135:35 UT	Bubble 2138:10 UT	Bubble 2142:32 UT	Bubble 2143:04 UT
R_{burst} (m)	28	25	29	31
f_v (Hz)	0.46	1.5	1.8	1
f_b (Hz)	6	7	6	5.5
FFT- f_α (Hz)	1.85 *(6 Pa)*	1.95 *(5 Pa)*	1.9 *(5.4 Pa)*	1.8 *(5.2 Pa)*
FFT- f_β^1 (Hz)	6.2 *(0.44 Pa)*	8.35 *(0.36 Pa)*	5.8 *(0.56 Pa)*	6.25 *(0.31 Pa)*

Volume mode frequencies are still in agreement with visual analysis carried out on the main acoustic pulse of 9 large bubbles in section VI.3.2 (1.3 Hz). However, the energy released by the popping noise (balloon bursting model) is likely to be low, require a more detailed analysis of the spectral content.

A Fast Fourier Transform (FFT) is performed during the main pulse in acoustic pressure for duration of 10 s; also, the use of logarithmic scales has permitted to point out low-amplitude peaks. Figure VI.18 shows for the bubble at 2135:35 UT a first high-amplitude peak (termed f_α) lying at about 1.85 Hz and reaching 6 Pa. Then we observe 3 successive frequencies of lower amplitudes and peaking at about 6, 12, and 18 Hz. This arithmetic sequence suggests a fundamental frequency of 6 Hz (termed f_β^1) with two harmonics $f_\beta^2 = 12$ Hz and $f_\beta^3 = 18$ Hz following the relation:

$$f_\beta^n = \frac{nc}{2R_{burst}} \qquad \text{(VI.21)}$$

Where *c* is the sound velocity in air taken as 340 m/s and *n* is the order of the harmonic. The fundamental frequency (f_β^1) is typically low amplitude with an acoustic pressure reaching 0.44 Pa, it means about one order of magnitude lower than the frequency peak f_α. Values of frequency and amplitude derived from the FFT analysis are given in Table VI.4 for each bubble. We obtain mean values of 1.9 Hz and 5.4 Pa for f_α, and mean values of 6.7 Hz and 0.4 Pa for f_β^1.

Frequencies f_β^1 are in agreement with values inferred from the balloon bursting model and show that this mechanism generating a very low-amplitude popping noise is probably at work on such explosions. However, frequencies f_α are clearly compatible with values derived from volume mode frequencies (f_v) and confirm that the oscillation of the bubble at the magma-air interface is also at work. Most of all, high amplitude values of f_α confirm the idea that this mechanism is dominant.

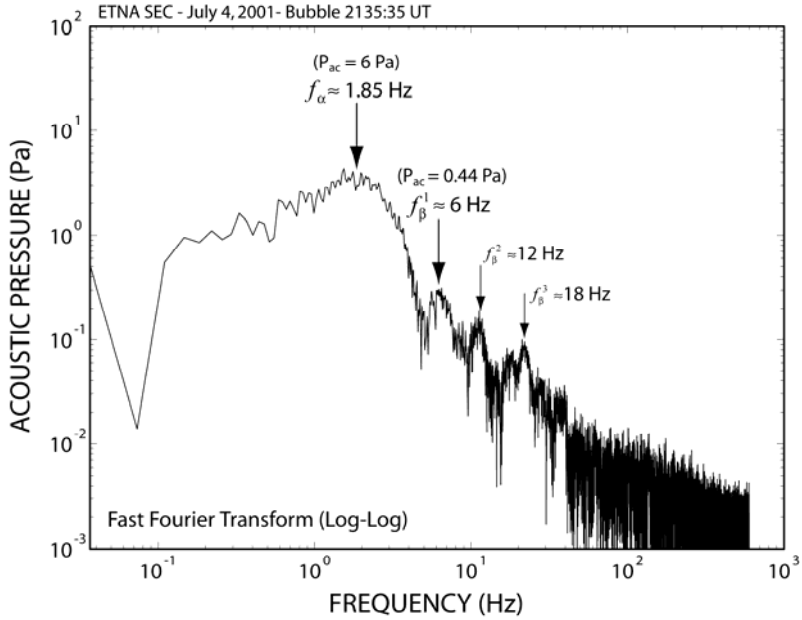

Figure VI.18. Fast Fourier Transform (FFT) of acoustic pressure on a time-window of 10 s in log-log scale on the bubble at 2135:35 UT.

VI.6. Conclusion

Acoustic measurements have long been used for volcanic applications and turn out to be a very powerful tool for remote sensing of hazardous volcanic targets. The great potential of acoustic methods is valuable particularly for the retrieval of volcanic source parameters that can be advantageously used into physical models of eruptions dynamics.

In this study we focus mainly on the mechanisms at the origin of the sound radiated by Strombolian explosions, and recorded as a strong acoustic pulse. Several previous studies (e.g., Vergniolle et al., 1996) have shown from synthetic models that the vibration of a bubble expanding at the surface of the magma column could be theoretically at the origin of the

recorded acoustic waveforms. We show in the present study from direct observations the very existence of a bubble oscillation at the magma-air interface as the source of sound.

Indeed, video snapshots analysis has permitted to give quantitative estimates of bubble radius, velocity and acceleration, and showed the evolution of these parameters with time, pointing out the cyclic expansion/contraction stages of the rising bubble. Then, these parameters have been used to derive the acoustic pressure and permit to build acoustic waveforms on four large bubbles occurring at Etna SEC during the eruption of July 4, 2001. The video analysis has brought some quantitative constraints on the bubble bursting mechanism, also in agreement with the theory. Indeed, we show that the rupture of the overlying magmatic film is most likely related the development of instabilities on the bubble-magma interface. The ones are directly produced by the oscillation (expansion/contraction) of the bubble. Figure VI.19 shows the schematic successive step of a bubble (only the upper hemisphere), from the onset of visual observations, i.e., when the bubble rises above the crater rims, until it bursts. We suggest that the membrane punctured close to R_{min}, at the maximum instability of the bubble-magma interface. At this stage, the velocity of the membrane is assumed to be zero, and the acceleration positive.

We suppose that the expansion/contraction cycle, during which the magma layer breaks, partly controls the ejection velocity of fragmented pyroclasts, as well as the state of pressurization of the bubble. Considering the last stage on Figure VI.19, the bubble is in its contraction stage between $R_{eq} - R_{min}$, and in expansion between $R_{min} - R_{eq}$, reaching a maximum internal pressure at R_{min}.

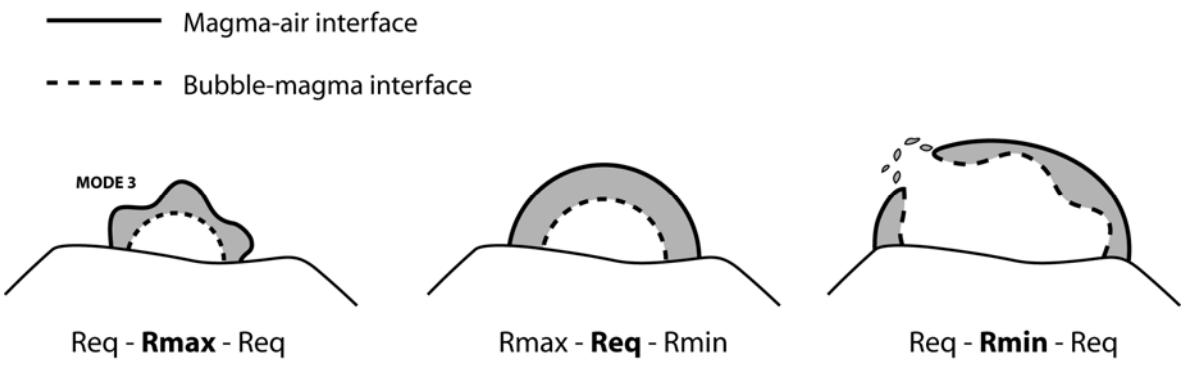

Figure VI.19. Sketch of the successive steps of a typical life-ending bubble rising above the crater rims, showing the stability/instability phases on both interfaces (bubble-magma/magma-air) until the bubble breaks.

However, the state of pressurisation of the bubble, at the moment where the magma-layer breaks, is also very important, and should mostly control the ejection velocity of pyroclasts through the gas release velocity. The combination of both effects may thus be responsible for the large range of ejecta velocity encountered. In the case of an overpressurized bubble, bursting during the expansion stage, we assume that ejecta are expelled with high velocity. At the opposite, in the case of an underpressurized bubble, bursting during the contraction stage, the velocity of pyroclasts is assumed to be low.

We have shown that the video-derived waveform is in fairly good agreement with both synthetic and recorded acoustic waveforms, which first confirms that the vibration of a large overpressurized bubble can generate sound with amplitude equal to the sound level recorded; and then validates the synthetic model of bubble vibration. Therefore, the bubble vibration model is used with some confidence to calculate fundamental source parameters. We give particularly a quantitative estimate of the mean overpressure inside the bubble when reaching the top of the magma column of $\Delta P = 0.36$ MPa. We provide the mean internal bubble pressure and volume at bursting time reaching $P_g = 0.23$ MPa and $V_g = 1.6 \times 10^3$ m^3 respectively.

The spectral content analysis of recorded acoustic main pulses has given characteristic frequency values ranging in average between 1 – 2 Hz. These values are in agreement with frequencies calculated theoretically on the basis of the bubble vibration model (volume mode). Nevertheless, we also point out an alternative mechanism as a possible source of sound. Indeed the spectral content analysis has revealed higher frequencies with very low amplitude, corresponding to theoretical frequency values calculated on the basis of the balloon bursting model lying around 6 Hz. We thus consider that the bubble bursting mechanism is a possible additional source of sound, although it shows amplitude about one order of magnitude lower. This result supports the idea that the bubble membrane oscillation prior to bursting is much more energetic, and confirms the bubble vibration model as dominant mechanism.

The complexity of bubble vibration and bursting mechanisms, associated with the difficulties to study large scale phenomena in the natural environment, suggest that further experimental investigations would probably enhance the understanding of life-ending bubble mechanisms.

CHAPTER VII

Acoustic-radar correlations: constraints on the shallow dynamics of Strombolian explosions

VII.1. Introduction

Studies carried out in this thesis focused on the better understanding of radar signals through numerical modelling and detailed analysis of Doppler radar measurements and to some extent, on acoustic measurements. The objective of this section is to combine both methods in order to bring further constraints on the Strombolian dynamics. This study is a preliminary work and necessitates further investigations. Acoustic measurements depict sub-surface mechanisms directly at the origin of the surface activity monitored by VOLDORAD.

The study of acoustic signals has provided particularly quantitative information on the internal bubble pressure. This parameter is potentially very important for the understanding of source mechanisms at the origin of gas and hence particles ejection. On the other hand, the study of Doppler radar signals has brought accurate constraints on particle and gas velocities.

We first focus in this preliminary work on temporal correlations between Acoustic pressure and Doppler radar signals. Then we study the quantitative correlations between, mainly, acoustic pressure and radial velocities recorded by VOLDORAD. Finally, we present a method to derive the initial gas velocity from acoustic power calculation, subsequently compared with radar-derived initial gas velocities. This work has been carried out on various time scales, during the eruption of July 4, 2001 at Etna SEC.

VII.2. Temporal correlations of acoustic and radar measurements

VII.2.1. The case of four large bubbles

We show here the temporal correlation (Figure VII.1) between acoustic and Doppler radar measurements on one of the four large bubbles studied previously, performed on short sequence of time, and occurring at 2143:04 UT. We provide in the first subplot the recorded acoustic pressure, sampled at 1200 Hz. In the second and third subplot we present respectively the radar power and velocity sampled at about 10 Hz. The radar power (P^+) given here corresponds to the reflectivity of ascending particles in the range gate G_3, and the velocity (V^+_{max}) corresponds to the maximum radial velocity of presumably fine particles in the range gate G_3. For the first time, radar and acoustic temporal series can be compared simultaneously. Many qualitative information are revealed from these preliminary correlations.

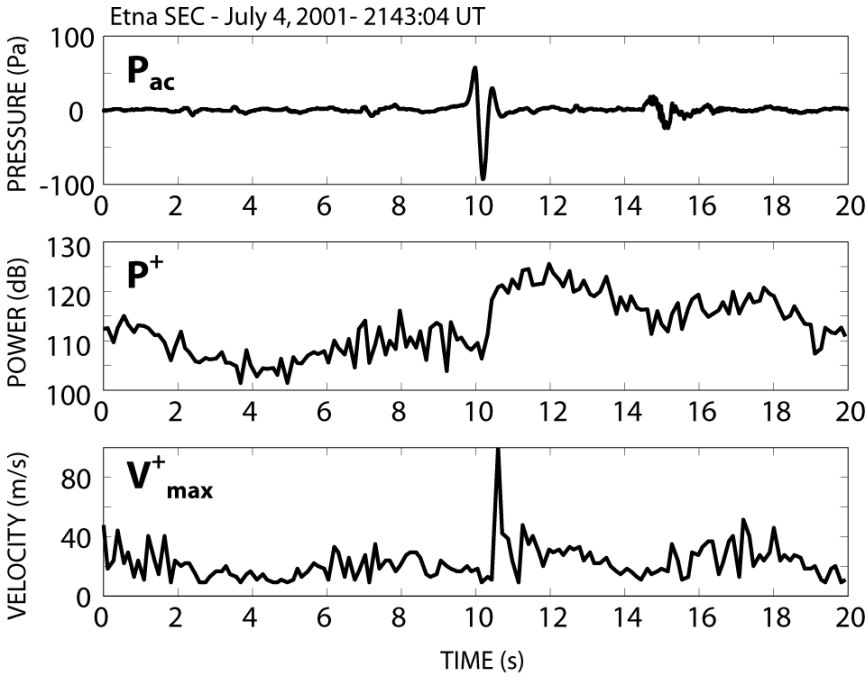

Figure VII.1. Time series of acoustic pressure (P_{ac}) sampled at 1200 Hz, with radar power (P^+) and radial velocity (V^+_{max}) sampled at about 10 Hz, carried out at Etna SEC during the eruption of July 4, 2001. The correlation is performed on a short sequence of 20 seconds centred on the large bubble occurring at 2143:04 UT.

Firstly we observe for both radar power and velocity time series an important signal increase around 10 s, clearly corresponding to the main acoustic pulse. Secondly, we notice that the onset of both power and velocity peaks is impulsive as well as the acoustic one. However, immediately after emergence of radar signals, we observe that the power keeps high values for at least few seconds, whereas the velocity dramatically decrease and gets back to its initial level within about one second. Actually, the radar signals increase starts when ejecta come into the range gate G_3, theoretically a few tenths of a second after the acoustic pulse. Note that we cannot synchronize acoustic and radar signals, so they have been adjusted here by matching the onset of the main peak. So, the time for particles to cross entirely the range gate is responsible for high power values sustained over a few seconds. In contrast, immediately after the pyroclasts ejection, fine particles particularly, severely slow down. As a consequence, in the following we will use preferentially the velocity parameter, as it gives a better temporal resolution, and also permits an accurate detection of small discrete events. On this short sequence of time we are able to observe small acoustic precursors and a secondary

event occurring at about 15 s. These low-amplitude signals are also observed on radar signals with lower power and velocity values but not temporally well-defined. This result would suggest that the amount and velocity of volcanic material ejected could depend, to some extent at least, on the bubble overpressure.

VII.2.2. Analysis of a 100-s sequence of Strombolian activity

Now we compare the acoustic pressure (1200 Hz) and the maximum radial velocity (10 Hz) time series on a longer period of time (100 s) starting during the paroxysm of the July-4 eruption at 2136:00 UT (Figure VII.2). The analysis of this sequence confirms the good temporal correlation peak-to-peak. We show particularly that for most of acoustic pressure peaks, we can observe a high velocity value recorded by the radar, which corroborates first observations on the correlation of both parameters. However in some cases, we also observe relatively high radar velocity values corresponding to very low acoustic pressure. Some examples to illustrate this singular discrepancy are shown in Figure VII.2 by dotted rectangles.

The acoustic pressure is assumed to be generated by the oscillation of bubbles reaching the top of the magma column prior to bursting (Chapter VI), and depends particularly on the radius and overpressure of the bubble. Therefore, we suggest that small bubbles highly pressurized cannot generate high acoustic values, whereas ejecta velocity, depending mostly on the gas phase expansion (i.e., the internal bubble pressure at bursting time), can reach relatively high values.

Other mechanisms can also be considered to explain these occasional discrepancies. Mainly, the passive degassing can induce significant rising velocities of very small particles and gas above the vent, but the sound radiated by such a depressurized mechanism is almost certainly not detected by the acoustic sensor. We also suppose that small instabilities mechanisms developing at the surface of the magma column when the rising bubble is still at depth. Indeed if the magma-air interface distorts sufficiently, some lava fragments can disconnect from the magma layer and cross the above radar range gate with a significant velocity.

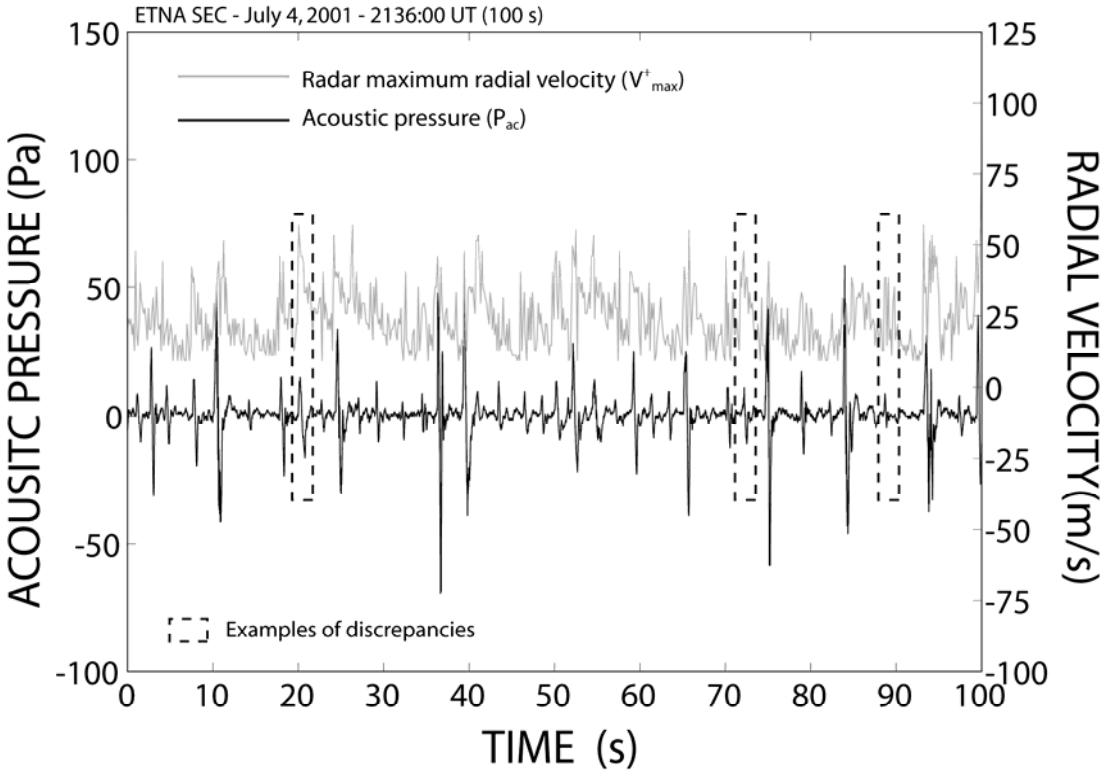

Figure VII.2. Time series of acoustic pressure and radar radial velocity realized on a 100-s sequence starting at 2136:00 UT, during the July-4 eruption.

Generally, in spite of some differences occurring punctually, we show the very existence of a temporal correlation between acoustic pressure and particles velocity ejected upward. Also, we point out a relation, qualitative at least, between both parameters (acoustic pressure and particles velocity) suggesting that the internal gas bubble pressure is responsible at first order of the velocity of ejecta.

VII.2.3. Acoustic pressure as a function of the radial velocity

In order to better interpret this result we have carried out further acoustic and radar velocity measurements related to peak values only, for about 80 explosions occurring during the paroxysm (Figure VII.3). Acoustic pressure values range from about 5 to 50 Pa and correspond to explosions of low to mild amplitude. Comparatively, we obtain radial velocities ranging from 25 to 90 m/s. We show a positive correlation between acoustic pressure and radial velocity for explosions of small intensity. Over about 30 Pa and 50 m/s, the dispersion

increases significantly. We finally calculate the best fit for all explosions measured, which gives a quadratic relation as $P_{ac} = 0.01(V^{+}_{max})^2$.

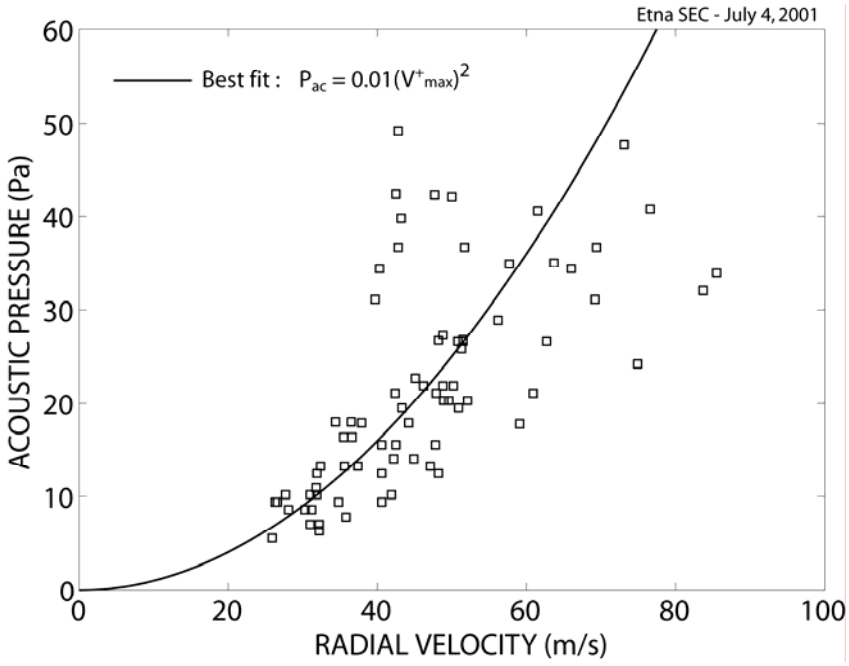

Figure VII.3. Plot of the acoustic pressure as a function of the radial velocity recorded by the Doppler radar on about 80 explosions carried out at Etna SEC between 2100:00 UT and 2200:00 UT on July 4, 2001.

VII.3. Gas velocity correlations from acoustic and radar measurements

VII.3.1. Calculation of the gas velocity from acoustic measurements

The average gas velocity can be estimated from acoustic measurements, by using the acoustic power P_m (Woulff and McGetchin, 1976; Vergniolle et al., 2004):

$$V_{gas} = \left[\frac{P_m C_{air}}{K_m \rho_{air} \pi R_c^2} \right]^{\frac{1}{4}} \qquad \text{(VII.1)}$$

Where R_c is the conduit radius, estimated at about 5 m at Etna SEC, ρ_{air} is the air density (≈ 1 kg/m^3), C_{air} the sound velocity in air (≈ 340 m/s), and K_m a constant equal to 1 for a sphere.

VII.3.2. Example on 9 large bubbles

We have carried out gas velocity estimations from maximum radial velocity (V^{+}_{max}) and acoustic power (P_m) measurements on 9 large bubbles occurring during the paroxysm of the July-4 eruption, between about 2130:00 UT and 2145:00 UT (Figure VII.4). Importantly, gas velocities derived from acoustic measurement are source velocities, i.e., at the top of the magma column, therefore radar velocity measurements have to be extrapolated at the source (initial velocity). For this purpose, we use the source parameter retrieval method developed in Chapter III, applying the geometrical and elevation correction coefficients to obtain the initial gas velocity. We obtain (Figure VII.4) mean initial gas velocities of 118 and 50 m/s from radar and acoustic measurements respectively. The difference is quite large and we show that the dispersion of acoustic-derived gas velocities is important, with a standard deviation of 12 m/s (i.e., 24% of the mean value). In contrast, radar-derived gas velocities show a lower dispersion with a standard deviation of 8 m/s (i.e., 7% of the mean value). The low variability of radar data and the good correlation with video-derived gas velocities given in chapter III lead us to suggest that the acoustic estimation method underestimates initial gas velocity values by at least a factor of 2.

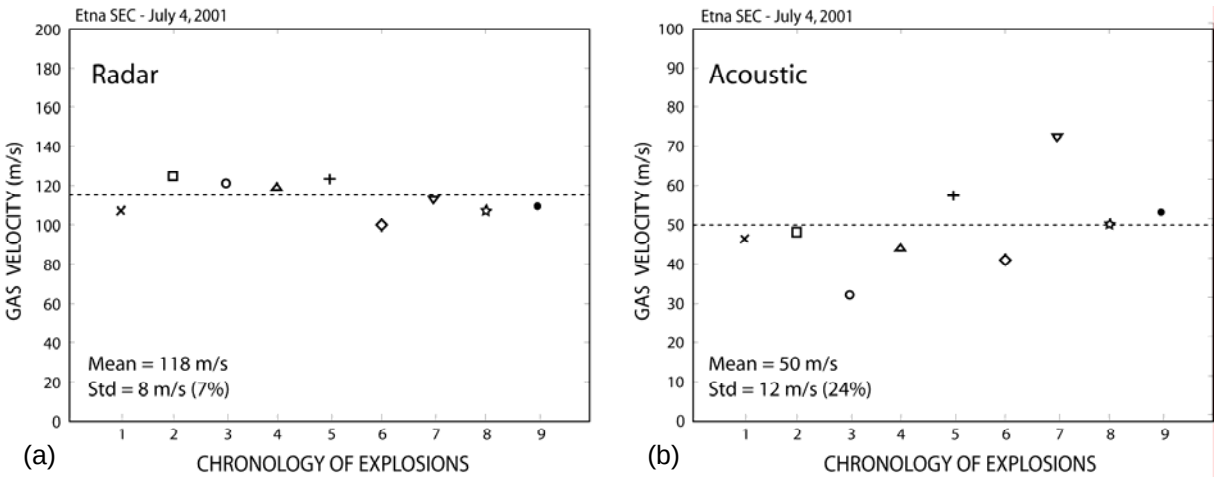

Figure VII.4. Plot of the initial gas velocity for 9 large bubbles (the same as in chapter III) occurring at Etna SEC during the eruption of July 4, 2001 between 2130:00 UT and 2145:00 UT derived from (a) Doppler radar measurements and (b) acoustic measurements.

VII.3.3. Analysis of a 100-s sequence of Strombolian activity

We have shown previously from Figure VII.2 punctual discrepancies between the acoustic pressure and the radial velocity recorded by VOLDORAD. We show here, in addition to the global underestimation of acoustic-derived gas velocities, the same occasional discrepancies. We provide in Figure VII.5, a 100-s time series of acoustic and radar initial gas velocities starting at 2136:00 UT. First we show, as well as for acoustic pressure, that the peak-to-peak temporal correlation between both sets of initial gas velocities is good. However, we also point out local discrepancies of velocity values. The best peak correlations are indicated with the number (1), and those which raise some uncertainties with the number (0). We observe for the peaks in the dotted rectangle that both acoustic-derived gas velocities are rather similar (~55m/s), whereas radar-derived velocities give significantly different values (80 – 120 m/s). As acoustic-derived gas velocities are calculated from the acoustic pressure, we suggest the same possible source of discrepancies (e.g., small bubbles highly pressurized, passive degassing, and instabilities). However, the variability of radar velocities from one explosion to another (see Chapter III) related to possible biases on radar measurements has also to be considered. Note that the mean gas velocity values for all referenced peaks reach 40 and 95 m/s from acoustic and radar methods respectively.

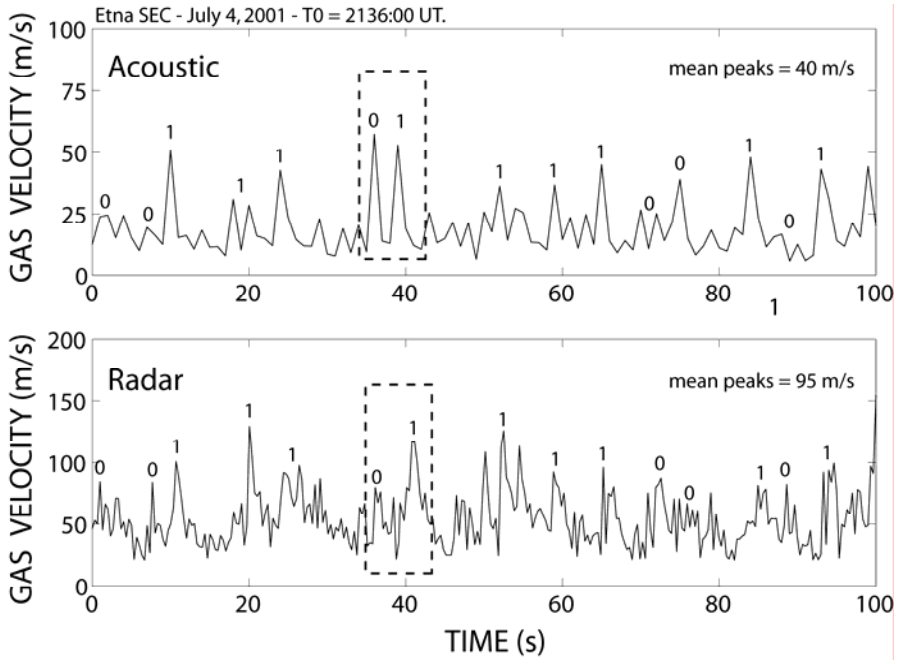

Figure VII.5. Time series of initial gas velocities derived from acoustic and Doppler radar measurements on a 100-s sequence starting at 2136:00 UT during the eruption of July 4, 2001 at Etna SEC.

VII.3.4. Long period correlation between acoustic and radar measurements

The analysis of relatively short sequences of Strombolian activity has shown some local quantitative discrepancies between acoustic-derived velocities or pressures and radar-derived velocities. Keeping in mind these differences, we point out now the very good agreement of both trends over long periods. We show in Figure VII.6 time series of initial gas velocity derived from acoustic and radar measurements, lasting 25 min at the end of the paroxysm (2200:00 UT – 2225:00 UT). We have chosen this period because at that time the activity is very irregular, showing alternately periods of quiescence and of intense activity, which allow us to compare more easily the long-term evolution of both signals. We observe in Figure VII.6, that both signals follow closely the same evolution. This similarity strongly confirms the relation between the acoustic-derived velocities, i.e., the acoustic pressure, and the radar-derived velocities.

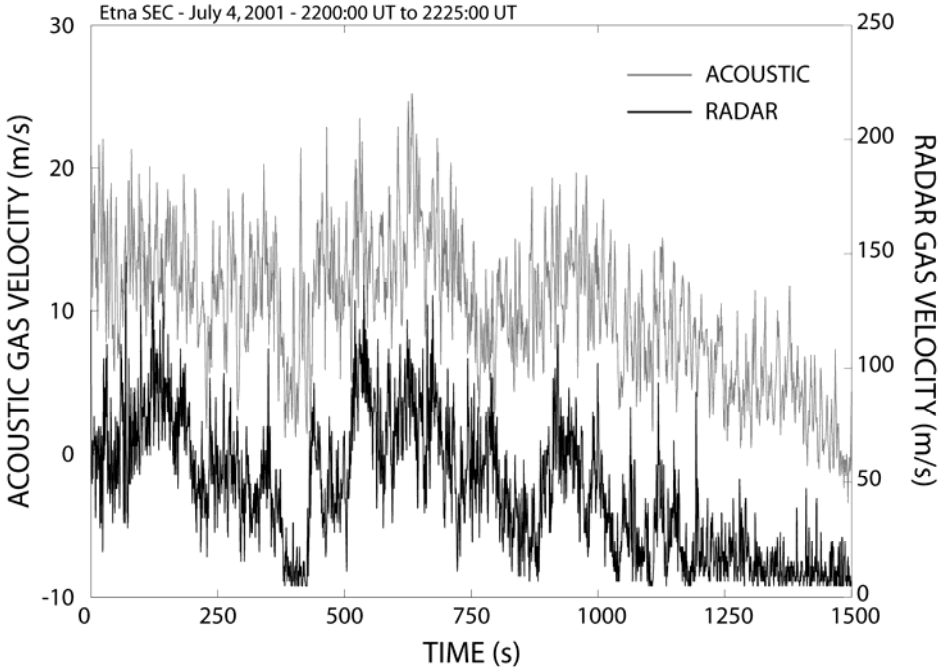

Figure VII.6. Time series of initial gas velocities derived from radar and acoustic measurements on a long sequence carried out from 2200:00 UT and 2225:00 UT at the end of the paroxysm of the July-4 eruption.

VII.4. Conclusion

This study on radar-acoustic correlations is a very preliminary work; however it has pointed out some important features on both signals. First we have shown that the temporal correlation from peak-to-peak events and the long term measurements are very good. Indeed, the acoustic method portrays sub-surface mechanisms (from a few meters to the magma-air interface) directly at the origin of surface manifestations recorded by the Doppler radar. Then, we show that the amplitude of acoustic pressure and radar velocity are in fairly good agreement following roughly a quadratic power law. We have also pointed out that some discrepancies remain punctually between the acoustic pressure and radar velocities. We suggest principally as possible sources of differences, the presence of smaller bubbles highly pressurized, passive degassing or instabilities developing at the surface of the magma column. Finally, estimations of initial gas velocities have been achieved from the calculation of the acoustic power. It reveals initial gas velocity values (40 – 50m/s) underestimated at least by a factor 2 compared to the Doppler radar estimations of initial gas velocity (95 – 118 m/s). The radar-acoustic correlation turns out to be potentially valuable for the understanding of shallow processes at work during Strombolian explosions. This multidisciplinary approach could be further strengthened by using loading parameters (e.g., gas/particles mass flux) inferred particularly from the backscattered power measured by VOLDORAD.

CONCLUSIONS AND FURTHER WORKS

First part: Doppler radar study

The objective of this thesis was to bring more stringent constraints, particularly from the development of methodological procedures, on the interpretation of Doppler radar data with the final aim of better understanding eruption processes.

The thorough analysis of Strombolian explosions carried out by ground-based Doppler radar at Etna Southeast Crater (SEC) in July 4, 2001, has permitted to obtain a wide range of source parameters, mainly related to kinetic, loading and geometrical features. The kinetic study has allowed the determination of a minimum estimate of the initial gas velocity, i.e., close to the vent, from V^{+}_{max} parameter. We provide on more than 150 explosions selected during the paroxysm, a mean initial gas velocity of about 144 m/s. We gain from V^{+}_{mean} a first order estimate of the mean initial particle velocity (67 m/s) and mean particle diameter (0.26 m). These estimations have been corroborated in average by video-derived velocities, although we have shown that some individual discrepancies remain. Indeed, in addition to possible errors inherent of both methods, we mention as potential further biases the high sensitivity of gas velocity calculation, particularly, to the geometry of the explosion. Finally, the acquisition of initial gas velocity has permitted us to calculate velocity-derived parameters such as gas masses and volumes released during the Strombolian eruption occurring on July 4, 2001 at Etna SEC. We obtain an average gas volume flux of $Q_g = 6.03 \times 10^3$ m^3/s, and a gas mass flux of about $M_g = 2.4 \times 10^3$ Kg/s.

In addition to the kinetic data, we have achieved a new step to recover the mass of ejected pyroclasts from remote measurements of particles reflectivity with a volcano Doppler radar (Gouhier and Donnadieu, 2008). Results obtained for two Strombolian explosions occurring in July 4, 2001, at Etna SEC give a total mass of ejected pyroclasts of about 58 tons for a low concentration lava jet and 206 tons for a dense lava jet. The ejected volumes of pyroclasts are evaluated at 28 and 103 m^3 (DRE volumes: 21.6 m^3 and 76.3 m^3) with a mass concentration over the sampling volume of about 18 $g.m^{-3}$ and 63.6 $g.m^{-3}$ for explosions 1 and 2 respectively. We deduce a mean kinetic energy of $4.2.10^7$ J and $3.9.10^8$ J, from the time-averaged maximum radial velocities, 37.9 m/s and 61.6 m/s for explosion 1 and 2 respectively. Finally we provide the ejecta mass flux of each explosions, 26.4 t/s and 73.6 t/s from the explosion duration of 2.2 s and 2.8 s respectively. These results are inferred from a

polydisperse particle size distribution model, but we also developed a monodisperse approximation, with an accuracy of about 25% with respect to the pluridisperse model, that enables first order assessment of the pyroclasts mass in real-time, useful for volcano monitoring.

Finally, we have provided some interesting geometrical features on typical Strombolian jets. Particularly, we point out two distinct signatures: Top-hat-shaped Doppler spectrum related to isotropic ejection angle distribution, and Triangular-shaped Doppler spectrum related to anisotropic ejection angle distribution. In addition we were able to give statistical quantitative information on geometrical features carried out on a large number of typical Strombolian explosions. Particularly we find that 30-40° might be a statistically representative value for the isotropic ejection cone of Strombolian lava jets, at least at Etna, and we search out that typical Strombolian explosions contain most of their ejecta (80–90%) within a relatively narrow dispersion cone (30–40°) centred vertically.

This work has been achieved from Doppler radar (VOLDORAD) measurements carried out at Etna SEC during the eruption of July 4, 2001, and solely focus on the Strombolian dynamics. Nevertheless, results emphasized in this study have to be regarded with the scope of a more general application. Processing methods, theoretical forward models and inversion procedures developed here can hence be utilized as starting point for further works on other eruption styles at different volcanoes. Generally we have shown that VOLDORAD has a great potential for the detection of even very dilute explosions, and hence turns out to be a powerful tool for real-time monitoring and early warnings of volcanic eruptions. In addition to its monitoring potential, we demonstrated its capability for the detailed analysis of lava jets and quantitative assessment of physical source parameters, valuable to the volcanological community as well as for ash dispersal prediction models, used for instance by VAACs (Volcanic Ash Advisory Centres), devoted to the risk mitigation.

Additional correlations with other remote sensing instruments that probe the surface activity would permit first the validation and improvement of Doppler radar estimates, and then it should bring further information on surface processes. For instance, infrared imagery method such as FLIR could replace conventional (visible) video and be utilized particularly for the detection as well as quantification of hot gases velocity. Besides, spectrometric techniques such as DOAS or FTIR, devoted to the study of gas concentration, could be advantageously

coupled with Doppler radar velocimetric measurements to derive accurate gas flux estimates. Also, a coupled approach with satellite-based and ground-based method would probably constitute a valuable step forward for the monitoring of active volcanoes from early warnings (ground-based) to the long range track evolution of ash dispersal (satellite-based).

Second part: multi-method approach

In the second part of this thesis we focused on the study of acoustic measurements carried out at Etna during the same eruption. This method is particularly interesting to describe shallow processes at the interface between the surface and the chamber, and comparison with methods that portray the surface activity (Video and Doppler radar) has brought interesting constraints on the decoupling of physical processes from depth to the surface.

First we gave some evidence, from direct coupled observations, of the very existence of a bubble oscillation at the magma-air interface as the source of sound. Indeed, video snapshots analysis has permitted to give quantitative estimates of bubble radius, velocity and acceleration that showed the cyclic evolution of expansion/contraction stages of the rising bubble. The thorough inspection of video snapshots, associated with theoretical evidences, has shown a magmatic film rupture mechanism by development of instabilities at the bubble-magma interface.

Then, the bubble vibration model is used with some confidence to calculate fundamental source parameters. We give particularly a quantitative estimate of the mean overpressure inside the bubble when reaching the top of the magma column of $\Delta P = 0.36$ MPa, and we provide the mean internal bubble pressure and volume at bursting time reaching $P_g = 0.23$ MPa and $V_g = 1.6 \times 10^3$ m^3 respectively.

However in spite of these strong constraints on the origin of sound, our results on the spectral content analysis do not exclude a possible source of sound from a bursting mechanism based on the balloon bursting model, although much less energetic showing an amplitude about one order of magnitude lower. The complexity of bubble vibration and bursting mechanisms, associated with the difficulties to study large scale phenomena in the natural environment, suggests that further experimental investigations would probably enhance the understanding of life-ending bubble mechanisms.

Finally the study of correlations between acoustic and Doppler radar measurements carried out in this thesis has to be regarded has preliminary work. However, it has pointed out some important features on the relationship of both signals.

First we have shown that the temporal correlation from peak-to-peak as well as long range measurements is very good. Indeed, the acoustic method portrays shallow physical mechanisms directly at the origin of surface manifestations recorded by the Doppler radar as overpressurized bubble bursting is at the origin of the fragmentation and ejection of lava clots subsequently recorded by VOLDORAD. This relationship is confirmed from measurements, carried out on about 80 Strombolian explosions, of acoustic pressure amplitude and radar radial velocities of fine particles ejected subsequently. We show particularly that both sets of data are in fairly good agreement following roughly a quadratic power law.

We have also pointed out punctual discrepancies between the acoustic pressure and radar velocities. We suggest that small bubbles highly pressurized, passive degassing, and instabilities developing at the surface of the magma column can be the possible source of difference Estimations of initial gas velocities has been realised from the calculation of acoustic power. It reveals initial gas velocity values (40 – 50 m/s) underestimated at least by a factor of 2 compared to the Doppler radar estimations of initial gas velocity (95 – 118 m/s). Although radar derived gas velocity can meet some biases, this difference between both methods has to be considered carefully, particularly for gas flux estimates from acoustic measurements.

This multidisciplinary approach would be further investigated by comparing pyroclasts mass that can be estimated from both acoustic and radar techniques. Furthermore, a better time synchronization of both signals would permits the in-depth analysis (<1 sec) of bubble membrane rupture processes.

REFERENCES

– A –

Adams, R. J., W. F. Perger, W. I. Rose, and A. Kostinski (1996), Measurements of the complex dielectric constant of volcanic ash from 4 to 19 GHz, J.Geophys.Res., 101, 8175-8185.

Allard, P. (1995), Mount Etna: a major source of volcanic volatiles to the troposphere (abstract), VIII Assembly Europ. Union of Geosciences, Strasbourg, IV-U, 101.

Allard, P. (1997), Endogeneous magma degassing and storage at Mount Etna, Geophys. Res. Lett., 24, 2219–2222.

Allard, P., N. Bruno, T. Catabiano, M.F. Grasso, N. Lefol, H. Loyer, R. Pinte, M. Porto, and R.Romano (1994a), Etna's crater plume emissions during June 93-March 94 post-eruptive activity: volatile fluxes and magma degassing rate, Proc. Int. Workshop Europ. Laboratory Volcanoes, Aci Castello, Italy, 68-75.

Allard, P., M. Burton and F. Murè (2005), Spectroscopic evidence for a lava fountain driven by previously accumulated magmatic gas, Nature, 433, 407-410, doi:10.1038/nature03246.

Allard, P., J. Carbonelle, M. Métrich, H. Loyer and P. Zettwoog (1994b), Sulfur output and magma degassing budget of Stromboli volcano, Nature, 368, 326-330.

Allard, P., J. Carbonnelle, D. Dajlevic, J.C. Le Bronec, P. Morel, J.M. Maurenas, M.C. Robe, R. Faivre-Pierret, J.C. Sabroux and P. Zettwoog (1991), Eruptive and diffuse emissions of carbon dioxide from Etna volcano, Nature, 351, 387-391.

Allard, P., B. Behncke, S.D'Amico, M. Neri, S. Gambino (2006), Mount Etna 1993–2005: Anatomy of an evolving eruptive cycle, Earth-Science Reviews 78, 85–114.

– B –

Batchelor, G. K. (1967), An Introduction to Fluid Dynamics, Cambridge Univ. Press, New York, 615 pp.

Behncke, B. and M. Neri (2003a), The July-August 2001 eruption of Mt. Etna (Sicily), Bull. Volcanol., 65, 461–476, doi:10.1007/s00445-003-0274-1.

Behncke, B. and M. Neri (2003b), Cycles and trends in the recent eruptive behaviout of Mt. Etna (Italy), Can. J. Earth Sci., 40, 1405-1411, doi:10.1139/E03-052.

Behncke, B., M. Neri, and G. Sturiale (2004), Rapid morphological changes at the summit of an active volcano: reappraisal of the poorly documented 1964 eruption of Mount Etna (Italy), Geomorphology, 63, 203–218, doi:10.1016/j.geomorph.2004.04.004.

Blackburn, E.A., L. Wilson and R.S.J. Sparks (1976), Mechanisms and dynamics of Strombolian activity, J. Geol. Soc. (Lond.), 132, 429-440.

Bluth, G.J.S., C.C. Schnetzler, A.J. Krueger and L.S. Walter (1993), The contribution of explosive volcanism to global atmospheric sulphur dioxide concentrations, Nature, 366, 327-329.

Bluth, G.J.S., J.M. Shannon, I.M. Watson, A.J. Prata and V.J. Realmuto (2007), Development of an ultra-violet digital camera for volcanic SO_2 imaging, J. Volcanol. Geotherm. Res., 161, 47-56, doi:10.1016/j.jvolgeores.2006.11.004.

Bohren, C. F., and D. R. Huffman (1983), Absorption and Scattering of Light by small Particles, Wiley-Interscience, New York, 489 pp.

Branca, S., M. Coltelli, G. Groppelli (2004), Geological Evolution of Etna Volcano, in Mt Etna: Volcano Laboratory, Geophys. Monogr. Ser., vol. 143, edited by A. Bonaccorso et al., pp. 49– 63, AGU, Washington, D.C.

Bruno, N., T. Caltabianoa, S. Giammanco, and R. Romanoa (2001), Degassing of SO_2 and CO_2 at Mount Etna (Sicily) as an indicator of pre-eruptive ascent and shallow emplacement of magma, J. Volcanol. Geotherm. Res., 110, 137-153, doi:10.1016/S0377-0273(01)00201-3.

Buckingham, M.J., and M.A. Garcès (1996), A canonical model of volcano acoustics, J. Geophys. Res., 101, 8129-8151.

Burton, M., P. Allard, F. Muré, A. La Spina (2007), Magmatic Gas Composition Reveals the Source Depth of Slug-Driven Strombolian Explosive Activity, *Science*, Vol. 317. no. 5835, pp. 227 – 230, DOI: 10.1126/science.1141900.

– C –

Caltabiano, T., R. Romano, and G. Budetta (1994), SO_2 flux measurements at Mount Etna (Sicily), J. Geophys. Res., 99, 12809–12819.

Carn, S. A., A. J. Prata, and S. Karlsdóttir (2008), Circumpolar transport of a volcanic cloud from Hekla (Iceland), J. Geophys. Res., 113, D14311, doi:10.1029/2008JD009878.

Chiarabba, C., A. Amato, E. Boschi, Barberi, F. (2000), Recent seismicity and tomographic modeling of the Mount Etna plumbing system, J. Geophys. Res., 105, 10923-10938, doi : 10.1029/1999JB900427.

Chouet, B., N. Hamisevicz, and T. R. McGetchin (1974), Photoballistics of Volcanic Jet Activity at Stromboli, Italy, J. Geophys. Res., 79, 4961-4976.

Chouet, B., G. Saccorotti, P. Dawson, M. Martini, R. Scarpa, G. De Luca, G. Milana and M. Cattaneo (1999), Broadband measurements of the sources of explosions at Stromboli volcano, Italy, Geophys. Res. Lett., 26, 1937-1940.

Clocchiatti, R., P. Schiano, L. Ottolini and P. Bottazzi (1998), Earlier alkaline and transitional magmatic pulsation of Mt Etna volcano, Earth Planet. Sci. Lett.,163, 399-407, doi:10.1016/S0012-821X(98)00170-8.

Coltelli, M., P. Del Carlo, M. Pompilio, and L. Vezzoli (2005), Explosive eruption of a picrite: The 3930 BP subplinian eruption of Etna volcano (Italy), *Geophys. Res. Lett.*, 32, L23307, doi:10.1029/2005GL024271.

Condomines, M., J-C. Tanguy and V. Michaud (1995), Magma dynamics at Mt Etna: Constraints from U-Th-Ra-Pb radioactive disequilibria and Sr isotopes in historical lavas, Earth Planet. Sci. Lett., 132, 25–41.

Corsaro R.A., M. Neri and M. Pompilio (2002), Paleo-environmental and volcano-tectonic evolution of the southeastern flank of Mt. Etna during the last 225 ka inferred from the volcanic succession of the 'Timpe', Acireale, Sicily, J. Volcanol. Geotherm. Res., 113, 289-306, doi:10.1016/S0377-0273(01)00262-1.

Corsaro, R.A., and M. Pompilio (2004a), Dynamics of magmas at Mount Etna, In: Calvari, S., A. Bonaccorso, M. Coltelli, C. Del Negro and S. Falsaperla (Eds.), Mt. Etna: Volcano Laboratory, Am. Geophys. Union Geophys. Monogr., 143, 91–110.

Corsaro, R.A., and M. Pompilio (2004b), Buoyancy-controlled eruption of magmas at Mt Etna, Terra Nova, 16, 16–22, doi:10.1046/j.1365-3121.2003.00520.x.

– D –

Dean, K., S. A. Bowling, G. Shaw, and H. Tanaka (1994), Satellite analyses of movement and characteristics of the Redoubt Volcano plume, J. Volcanol. Geotherm. Res., 62, 339-352.

De Gori, P., C. Chiarabba, and D. Patanè (2005), Qp structure of Mt. Etna: constraints for the physics of the plumbing system, J. Geophys. Res., 110, B05303, doi:10.1029/2003JB002875.

Dehn, J., K. Dean, and K. Engle (2000), Thermal monitoring of North Pacific volcanoes from space Geology, 28, 755-758.

Del Carlo, P., L. Vezzoli, and M. Coltelli (2004), Last 100 ka Tephrostratigraphic record of Mount Etna, in Mt Etna: Volcano Laboratory, Geophys. Monogr. Ser., vol. 143, edited by A. Bonaccorso et al., pp. 77– 89, AGU, Washington, D.C.

Donnadieu F., G. Dubosclard, P. Allard, R. Cordesses, C. Hervier, J. Kornprobst and J. F. Lénat (2003), Sondages des jets volcaniques par radar Doppler : applications à l'Etna. Rapport quadriennal /C.N.F.G.G/. 1999-2002, p.119-124/.

Donnadieu, F., G. Dubosclard, R. Cordesses, T. Druitt, C. Hervier, J. Kornprobst, J. F. Lénat, P. Allard, and M. Coltelli (2005), Remotely Monitoring Volcanic Activity with Ground-Based Doppler Radar, EOS Trans. AGU, 86, 204.

Donnadieu F., G. Dubosclard, R. Cordesses, C. Hervier, P. Allard, M. Gouhier. Monitoring of volcanic jets by Doppler radar: 1. Application to the July 2001 South East Crater activity on Etna. *in prep*.

Doviak, R. J., and D. S. Zrnic (1984), Doppler radar and weather observations, Academic Press, Inc., 562pp.

Dubosclard, G., R. Cordesses, P. Allard, C. Hervier, M. Coltelli, and J. Kornprobst (1999), First testing of a Volcano Doppler Radar (Voldorad) at Mt.Etna, Geophys. Res. Lett., 26, 3389-3392.

Dubosclard, G., F. Donnadieu, P. Allard, R. Cordesses, C. Hervier, M. Coltelli, E. Privitera, and J. Kornprobst (2004), Doppler radar sounding of volcanic eruption dynamics at Mount Etna, Bull. Volcanol., 66, 443-456, doi:10.1007/s00445-003-0324-8.

– F –

Fagents, S.A., and L. Wilson (1993), Explosive volcanic eruptions: VII. The range of pyroclasts ejected in transient explosions, Geophys. J. Int., 113, 359-370.

Francalanci, L., P. Manetti, and A. Pecerillo (1989), Volcanological and magmatological evolution of Stromboli volcano (Aeolian islands): The roles of fractional crystallization, magma mixing, crustal contamination and source heterogeneity, Bull. Volcanol., 51, 335-378.

Francis P., C. Chaffin, A. Maciejewski, and C. Oppenheimer (1996), Remote determination of SiF_4 in volcanic plumes : a new tool for volcano monitoring, Geophys. Res. Lett., 23, 249-252.

– G –

Garcès, M.A., S.R. McNutt, R.A. Hansen, and J.C. Eichelberger (2000), Application of wave-theoretical seismoacoustic models to the interpretation of explosion and eruption tremor signals radiated by Pavlov volcano, Alaska, J. Geophys. Res., 105, 3039-3058.

Gemellaro, C. (1858), La Vulcanologia dell'Etna, Accademia Gioenia di scienze Naturali, Rist. Maimone, 100–111.

Gillot, P.Y., G. Kieffer and R. Romano (1994), Evolution of Mt. Etna volcano in the light of potasium–argon dating, Acta Vulcanologica, 5, 81–87.

Gouhier, M., and F. Donnadieu (2006), Numerical modeling of Doppler radar signals of Strombolian eruptions, AGU Fall meeting, V04, 4177.

Gouhier, M., and F. Donnadieu (2008), Mass estimations of ejecta from Strombolian explosions by inversion of Doppler radar measurements, J. Geophys. Res., 113, B10202, doi:10.1029/2007JB005383.

Gu, Y., W. I. Rose, and G. J. S. Bluth (2003), Retrieval of mass and sizes of particles in sandstorms using two MODIS IR bands: A case study of April 7, 2001 sandstorm in China, Geophys. Res. Lett., 30, 1805, doi:10.1029/2003GL017405.

– H –

Hagerty, M.T., S.Y. Schwartz, M.A. Garcès and M. Protti (2000), Analysis of seismic and acoustic observations at Arenal Volcano, Costa Rica, 1995-1997, J. Volcanol. Geotherm. Res., 101, 27-65.

Harris, D. M., and W. I. Rose (1983), Estimating particles size, concentrations, and total mass of ash in volcanic clouds using weather radar, J. Geophys. Res., 88, 10969-10983.

Harris, D. M., W. I. Rose, R. Roe, and M. R. Thompson (1981), Radar observations of ash eruptions, U.S Geol. Surv. Prof. Pap., 1250, 323-333.

Haulet, R., P. Zettwoog, and J. C. Sabroux (1977), Sulphur dioxide discharge from Mount Etna, Nature, 268, 715-717, doi:10.1038/268715a0.

Head, J.W., and L. Wilson (1987), Lava fountain heights at Pu' u 'O'o, Kilauea, Hawaii: indicators of amount and variations of exsolved magma volatiles, J. Geophys. Res., 92, 13715-13719.

Hort, M., and R. Seyfried (1998), Volcanic eruption velocities measured with a micro radar, Geophys. Res. Lett., 25, 113-116.

Hort, M., R. Seyfried, and M. Vöge (2003), Radar Doppler velocimetry of volcanic eruptions: theoritical considerations and quantitative documentation of changes in eruptive behaviour at Stromboli, Italy, Geophys. J. Int., 154, 515-532.

– J –

Jaupart, C., and S. Vergniolle (1988), Laboratory models of Hawaiian and Strombolian eruptions, Nature, 331, 58– 60.

Jaupart, C., and S. Vergniolle (1989), The generation and collapse of foam layer at the roof of a basaltic magma chamber, J. Fluid Mech., 203, 347-80.

Johnson, J.B., J.M. Lees and E.I. Gordeev (1998), Degassing explosions at Karymsky volcano, Kamchatka, Geophys. Res. Lett., 25, 3999-4002.

Johnson, J.B., and J.M. Lees (2000), Plugs and chugs-seismic and acoustic observations of degassing explosions at Karymsky, Russia and Sangay, Ecuador, J. Volcanol. Geotherm. Res., 101, 67-82, doi:10.1016/S0377-0273(00)00164-5.

– K –

Kittleman, L. R. J. (1964), Application of Rosin's distribution in size frequency analysis of clastic rocks, J.Sediment. Petrol., 34, 483-502.

Kress, V.C., and I.S.E. Carmichael (1991), The compressibility of silicate liquids containing Fe_20_3 and the effect of composition, temperature, oxygen fugacity and pressure on their redox states, Contrib. Mineral. Petrol., 108, 82-92.

Krotkov, N. A., B. McClure, R. R. Dickerson, S. A. Carn, C. Li, P. K. Bhartia, K. Yang, A. J. Krueger, Z. Li, P. Levelt, H. Chen, P. Wang, and D. R. Lu (2008), Validation of SO_2 retrievals from the Ozone Monitoring Instrument (OMI) over NE China, J.Geophys.Res., 113, D16S40, doi:10.1029/2007JD008818.

Krueger, A.J. (1983), Sighting of El Chichón Sulfur Dioxide Clouds with the Nimbus 7 Total Ozone Mapping Spectrometer, Science, 220, 1377-1379.

– L –

Lacasse, C., S. Karlsdottir, G. Larsen, H. Soosalu, W. I. Rose.W, and G. G. J. Ernst (2004), Weather radar observations of the Hekla 2000 eruption cloud, Iceland, Bull. Volcanol., 66, 457-473.

Lanzafame, G., A. Leonardi, M. Neri, D. Rust (1997b), Late overthrust of the Apennine-Maghrebian Chain at the NE periphery of Mount Etna, Italy, Comptes rendus de l'Académie des sciences, Série 2, Sciences de la terre et des planètes, 324, 325-332.

Lentini, F. (1982), The geology of the Mt. Etna basement, Mem. Soc. Geol. Ital., 23, 7-25.

Leighton, T. G. (1994), The Acoustic Bubble, Academic, San Diego, Calif., 613 pp.

Lighthill, J. (1978), Waves in Fluids, Cambridge Univ. Press, New York, 504 pp.

– M –

Marzano, F. S., S. Barbieri, G. Vulpiani, and W. I. Rose (2006b), Volcanic Ash Cloud Retreival by Ground-Based Microwave Weather Radar, IEEE Trans. Geosci. Remote Sens., 44, 3235-3246.

Marzano, F. S., G. Vulpiani, and W. I. Rose (2006a), Microphysical Characterization of Microwave Radar Reflectivity Due to Volcanic Ash Clouds, IEEE Trans. Geosci. Remote Sens., 44, 313-327.

McGetchin, T. R., M. Settle, and B. Chouet (1974), Cinder cone growth modeled after Northeast Crater, Mount Etna, Sicily, J.Geophys.Res., 79, 3257-3272.

McGonigle A. J. S., C. Oppenheimer, B. Galle, T. A. Mather and D.M. Pyle (2002), Walking traverse and scanning DOAS measurements of volcanic gas emission rates, Geophys. Res. Lett., 29, 46.1-46.4.

Métrich N., P. Allard, N. Spilliaert, D. Andronico and M. Burton (2004), 2001 flank eruption of the alkali-and volatile-rich primitive basalt responsible for Mount Etna's evolution in the last three decades, Earth Planet. Sci. lett., 228, 1-17.

Mie, G. (1908), Beiträge zur Optik trüber Medien, speziell kolloidaler Metallösungen, Ann. Phys., 25.

Murru, M., C. Montuori, R. Console and A. Lisi (2005), Mapping of the *b* value anomalies beneath Mt. Etna, Italy, during July–August 2001 lateral eruption, Geophys. Res. Lett., 32, L05309, doi:10.1029/2004GL021545.

– N –

Nakamura, Y. (1984), The 1988 eruption of Bandai volcano, Japan: Grain size distribution, Int. Assoc. of Volcanol. and Chem. of the Earth's Interior, August,13-17.

Neuberg, J., R. Luckett, M. Ripepe, and T. Braun (1994), Highlights from a seismic broadband array on Stromboli volcano, Geophys. Res. Lett., 21, 749-752.

– P –

Parfitt, E.A. (1998), A study of clast size distribution, ash deposition and fragmentation in a Hawaiian-style volcanic eruption, J. Volcanol. Geotherm. Res., 84, 197-208.

Parfitt, E.A., and L. Wilson (1994), The 1983-86 Pu'u 'O'o eruption of Kilauea volcano, Hawaii: a study of dike geometry and eruption mechanisms for a long-lived eruption, J. Volcanol. Geotherm. Res., 59, 179-205.

Parfitt, E.A., and L. Wilson (1995), Explosive volcanic eruptions: IX. The transition between Hawaiian-style lava fountaining and Strombolian explosive activity, Geophys. J. Int., 121, 226-232.

Parfitt, E.A., and L. Wilson (1999), A Plinian treatment of fallout from Hawaiian lava fountains, J. Volcanol. Geotherm. Res., 88, 67-75.

Parfitt, E.A., (2004), A discussion of the mechanisms of explosive basaltic eruptions, J. Volcanol Geotherm Res., 134, 77– 107.

Patanè, D., C. Chiarabba, O. Cocina, P. De Gori, M. Moretti and E. Boschi (2002), Tomographic images and 3D earthquake locations of the seismic swarm preceding the 2001 eruption Mt Etna eruption: Evidence for dyke intrusion, Geophys. Res. Lett., 29/10, 135-1–135-4, doi:10.1029/2001GL014391.

Patanè, D., P. De Gori, C. Chiarabba and A. Bonaccorso (2003a), Magma ascent and the pressurization of Mount Etna's volcanic system, Science, 299, 2061–2063, doi:10.1126/science.1080653.

Patrick, M. R., A. J. L. Harris, M. Ripepe, J. Dehn, D. A. Rothery, and S. Calvari (2007), Strombolian explosive styles and source conditions: insights from thermal (FLIR) video, Bull. Volcanol., 69, 769-784.

Pierce, A.D. (1981), Acoustics: An Introduction to its Physical Principles and Applications, McGraw-Hill, New York, 678 pp.

Pointin, Y., J. Fournet-Fayard, and F. Donnadieu (2005), Calibration du radar UHF VOLDORAD 2, par comparaison de ses données avec celles du disdromètre du LaMP/OPGC., Internal report, Observatoire de Physique du Globe de Clermont-Ferrand, Note OPGC 144, 61pp.

Plesset, M. S., and A. Prosperetti (1977), Bubble dynamics and cavitation, Annu. Rev. Fluid Mech., 9, 145-185.

Prata, A. J., S. A. Carn, A. Stohl, and J. Kerkmann (2007), Long range transport and fate of a stratospheric volcanic cloud from Soufrière Hills volcano, Montserrat, Atmos. Chem. Phys., 7, 5093–5103.

Proussevitch, A.A., and V.A. Kutolin, Surface tension of magmatic melts (in russian), Geol. Geophys., 9, 58-67, 1986.

Proussevitch, A.A., and D.L. Sahagian (1996), Dynamics of coupled diffusive and decompressive bubble growth in magmatic systems, J. Geophys. Res., 101, 17447-17455.

Prosperetti, A. (1986), Bubble dynamics, Proc. Int. School Phys. E. Fermi, 93, 145-188.

– R –

Riley, C. M., I. R. Rose, and J. S. Bluth (2003), Quantitative shape measurements of distal volcanic ash, J.Geophys.Res., 108, 2504.

Ripepe, M. (1996), Evidence for gas influence on volcanic seismic signals recorded at Stromboli, J. Volcanol. Geotherm. Res., 70, 221-233.

Ripepe, M., M. Rossi, and G. Saccorotti (1993), Image processing of explosive activity at Stromboli, J. Volcanol. Geotherm. Res., 54, 335-351.

Ripepe, M., M. Coltelli, E. Privitera, S. Gresta, M. Moretti and D. Piccinini (2001), Seismic and Infrasonic Evidences for an Impulsive Source of the Shallow Volcanic Tremor at Mt. Etna, Italy, Geophys. Res. Lett., 28, 1071-1074.

Rittmann, A., 1973. Structure and evolution of Mount Etna, Philos. Trans. R. Soc. Lond., 274, 5–16.

Rivers, M. L., and I. S. E. Carmichael (1987), Ultrasonic studies of silicate melts, J. Geophys. Res., 92, 9247-9270.

Rogers, R., and M. Yau (1989), A Short Course on Cloud Physics, Pergamon, Oxford, UK.

Rymer, H., J. Cassidy, C.A. Locke and J.B. Murray (1995), Magma movement in Etna volcano associated with the major 1991-1993 lava eruption: evidence from gravity and deformation, Bull. Volcanol., 57, 451-461.

– S –

Sauvageot, H. (1992), Radar meteorology, Artech House Inc., 366pp.

Scandone, R. (1981), Models of volcanic processes: a review and some new ideas, Bull. Volcanol., 44, 256-267, Doi : 10.1007/BF02600563.

Schiano P., R. Clocchiatti, L. Ottolini and T. Busa (2001), Transition of Mount Etna lavas from a mantle-plume to an island-arc magmatic source, Nature, 412, 900-904.

Self, S. (1976), The recent volcanology of Terceira, Azores, J. Geol. Soc. (Lond.), 132, 645-666.

Self, S., R. S. J. Sparks, B. Booth, and G. P. L. Walker (1974), The 1973 Heimaey Strombolian Scoria deposit, Iceland, Geol.Mag., 111, 539-548.

Seyfried, R., and M. Hort (1999), Continuous monitoring of volcanic eruption dynamics: a review of various techniques and new results from a frequency-modulated radar Doppler system, Bull. Volcanol., 60, 627-239, doi:10.1007/s004450050256

Seyfried, R., and A. Freundt (2000), Experiments on conduit flow and eruption behaviour of basaltic volcanic eruptions, J. Geophys. Res., 105, 23727-23740.

Sheridan, M. F. (1971), Particle-size characteristics of pyroclastic tuffs, J.Geophys.Res., 76, 5627-5634.

Sheridan, M. F., K. H. Wohletz, and J. Dehn (1987), Discrimination of grain-size subpopulations in pyroclastic deposits, Geology, 15, 367-370.

Sparks, R.S.J. (1978), The dynamics of bubble formation and growth in magmas: a review and analysis, J. Volcanol. Geotherm. Res., 3, 1-37.

Sparks, R. S. J., and L. Wilson (1982), Explosive volcanic eruptions - V. Observations of plume dynamics during the 1979 Soufrière eruption, St Vincent, Geophys. J. Int., 69, 551 – 570, doi: 10.1111/j.1365-246X.1982.tb04965.x.

Spieler, O., M. Alidibirov, and D. B. Dingwell (2003), Grain-size characteristics of experimental pyroclasts of 1980 Mount St. Helens cryptodome dacite: effects of pressure drop and temperature, Bull. Volcanol., 65, 90-104.

Spilliaert, N., N. Métrich and P. Allard (2006), S-Cl-F degassing pattern of water-rich alkali basalt: Modelling and relationship with eruption styles on Mount Etna volcano, Earth Planet. Sci. Lett., 248, 772-786.

Steinberg, G.S., and J.I. Babenko (1978), Experimental velocity and density determination of volcanic gases during eruption, J. Volcanol. Geotherm. Res., 3, 89-98.

– T –

Tanguy, J-C., and G. Kieffer (1993), Les éruptions de l'Etna et leurs mécanismes, Mem. Soc. Geol. France, 163, 239-252.

Tanguy, J-C., M. Condomines and G. Kieffer (1997), Evolution of Mount Etna magma: Constraints on the present feeding system and eruptive mechanism, J. Volcanol. Geotherm. Res., 75, 221-250.

– U –

Uhira, K., and M. Takeo (1994), The source of explosive eruptions of Sakurajima volcano, Japan, J. Geophys. Res., 99, 17775-17789.

– V –

Vergniolle, S. (1996), Bubble size distribution in magma chambers and dynamics of basaltic eruptions, Earth Planet. Sci. Lett., 140, 269-279.

Vergniolle, S., Boichu M. and J. Caplan-Auerbach (2004), Acoustic measurements of the 1999 basaltic eruption of Shishaldin volcano, Alaska: 1) Origin of Strombolian activity, J. Volcanol. Geotherm. Res., 137, 109-134.

Vergniolle, S. and Brandeis, G. (1994), Origin of sound generated by Strombolian explosions, Geophys. Res. Lett., 21, 1959-1962.

Vergniolle, S. and Brandeis, G. (1996a), Strombolian explosions: 1. A large bubble breaking at the surface of a lava column as a source of sound, J. Geophys. Res., 101, 20433-20447.

Vergniolle, S., Brandeis, G., Mareschal, J.-C. (1996b), Strombolian explosions: 2. Eruption dynamics determined from acoustic measurements, J. Geophys. Res., 101, 20449-20466.

Vergniolle, S. and C. Jaupart (1986), Separated two-phase flow and basaltic eruptions, J. Geophys. Res., 91, 12842–12860.

Vergniolle, S. and C. Jaupart, (1990), Dynamics of degassing at Kilauea volcano, Hawaii, J. Geophys. Res., 95, 2793-2809.

Vergniolle, S. and M. Ripepe (2008), From Strombolian explosions to fire fountains at Etna Volcano (Italy): what do we learn from acoustic measurements?, Geol. Soc. (Lond.), Special Publications, 307, 103-124.

Vosteen, H. D., and R. Schellschmidtb (2003), Influence of temperature on thermal conductivity, thermal capacity and thermal diffusivity for different types of rock, Physics and Chemistry of the Earth, 28, 499-509.

– W –

Wadge G., D.G. Macfarlane, D.A. Robertson, A.J. Hale, H. Pinkerton, R.V. Burrell, G.E. Norton, eand M.R. James (2005), AVTIS: A novel millimetre-wave ground based instrument for volcano remote sensing, J. Volcanol. Geotherm. Res., 146, 307-318, doi:10.1016/j.jvolgeores.2005.03.003.

Walker, G.P.L. (1973), Explosive volcanic eruptions - new classification scheme, Geol. Rundsch., 62, 431– 446.

Wallis, G. B. (1969), One Dimensional Two-Phase Flows, McGraw-Hill, New-York, 408 pp.

Watson, I. M., V. J. Realmuto, W. I. Rose, A. J. Prata, G. J. S. Bluth, Y. Gu, C. E. Bader and T. Yu (2004), Thermal infrared remote sensing of volcanic emissions using the moderate resolution imaging spectroradiometer, J. Volcanol. Geotherm. Res., 135, 75-89.

Weibull, W. (1939), A statistical theory of the strength of materials, Roy. Swed. Inst. Eng. Res., 151.

Weill, A., G. Brandeis, S. Vergniolle, F. Baudin, J. Bilbille, J. F. Fèvre, B. Piron, and X. Hill (1992), Acoustic sounder measurements of the vertical velocity of volcanic jets at Stromboli volcano, Geophys. Res. Lett., 19, 2357-2360.

Williams, H., and A. R. McBirney (1979), Volcanology, Freeman Cooper, San Francisco, 397pp.

Wilson, L. (1980). Relationships between pressure, volatile content and ejecta velocity in three types of volcanic explosion, J. Volcanol. Geotherm. Res., 8, 297– 313.

Wohletz, K. H., M. F. Sheridan, and W. K. Brown (1989), Particle Size Distributions and the Sequential Fragmentation/Transport Theory Applied to Volcanic ash, J.Geophys.Res., 94, 703-715,721.

Wolf, S., and N. V. Voshchinnikov (2004), Mie scattering by ensembles of particles with very large size parameters, Comput. Phys. Commun., 162, 113-123.

Woods A. W. (1993), Moist convection and the injection of volcanic ash into the atmosphere, J. Geophys. Res., 98, 17627-17636.

Woods, A. W., and M. I. Bursik (1991), Particle fallout, thermal disequilibrium and volcanic plumes, Bull. Volcanol., 53, 559-570

Woulff, G., T. R. McGetchin (1976), Acoustic Noise from Volcanoes: Theory and Experiment, Geophys. J. Int., 45, 601–616.

APPENDIX

Appendix A

Ballistic model equations and code

Ballistic model equations

To simulate the ejection of pyroclasts during a Strombolian explosion, we use and enhanced a two-dimensional ballistic model initially developed by Dubosclard et al. (2004). The ballistic model assumes that two forces are acting on the particle of mass m_p: the drag force F_D (with a direction opposite to the velocity vector) and the gravitational force. So, the equations of motion can be written as:

$$\frac{d^2x}{dt^2} = \frac{F_{Dx}}{m_p}$$
$$\frac{d^2z}{dt^2} = \frac{F_{Dz}}{m_p} - g \qquad \text{(A1)}$$

where F_{Dx} and F_{Dz} are the components of the drag force and g is the acceleration due to gravity. F_D is given by (e.g. Chow 1979):

$$F_D = \frac{1}{2}\rho_g A C_D \left(v_g - v_p\right)^2 \qquad \text{(A2)}$$

where ρ_g is the gas density, A is the cross-sectional area of the particle, C_D is the particle drag coefficient deduced from the Reynolds number calculation according to the method suggested by Chow (1979), v_g (components: u_g, v_g) and v_p (components: u_p, v_p) are the gas and particle velocities. After some rearrangement, equation. 2 can be rewritten as:

$$\frac{d^2x}{dt^2} = \left(\frac{3}{4}\frac{\rho_g}{\rho_p}\frac{C_D}{D}\right)\left(u_g - u_p\right)|w|$$
$$\frac{d^2z}{dt^2} = \left(\frac{3}{4}\frac{\rho_g}{\rho_p}\frac{C_D}{D}\right)\left(v_g - v_p\right)|w| - g \qquad \text{(A3)}$$

where ρ_p is the particle density, taken equal to 1530 Kg.m^{-3} (e.g. McGetchin et al., 1974), D its diameter and:

$$|w| = \sqrt{\left(u_g - u_p\right)^2 + \left(v_g - v_p\right)^2} \tag{A4}$$

For simplifications, the particles are taken spherical and compositionally homogeneous. They are launched at the volcano vent (origin of the coordinate system) at time t=0 with an initial velocity V_0^p and an initial ejection angle α_0. The initial velocity of a particle with a diameter D is taken as (Steinberg and Babenko, 1978):

$$V_0^p(D) = V_0^g - k\sqrt{D} \tag{A5}$$

where k is a constant taken equal to 150, as inferred from previous studies [*Chouet et al.*, 1974; *Ripepe et al.*, 1993]. The velocity of particles directly depends on the initial gas velocity V_0^g that decreases exponentially with height [Blackburn et al., 1976] according to:

$$V_g(z) = V_0^g \exp\left(\frac{-\gamma z}{z_{ref}}\right) \tag{A6}$$

where γ is a constant taken equal to 4.6 and z_{ref} is the height above the vent such as $V_g\left(z_{ref}\right) = 0.01 V_0^g$ [Blackburn et al., 1976].In order to simulate the radar signal received from an explosion, the system (Eqs. 3) is numerically integrated by using a fourth-order Runge-Kutta method, with a time step of 0.01 s. At t=0, a set of N particles with different diameters (D) defining a specific particle size distribution $N(D)$ (e.g., exponential, log-normal or Gaussian) are launched over a range of ejection angles from the origin of coordinates. At each time step, the coordinates of all particles are determined. Then, for all the particles located inside the selected range gates, our model calculates their velocity.

Ballistic model code

```
%-------------------------------------------------------%
%-------------------- Initialisation -------------------%
%-------------------------------------------------------%

nbdiamdeb = 1;
nbdiamfin = nbdiam;
l = lambda(1)*1000;
rhob = rhog/rhop;
A = 1+(rhob/2);
B = (1-rhob)*g;

for aa = 1:nbdiam
   D = diam(aa);
   D3(aa) = exp(3*log(D*1000));
   D6(aa) = exp(6*log(D*1000));

   for ii = 1:nbangles

      tbx(aa,ii) = 0;
      tby(aa,ii) = 0;
      w0 = vg0-150*sqrt(diam(aa));
      tbu(aa,ii) = w0*cos(pi*angles(ii)/180);
      tbv(aa,ii) = w0*sin(pi*angles(ii)/180);

      tbx2(aa,ii) = 0;
      tby2(aa,ii) = 0;
      tbu2(aa,ii) = w0*cos(pi*angles2(ii)/180);
      tbv2(aa,ii) = w0*sin(pi*angles2(ii)/180);

      tbx3(aa,ii) = 0;
      tby3(aa,ii) = 0;
      tbu3(aa,ii) = w0*cos(pi*angles3(ii)/180);
      tbv3(aa,ii) = w0*sin(pi*angles3(ii)/180);

      tbx4(aa,ii) = 0;
      tby4(aa,ii) = 0;
      tbu4(aa,ii) = w0*cos(pi*angles4(ii)/180);
      tbv4(aa,ii) = w0*sin(pi*angles4(ii)/180);

   end
end

%-------------------------------------------------------%
%---------------------- Cal_param ----------------------%
%-------------------------------------------------------%

vmaxi=9.2; vmoy=0; refl=0; masse=0; Masse_tot=0;  t=0;
val_t = 0; ctv = 0;
flag = 0; P = 0; T = 0;

fid1 = fopen('param.txt','w');
while val_t<tfin;

if ctv == 0
vmoy = 0;
else
vmoy = vmoy/ctv;
end

if t>=tdeb
  fprintf(fid,'%5.4f %5.4f %5.4f %5.4f %5.4f
%5.4f\n',t,vmaxi,vmoy,masse,refl,P);
  refl = 0; masse = 0; vmaxi = 9.2; vmoy = 0; ctv = 0; P =
0;
end

if val_t>=inter_pulse
     val_t2 = val_t-inter_pulse;

for ii = 1:nbangles
   theta0 = angles2(ii);
for aa = nbdiamdeb : nbdiamfin
   C = 0.75*rhob/diam(aa);
   x2 = tbx2(aa,ii);
   y2 = tby2(aa,ii);
   u2 = tbu2(aa,ii);
   v2 = tbv2(aa,ii);
   t2 = val_t2;
   r2 = sqrt(x2^2+y2^2);

if y == 0
  beta = 0;
else
  beta = atan(x/y);
end

w = vg0*exp(-gamma*r2/r_ref);
ug = w*sin(beta);
vg = w*cos(beta);

%-------------------------------------------------------%
%---------------------- Cal_ Cd ----------------------%
%-------------------------------------------------------%

Re = abs(v2)*D/nu;
if Re == 0
    Cd = 0;
elseif Re>0 & Re <=1
    Cd = 24/Re;
elseif Re>1 & Re<=400
   Cd = 24/Re^0.646;
elseif Re>400 & Re<=300000
   Cd = 0.5;
elseif Re>300000 & Re<=2000000
   Cd = 0.000366*Re^0.4275;
elseif Re>2000000
   Cd = 0.18;
end

%-------------------------------------------------------%
%------------------ Runge Kutta 4 ----------------%
%-------------------------------------------------------%

 h=delta_t;
 d1x=h*u2;
 d1y=h*v2;
 d1u=h*(C*Cd*(ug-u2)*(sqrt((ug-u2)^2+(vg-v2)^2)))/A;
 d1v=h*(-B+(C*Cd*(vg-v2)*(sqrt((ug-u2)^2+(vg-v2)^2))))/A;

 d2x=h*(u2+d1u/2);
 d2y=h*(v2+d1v/2);
 d2u=h*(C*Cd*(ug-(u2+d1u/2))*(sqrt((ug-(u2+d1u/2))^2+(vg-
(v2+d1v/2))^2)))/A;
 d2v=h*(-B+(C*Cd*(vg-(v2+d1v/2))*(sqrt((ug-(u2+d1u/2))^2+(vg-
(v2+d1v/2))^2))))/A;

 d3x=h*(u2+d2u/2);
 d3y=h*(v2+d2v/2);
 d3u=h*(C*Cd*(ug-(u2+d2u/2))*(sqrt((ug-(u2+d2u/2))^2+(vg-
(v2+d2v/2))^2)))/A;
 d3v=h*(-B+(C*Cd*(vg-(v2+d2v/2))*(sqrt((ug-(u2+d2u/2))^2+(vg-
(v2+d2v/2))^2))))/A;

 d4x=h*(u2+d3u);
 d4y=h*(v2+d3v);
 d4u=h*(C*Cd*(ug-(u2+d3u/2))*(sqrt((ug-(u2+d3u/2))^2+(vg-
(v2+d3v/2))^2)))/A;
 d4v=h*(-B+(C*Cd*(vg-(v2+d3v/2))*(sqrt((ug-(u2+d3u/2))^2+(vg-
(v2+d3v/2))^2))))/A;

 dx2=(d1x+2*d2x+2*d3x+d4x)/6;
 dy2=(d1y+2*d2y+2*d3y+d4y)/6;
 du2=(d1u+2*d2u+2*d3u+d4u)/6;
 dv2=(d1v+2*d2v+2*d3v+d4v)/6;
 %-------------------------------------------------------------------%
x2 = x2+dx2; y2 = y2+dy2; u2 = u2+du2; v2 = v2+dv2; t2 =
t2+delta_t;
```

```
 if sens==0
 flag=0;
 elseif y2>tby2(aa,ii)
 flag=1;
 flag=flag-sens;
 elseif y2<tby2(aa,ii)
 flag=2;
 flag=flag-sens;
 end

 tbx2(aa,ii) = x2;
 tby2(aa,ii) = y2;
 tbu2(aa,ii) = u2;
 tbv2(aa,ii) = v2;

 xr = x2+935 ; yr = y2+270;
 alpha = atan(yr/xr);
 rr = sqrt(xr^2+yr^2);
 fprintf(fid1,'%5.5f %5.5f\n',xr,yr);

 if pos==1
rvr1 = 985;
rvr2 = 1227;

 elseif pos==2
rvr2 = 985;
rvr1 = 0;
 elseif pos==0
rvr1 = 0;
rvr2 = 1227;
 end

 if r0<rr & rr<r1 & a0<alpha & alpha<a1 & rr>rvr1 & rr<rvr2

    if flag == 0
   refl = refl+exp(-((site-
alpha)^2)/0.10482)*exp(l*diam(aa))*D6(aa);
   masse = masse+exp(l*diam(aa))*D3(aa);

   P = 10*log10(refl);
   if P <60
      P = 60;
   end

anglvise = atan(yr/xr);

 if v2 == 0
   vr = u2*cos(anglvise);
 else
   vr= sqrt(u2^2+v2^2);
   psi = abs(atan(u2/v2));
 end

%-------------------------------------------------%
%------------------ Cal_Vrad ------------------%
%------------------------------------------------ -%

if u2 >= 0 & v2>0
    vr = vr*sin(anglvise+psi);
elseif u2 <= 0 & v2>0
    vr = vr*sin(anglvise-psi);
elseif u2 <= 0 & v2<0
    vr = -vr*sin(anglvise+psi);
elseif u2 >= 0 & v2<0
    vr = -vr*sin(anglvise-psi);
end

fprintf(fid2,'%5.5f %5.5f %5.5f\n',t,vr,refl);

if flag == 0 & vr>0
  vmoy = vmoy+vr;
  ctv = ctv+1;
  if sens==0 & pos==0 & vmoy >0
      vmoy=0;
  end

if abs(vr)>vmaxi
   vmaxi = vr;

if vmaxi<9.2 & vmaxi>=0
     vmaxi = 9.2;
end

if vmaxi<0 & vmaxi>-9.2
      vmaxi = -9.2;
end

if sens==0 & pos ==0 & vmaxi>9.2
 vmaxi = 9.2;
end

end
end
end
end
end
end
end
```

Appendix B

Electromagnetic scattering model equations, code and graphical interface

Electromagnetic scattering model equations (Mie)

Considering the wide range of particle diameters characterizing volcanic activity, the complete scattering theory is required to account for the effects of large particles. A general solution of electromagnetic wave scattering was given by *Mie* [1908]. The derivation of the electromagnetic scattering model specifically applied to the case of volcanic studies is developed in this section. In this first approach of scattering by volcanic ejecta, we apply Maxwell's equations for plane-wave scattered by spherical particles in a homogeneous medium at a large distance [e.g., *Bohren and Huffman,* 1983].

Starting with Maxwell's equation for plane waves:

$$\nabla \bullet E = 0 \tag{B1}$$

$$\nabla \bullet H = 0 \tag{B2}$$

$$\nabla \times E = i\omega\mu H \tag{B3}$$

$$\nabla \times H = -i\omega\varepsilon E \tag{B4}$$

where E and H are the electric and magnetic fields. ε is the dielectric permittivity, μ is the magnetic permeability, and ω is angular frequency. Taking the curl of (A3) and (A4), gives:

$$\begin{aligned} \nabla \times (\nabla \times E) &= i\omega\mu\nabla \times H = \omega^2 \varepsilon\mu E \\ \nabla \times (\nabla \times H) &= -i\omega\varepsilon\nabla \times E = \omega^2 \varepsilon\mu H \end{aligned} \tag{B5}$$

If we use the vector identity,

$$\nabla \times (\nabla \times A) = \nabla(\nabla \bullet A) - \nabla \bullet (\nabla A) \tag{B6}$$

we obtain

$$\nabla^2 E + \omega^2 \varepsilon\mu E = 0 \qquad \nabla^2 H + \omega^2 \varepsilon\mu H = 0 \tag{B7}$$

where $\nabla^2 A = \nabla\bullet(\nabla A)$. Thus, E and H satisfy the wave equation. The field inside the particle is denoted by (E_1, H_1); the field in the medium surrounding the particle (E_2, H_2) is the superposition of the incident field (E_i, H_i) and the scattered field (E_s, H_s):

$$E_2 = E_i + E_s \qquad H_2 = H_i + H_s \tag{B8}$$

The electromagnetic field is required to satisfy the Maxwell equations at points where ε and μ are continuous. However, there is a discontinuity at the boundary of the particle, where the following conditions on the fields are imposed:

$$\begin{aligned} \left[H_2(x) - H_1(x)\right] \times n_s &= 0 \\ \left[E_2(x) - E_1(x)\right] \times n_s &= 0 \end{aligned} \tag{B9}$$

where n_s is the outward-directed normal to the surface of the particle. Under the conditions of our study (far-field region and spherical particle), the scattered field E_s is mainly transverse and can be resolved into components parallel ($E_{//}$) and perpendicular ($E_{\perp}$) to the scattering plane. The relationship between incident and scattered field amplitudes can be written in matrix form:

$$\begin{pmatrix} E_{//s} \\ E_{\perp s} \end{pmatrix} = \frac{e^{ik_n(R-r_z)}}{-ik_n R} \begin{pmatrix} S_2 & 0 \\ 0 & S_1 \end{pmatrix} \begin{pmatrix} E_{//i} \\ E_{\perp i} \end{pmatrix} \tag{B10}$$

where $k_n = 2\pi/\lambda$ is the wave number, R, the distance to the particle, and r_z, the component of R on the direction of propagation of the incident wave. The radiation of an electromagnetic wave can be described in terms of intensity from the four Stokes parameters (I, Q, U, V) describing the various states of polarization: not polarized (I), polarized horizontally ($+Q$) , polarized vertically ($-Q$), polarized at +45° ($+U$) , polarized at -45° ($-U$), right-circularly polarized ($+V$) or left-circularly polarized ($-V$). The relationship between incident and scattered Stokes parameters (indexed i and s respectively) follows from the amplitude scattering matrix, also called the Mueller matrix [*Bohren and Huffman*, 1983; *Wolf and Voshchinnikov*, 2004]:

$$\begin{pmatrix} I_s \\ Q_s \\ U_s \\ V_s \end{pmatrix} = \frac{\lambda^2}{4\pi^2 R^2} \begin{pmatrix} S_{11}(\Theta) & S_{12}(\Theta) & 0 & 0 \\ S_{12}(\Theta) & S_{11}(\Theta) & 0 & 0 \\ 0 & 0 & S_{33}(\Theta) & S_{34}(\Theta) \\ 0 & 0 & -S_{34}(\Theta) & S_{33}(\Theta) \end{pmatrix} \begin{pmatrix} I_1 \\ Q_i \\ U_i \\ V_i \end{pmatrix} \tag{B11}$$

The scattering matrix elements ($S_{i,j}$) depend on Θ, which is the angle between the direction of the incident and the scattered radiation of wavelength λ. VOLDORAD transmits power through a square array of four Yagi antennas, such that the incident wave has a horizontal linear polarization (I_i=1, Q_i=1, U_i=0, V_i=0). Thus, in our case, we denote by $i_{//}$ the corresponding scattered irradiance that only depends on the two first scattering matrix elements (S_{11}, S_{12}):

$$i_{//} = S_{11} + S_{12} = |S_2|^2 \tag{B12}$$

with

$$\begin{aligned} S_{11}(\Theta) &= \frac{1}{2}\left(|S_2(\Theta)|^2 + |S_1(\Theta)|^2\right) \\ S_{12}(\Theta) &= \frac{1}{2}\left(|S_2(\Theta)|^2 - |S_1(\Theta)|^2\right) \end{aligned} \tag{B13}$$

The sum of the two first scattering matrix elements can then be derived from the single complex amplitude function S_2 in the form of a convergent series:

$$S_2(\Theta) = \sum_{n=1}^{\infty} \frac{2n+1}{n(n+1)}\left(a_n \tau_n(\Theta) + b_n \pi_n(\Theta)\right) \tag{B14}$$

where n is a positive integer, a_n and b_n are the complex scattering coefficients (Mie coefficients), and τ_n and π_n are the angular functions. The series can be terminated after n_c sufficiently large terms. The complex scattering coefficients depend particularly on the size parameter x and the refractive index m of the material [Sauvageot, 1992] and are defined as:

$$\begin{aligned} a_n &= \frac{m\psi_n(mx)\psi_n'(x) - \psi_n(x)\psi_n'(mx)}{m\psi_n(mx)\xi_n'(x) - \xi_n(x)\psi_n'(mx)} \\ b_n &= \frac{\psi_n(mx)\psi_n'(x) - m\psi_n(x)\psi_n'(mx)}{\psi_n(mx)\xi_n'(x) - m\xi_n(x)\psi_n'(mx)} \end{aligned} \tag{B15}$$

The size parameter $x = kr$ is a dimensionless variable, r, being the radius of the spherical particle. Ψ and ξ are the Riccati-Bessel functions of first and second kind and can be defined by:

$$\psi_n(x) = x.j_n(x)$$
$$\xi_n(x) = j_n(x) + i.y_n(x) \tag{B16}$$

where j_n and y_n are the spherical Bessel functions of first and second kind defined as:

$$j_n(x) = \sqrt{\frac{\pi}{2x}} J_{n+1/2}(x)$$
$$y_n(x) = \sqrt{\frac{\pi}{2x}} Y_{n+1/2}(x) \tag{B17}$$

The spherical Bessel functions satisfy the recurrence relations:

$$z_{n-1}(x) + z_{n+1}(x) = \frac{2n+1}{x} z_n(x)$$
$$(2n+1)\frac{d}{dp} z_n(x) = n z_{n-1}(x) - (n+1) z_{n+1}(x) \tag{B18}$$

The angular functions τ_n and π_n depend only on Θ, and are defined by the Legendre polynomials,

$$\pi_n(\Theta) = \frac{P_n^1(\Theta)}{\sin\Theta}$$
$$\tau_n(\Theta) = \frac{dP_n^1(\Theta)}{d\Theta} \tag{B19}$$

and can be found from the recurrence relations:

$$\tau_n(\Theta) = n\cos\Theta\,\pi_n(\Theta) - (n+1)\pi_{n-1}(\Theta)$$
$$\pi_n(\Theta) = \frac{2n-1}{n-1}\cos\Theta\,\pi_{n-1}(\Theta) - \frac{n}{n-1}\pi_{n-2}(\Theta) \tag{B20}$$

The scattered irradiance can now be calculated for any particle size, under the special conditions of our sounding using VOLDORAD at Mt. Etna (Figure 1). Determining the scattering matrix elements enables us to define the scattering cross section of each particle; this then relates irradiance to reflectivity through the Mie coefficients. VOLDORAD is a monostatic radar (i.e., the same antenna is used for transmission and reception), thus we define a backscattering cross section (σ_{bks}) for horizontal linear polarization:

$$\sigma_{bks} = \frac{\lambda^2}{4\pi}\left|\sum_{n=1}^{\infty}(-1)^2(2n+1)(a_n - b_n)\right|^2 \tag{B21}$$

Note that we often use the backscattering efficiency defined as the cross section coefficient normalized by the particle section such as:

$$Q_{bks} = \frac{\sigma_{bks}}{\pi r^2} \tag{B22}$$

The theoretical radar power for a distributed target in a sampling volume (V_s) at a given distance (R) can then be deduced from the radar reflectivity (η), which is simply the sum of the backscattering cross section (σ_{bks}) of each particle over a unit volume [*Doviak and Zrnic*, 1984; *Sauvageot*, 1992],

$$P_{synth} = \frac{C_r V_s \eta}{R^4} \tag{B23}$$

$$\eta = \sum_{i=1}^{n}\frac{\sigma_{bks}}{V_s} \tag{B24}$$

where C_r is the radar constant defined by a set of technical parameters related to the radar configuration.

Mie/Rayleigh code

```
%---------------------------------------------------------------%
%------ Mie scattering coefficients (An, Bn) ------%
%---------------------------------------------------------------%

xmax = size(x,2);
for j = 1:xmax
compteur_j = j;

m = real(m);
N = (1:nmax)';

%-- Décomposition en Série infinie de Ricatti-Bessel (Ordre 1) --%
nst = ceil(nmax + sqrt(101+x(j)));
phi(nst,1) = 0;
phi(nst-1,1) = 1e-10;
for n=nst-2:-1:1
phi(n,1) = (2*n+3)*phi(n+1)/x(j) - phi(n+2);
end
phi0 = 3*phi(1)/x(j) - phi(2);
phi0 = sin(x(j))/phi0;
phi = phi(1:nmax,:) * phi0;

%-- Décomposition en Série infinie de Ricatti-Bessel (Ordre 1) --%
nst = ceil(nmax + sqrt(101+(m*x(j))));
phim(nst,1) = 0;
phim(nst-1,1) = 1e-10;
for n=nst-2:-1:1
phim(n,1) = (2*n+3)*phim(n+1)/(m*x(j)) - phim(n+2);
end
phi0 = 3*phim(1)/(m*x(j)) - phim(2);
phi0 = sin(m*x(j))/phi0;
phim = phim(1:nmax,:) * phi0;

%-- Décomposition en Série infinie de Ricatti-Bessel (Ordre 2) --%
zeta(1,1) = -cos(x(j))/(x(j)) - sin(x(j));
zeta(2,1) = 3*zeta(1)/(x(j)) + cos(x(j));
for n=3:nmax
zeta(n,1) = (2*n-1)*zeta(n-1)/(x(j)) - zeta(n-2);
end

%-- Décomposition en série infinie de Hankel(1) --%
xi = phi + i * zeta;
phin_1 = [sin(x(j));phi(1:nmax-1)];
phimn_1 = [sin(m*x(j));phim(1:nmax-1)];
zetan_1 = [-cos(x(j));zeta(1:nmax-1)];

%--- Calcul de dérivées des séries de RB (1&2) et H(1) ---%
dphi = phin_1-N.*phi/x(j);
dphim = phimn_1-N.*phim/(m*x(j));
dzeta = zetan_1-N.*zeta/x(j);
dxi = dphi + i * dzeta;

%---------- Coefficient de Mie a(n) et b(n) f(nmax) ----------%
a = (m*phim.*dphi - phi.*dphim) ./ (m*phim.*dxi -xi.*dphim);
b = (phim.*dphi - m*phi.*dphim) ./ (phim.*dxi -m*xi.*dphim);


%---------------------------------------------------------------%
%--- Cross sections calculation  (Q, Sigma) ----%
%---------------------------------------------------------------%

Qs = 0;
Qe = 0;
Qb = 0;

for n = 1:nmax

% Qs : Scattering efficiency
Qs = (2*n+1)*(abs(a(n)^2)+abs(b(n)^2))+Qs;

% Qe : Extinction efficiency
Qe = (2*n+1)*real(a(n)+b(n))+Qe;

% Qb : Backscattering efficiency
Qb = abs((2*n+1)*(-1)^2*(a(n)-b(n)))^2+Qb

end

qext = (2*Qe)/x(j).^2;
qsca  = (2*Qs)/x(j).^2;
qabs = qext-qsca;
qbsk = Qb/x(j).^2;

Qext = [Qext,qext];
Qsca = [Qsca,qsca];
Qabs = [Qabs,qabs];
Qbsk = [Qbsk,qbsk];

A = [A,pi*r(j).^2];
rj = [rj,r(j)];
xj = [xj,x(j)];

end

end

Sigma_sca = Qsca.*A;        % Scattering cross section
Sigma_ext = Qext.*A;        % Extinction cross section
Sigma_abs = Qabs.*A;        % Absorption cross section
Sigma_bsk = Qbsk.*A;        % Backscattering cross section


%-------------------------------------------------------------------------%
%---------------------- Rayleigh approximation ------------------%
%-------------------------------------------------------------------------%

%Scattering efficiency
QRsca = ((128*pi^4*rj.^4)/(3*lambda^4))*abs(K)^2;

%Absorbtion efficiency
QRabs = ((8*pi*rj)/(lambda))*imag(K);

%Extinction efficiency
QRext = QRabs + QRsca;

%Backscattering efficiency
QRbsk = ((64*pi^4*rj.^4)/(lambda^4))*abs(K)^2;

SigmaR_sca = QRsca.*A;      % Scattering cross section
SigmaR_abs = QRabs.*A;      % Absorption cross section
SigmaR_ext = QRext.*A;      % Extinction cross section
SigmaR_bsk = QRbsk.*A;      % Backscattering cross section

%-------------------------------------------------------------------------%
```

Graphical interface (ZVMM): **Z**: reflectivity (dBZ) **VMM**: max and mean velocities (m/s)

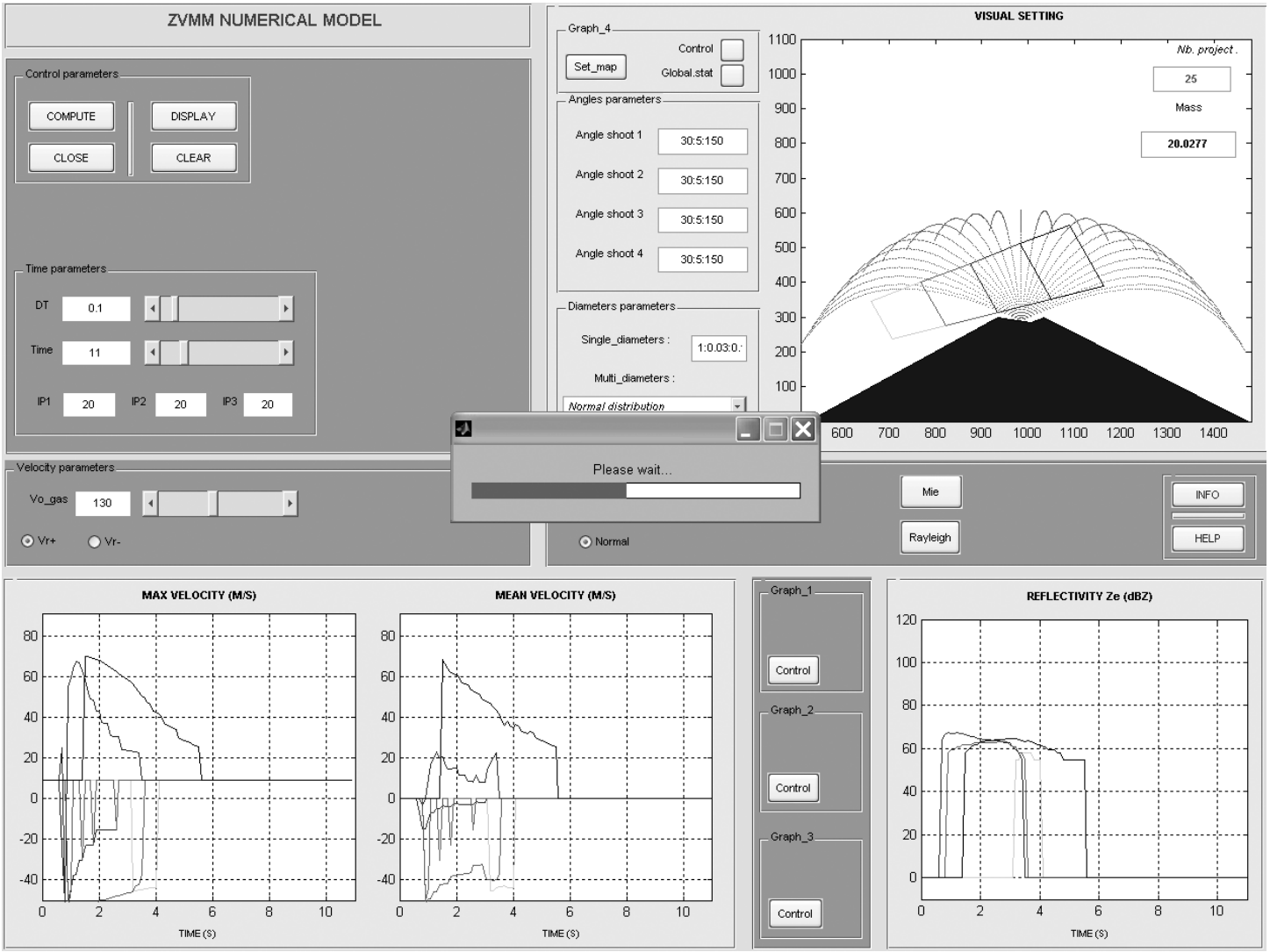

Snapshot of the ZVMM graphical interface developed and used during this thesis for the calculation of (1) synthetic time series of maximum and mean velocities derived from the ballistic model, and (2) synthetic power from the electromagnetic scattering model of Mie and Rayleigh. The particles size distribution (PSD) and the ejection angle distribution (EAD) can be widely varied, and several successive explosions can also be modelled.

Appendix C

Gouhier, M., and F. Donnadieu (2008), Mass estimations of ejecta from Strombolian explosions by inversion of Doppler radar measurements, J. Geophys. Res., 113, B10202, doi:10.1029/2007JB005383.

JOURNAL OF GEOPHYSICAL RESEARCH, VOL. 113, B10202, doi:10.1029/2007JB005383, 2008

Click Here for Full Article

Mass estimations of ejecta from Strombolian explosions by inversion of Doppler radar measurements

Mathieu Gouhier[1] and Franck Donnadieu[1]

Received 13 September 2007; revised 25 June 2008; accepted 23 July 2008; published 4 October 2008.

[1] We present a new method for estimating particle loading parameters (mass, number, volume) of eruptive jets by inversion of echo power data measured using a volcano Doppler radar (VOLDORAD) during typical Strombolian activity from the southeast (SE) crater of Mount Etna on 4 July 2001. Derived parameters such as mass flux, particle kinetic and thermal energy, and particle concentration are also estimated. The inversion algorithm uses the complete Mie (1908) formulation of electromagnetic scattering by spherical particles to generate synthetic backscattered power values. In a first data inversion model (termed the polydisperse model), the particle size distribution (PSD) is characterized by a scaled Weibull function. The mode of the distribution is inferred from particle terminal velocities measured by Doppler radar for each explosion. The distribution shape factor is found to be 2.3 from Chouet et al.'s (1974) data for typical Strombolian activity, corresponding to the lognormal PSDs commonly characteristic of other Strombolian deposits. The polydisperse model inversion converges toward the Weibull scale factor producing the best fit between synthetic and measured backscattered power. A cruder, alternative monodisperse model is evaluated on the basis of a single size distribution assumption, the accuracy of which lies within 25% of that of the polydisperse model. Although less accurate, the monodisperse model, being much faster, may be useful for rapid estimation of physical parameters during real-time volcano monitoring. Results are illustrated for two explosions at Mount Etna with contrasted particle loads. Estimates from the polydisperse model give 58,000 and 206,000 kg as maxima for the total mass of pyroclasts, 26,400 and 73,600 kg s^{-1} for mass flux rates, 38 and 135 m^3 (22 and 76 m^3 equivalent magma volume) for the pyroclast volumes, and 0.02–0.4 and 0.06–0.12 kg m^{-3} for particle concentrations, respectively. The time-averaged kinetic energy released is found to be equal to 4.2×10^7 and 3.9×10^8 J, and thermal energy is estimated at 8.4×10^{10} and 3×10^{11} J.

Citation: Gouhier, M., and F. Donnadieu (2008), Mass estimations of ejecta from Strombolian explosions by inversion of Doppler radar measurements, *J. Geophys. Res.*, *113*, B10202, doi:10.1029/2007JB005383.

1. Introduction

[2] Volcanic explosions are important sources of information for understanding eruption mechanisms. The masses and velocities of gas and pyroclasts are particularly important parameters controlling the dynamics of an eruption as they define crucial parameters such as mass fluxes, kinetic and thermal energies released by an explosion. In order to better understand the dynamics of explosive eruptions, satellite imagery, and ground-based weather radars particularly have been used for the sounding of volcanic ash plumes from large eruptions [*Harris et al.*, 1981; *Harris and Rose*, 1983; *Weill et al.*, 1992; *Dean et al.*, 1994; *Dehn et al.*, 2000; *Lacasse et al.*, 2004]. These techniques probe the upper convective parts of high eruption columns and provide information primarily on the small particles that ultimately constitute the distal volcanic products. A major challenge is now to measure physical parameters, such as ejecta velocities and masses, close to the vent in order to retrieve directly the true source parameters. A first approach to measure jet velocities was used at Stromboli with an acoustic Doppler sounder (sodar) [*Weill et al.*, 1992]. Other techniques that potentially provide information on both velocity and mass parameters are ground-based portable Doppler radar, either pulsed such as volcano Doppler radar (VOLDORAD) [*Dubosclard et al.*, 1999; *Dubosclard et al.*, 2004] or frequency-modulated such as VERDEMOS [*Hort and Seyfried*, 1998; *Seyfried and Hort*, 1999]. These techniques allow direct measurement of particle velocities and reflectivities immediately above the vent. In addition to their significant monitoring potential, these radar systems allow us to study, under any weather conditions, explosions

[1]Laboratoire Magmas et Volcans, Clermont-Université, Observatoire de Physique du Globe de Clermont-Ferrand, Clermont-Ferrand, France.

Copyright 2008 by the American Geophysical Union.
0148-0227/08/2007JB005383$09.00

Table 1. Characteristics of VOLDORAD Version 2

Characteristic	Symbol	VOLDORAD 2
Transmitted frequency (MHz)	f_t	1274
Wavelength (cm)	λ	23.5
Peak power (W)	P_t	60
Pulse repetition period[a] (μs)	t_r	100
Pulse duration[a] (μs)	τ	0.8
Range resolution[a] (m)	L	120
Antenna beam width (deg)	α	9
Antenna beam elevation[a] (deg)	θ	23

[a]Parameters set for the sounding at Etna SE crater on 4 July 2001.

of lesser intensity barely imaged by satellites or weather radars.

[3] VOLDORAD was used to record several eruptive episodes at Etna in July 2001, ranging from mild Strombolian activity to paroxysmal lava fountains [*Donnadieu et al.*, 2005]. A new method based on inversion of echo power data measured using VOLDORAD is now presented for estimating the masses of pyroclasts ejected during individual explosions. The method also provides first-order estimates of mass-related parameters such as mass flux, ejecta volume, particle concentration, thermal and kinetic energy at the vent. The method was applied to two Strombolian explosions with contrasted particle loads that occurred during an eruptive episode of Mount Etna southeast (SE) crater on 4 July 2001. First, an algorithm is developed to simulate radar echoes from pyroclasts of various sizes, using the complete electromagnetic scattering formulation [*Mie*, 1908]. This approach provides synthetic data of power backscattered by particles (P_{synth}) at the particular wavelength employed by VOLDORAD. Second, as an input to the model, a scaled Weibull function [*Weibull*, 1939] is used to characterize the particle size distribution (PSD). The general shape of the Weibull distribution is constrained from published data for typical Strombolian activity [*Chouet et al.*, 1974], and the mode of the PSD is estimated from our own radar velocity measurements for each explosion. All Weibull parameters characterizing a polydisperse (multiple particle size) distribution, such as shape, shift, and scale factors, can then be deduced and used to compute synthetic values of backscattered power. Last, a recursive inversion algorithm is applied in order to obtain a PSD such that the synthetic power (P_{synth}) best fit the measured radar power (P_{mes}). The mass of ejected material and related parameters are then deduced. An alternative model is proposed on the basis of a monodisperse (single particle size) PSD, which turns out to be an acceptable approximation of the polydisperse model. This approach reduces computing time, making it useful for real-time quantitative assessment of ejected mass during volcano monitoring.

2. VOLDORAD: Volcano Doppler Radar

2.1. Radar Description

[4] VOLDORAD is a pulsed volcano Doppler radar developed by the Observatoire de Physique du Globe in Clermont-Ferrand (France) specifically for the active remote sensing of volcanic eruption jets and plumes. The second version of the system is a medium-power (60 W) Doppler radar of limited weight ($\sim$70 kg, including PC and antenna), with a 9° beam width (α) and a working wavelength (λ) of 23.5 cm [*Donnadieu et al.*, 2005]. VOLDORAD is designed to monitor all types of explosive volcanic activity of variable magnitude. It operates at a medium distance range (0.4–12 km) under all weather conditions with a high sampling rate ($\geq$10 Hz) that permits detailed analysis of early eruptive processes. The portability and lower electric consumption of this version compared to a first version of VOLDORAD is a valuable technical improvement. The pulse repetition period (t_r) is taken as 100 μs and directly defines the maximum velocity that can be measured by the radar:

$$V_{\max} = \frac{\lambda}{4N_c t_r} \tag{1}$$

where N_c is the number of coherent integrations of radar pulses. Note that the maximum velocity that can be measured in theory by VOLDORAD is very high (1175 m/s). This is valuable in particular for measuring the velocities of small particles traveling with speeds close to that of the gas. The pulse duration (τ) can be varied from 0.4 to 1.5 μs, and a value of 0.8 μs was used during the eruption of Mount Etna SE crater on 4 July 2001. This corresponds to a suitable range resolution of the sampling volume, the so-called range gate, of 120 m (Table 1).

[5] Volcanic ejecta crossing the antenna beam generate radar echoes backscattered to the receiver with an angular frequency Doppler shift ($d\varphi/dt$) between the transmitted and received signal that is related to the particle velocity along the beam axis:

$$\frac{d\varphi}{dt} = \omega = 2\pi f_d \tag{2}$$

where ω is the angular frequency and f_d is the Doppler frequency. Indeed, the Doppler velocity spectrum is related to the frequency spectrum via the relationship

$$f_d = \frac{-2V_r}{\lambda} \tag{3}$$

where V_r is the radial velocity and λ is the radar wavelength. When the target moves away from the radar ($V_r > 0$), the Doppler shift ($d\varphi/dt$) is negative, and vice versa when the target approaches.

2.2. Experimental Conditions

[6] After more than 8 months of minor activity (slow lava flows, degassing, light ash emission, and low-level Strombolian activity), a new episode of vigorous activity began at the SE crater on 9 May. From then until July–August 2001, there were eruptions from the SE crater every 3–5 days, each lasting on average a few hours and involving multiple Strombolian explosions and lava fountaining. Radar soundings reported here were carried out over about 5 h during an eruption on 4 July. The activity began at about 1800 UT and at first involved small explosions repeated every $\sim$10 s. The intensity then increased progressively, culminating in very powerful Strombolian explosions every 2–3 s, with the bursting of very large bubbles between 2100 UT and 2200 UT but without real lava fountains. The eruption intensity then decreased rapidly from 2200 UT and ended at 2300 UT after about 5 h of Strombolian activity.

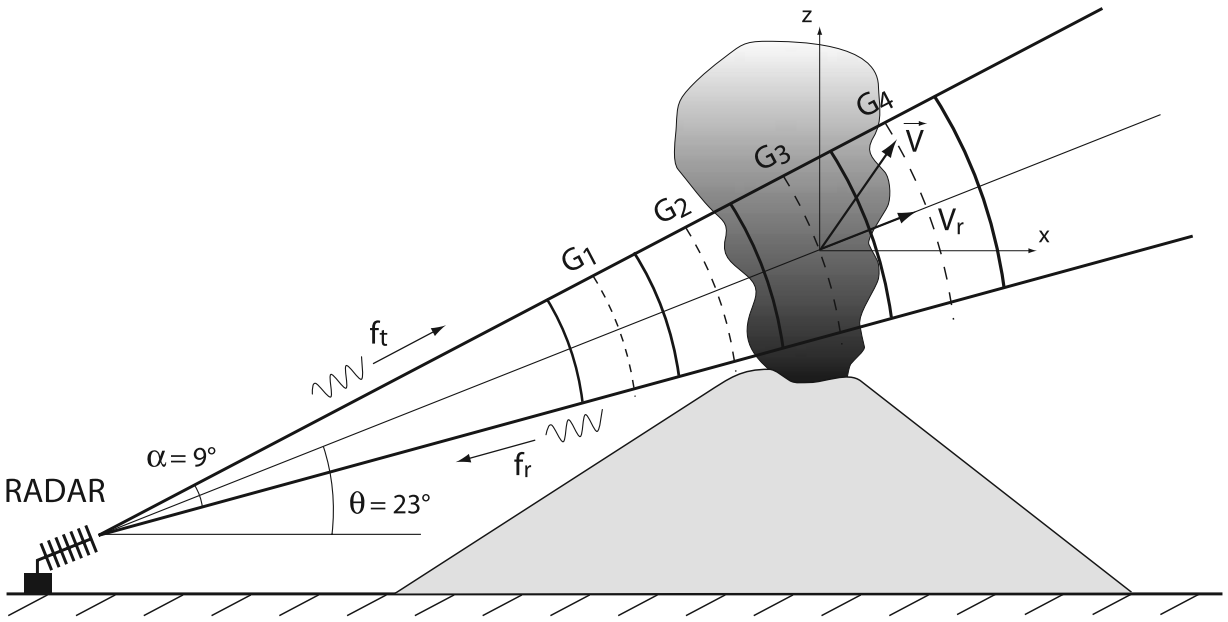

Figure 1. Sketch of the radar sounding geometry used for the acquisition campaign on Mount Etna, on 4 July 2001. VOLDORAD was set up at an altitude of 3000 m, at a slanting distance of 930 m to the crater rim, 280 m below the summit of the SE crater, and with an antenna elevation angle θ of 23°. Note that range gate G_3 is centered above the vent and provides most of the echo power.

VOLDORAD was set up at an altitude of 3000 m, at a slanting distance of 930 m to the crater rim, 280 m below the summit of the SE crater, and with an antenna elevation angle θ of 23° (Figure 1).

[7] Moving particles were detected in successive range gates (G_1 to G_4) corresponding to a slant distance of 807–1167 m (Table 2). In this configuration, particles ascending above the crater in range gate G_3 were recorded mainly with positive radial velocities (away from the antenna) in the Doppler spectra, whereas descending particles were mainly recorded with negative velocities.

2.3. Radar Parameters

[8] Data from successive range gates are displayed in real time as Doppler spectra representing the power spectral density versus radial velocity. From the processing of the series of Doppler spectra, two sets of parameters are directly retrieved for ascending (positive parameters indexed by a plus) and descending (negative parameters indexed by a minus) ejecta crossing the successive range gates above, or on either side of, the eruptive jet axis: (1) velocity information, in particular maximum and mean radial velocity (V^+_{max}, V^-_{max}, V^+_{mean}, V^-_{mean}) and (2) power (P_+, P_-) backscattered by particles contained in the sampling volume at a given instant [*Dubosclard et al.*, 2004].

[9] The received echo power from the particles (spectral moment of order 0) can be defined by the integral of the spectral power density $S(v)$ in a velocity interval between

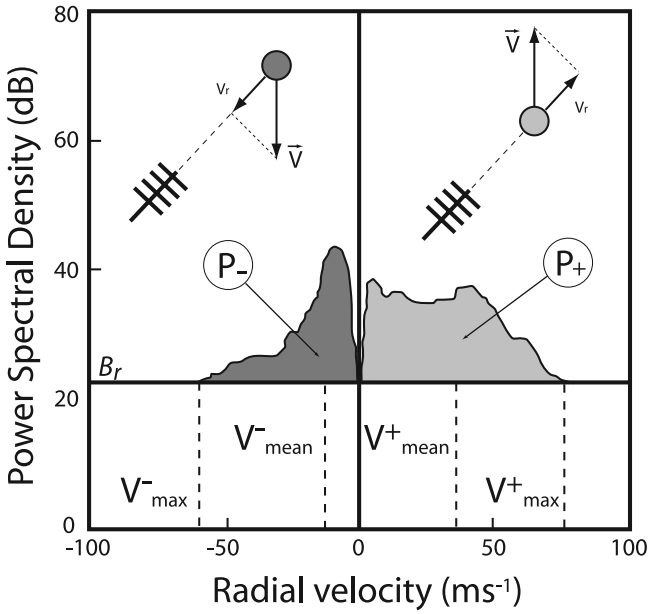

Figure 2. Sketch of a typical Doppler spectrum obtained by VOLDORAD. The power spectral density is displayed as a function of the radial velocity in a given range. The horizontal line (B_r) corresponds to the background noise level. Total echo power and maximum and mean velocities can be deduced from Doppler spectra. They are indexed (plus) and (minus) for ejecta with the radial component of their velocity vector moving away and toward the antenna, respectively.

Table 2. Gate Center Coordinates[a]

	G_1	G_2	G_3	G_4
Gate angle to the vertical (deg)	78	34	−23	−43
Slanting distance to the radar (m)	807	927	1047	1167
Horizontal distance to the crater (m)	−166	−56	54	165
Elevation above crater rim (m)	33	80	127	174
Gate height (m)	127	146	165	184

[a] G_1 to G_4, for an elevation angle of 23° and pulse duration of 0.8 μs.

v and $v + dv$, from 0 to $V^+_{\max}$ for ascending particles and from $V^-_{\max}$ to 0 for descending particles. The power measured in the Doppler spectra has been calibrated in the laboratory by means of an input signal, the power of which was known, delivered by an external frequency generator:

$$P_+ = \int_0^{V^+_{\max}} S(v)dv, \quad P_- = \int_{V^-_{\max}}^0 S(v)dv \tag{4}$$

Maximum radial velocities in the directions toward and opposite to the radar, $V^-_{\max}$ and $V^+_{\max}$, respectively, are defined where $S(v)$ is equal to the background noise level B_r (Figure 2). Likewise, for a given Doppler spectrum, V^+_{mean} and V^-_{mean} (spectral moment of order 1) of the ejecta are given by

$$V^+_{\text{mean}} = \frac{\int_0^{V^+_{\max}} vS(v)dv}{\int_0^{V^+_{\max}} S(v)dv}, \quad V^-_{\text{mean}} = \frac{\int_{V^-_{\max}}^0 vS(v)dv}{\int_{V^-_{\max}}^0 S(v)dv} \tag{5}$$

3. Electromagnetic Scattering Model

[10] The aim of this study is to estimate masses of volcanic ejecta from two Strombolian explosions with contrasted particle loads by inversion of the Doppler radar measurements. For this purpose, a comparison between the backscattered power measured by the radar (P_{mes}) and the synthetic (i.e., calculated) backscattered power (P_{synth}) is needed (see section 4. for more details on the inversion method). In this section, we first describe how to retrieve P_{mes}, and then we derive P_{synth} using the electromagnetic scattering theory of *Mie* [1908]. As shown by Figure 2, processing of the Doppler spectra yields the total backscattered power ($P_{\text{tot}} = P_- + P_+$). Raw power values ($P_{\text{mes}}$) can then be deduced directly from the radar conversion constant (C_c) that depends on technical characteristics of the radar acquisition line:

$$P_{\text{mes}} = P_{\text{tot}} C_c \tag{6}$$

On the other hand, P_{synth} can be derived from an electromagnetic scattering model. A good approximation for small particles is the Rayleigh scattering theory, the validity limit of which depends on the radar wavelength [*Sauvageot*, 1992]. This method is commonly used in meteorology, because the typical diameter of water droplets is small compared to the wavelengths of meteorological radars. In our case (λ = 23.5 cm), the Rayleigh theory can only be applied for particles of diameter (D_L) smaller than $\lambda/4$, which corresponds to ~5.9 cm [*Gouhier and Donnadieu*, 2006]. However, considering the wide range of particle diameters characterizing volcanic activity, the complete scattering theory is required to account for the effects of larger particles. A general solution of electromagnetic wave scattering was given by *Mie* [1908]. This approach applies Maxwell's equations for plane waves scattered by compositionally homogeneous particles (Appendix A). For application to volcanic eruptions, we focus on waves scattered at a large distance by spherical particles, which we assume are homogeneously distributed in space. Theoretically, the power backscattered to the radar by a population of such particles in a given range gate is proportional to their radar reflectivity (η). The synthetic power can then be defined as

$$P_{\text{synth}} = \frac{C_r V_s \eta}{R^4} \tag{7}$$

where C_r is the radar constant, V_s, the sampling volume, and R, the slant distance between the radar and the target. The radar constant is defined by a set of technical parameters related to the radar configuration. The radar constant has been calibrated using a classical method comparing the reflectivity of rainfalls probed by the radar and the reflectivity calculated from the drop size distribution and velocity of the falling hydrometeors measured simultaneously with a disdrometer [*Pointin et al.*, 2005]. The radar reflectivity (η) is the sum of the backscattering cross sections (σ_{bks}) of the individual particles per unit volume. The reflectivity factor (Z) is defined by *Sauvageot* [1992] as

$$\eta = \sum_{i=1}^{n} \frac{\sigma_{\text{bks}_{(i)}}}{V_s} \tag{8}$$

and

$$Z = \frac{\eta \lambda^4}{\pi^5 |K|^2} 10^{18} \tag{9}$$

Z (commonly confused with η in the literature) is often expressed in logarithmic units as dBZ and is related to η through the radar wavelength λ, and the particle complex dielectric factor $K = (m^2 - 1)/(m^2 + 2)$. Scattering and attenuation by compositionally homogeneous spheres are significantly influenced by the complex refractive index (m). VOLDORAD transmits power through a square array of four Yagi antennas, such that the incident electromagnetic wave is polarized parallel to the scattering plane. Being a monostatic radar (i.e., the same antenna is used for transmission and reception), we define a backscattering cross section (σ_{bks}) for horizontal linear polarization:

$$\sigma_{\text{bks}} = \frac{\lambda^2}{4\pi} \left| \sum_{n=1}^{\infty} (-1)^2 (2n+1)(a_n - b_n) \right|^2 \tag{10}$$

where a_n and b_n are the complex scattering coefficients (so-called Mie coefficients). Examples of Mie versus Rayleigh scattering patterns of an electromagnetic wave scattered by homogeneous spheres of four different sizes are shown in Figure 3 for a signal at the wavelength used by

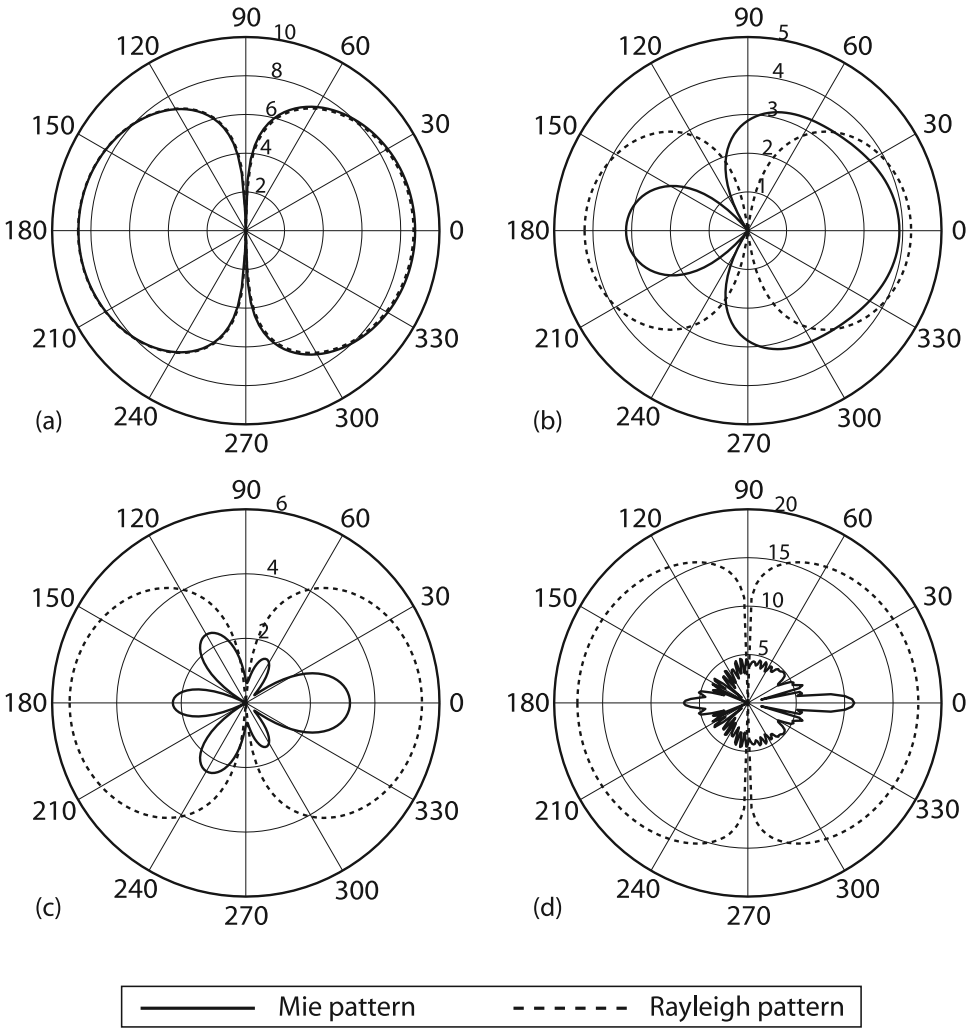

Figure 3. Mie versus Rayleigh scattering patterns of an electromagnetic wave, parallel polarized, scattered by a single homogeneous sphere with the complex dielectric factor of volcanic ash, $|K|^2 = 0.39$ [*Adams et al.*, 1996], and $\lambda = 23.5$ cm. The wave arrives from the left, and the particle is situated at the center of the pattern. Irradiance amplitude is normalized to that of Mie and expressed on a logarithmic scale. (a) Example of a small particle of diameter 2 cm. The Rayleigh and Mie scattering patterns are identical and symmetrical. Irradiance intensity is the same in front of and behind the particle. (b) Particle of diameter 14 cm. The Rayleigh and Mie scattering patterns are now significantly different. The Mie pattern still has two main lobes but is strongly asymmetric, as the backscattered intensity is lower than the forward scattered intensity. (c) Particle of diameter 20 cm. The Rayleigh pattern is still symmetrical, whereas the Mie pattern is divided into several lobes and shows much lower values of irradiance. (d) For a diameter of 2 m, the Mie (true) scattering pattern becomes very complex and shows always much lower values of irradiance than the Rayleigh approximation.

VOLDORAD ($\lambda = 23.5$ cm) and with the complex dielectric factor of volcanic ash ($|K|^2 = 0.39$) [*Adams et al.*, 1996]. These patterns illustrate the large discrepancy between the Rayleigh and Mie formulations for particle diameters larger than a few centimeters at 23.5 cm wavelength. Note that, at smaller radar wavelengths, this discrepancy occurs at even smaller particle diameters, making the complete Mie formulation absolutely necessary for studies of volcanic ejecta from radar measurements.

[11] Figure 4 shows the reflectivity factor (Z) as a function of particle diameter, using both the Mie and Rayleigh formulations for a wavelength of 23.5 cm. Note the overestimation of Z when computed using the Rayleigh approximation for particle diameters greater than ~5.9 cm.

4. Inversion Method

[12] Model inversions are frequently used in geophysics to recover initial parameters and boundary conditions from observed data of natural phenomena. In this case, backscattered power values (P_{mes}) are retrieved from radar measurements, and synthetic power data (P_{synth}) are determined from the forward electromagnetic-scattering model. The inversion algorithm thus seeks the best correlation between P_{mes} and P_{synth}, providing the optimum variable

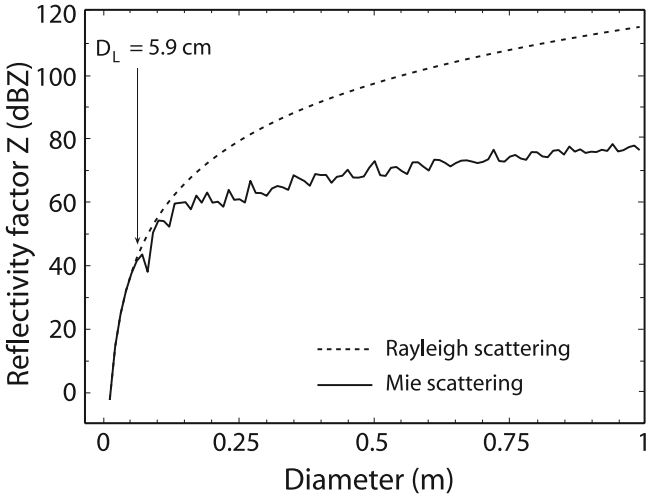

Figure 4. Synthetic reflectivity factor (Z, expressed in dBZ) as a function of particle diameter. Note the large overestimation of Z for large diameters when computed using the Rayleigh approximation. The validity domain depends on the radar wavelength. In the case of VOLDORAD (λ = 23.5 cm), the validity limit (D_L) lies close to 5.9 cm, i.e., $\sim\lambda/4$ [*Gouhier and Donnadieu*, 2006].

input parameters defined by the vector (X) that characterizes the PSD. Physical parameters such as particle mass and volume are then deduced from the PSD. The model takes into account two main classes of parameters: (1) constant parameters describing the geometry of the system, the technical characteristics of the radar or material physical properties; (2) the vector of variable input parameters (X; see below) defining the Weibull function of the PSD. A least squares estimation method is used on the basis of the minimization function $S(X)$ characterized by the squared residual between radar measured data and synthetic data:

$$S(X) = \sum \left[P_{\text{mes}} - P_{\text{synth}}(X)\right]^2 \tag{11}$$

Finally, a comparison criterion between radar-measured (P_{mes}) and synthetic (P_{synth}) power data is used to stop the recursive loop when the fitting criterion is reached. The successive steps of the inversion algorithm are summarized below.

[13] Step 0 is attribution of initial values for estimation of the input parameters:

$$X_j \equiv [X_1, X_2, \ldots, X_n]$$

[14] Step 1 is resolution of the direct model (Mie scattering):

$$X \rightarrow P(X)_{\text{synth}}$$

[15] Step 2 is calculation of the minimization function:

$$S(X) = \sum \left[P_{\text{mes}} - P_{\text{synth}}(X)\right]^2$$

[16] Step 3 is characterization of the iterative comparison criterion:

$$\Delta P(X^i) = S(X^{i-1}) - S(X^i)$$

[17] Step 4 is testing of the fitness criterion:

$$\Delta P(X) < 0$$

where $\Delta P(X)$ is the fitness criterion, and indices i and j refer to the step of the iterative procedure and the number of variable parameters, respectively. When a satisfactory solution is reached, the iterative procedure stops. The computational procedure is summarized in Figure 5.

5. Polydisperse Particle Size Model

5.1. Particle Size Distribution

[18] Solving the inverse problem consists of estimating the shape of the PSD by best fit matching of synthetic and observed data. Various PSDs have been used in, or inferred from, previous studies of volcanic ejecta: exponential [*Ripepe et al.*, 1993], lognormal [*Sheridan*, 1971; *Chouet et al.*, 1974; *McGetchin et al.*, 1974; *Self et al.*, 1974], Rosin

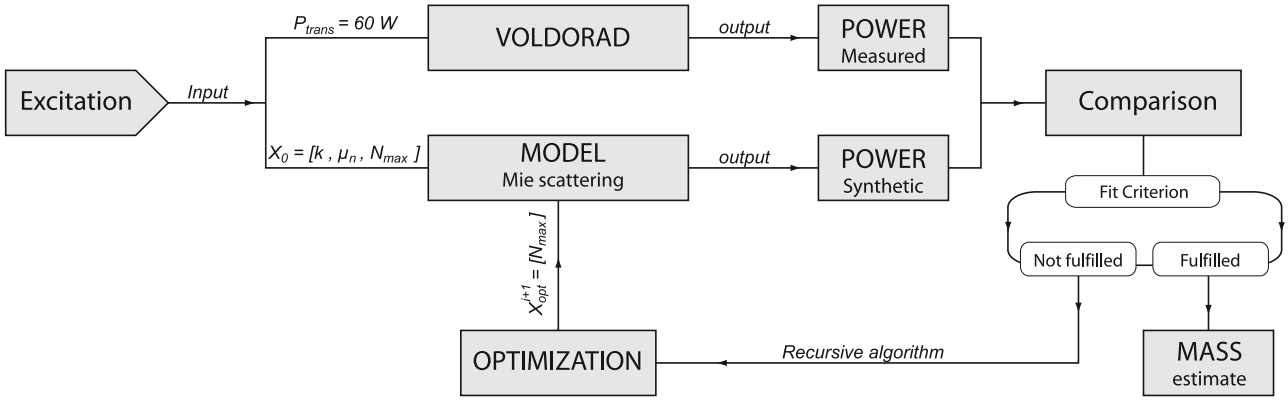

Figure 5. Sketch of the inversion approach. Synthetic radar power data (P_{synth}) are provided from the theoretical model (Mie formulation) and compared to the power data measured (P_{mes}) by VOLDORAD. If the fit criterion is met, the procedure stops and gives the best result. Otherwise, the input parameters (X) are optimized in the recursive loop, and the calculation is repeated.

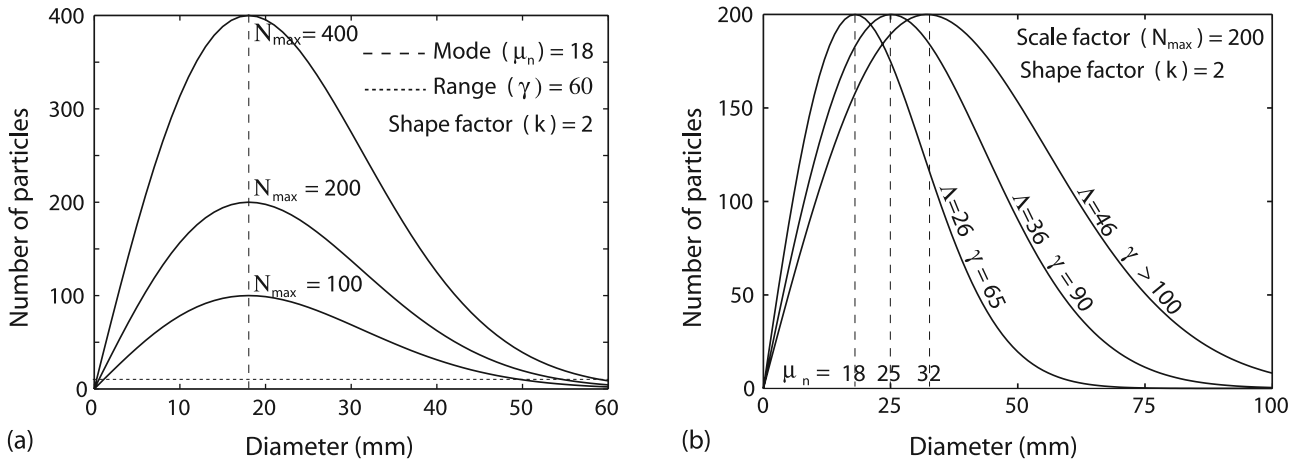

Figure 6. Evolution of the particle size distribution (PSD) for different values of shift (Λ) and scale factors ($N_{\max}$). For both examples, the shape factor is constant at $k = 2$. (a) The scale factor ($N_{\max}$) represents the maximum number of particles with diameter μ_n and, therefore, directly controls the total number of particles. (b) The mode (μ_n) and range (γ) of the distribution evolve jointly with the shift factor.

Rammler [*Kittleman*, 1964; *Spieler et al.*, 2003], Weibull [*Nakamura*, 1984; *Marzano et al.*, 2006a, 2006b], polymodal [*Sheridan et al.*, 1987; *Riley et al.*, 2003] and sequential fragmentation/transport (SFT) [*Wohletz et al.*, 1989]. However, there is still a lack of consensus on which PSD best characterizes Strombolian activity, particularly for the largest particle diameters. For this reason, a scaled Weibull function is used, because its overall shape may be varied widely from exponential to Gaussian by means of only three factors: shape (k), shift (Λ), and scale ($N_{\max}$). The PSD can then be adjusted easily during the optimization phase of the data inversion procedure. The scaled Weibull distribution S_w is defined through a probability density function f_w of particles with diameter D:

$$S_w(D;k,\Lambda,N_{\max}) = \frac{f_w(D;k,\Lambda)}{\max[f_w(D;k,\Lambda)]} N_{\max} \tag{12}$$

with

$$f_w(D;k,\Lambda) = \left(\frac{k}{\Lambda}\right)\left(\frac{D}{\Lambda}\right)^{(k-1)} \exp\left(\frac{-D}{\Lambda}\right)^{k} \tag{13}$$

The shape factor (k) allows us to choose from an exponential ($k = 1$) to Gaussian ($k = 3$) distribution, along with all intermediate lognormal distributions ($1 < k < 3$). The shift factor (Λ) directly depends on the mode (μ_n) of the PSD and on the shape factor (k). It can be defined by using

$$\Lambda = \mu_n \left(\frac{k-1}{k}\right)^{-1/k} \tag{14}$$

$N_{\max}$ is the maximum number of particles of diameter μ_n in the scaled Weibull distribution (Figure 6a). It is the dominant term in the computation of the synthetic power because it strongly influences the estimate of particle mass.

[19] The three variable parameters (k, μ_n, $N_{\max}$) controlling the PSD make up the vector X of input parameters to the model. However, in order to obtain a unique solution to the inverse problem, the number of variable parameters is reduced. This also increases the efficiency and speed of the algorithm. Parameters k and μ_n are constrained from the following assumptions argued in subsequent sections: (1) the PSD of Strombolian explosions can be characterized on average by a single shape factor k; (2) the mode of the PSD (μ_n) can be determined from mean particle terminal velocity estimated from the radar measurements. These assumptions then reduce the optimization procedure to a single free parameter ($N_{\max}$).

5.2. Parameter Constraints

5.2.1. Shape Factor, *k*

[20] Data on Strombolian PSDs are scarce in the literature. However, *Chouet et al.* [1974] gave an exhaustive description of two explosions at Stromboli Volcano by photoballistic analysis. They made an estimate of the PSD for inflight ejecta (which is what a radar records), and determined the modes, ranges, numbers and sizes of particles for two explosions. They also deduced eruptive parameters such as number, mass and volume of ejected particles, and found that one explosion contained a number and mass of particles about 17 times greater than the other (Table 3). We use this study, where all output parameters are already known, to determine the input parameter (k) that best describes the two Strombolian explosions observed by *Chouet et al.* [1974]. With this aim, we first calculate the "equivalent" radar power corresponding to the total ejected mass estimated by *Chouet et al.*'s [1974] observations for two Strombolian explosions. Then synthetic radar powers are computed for different values of shape factor k. Finally, the recursive procedure stops when synthetic radar powers match the equivalent radar power and when synthetic particle loading parameters (number, mass, volume) corre-

Table 3. Comparison Between Values Observed by *Chouet et al.* [1974] on Two Explosions at Stromboli and Synthetic Values Calculated by the Inversion Algorithm[a]

		Explosion 1: Sep 1971		Explosion 2: Sep 1971	
	Symbol	Observed Data	Synthetic Data	Observed Data	Synthetic Data
Number of particles	N	2588	2588	146	144
Mode (m)	μ_n	0.022	0.022	0.025	0.025
Range (m)	γ	?–0.06	0.004–0.06	?–0.06	0.001–0.06
Volume (m^3)	V	0.033	0.035	0.002	0.0027
Mass (kg)	M	51	53	3	4.1

[a]Note that the best fit for both sets of data is reached for the same shape factor $k = 2.3$ (lognormal particle size distribution).

spond to those described by *Chouet et al.* [1974]. Note that an alternative method would have been simply to determine k from a best fit function of the *Chouet et al.* [1974] PSD. However, our chosen approach had the advantage of additionally testing our inversion algorithm.

[21] The best fit between the observed and synthetic PSDs is reached in both cases for the same value of $k = 2.3$, which describes a lognormal distribution. The equivalent synthetic power achieved is about 3.3×10^{-9} and 3.2×10^{-10} mW for explosions 1 and 2 respectively, and corresponds to equivalent reflectivity factors (Z) of 61 and 51 dBZ. The inversion procedure yields three parameters (number, mode and range) characterizing the synthetic PSDs, from which two eruptive parameters (mass and volume) are directly deduced (Table 3). The agreement between observed and synthetic parameters is very good and validates our inversion algorithm. Shape factor estimation can then be used afterward with reasonable confidence. Furthermore lognormal PSDs have also been inferred from deposits of Strombolian activity on other volcanoes, like Etna [*McGetchin et al.*, 1974] and Heimaey [*Self et al.*, 1974]. Although k may vary between individual explosions on Stromboli, as well as between Strombolian eruptions at different volcanoes, we assume in what follows that the value $k = 2.3$, found for both explosions at Stromboli, represents a suitable average value for Strombolian PSDs and use it as input to the model. Moreover, sensitivity tests reveal a limited dependence of the total ejected mass on k, varying only by a factor of two for values of k ranging from 2.0 to 2.6.

5.2.2. Shift Factor, Λ

[22] The shift factor (Λ) is linked to the mode (μ_n) and range (γ) via the shape factor (k) (Figure 6b). The mode of the distribution is estimated directly from radar measurements using the terminal settling velocities of ejected particles. Indeed, under the assumptions of vertical trajectories, no wind influence, and terminal fall velocity, an average particle diameter D_p can be deduced from the mean negative radial velocity weighted by the power spectral density [*Rogers and Yau*, 1989; *Hort et al.*, 2003]

$$D_p = \frac{C_s}{P_-} \sum_{V_{\max}^-}^{0} S(v) \left(\frac{V_r}{\sin\theta} \right)^2 \tag{15}$$

where $S(v)$ is the spectral power in a velocity interval. P_- refers to the power backscattered mainly by descending particles (left part of the Doppler spectrum), and θ stands for the antenna beam elevation angle. C_s is the shape coefficient, which for a spherical particle is:

$$C_s = \frac{3}{4} C_d \frac{\rho_a}{\rho_p g} \tag{16}$$

with C_d being the drag coefficient, g the gravitational acceleration and ρ_a, ρ_p the densities of air and particles respectively. Importantly, the interpretation of D_p retrieved from Doppler radar spectra differs significantly from μ_n (the mode of the PSD). Indeed, μ_n corresponds to the particle diameter that is most represented in the particle size distribution, i.e., the top of the curve. In radar meteorology, D_p is approximately equal to μ_n because the size distributions of atmospheric water droplets are typically Gaussian and very narrow. In a volcanic jet however, the power spectrum is much wider [e.g., *Dubosclard et al.*, 1999], and the physical interpretation of D_p is therefore more complex. D_p and μ_n are offset by a factor based on the dependence of the reflectivity (calculated at a given radar wavelength) on the number (N) and diameter (D) of particles. Thus μ_n is obtained from D_p using a scattering formulation adequate for the range of particle sizes characterizing explosive volcanic activity [*Woods and Bursik*, 1991; *Gouhier and Donnadieu*, 2006]. Once k and μ_n are obtained, the shift factor Λ can be calculated from equation (14).

5.2.3. Scale Factor, $N_{\max}$

[23] By assuming that k and μ_n are constant throughout the inversion procedure, the parameter vector X then becomes dependent on just a single free parameter, the scale factor, $N_{\max}$. This characterizes the maximum of the scaled Weibull distribution curve (S_w) and evolves during the optimization phase of the algorithm. It describes, along with k and μ_n, the total number of particles ejected during the explosion, and hence controls the erupted mass estimation. The accuracy of the results depends on the step chosen between two successive values of $N_{\max}$ in the recursive loop. However, although a small step leads to a more accurate estimation, it increases considerably the computing time.

6. Monodisperse Particle Size Model

[24] An alternative data inversion model based on a monodisperse PSD approximation is now presented. In this model, the single particle size equals μ_n, as well as D_p.

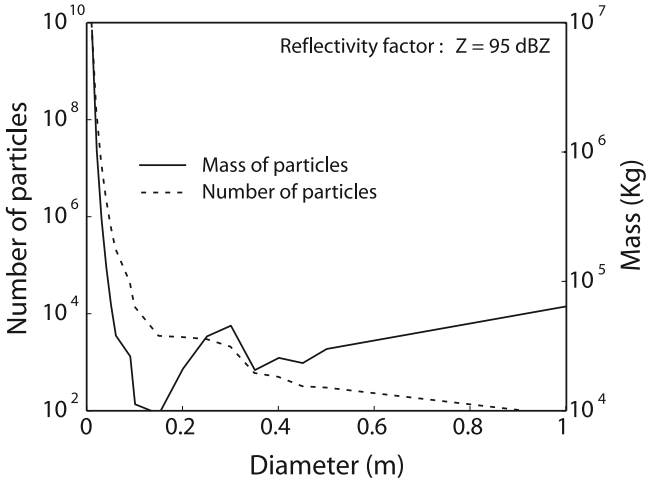

Figure 7. Plot of the total mass and number of particles as a function of their diameter in the monodisperse model for a reflectivity factor $Z = 95$ dBZ. Small particles contribute the most to the total ejected mass, for example, 8.8×10^6 kg for a diameter of 0.01 m, compared to 6.4×10^4 kg for a diameter of 1 m, i.e., a difference of 2 orders of magnitude.

Figure 7 shows that the number of small particles required to generate a given reflectivity can be up to several orders of magnitude larger than the number of corresponding large particles. Because of this huge difference in particle number, the fraction of small ejecta contributes most to the total estimated mass. For example, a reflectivity of 95 dBZ requires 8.8×10^6 kg of 0.01 m particles compared to 6.4×10^4 kg of 1 m particles, a difference of 2 orders of magnitude. This result illustrates that large blocks are not so important in first-order estimations of total ejected mass.

This monodisperse PSD model significantly reduces computing time and ensures fast synthetic power calculations. Mass estimations are provided in Figure 8 for a wide range of realistic values of D_p and Z. Since these parameters are derived directly from the Doppler spectra, the corresponding mass can be retrieved instantaneously without any computing phase. This alternative method is valuable because a first-order mass estimate of ejected pyroclasts can be obtained in real time and used for volcano monitoring.

7. Radar Data

[25] Strombolian explosions and lava fountains were monitored with VOLDORAD for several hours during eruptive episodes of the SE crater on 4, 7, and 13 July 2001. We focus on data acquired during two explosions that occurred at 2141:53 and 2141:56 UT during the eruption of 4 July. The two explosions were each short-lived, with durations of about 3 s. Temporal series (Figure 9) of radar power are computed from the power spectral density $S(v)$, and sampled at a high frequency (10 Hz) suitable for such short-lived explosions.

[26] It is important that the power used as input to the inversion model be defined carefully. First, it is essential to ensure that the total power at a given instant is the sum of P_{tot} across the different range gates along the beam axis. Were the jet wider than the width of a single range gate (120 m), it would be necessary to integrate across several range gates in order to obtain the total reflected power. However, in the cases studied here, both jets were sufficiently narrow as to fit within a single range gate (G_3). This is deduced from (1) visual inspection of video snapshots and (2) the lack of echo power signal from neighboring range

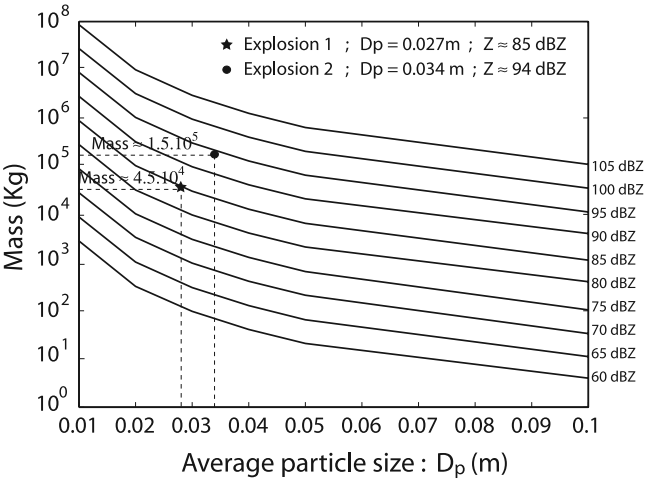

Figure 8. Mass estimate as a function of average particle size (D_p) retrieved from the power spectral density using the monodisperse model for different reflectivity factors (Z) of ejected particles. First-order mass assessments can be given simply from the reflectivity factor (Z) and the average particle size (D_p) determined directly from the Doppler spectra, without any computation phase. Masses of 4.5×10^4 kg and 1.5×10^5 kg are roughly estimated for explosions 1 and 2, respectively.

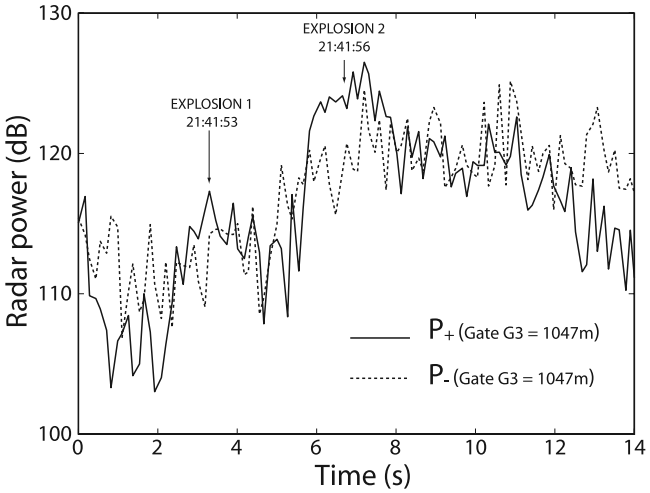

Figure 9. Temporal evolution of radar echo power during the two explosions studied at Mount Etna on 4 July 2001, sampled at 10 Hz. Both echo powers of particles moving away from (P_+) and toward (P_-) the antenna are plotted in order to infer the total power at a given instant in the range gate (G_3) located above the vent. Both explosions are brief, lasting 2.2 and 2.8 s, respectively. The second explosion is much more powerful (125 and 123 dB for P_+ and P_-, respectively) than the first (117 and 115 dB).

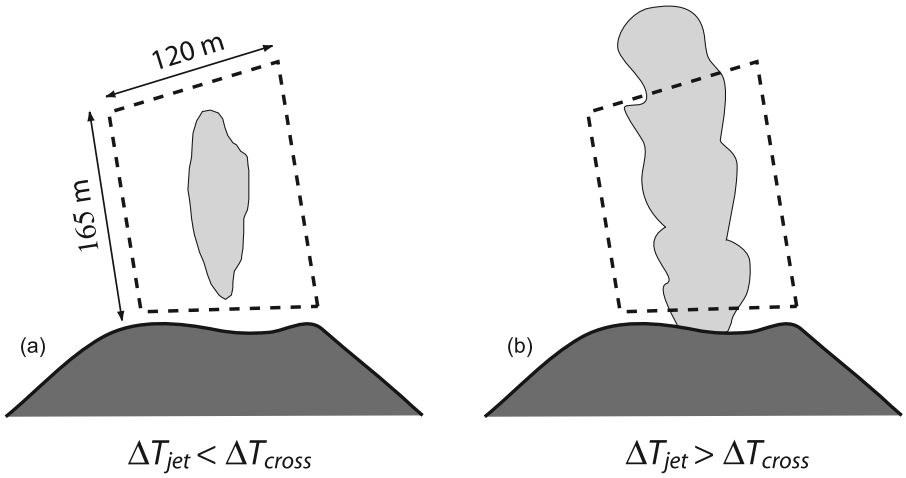

Figure 10. Sketch illustrating the two hypotheses made in the calculation of total power. Δt_{jet} is the duration of jet production, and Δt_{cross} is the time necessary for the jet to traverse vertically the range gate. (a) Example of a short-lived jet ($\Delta t_{jet} < \Delta t_{cross}$): the jet is short enough to be wholly enclosed in the sampling volume. A single Doppler spectrum can then be used for the calculation of total power. (b) Example of a long-lived jet ($\Delta t_{jet} > \Delta t_{cross}$): the jet is too long to be contained entirely in the sample volume at a given instant. The maximum radar echo power represents only a fraction of the total amount of ejected particles, and several Doppler spectra have to be taken into account for the calculation of the total power. The two explosions jets of 4 July 2001 at Mount Etna studied in this paper were both short-lived.

gates (G_2 and G_4). Integration along the beam axis is therefore unnecessary.

[27] The second requirement is that the reflected power be integrated throughout the entire duration of the explosion as the jet passes vertically across the range gate concerned (G_3). In this case, two situations can be envisaged, as shown schematically in Figure 10. To explain these two cases, we consider two time durations: Δt_{jet}, the duration of jet production, and Δt_{cross}, the time necessary for the jet to traverse vertically the given range gate. In the first case (Figure 10a), $\Delta t_{jet} < \Delta t_{cross}$ and the jet is thus short enough for most of the particles to be recorded at the same instant inside a single sampling volume. The peak of radar echo power can therefore be considered as representative of the entire jet and the input parameters to the model can be derived on the basis of a single Doppler spectrum. When $\Delta t_{jet} \geq \Delta t_{cross}$ (Figure 10b), the jet is never entirely contained within a single range gate, and the peak of echo power represents only a fraction of the constituent particles. Integration over the duration of the jet (Δt_{jet}) is therefore essential. Note that for lava fountaining sustained over longer periods of time at a relatively steady rate, the mean residence time of ejecta inside the range gate would need to be taken into account. This could be inferred from velocities measured by the radar and from the sounding geometry, leading to estimation of the mass flux. The total mass of lava ejected could then be calculated using the duration of the lava fountain.

[28] In the explosions considered here, the average time Δt_{cross} taken by the jet to cross the range gate (G_3) is 4.7 s at an average velocity of 38 m s^{-1} for explosion 1, and 2.9 s at 62 m s^{-1} for explosion 2. By comparison, Δt_{jet} is estimated from videos and radar time series at 2.2 and 2.8 s for explosions 1 and 2, respectively. In both cases, therefore, $\Delta t_{jet} < \Delta t_{cross}$; no time integration is necessary, and data analysis can be based on a single Doppler spectrum. Moreover, the explosion jets commonly become depleted in blocks, and proportionally richer in gas toward the waning stage of their emission, so that the relevant values for Δt_{jet} might actually even be lower.

8. Results

[29] Results of the polydisperse and monodisperse models are shown in Tables 4a–4c and 5a–5c. The fitness between observed and synthetic power data is very good, with 98.7% and 97.8% for explosions 1 and 2, respectively.

8.1. Particle Loading Parameters

[30] Using the more accurate polydisperse model, the total mass of pyroclasts ejected by the first explosion (Tables 4a–4c) is estimated at 58,400 kg, corresponding

Table 4a. Synthetic Results for Explosion 1 (2141:53 UT) at Mount Etna SE Crater[a]

		Synthetic Results	
	Symbol	Monodisperse PSD	Polydisperse PSD
Number of particles	N	2.75×10^6	13.9×10^6
Mode (m)	μ_n	0.027	0.013
Volume (m^3)	V	28.4	38.2
Mass (kg)	M	43.4×10^3	58.4×10^3
Concentration[b] (kg m^{-3})	C	0.01–0.2	0.02–0.4
Reflectivity factor (dBZ)	Z	85.16	85.13
Power (mW)	P_{synth}	8.14×10^{-7}	8.08×10^{-7}

[a]Results are from using both the polydisperse particle size distribution model and the monodisperse approximation.

[b]Concentration parameters are poorly constrained and have to be regarded as rough approximations (see text for details).

Table 4b. Model Parameters for Explosion 1 (2141:53 UT) at Mount Etna SE Crater

Parameters	Input/Output
μ_n	0.0129
D_p	0.027
Λ	0.0165
k	2.3
γ	0.01–0.056
N_{max}	8.00×10^5
Fit (%)	98.68

to a volume of 38 m^3 assuming a pyroclast density of 1530 kg m^{-3} [*McGetchin et al.*, 1974] and a reflectivity factor of 85 dB*Z*. The equivalent magma volume (DRE), for a density of 2700 kg m^{-3} [*Williams and McBirney*, 1979] is 22 m^3. The second explosion (Tables 5a–5c) yields higher values of the different parameters, with an ejecta mass of 206,000 kg, a pyroclast volume of 135 m^3, a reflectivity factor of 94 dB*Z*, and a magma volume of 76 m^3. The difference between the reflectivity factors of the two explosions is 9 dB*Z*, meaning that the second explosion jet is about 8 times more reflective than the first, and the ejecta volume and mass are consequently about 3.5 times higher. This agrees with visual observations which show clearly that the first explosion involved a smaller quantity of incandescent lava clots than the second explosion (Figure 11).

[31] Particles numbers, masses and volumes estimated using the monodisperse model lie within ~25% of those of the polydisperse model for both explosions (Tables 4a–4c and 5a–5c). This underestimation is accounted for by small particles that are not considered in the monodisperse model, but that in reality contribute most to the total mass, owing to the great particle number required to match a given reflectivity.

[32] It is instructive to compare the measured reflectivity factors of the two Etna explosions with those theoretically calculated at Stromboli from the *Chouet et al.* [1974] observations. Recall that reflectivity factor (Z) is a positive function of the number (N) and diameters (D) of ejected particles. The two explosions at Stromboli give reflectivity factors of 61 dB*Z* and 51 dB*Z* (Table 3), whereas the two explosions at Etna give 85 and 94 dB*Z* (Tables 4a–4c and 5a–5c). Thus, even a small explosion at Etna is over 250 times more reflective than a large one at Stromboli, and involves a mass of ejecta 3 orders of magnitude higher (Table 3). For comparison, very heavy rainfall induces maximum reflectivity factors of ~60 dB*Z* [*Sauvageot*, 1992].

Table 4c. Characteristics for Explosion 1 (2141:53 UT) at Mount Etna SE Crater

Characteristic	Value
Date	4 July 2001
Time (UT)	2141:53
t_{jet} (s)	2.2
$\bar{V}^+_{max}$ (m/s)	60
$\bar{V}^{+\,a}_{max}$ (m/s)	37.9
Z (dBZ)	85.12
P_{mes} (mW)	8.10×10^{-7}

[a]The parameter $\bar{V}^+_{max}$ is the time-averaged maximum velocity and differs from the mean velocity calculated by the radar.

Table 5a. Synthetic Results for Explosion 2 (2141:56 UT) at Mount Etna SE Crater[a]

		Synthetic Results	
	Symbol	Monodisperse PSD	Polydisperse PSD
Number of particles	N	5.00×10^6	23.3×10^6
Mode (m)	μ_n	0.034	0.016
Volume (m^3)	V	102.9	134.7
Mass (kg)	M	157×10^3	206×10^3
Concentration[b] (kg m^{-3})	C	0.05–0.1	0.06–0.12
Reflectivity factor (dBZ)	Z	93.78	93.77
Power (mW)	P_{synth}	5.92×10^{-6}	5.87×10^{-6}

[a]Results are from using both the polydisperse particle size distribution model and the monodisperse approximation.

[b]Concentration parameters are poorly constrained and have to be regarded as rough approximations (see text for details).

8.2. Derived Parameters

[33] The mean mass fluxes of ejecta, estimated from the duration of each explosion (Tables 4a–4c and 5a–5c), reach 26,400 and 73,600 kg s^{-1} for explosions 1 and 2, respectively. These represent time-averaged values, and are not expected to be constant over the duration of each explosion.

[34] We have also attempted to estimate particle concentrations in the two explosion jets at Etna. This is difficult since, although the radar data provide estimates of total particle mass, the jet volumes are poorly constrained. One possibility is to make the assumption that each jet filled completely and homogeneously the range gate volume. In this case, concentration estimates have to be regarded as minima. Using the volume of range gate (G_3) above the crater yields values of 0.02 and 0.06 kg m^{-3} for explosions 1 and 2, respectively. However, inspection of video footage (Figure 11) shows that this assumption is probably not realistic. The other option is to make an estimate of the jet volume from video snapshot analysis, but two difficulties are inherent in this approach: first, the jets are spatially heterogeneous, and, second, only large lava clots are visible and the volume occupied by ash and small laplli cannot be estimated. However, taking limiting edges on video snapshots yields that the jets of explosions 1 and 2 represent approximately 5% and 50%, respectively, of the range gate volume. Using these values gives maximum particle concentrations estimates of about 0.4 and 0.12 kg m^{-3} for explosion jets 1 and 2, respectively (Tables 4a–4c and 5a–5c). Note that these concentrations represent spatially averaged values over the estimated jet volume; however, much higher ejecta concentrations can be found locally especially close to the vent.

[35] The high data sampling rate (~10 Hz in the configuration used for this study) allows VOLDORAD to measure rapid signal fluctuations on the timescale of an individual

Table 5b. Model Parameters for Explosion 1 (2141:56 UT) at Mount Etna SE Crater

Parameters	Input/Output
μ_n	0.0164
D_p	0.034
Λ	0.021
k	2.3
γ	0.01–0.072
N_{max}	1.05×10^6
Fit (%)	97.82

Table 5c. Characteristics for Explosion 2 (2141:56 UT) at Mount Etna SE Crater

Characteristic	Value
Date	4 July 2001
Time (UT)	2141:56
t_{jet} (s)	2.8
$\bar{V}^{+}_{max}$ (m/s)	100
$\bar{V}^{+}_{max}$ [a](m/s)	61.6
Z (dBZ)	93.83
P_{mes} (mW)	6.00×10^{-6}

[a]The parameter $\bar{V}^{+}_{max}$ is the time-averaged maximum velocity and differs from the mean velocity calculated by the radar.

explosion. It is therefore possible to calculate an average ejecta velocity, and hence a mean kinetic energy for an explosion, using

$$E_k = \frac{1}{2} M \left(\frac{1}{N_t} \sum_{i=1}^{n} V^{+}_{max}(i) \right)^2 \quad (17)$$

where M is the total ejected mass given in Tables 4a and 5a and $\bar{V}^{+}_{max}$ is the maximum radial velocity, given in Tables 4c and 5c Doppler spectrum (i) recorded in the sampling volume. N_t is the total number of Doppler spectra acquired during a given explosion. A mean kinetic energy of 4.2×10^7 J is obtained for a time-averaged maximum radial velocity ($\bar{V}^{+}_{max}$) of 38 m s^{-1} for explosion 1 and 3.9×10^8 J for 62 m s^{-1} for explosion 2. These values can be compared with the thermal energies of explosions 1 and 2 from equation (18), which are estimated at 8.4×10^{10} J and 3×10^{11} J, respectively, assuming a magma temperature T of 1373 K [*Francalanci et al.*, 1989] and a magma specific heat capacity, C_p, of 1050 J kg^{-1} K^{-1} [*Vosteen and Schellschmidtb*, 2003]:

$$E_T = MTC_p \quad (18)$$

The thermal energies of the two explosions therefore exceed the kinetic energies by approximately 3 orders of magnitude. Note that the kinetic and thermal energies of the gas phase are not taken into account in these calculations.

8.3. Possible Effects of Outsized Particles

[36] The numerical approach to the inverse problem requires us to define a continuous theoretical function for the PSDs characterizing the explosions. In reality, however, explosion-generated PSDs might contain a coarse tail of large, discrete blocks which, although relatively small in number, could have a nonnegligible effect on the mass estimation. For example, the PSDs estimated photoballistically by *Chouet et al.* [1974] at Stromboli contained such coarse tails of blocks. Large blocks ejected during Strombolian explosions at Mount Etna have also been documented by *McGetchin et al.* [1974]. In the present study these have been neglected because they cannot be described by the type of continuous PSD function required by our automatized inversion algorithm. Manual runs have therefore been carried out to assess the sensitivity of mass calculations to an additional fraction of large particles. We define a composite PSD with a continuous part and an additional discrete part that constitute the lower and upper ranges, respectively, of the natural PSD (Figure 12). The coarse tail, consisting of 85 discrete blocks, is represented by an exponential distribution from 0.1 to 1 m in diameter with a median size of 0.23 m, i.e., close to that observed by

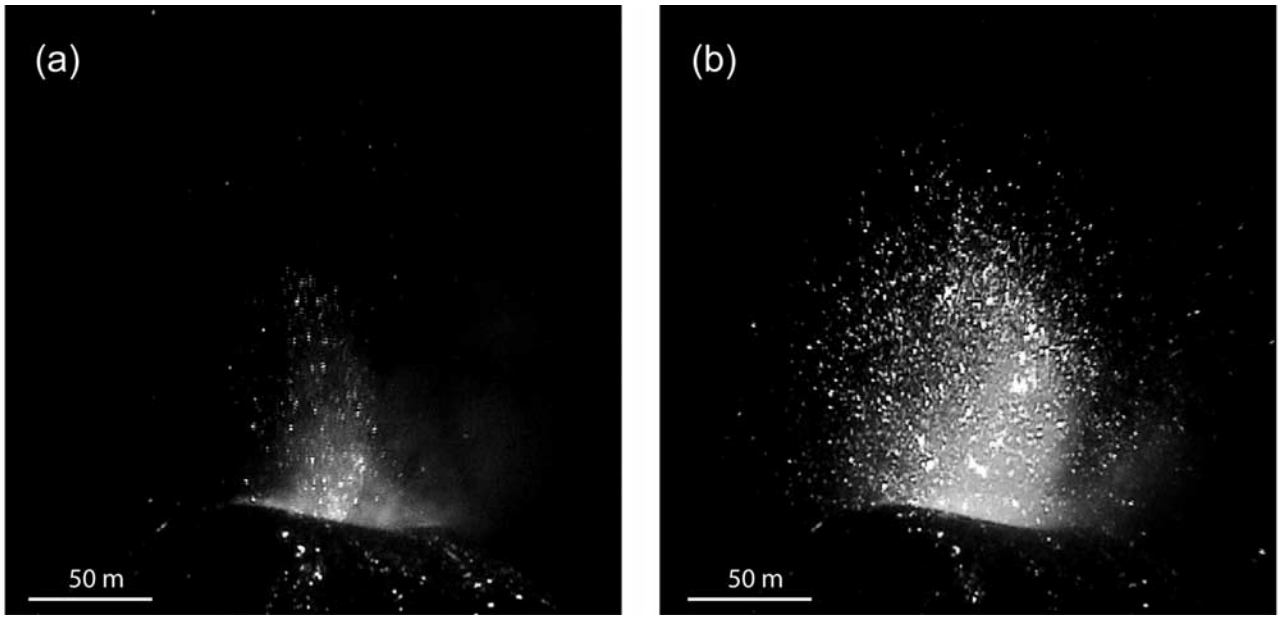

Figure 11. Snapshots of the two explosions from the SE crater of Mount Etna on 4 July 2001. Images are shown at maximum brightness, corresponding to the highest radar reflectivity from lava fragments. (a) The first explosion, occurring at 2141:53 UT, displays a low quantity of lava fragments and lasts 2.2 s, and (b) the second explosion, occurring at 2141:56 UT, displays a much higher number of lava fragments and lasts 2.8 s.

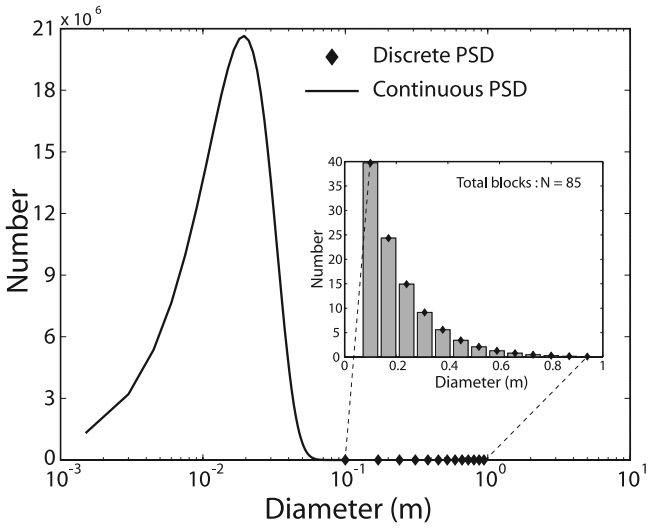

Figure 12. Composite particle size distribution comprising a continuous function to describe the smaller end of the PSD, with an additional coarse tail of large, discrete blocks. The continuous part refers to the PSD of explosion 2 calculated from our algorithm. The coarse tail is constrained from the data of *McGetchin et al.* [1974]; it consists of a total of only 85 blocks with a median size of 0.23 m, but that represents about 10% of the total reflectivity.

McGetchin et al. [1974] at the NE crater of Mount Etna (~0.2 m). Although numerically less abundant by more than 5 orders of magnitude than the smaller particles constituting the continuous PSD (Figure 12), the blocks of this coarse tail account for ~10% of the total reflectivity. This composite PSD is probably a more realistic representation of the explosion ejecta, and gives a total mass of 187,000 kg for explosion 2, in comparison to 206,000 kg for the continuous PSD lacking a coarse tail. We conclude that neglecting large blocks results in overestimation of the mass by only 9% for this explosion. This is because the total mass of pyroclasts is mostly controlled by the large number of small particles, as shown in Figure 7. As a result, all the mass-related parameters listed in Tables 4a–4c and 5a–5c can be regarded as maxima.

9. Discussion

[37] A Doppler radar (VOLDORAD) has been used to estimate for the first time a wide range of physical parameters characterizing Strombolian explosions at Mount Etna. In addition to the velocity data routinely provided by Doppler radar [*Donnadieu et al.*, 2005], the results yield estimates of particle loading (number, mass and volume), as well as derived parameters such as mass flux, time-averaged particle kinetic and thermal energies and, more approximately, particle concentration in the eruptive jet.

[38] Our approach in estimating particle loading, and the parameters derived from it, involves certain assumptions. For example, the electromagnetic scattering model assumes that all particles are smooth, spherical and compositionally homogeneous, which is not the case for pyroclasts. However, bearing in mind the statistical effects of a very large number of rough and complexly shaped particles, as well as our objective of first-order estimation, these simplifications seem reasonable. Another assumption concerns the particle size distribution (PSD) used for data inversion. The inversion procedure involves three physical parameters: two constants defining the PSD (mode and shape factor), and the third being the number of particles corresponding to the mode that evolves during the optimization phase of the inversion procedure. In the present study the mode was constrained from the radar measurements at Mount Etna. On the other hand, the shape factor was constrained independently using published photoballistic data of *Chouet et al.* [1974] from explosions at Stromboli, and was assumed to be representative of the explosion ejecta at Mount Etna. Many problems are inherent in this approach. For example, the photoballistically derived PSD of *Chouet et al.* [1974], while not skewed by atmospheric or depositional processes, is inadequate to describe the fine tail of the distribution, particles of which are too small to be detectable on photographs. On the other hand, *McGetchin et al.* [1974] constructed a PSD at Mount Etna from grain size measurements of Strombolian deposits, but this method also failed to take into account the smallest particles, which are dispersed far from source by the wind. Other difficulties involved in determining PSDs from deposits may also arise from bomb agglutination or from block breakage on impact. In addition, such studies probably fail to sample volumes of ejecta large enough to be statistically representative of real amounts of large blocks. Both photoballistic and ground deposits methods therefore fail to take into account small particles, whose contribution to the total mass is important. In contrast, UV satellite methods such as TOMS or more recently OMI [*Carn et al.*, 2008; *Krotkov et al.*, 2008], succeed in imaging gas (particularly SO2), ash and aerosols released by volcanic eruptions. The IR satellite methods such as Meteosat or MODIS [*Watson et al.*, 2004] are further able to provide estimates of the distal ash content of large eruptive clouds far from the emission source that are mainly composed of small particles. But these satellite-based methods fail to image the larger size fractions segregated earlier during plume ascent. These methods might also be biased by atmospheric effects on particles, such as water vapor content and ice formation. Nevertheless, the comparison of near-source estimates of ejecta mass from ground-based Doppler radar with the mass of distal fine ash estimated by satellite-based methods could bring valuable constraints on the particle segregation from ash clouds through space and time and hence on models of ash dispersal. In order to obtain more accurate values of the mass of ejecta, a more thorough knowledge must be acquired of total source granulometries of volcanic explosions, and of their variability for different eruptive regimes. Insights into such source PSDs could be gained for instance by high-resolution imagery and remote sensing methods working at different wavelengths. Such methods should target regions of the eruptive jet close to the vent in order for all ejected particles to be included. Their combination with ground ash collectors would bring even more stringent constraints. Knowledge acquired on PSDs would additionally provide further valuable insights into fragmentation and explosion processes during volcanic eruptions.

[39] By fixing the explosion source PSD shape factor independently, and by determining the PSD mode using the radar measurements, we obtain a way of estimating the particle loading parameters to a first approximation. Neglecting the inevitable coarse tail of large blocks appears justified on the basis of our calculations. The two PSD assumptions used in this paper each have different advantages. The polydisperse model requires an inversion procedure that takes a long time to compute, but which results in mass estimation to a reasonable first-order accuracy. This approach is probably best adapted to studies of eruption dynamics, where the most accurate possible parameter estimates are required. The monodisperse PSD model, on the other hand, does not require any computing phase, so that mass estimation is fast and straightforward. The disadvantage of this method is that it underestimates the particle loading. This monodisperse model is most suitable for volcano monitoring, where the eruptive parameters could be calculated automatically in real time from the Doppler spectra, but where a lower degree of accuracy could probably be tolerated.

[40] This study has shown that Doppler radar is a powerful, as yet underexploited, tool for quantitative studies of eruptive dynamics. The wide range of physical parameters accessible is potentially valuable for testing mathematical models of eruption jets and plumes. VOLDORAD is also well suited to the routine monitoring of active volcanoes. It can be sited at distances of up to 12 km from the vent, making it useful for the monitoring of large, highly explosive edifices. It functions under harsh weather conditions and has a data sampling rate suitable for the study of explosive activity. The relatively low energy consumption allows us either to set up the system quickly in the field with a small power generator for a limited period of time, or to run the radar continuously at a site supplied with electric power. In addition to classical continuous records of temporal series, VOLDORAD has a ''trigger'' mode, in which sequences of raw data can be recorded at high sampling rate, without basic processing and hence visualization. The system can be activated either on command of the operator [*Dubosclard et al.*, 2004], or by an eruptive seismic signal of some predefined threshold potentially linked to an alarm system. This option is useful when monitoring isolated explosions interspersed with long intervals of quiet activity, as characteristic of many volcanoes. In addition to the immediate benefits for operational surveillance, the long-term deployment of such radar on active volcanoes would enable to document the variability of eruptive behaviors and to build databases potentially useful for future eruptions. Combination with other ground-based methods, such as visual and infrared imagery, broadband seismic, ultrasound detection and gas analysis would shed light on the complex interactions among various eruptive processes. Thermal video such as Forward Looking Infrared Radiometer (FLIR) would be particularly helpful for the study of Strombolian activity. Its capacity to detect both fine ash plumes and large blocks can bring additional constraints on PSDs. This method can also provide further insights on Strombolian source conditions [*Patrick et al.*, 2007]. Besides, our methodology of particle loading estimation could be extended to the study and monitoring of volcanic ash plumes. With this aim, the coupling of multichannel satellite imagery with ground-based radar measurements would be particularly relevant for the mitigation of risks related to ash clouds and for the investigations on ash plume dynamics.

Appendix A: Electromagnetic Scattering Equations

[41] Considering the wide range of particle diameters characterizing volcanic activity, the complete scattering theory is required to account for the effects of large particles. A general solution of electromagnetic wave scattering was given by *Mie* [1908]. The derivation of the electromagnetic scattering model specifically applied to the case of volcanic studies is developed in this section. In this first approach of scattering by volcanic ejecta, we apply Maxwell's equations for plane wave scattered by spherical particles in a homogeneous medium at a large distance [e.g., *Bohren and Huffman*, 1983].

[42] Starting with Maxwell's equation for plane waves:

$$\nabla \cdot E = 0 \tag{A1}$$

$$\nabla \cdot H = 0 \tag{A2}$$

$$\nabla \times E = i\omega\mu H \tag{A3}$$

$$\nabla \times H = -i\omega\varepsilon E \tag{A4}$$

where E and H are the electric and magnetic fields. ε is the dielectric permittivity, μ is the magnetic permeability, and ω is angular frequency. Taking the curl of (A3) and (A4), gives:

$$\begin{aligned} \nabla \times (\nabla \times E) &= i\omega\mu\nabla \times H = \omega^2\varepsilon\mu E \\ \nabla \times (\nabla \times H) &= -i\omega\varepsilon\nabla \times E = \omega^2\varepsilon\mu H \end{aligned} \tag{A5}$$

If we use the vector identity,

$$\nabla \times (\nabla \times A) = \nabla(\nabla \bullet A) - \nabla \bullet (\nabla A) \tag{A6}$$

we obtain

$$\nabla^2 E + \omega^2\varepsilon\mu E = 0 \quad \nabla^2 H + \omega^2\varepsilon\mu H = 0 \tag{A7}$$

where $\nabla^2 A = \nabla \cdot (\nabla A)$. Thus, E and H satisfy the wave equation. The field inside the particle is denoted by (E_1, H_1); the field in the medium surrounding the particle (E_2, H_2) is the superposition of the incident field (E_i, H_i) and the scattered field (E_s, H_s):

$$E_2 = E_i + E_s \quad H_2 = H_i + H_s \tag{A8}$$

The electromagnetic field is required to satisfy the Maxwell equations at points where ε and μ are continuous. However, there is a discontinuity at the boundary of the particle, where the following conditions on the fields are imposed:

$$\begin{aligned} [H_2(x) - H_1(x)] \times n_s &= 0 \\ [E_2(x) - E_1(x)] \times n_s &= 0 \end{aligned} \tag{A9}$$

where n_s is the outward directed normal to the surface of the particle. Under the conditions of our study (far-field region and spherical particle), the scattered field E_s is mainly transverse and can be resolved into components parallel ($E_{//}$) and perpendicular ($E_\perp$) to the scattering plane. The relationship between incident and scattered field amplitudes can be written in matrix form:

$$\begin{pmatrix} E_{//s} \\ E_{\perp s} \end{pmatrix} = \frac{e^{ik_n(R-r_z)}}{-ik_nR} \begin{pmatrix} S_2 & 0 \\ 0 & S_1 \end{pmatrix} \begin{pmatrix} E_{//i} \\ E_{\perp i} \end{pmatrix} \tag{A10}$$

where $k_n = 2\pi/\lambda$ is the wave number, R, the distance to the particle, and r_z, the component of R on the direction of propagation of the incident wave. The radiation of an electromagnetic wave can be described in terms of intensity from the four Stokes parameters (I, Q, U, V) describing the various states of polarization: not polarized (I), polarized horizontally ($+Q$), polarized vertically ($-Q$), polarized at $+45°$ ($+U$), polarized at $-45°$ ($-U$), right circularly polarized ($+V$) or left circularly polarized ($-V$). The relationship between incident and scattered Stokes parameters (indexed i and s, respectively) follows from the amplitude scattering matrix, also called the Mueller matrix [*Bohren and Huffman*, 1983; *Wolf and Voshchinnikov*, 2004]:

$$\begin{pmatrix} I_s \\ Q_s \\ U_s \\ V_s \end{pmatrix} = \frac{\lambda^2}{4\pi^2R^2} \begin{pmatrix} S_{11}(\Theta) & S_{12}(\Theta) & 0 & 0 \\ S_{12}(\Theta) & S_{11}(\Theta) & 0 & 0 \\ 0 & 0 & S_{33}(\Theta) & S_{34}(\Theta) \\ 0 & 0 & -S_{34}(\Theta) & S_{33}(\Theta) \end{pmatrix} \begin{pmatrix} I_1 \\ Q_i \\ U_i \\ V_i \end{pmatrix} \tag{A11}$$

The scattering matrix elements ($S_{i,j}$) depend on Θ, which is the angle between the direction of the incident and the scattered radiation of wavelength λ. VOLDORAD transmits power through a square array of four Yagi antennas, such that the incident wave has a horizontal linear polarization ($I_i = 1$, $Q_i = 1$, $U_i = 0$, $V_i = 0$). Thus, in our case, we denote by $i_{//}$ the corresponding scattered irradiance that only depends on the two first scattering matrix elements (S_{11}, S_{12}):

$$i_{//} = S_{11} + S_{12} = |S_2|^2 \tag{A12}$$

with

$$\begin{aligned} S_{11}(\Theta) &= \tfrac{1}{2}\left(|S_2(\Theta)|^2 + |S_1(\Theta)|^2\right) \\ S_{12}(\Theta) &= \tfrac{1}{2}\left(|S_2(\Theta)|^2 - |S_1(\Theta)|^2\right) \end{aligned} \tag{A13}$$

The sum of the two first scattering matrix elements can then be derived from the single complex amplitude function S_2 in the form of a convergent series:

$$S_2(\Theta) = \sum_{n=1}^{\infty} \frac{2n+1}{n(n+1)} \left(a_n\tau_n(\Theta) + b_n\pi_n(\Theta)\right) \tag{A14}$$

where n is a positive integer, a_n and b_n are the complex scattering coefficients (Mie coefficients), and τ_n and π_n are the angular functions. The series can be terminated after n_c sufficiently large terms. The complex scattering coefficients depend particularly on the size parameter x and the refractive index m of the material [*Sauvageot*, 1992] and are defined as

$$\begin{aligned} a_n &= \frac{m\psi_n(mx)\psi_n'(x) - \psi_n(x)\psi_n'(mx)}{m\psi_n(mx)\xi_n'(x) - \xi_n(x)\psi_n'(mx)} \\ b_n &= \frac{\psi_n(mx)\psi_n'(x) - m\psi_n(x)\psi_n'(mx)}{\psi_n(mx)\xi_n'(x) - m\xi_n(x)\psi_n'(mx)} \end{aligned} \tag{A15}$$

The size parameter $x = k_{nr}$ is a dimensionless variable, r, being the radius of the spherical particle. Ψ and ξ are the Riccati-Bessel functions of first and second kind and can be defined by

$$\begin{aligned} \psi_n(x) &= xj_n(x) \\ \xi_n(x) &= j_n(x) + iy_n(x) \end{aligned} \tag{A16}$$

where j_n and y_n are the spherical Bessel functions of first and second kind defined as

$$\begin{aligned} j_n(x) &= \sqrt{\tfrac{\pi}{2x}} J_{n+1/2}(x) \\ y_n(x) &= \sqrt{\tfrac{\pi}{2x}} Y_{n+1/2}(x) \end{aligned} \tag{A17}$$

The spherical Bessel functions satisfy the recurrence relations:

$$\begin{aligned} z_{n-1}(x) + z_{n+1}(x) &= \tfrac{2n+1}{x} z_n(x) \\ (2n+1)\tfrac{d}{dp} z_n(x) &= nz_{n-1}(x) - (n+1)z_{n+1}(x) \end{aligned} \tag{A18}$$

The angular functions τ_n and π_n depend only on Θ and are defined by the Legendre polynomials,

$$\begin{aligned} \pi_n(\Theta) &= \frac{P_n^1(\Theta)}{\sin\Theta} \\ \tau_n(\Theta) &= \frac{dP_n^1(\Theta)}{d\Theta} \end{aligned} \tag{A19}$$

and can be found from the recurrence relations:

$$\begin{aligned} \tau_n(\Theta) &= n\cos\Theta\pi_n(\Theta) - (n+1)\pi_{n-1}(\Theta) \\ \pi_n(\Theta) &= \tfrac{2n-1}{n-1}\cos\Theta\pi_{n-1}(\Theta) - \tfrac{n}{n-1}\pi_{n-2}(\Theta) \end{aligned} \tag{A20}$$

The scattered irradiance can now be calculated for any particle size, under the special conditions of our sounding using VOLDORAD at Mount Etna (Figure 1). Determining the scattering matrix elements enables us to define the scattering cross section of each particle; this then relates irradiance to reflectivity through the Mie coefficients. VOLDORAD is a monostatic radar (i.e., the same antenna is used for transmission and reception), thus we define a

backscattering cross section (σ_{bks}) for horizontal linear polarization:

$$\sigma_{bks} = \frac{\lambda^2}{4\pi}\left|\sum_{n=1}^{\infty}(-1)^2(2n+1)(a_n - b_n)\right|^2 \quad \text{(A21)}$$

Note that we often use the backscattering efficiency defined as the cross section coefficient normalized by the particle section such as

$$Q_{bks} = \frac{\sigma_{bks}}{\pi r^2} \quad \text{(A22)}$$

The theoretical radar power for a distributed target in a sampling volume (V_s) at a given distance (R) can then be deduced from the radar reflectivity (η), which is simply the sum of the backscattering cross section (σ_{bks}) of each particle over a unit volume [*Doviak and Zrnic*, 1984; *Sauvageot*, 1992],

$$P_{synth} = \frac{C_r V_s \eta}{R^4} \quad \text{(A23)}$$

$$\eta = \sum_{i=1}^{n}\frac{\sigma_{bks}}{V_s} \quad \text{(A24)}$$

where C_r is the radar constant defined by a set of technical parameters related to the radar configuration.

Notation

α radar beam width (deg).
A_0 amplitude of electromagnetic wave.
a_n, b_n complex scattering coefficients (magnetic and electric mode).
B_r noise of Doppler spectrum (mW).
C mass particle concentration (kg m^{-3}).
C_c constant of conversion.
C_d drag coefficient.
C_p magma specific heat capacity (J kg^{-1} K^{-1}).
C_r radar constant (mW m^2).
C_s shape coefficient of a spherical particle.
D diameter of particle (m).
D_L validity limit diameter (m).
D_p average particle diameter (m).
Δt_{cross} duration for the jet to cross a range gate (s).
Δt_{jet} duration of jet production (s).
E,H electric and magnetic fields (N C^{-1}; A m^{-1}).
ε dielectric permittivity (F m^{-1}).
E_k kinetic energy (J).
E_T thermal energy (J).
f_d Doppler frequency (Hz).
f_t transmitted frequency (Hz).
f_w scaled Weibull probability density function.
γ range of the particle size distribution (m).
G_n range gates (sampling volume).
η radar reflectivity (cm^{-1}).
$i_{//}$ parallel scattered irradiance (W m^{-2}).
j_n, y_n spherical Bessel functions of first and second kind.
K complex dielectric factor.
k shape factor.
k_n wave number (rad m^{-1}).
Λ shift factor.
L length of the range gate (m).
m complex refractive index.
M mass of particles (kg).
μ magnetic permeability (H m^{-1}).
μ_n mode of the particle size distribution (m).
∇ vector differential operator (nabla symbol).
$\nabla \bullet A$ divergence of a vector field A.
$\nabla \times A$ curl of a vector field A.
$\nabla^2 A$ Laplacian of a vector field A.
N number of particles.
N_c number of coherent integrations of radar pulses.
N_{max} scale factor.
N_t characteristic Number of Doppler spectra.
ω angular frequency (rad s^{-1}).
$P_{\pm}$ radar power received (mW).
P_{mes} radar raw power received (mW).
P_{synth} radar synthetic power received (mW).
P_t peak power (W).
P_{tot} total radar power received (mW).
Θ angle between incident and scattered radiation (deg).
θ antenna beam elevation angle (deg).
Q_{bks} backscattering efficiency.
r radius of the particle (m).
R slant distance between radar and target (m).
r_z component of R on the incident wave direction.
ρ_a, ρ_p densities of air and particles (kg m^{-3}).
σ_{bks} backscattering cross section (m^2).
$S(v)$ power spectral density.
S_2 complex amplitude function (parallel component).
S_{11}, S_{12} scattering Mueller matrix elements.
S_w scaled Weibull distribution.
τ pulse duration (μs).
π_n, τ_n angular functions.
T magma temperature (K).
t_r pulse repetition period (μs).
V volume of pyroclasts (m^3).
$\bar{V}^{+}_{max}$ average maximum velocity of ejected pyroclasts (m s^{-1}).
$V^{\pm}_{max}$ maximum velocities of ejected pyroclasts (m s^{-1}).
$V^{\pm}_{mean}$ mean velocities of ejected pyroclasts (m s^{-1}).
V_r radial velocity of ejected pyroclasts (m s^{-1}).
V_s radar sampling volume (m^3).
x size parameter.
X vector of variable input parameters.
ψ, ξ Riccati–Bessel functions of first and second kind.
Z radar reflectivity factor (mm^6 m^{-3}).
λ radar wavelength (cm).
$(I,Q,U,V)_{i,s}$ incident and scattered Stokes parameters (polarization state).

[43] **Acknowledgments.** We acknowledge Geoff Wadge and an anonymous reviewer for their thoughtful reviews that significantly enhanced this

paper, and we thank Richard Arculus and Michael P. Ryan for handling the paper. We also thank T. H. Druitt for his insightful comments that considerably improved the manuscript and S. Vergniolle for discussions on this topic. Georges Dubosclard, Roland Cordesses, and Claude Hervier are especially acknowledged for the precious radar measurements carried out in the field, without which this work could not have been achieved. M. Gouhier's Ph.D. work was supported by a French MESR fellowship. Field work on Etna was possible thanks to the logistical help of the INGV Catania and was funded by the CNRS-INSU PNRN programs 1999–2001.

References

Adams, R. J., W. F. Perger, W. I. Rose, and A. Kostinski (1996), Measurements of the complex dielectric constant of volcanic ash from 4 to 19 GHz, *J. Geophys. Res.*, *101*, 8175–8185, doi:10.1029/96JB00193.

Bohren, C. F., and D. R. Huffman (1983), *Absorption and Scattering of Light by Small Particles*, 489 pp., Wiley-Interscience, New York.

Carn, S. A., A. J. Prata, and S. Karlsdóttir (2008), Circumpolar transport of a volcanic cloud from Hekla (Iceland), *J. Geophys. Res.*, *113*, D14311, doi:10.1029/2008JD009878.

Chouet, B., N. Hamisevicz, and T. R. McGetchin (1974), Photoballistics of Volcanic Jet Activity at Stromboli, Italy, *J. Geophys. Res.*, *79*, 4961–4976, doi:10.1029/JB079i032p04961.

Dean, K., S. A. Bowling, G. Shaw, and H. Tanaka (1994), Satellite analyses of movement and characteristics of the Redoubt Volcano plume, *J. Volcanol. Geotherm. Res.*, *62*, 339–352, doi:10.1016/0377-0273(94)90040-X.

Dehn, J., K. Dean, and K. Engle (2000), Thermal monitoring of North Pacific volcanoes from space, *Geology*, *28*, 755–758, doi:10.1130/0091-7613(2000)28<755:TMONPV>2.0.CO;2.

Donnadieu, F., G. Dubosclard, R. Cordesses, T. Druitt, C. Hervier, J. Kornprobst, J. F. Lénat, P. Allard, and M. Coltelli (2005), Remotely monitoring volcanic activity with ground-based Doppler radar, *Eos Trans. AGU*, *86*, 204, doi:10.1029/2005EO210001.

Doviak, R. J., and D. S. Zrnic (1984), *Doppler Radar and Weather Observations*, 562 pp., Academic, Orlando, Fla.

Dubosclard, G., R. Cordesses, P. Allard, C. Hervier, M. Coltelli, and J. Kornprobst (1999), First testing of a volcano Doppler radar (Voldorad) at Mt. Etna, *Geophys. Res. Lett.*, *26*, 3389–3392, doi:10.1029/1999GL008371.

Dubosclard, G., F. Donnadieu, P. Allard, R. Cordesses, C. Hervier, M. Coltelli, M. Privitera, and J. Kornprobst (2004), Doppler radar sounding of volcanic eruption dynamics at Mount Etna, *Bull. Volcanol.*, *66*, 443–456, doi:10.1007/s00445-003-0324-8.

Francalanci, L., P. Manetti, and A. Pecerillo (1989), Volcanological and magmatological evolution of Stromboli volcano (Aeolian islands): The roles of fractional crystallization, magma mixing, crustal contamination and source heterogeneity, *Bull. Volcanol.*, *51*, 355–378, doi:10.1007/BF01056897.

Gouhier, M., and F. Donnadieu (2006), Numerical modeling of Doppler radar signals of Strombolian eruptions, *Eos Trans. AGU*, *87*(52), Fall Meet. Suppl., Abstract V43B-1794.

Harris, D. M., and W. I. Rose (1983), Estimating particles size, concentrations, and total mass of ash in volcanic clouds using weather radar, *J. Geophys. Res.*, *88*, 10,969–10,983, doi:10.1029/JC088iC15p10969.

Harris, D. M., W. I. Rose, R. Roe, and M. R. Thompson (1981), Radar observations of ash eruptions, *U.S. Geol. Surv. Prof. Pap.*, *1250*, 323–333.

Hort, M., and R. Seyfried (1998), Volcanic eruption velocities measured with a micro radar, *Geophys. Res. Lett.*, *25*, 113–116.

Hort, M., R. Seyfried, and M. Vöge (2003), Radar Doppler velocimetry of volcanic eruptions: Theoritical considerations and quantitative documentation of changes in eruptive behaviour at Stromboli, Italy, *Geophys. J. Int.*, *154*, 515–532, doi:10.1046/j.1365-246X.2003.01982.x.

Kittleman, L. R. J. (1964), Application of Rosin's distribution in size frequency analysis of clastic rocks, *J. Sediment. Petrol.*, *34*, 483–502.

Krotkov, N. A., et al. (2008), Validation of SO_2 retrievals from the Ozone Monitoring Instrument over NE China, *J. Geophys. Res.*, *113*, D16S40, doi:10.1029/2007JD008818.

Lacasse, C., S. Karlsdóttir, G. Larsen, H. Soosalu, W. I. Rose, and G. G. J. Ernst (2004), Weather radar observations of the Hekla 2000 eruption cloud, Iceland, *Bull. Volcanol.*, *66*, 457–473, doi:10.1007/s00445-003-0329-3.

Marzano, F. S., G. Vulpiani, and W. I. Rose (2006a), Microphysical characterization of microwave radar reflectivity due to volcanic ash clouds, *IEEE Trans. Geosci. Remote Sens.*, *44*, 313–327, doi:10.1109/TGRS.2005.861010.

Marzano, F. S., S. Barbieri, G. Vulpiani, and W. I. Rose (2006b), Volcanic ash cloud retreival by ground-based microwave weather radar, *IEEE Trans. Geosci. Remote Sens.*, *44*, 3235–3246, doi:10.1109/TGRS.2006.879116.

McGetchin, T. R., M. Settle, and B. Chouet (1974), Cinder cone growth modeled after northeast crater, Mount Etna, Sicily, *J. Geophys. Res.*, *79*, 3257–3272, doi:10.1029/JB079i023p03257.

Mie, G. (1908), Beiträge zur Optik trüber Medien, speziell kolloidaler Metallösungen, *Ann. Phys.*, *330*(3), 377–445.

Nakamura, Y. (1984), The 1888 eruption of Bandai volcano, Japan: Grain size distribution, paper presented at IAVCEI Meeting, Int. Assoc. of Volcanol. and Chem. of the Earth's Interior, Rome, 13–17 Aug.

Patrick, M. R., A. J. L. Harris, M. Ripepe, J. Dehn, D. A. Rothery, and S. Calvari (2007), Strombolian explosive styles and source conditions: Insights from thermal (FLIR) video, *Bull. Volcanol.*, *69*, 769–784, doi:10.1007/s00445-006-0107-0.

Pointin, Y., J. Fournet-Fayard, and F. Donnadieu (2005), Calibration du radar UHF VOLDORAD 2, par comparaison de ses données avec celles du disdromètre du LaMP/OPGC., *Note OPGC 144*, 61 pp., Obs. de Phys. du Globe, Clermont-Ferrand, France.

Riley, C. M., W. I. Rose, and G. J. S. Bluth (2003), Quantitative shape measurements of distal volcanic ash, *J. Geophys. Res.*, *108*(B10), 2504, doi:10.1029/2001JB000818.

Ripepe, M., M. Rossi, and G. Saccorotti (1993), Image processing of explosive activity at Stromboli, *J. Volcanol. Geotherm. Res.*, *54*, 335–351, doi:10.1016/0377-0273(93)90071-X.

Rogers, R., and M. Yau (1989), *A Short Course on Cloud Physics*, Pergamon, Oxford, U.K.

Sauvageot, H. (1992), *Radar Meteorology*, 366 pp., Artech House, Boston, Mass.

Self, S., R. S. J. Sparks, B. Booth, and G. P. L. Walker (1974), The 1973 Heimaey Strombolian Scoria deposit, Iceland, *Geol. Mag.*, *111*, 539–548.

Seyfried, R., and M. Hort (1999), Continuous monitoring of volcanic eruption: A review of various techniques and new results from a frequency-modulated radar Doppler system, *Bull Volcanol.*, *60*, 627–639.

Sheridan, M. F. (1971), Particle-size characteristics of pyroclastic tuffs, *J. Geophys. Res.*, *76*, 5627–5634, doi:10.1029/JB076i023p05627.

Sheridan, M. F., K. H. Wohletz, and J. Dehn (1987), Discrimination of grain-size subpopulations in pyroclastic deposits, *Geology*, *15*, 367–370, doi:10.1130/0091-7613(1987)15<367:DOGSIP>2.0.CO;2.

Spieler, O., M. Alidibirov, and D. B. Dingwell (2003), Grain-size characteristics of experimental pyroclasts of 1980 Mount St. Helens cryptodome dacite: Effects of pressure drop and temperature, *Bull. Volcanol.*, *65*, 90–104.

Vosteen, H. D., and R. Schellschmidtb (2003), Influence of temperature on thermal conductivity, thermal capacity and thermal diffusivity for different types of rock, *Phys. Chem. Earth*, *28*, 499–509.

Watson, I. M., V. J. Realmuto, W. I. Rose, A. J. Prata, G. J. S. Bluth, Y. Gu, C. E. Bader, and T. Yu (2004), Thermal infrared remote sensing of volcanic emissions using the moderate resolution imaging spectroradiometer, *J. Volcanol. Geotherm. Res.*, *135*, 75–89, doi:10.1016/j.jvolgeores.2003.12.017.

Weibull, W. (1939), A statistical theory of the strength of materials, *R. Swed. Inst. Eng. Res.*, *151*.

Weill, A., G. Brandeis, S. Vergniolle, F. Baudin, J. Bilbille, J. F. Fèvre, B. Piron, and X. Hill (1992), Acoustic sounder measurements of the vertical velocity of volcanic jets at Stromboli volcano, *Geophys. Res. Lett.*, *19*, 2357–2360, doi:10.1029/92GL02502.

Williams, H., and A. R. McBirney (1979), *Volcanology*, 397 pp., Freeman Cooper, San Francisco, Calif.

Wohletz, K. H., M. F. Sheridan, and W. K. Brown (1989), Particle size distributions and the sequential fragmentation/transport theory applied to volcanic ash, *J. Geophys. Res.*, *94*, 15,703–15,715, 721, doi:10.1029/JB094iB11p15703.

Wolf, S., and N. V. Voshchinnikov (2004), Mie scattering by ensembles of particles with very large size parameters, *Comput. Phys. Commun.*, *162*, 113–123, doi:10.1016/j.cpc.2004.06.070.

Woods, A. W., and M. I. Bursik (1991), Particle fallout, thermal disequilibrium and volcanic plumes, *Bull. Volcanol.*, *53*, 559–570, doi:10.1007/BF00298156.

F. Donnadieu and M. Gouhier, Laboratoire Magmas et Volcans (UMR 6524 CNRS-IRD), 5, rue Kessler, F-63038 Clermont-Ferrand, France. (F.Donnadieu@opgc.univ-bpclermont.fr; M.Gouhier@opgc.univ-bpclermont.fr)

Abstract

VOLDORAD, a low power UHF Doppler radar, is a portable ground-based system, developed by the Observatoire de Physique du Globe de Clermont-Ferrand (France), especially for the study of explosive volcanic activity. The capabilities of such remote sensing methods to probe safely hazardous eruption jets and plumes constitute a real step forward regarding the in-depth analysis of physical processes controlling the dynamics of volcanic eruptions. The main objective of this work is to bring more stringent constraints, particularly from the development of methodological procedures, on the interpretation of Doppler radar data, with the final aim of better understanding the explosive dynamics. This study has been achieved from Doppler radar measurements carried out at Etna Southeast crater during the eruption of July 4, 2001, and focused on the Strombolian activity. However, processing methods, theoretical forward models and inversion procedures developed here have been achieved with the scope of a more general application, i.e., for various types of eruptions. The thorough analysis of Strombolian explosions by ground-based Doppler radar has permitted to obtain a wide range of source parameters, mainly related to kinetic, loading and geometrical features. Accurate quantitative assessment of these parameters and their evolution with time is crucial for (1) monitoring and early warning of active volcanoes, and (2) to provide better constraints on assumptions included in models of eruptive dynamics, useful for the volcanological community, as well as for ash dispersal prediction models used for risk mitigation.

Résumé

VOLDORAD, un radar Doppler UHF moyenne puissance, est un système portable basé au sol, développé par l'Observatoire de Physique du Globe de Clermont-Ferrand (France), spécifiquement pour l'étude de l'activité volcanique explosive. La capacité de ces méthodes de télédétection à sonder l'intérieur des jets et des panaches volcaniques dangereux constitue un vrai pas en avant concernant l'analyse des paramètres physiques qui contrôlent la dynamique des éruptions volcaniques. L'objectif principal de cette thèse est d'apporter des contraintes plus précises, notamment à partir du développement de procédures méthodologiques, sur l'interprétation des données radar Doppler, dans le but final d'améliorer notre compréhension de la dynamique explosive. Ce travail a été réalisé à partir de mesures radar Doppler acquises pendant l'éruption du cratère Sud-est de l'Etna en Juillet 2001, et s'intéresse plus particulièrement à l'activité Strombolienne. Cependant, les méthodes de traitement, les modèles directs et les procédures d'inversion développés dans cette étude ont été réalisés dans une optique plus générale, et applicable sur différents types de dynamismes. L'étude détaillée de l'activité Strombolienne par la méthode radar Doppler a permis d'obtenir une large gamme de paramètres sources, notamment : les vitesses et masses de gaz et de particules, ainsi que les caractéristiques géométriques des jets. L'estimation quantitative précise de ces paramètres, et de leur évolution au cours du temps est cruciale pour (1) la surveillance et la détection précoce de l'activité volcanique, ainsi que (2) pour l'apport de contraintes sur les hypothèses formulées dans les modèles de dynamique éruptive et dans les modèles de prédiction de dispersion des cendres, indispensables à la minimisation des risques.

Mots-clés : radar Doppler, dynamique éruptive, activité Strombolienne, vitesses de gaz et d'éjecta, flux de masse, Mt. Etna, surveillance, corrélations acoustique et vidéo, modélisation numérique

---

Discipline: Volcanologie
UMR 6524 – Laboratoire Magmas et Volcans
5, rue Kessler 63038 Clermont-Ferrand, France